Electronic contributions to te elastic constants of bismuth and bismuth alloys

Lichnowski, A. J.

ELECTRONIC CONTRIBUTIONS TO THE ELASTIC CONSTANTS OF BISMUTH AND BISMUTH ALLOYS

A thesis

by

ANDREW JERZY LICHNOWSKI B Sc. (Dunelm)

of

Hatfield College

in candidature for the degree of

Doctor of Philosophy

at the University of Durham

October 1975

Department of Applied Physics and Electronics
Science Laboratories, South Road, Durham City

ABSTRACT

The Keyes model has been used to formulate the free electron contribution to the elastic constants of bismuth and its alloys with antimony (0-10 at.% Sb) The electronic contribution has been shown theoretically to be negligible in the intrinsic materials but to be observable in highly donor doped bismuth

The elastic stiffness constant tensor components of single crystals of bismuth and its alloys (3 at.% Sb, 5 at % Sb, 7 at.% Sb and 10 at.% Sb) with antimony have been obtained between 4.2 K and room temperature from measurements of ultrasonic wave velocities made by the pulse echo overlap technique. In contradiction with previous work on polycrystalline alloys the ultrasonic velocities are found to increase monotonically with antimony composition No electronic contribution to the elastic constants can be observed. The temperature dependences of the elastic constants are independent of the antimony concentration.

The elastic constants of bismuth doped with tellurium (0-0.4 at.% Te) have been measured between 4.2 K and room temperature. Changes in some of the elastic moduli have been attributed to electronic contributions, the magnitudes of which are in reasonable agreement with the theoretical predictions. The temperature variation of the ultrasonic velocities, which are independent of tellurium composition, have been explained on the basis of temperature dependent deformation potentials

ACKNOWLEDGEMENTS

First and foremost my thanks go to Dr G.A. Saunders (now Professor Saunders) for his sustained enthusiasm and help, and constant encouragement My thanks are due to Professor D A. Wright for allowing the use of the facilities provided in the Department of Applied Physics and Electronics in the University of Durham. I am indebted to all the technical staff, headed by Mr F Spence, particularly Mr. R. Waite, whose friendly assistance has considerably eased the completion of this research project. I have benefitted from many useful discussions with past and present members of Dr. G.A. Saunders' research group, especially with Cevdet Akgoz and Mike Farley.

For financial assistance I am indebted to the Science Research Council.

CONTENTS

CHAPTER 1

INTRODUCTION

Study of the propagation behaviour of high frequency elastic waves in solids is well established as an effective way of examining the elastic and anelastic properties of materials. The elastic constants of a solid relate directly the total crystal energy, part of which may be electronic in origin. Electronic energy is responsible for the interatomic binding and elastic properties of many solids especially metals, in which an ordered array of cations is held together by a flux of valency electrons. In semiconductors and semimetals the bonding between atoms is localised, either purely covalent, as found in silicon or germanium, or of the mixed covalent-ionic type, as found in the III-V compounds.

Straining of a degenerate semiconductor or semimetal may result in an energy change of the electronic energy bands. If the symmetry of the strain allows for the relative motion of the degenerate bands, the charge carriers become a function of the local strain. The elastic properties may be defined in terms of the free energy with respect to the strain. In semiconductors and semimetals the free energy contains a contribution from the carriers which depends on their distribution over the electronic energy levels. If the strain alters the distribution of the carriers there will be a contribution from this source to the derivatives of the free energy with respect to the strain components, i.e. a contribution to the elastic constants Keyes (1961) was the first to outline the basic principles associated with the contribution to the free energy and to derive the form of the contribution to the elastic constants of the cubic semiconductors silicon and germanium. The electronic contribution to the elastic constants of silicon and germanium has now been well resolved both theoretically and experimentally.

The present work was initially inspired by the paper of Gopinathan and Padmini (1974a) which indicated that the elastic moduli of polycrystalline bismuth-antimony alloys vary extensively in the composition range 0-10 at % antimony, which they partly attributed to a variation in the electronic contribution to the elastic constants.

The first objective has been the determination of the components of the elastic stiffness tensor for a number of bismuth-antimony alloys in the range of composition 0-10 at.% antimony and in the temperature range 4 2 K to 300 K by pulse echo overlap measurements of ultrasound velocity. The theoretical electronic contribution has been formulated from first principles and the expected magnitude has been calculated using the parameters from the literature. The electronic contribution to the free energy is a function of the total electron population, which may be increased by doping the material with elements from neighbouring columns of the periodic table. For example, in n-type silicon and germanium the relative change in the electronic contribution can be two orders of magnitude greater than the atomic fraction of the donor. In the present work the electron population of pure bismuth has been varied by the addition of tellurium, a monovalent donor, and the elastic stiffness constants have been measured as a function of temperature.

In chapter two the band structures of bismuth and bismuth-antimony alloys are reviewed, with particular emphasis on the points pertinent to the present study. In chapter three the formal theory of anisotropic elasticity is applied to rhombohedral crystals and the relationship between ultrasound velocity and the elastic stiffness tensor is established. Chapter four outlines the experimental techniques employed crystal growth and the preparation of samples, the principles of the ultrasonic methods and details of the measuring system are given In chapter five the Keyes model is extended to the bismuth band structure and the form of the electronic contribution to the elastic constants is derived. The magnitude of the electronic contribution is then computed both as a function of composition and temperature in chapter six. The results of ultrasonic velocity measurements on bismuth-antimony alloys in the composition range 0-10 at.% antimony are presented in chapter seven and the elastic behaviour is described Chapter eight presents the results of ultrasound measurements on bismuth doped with tellurium and the electronic contribution to the elastic constants is identified.

CHAPTER 2

THE CRYSTALLOGRAPHY AND BAND STRUCTURE

2.1 Introduction

The group V semimetals bismuth and antimony have been the subject of intense investigation and many important effects in solid state physics were first observed in these solids. These materials contain two atoms in the unit cell each contributing five electrons which are accommodated by the first five Brillouin zones The fifth and sixth Brillouin zones overlap in pure bismuth and antimony allowing some electrons to spill over into the sixth zone, thus, by virtue of the simultaneous occurrence of free electrons and holes. these elements are electrically conductive at all temperatures and therefore resemble metals. However, their carrier properties and their great sensitivity to impurities give them many similarities to semiconductors: thus the term semimetal. Over most of the range of composition the alloys of bismuth and antimony also show semimetallic behaviour, but in the range 8-22 at.% antimony the overlap between the fifth and sixth Brillouin zones disappears and the material behaves as a narrow-gap semiconductor

The exceedingly large number of papers which have been published on bismuth and the bismuth-antimony alloys makes a complete review of the subject a daunting task, for a more comprehensive guide to the literature, the reader is referred to Noothoven van Goor (1971), Boyle and Smith (1962) and Goldsmid (1970). This chapter will discuss only the crystallography and band structure pertinent to the present investigation

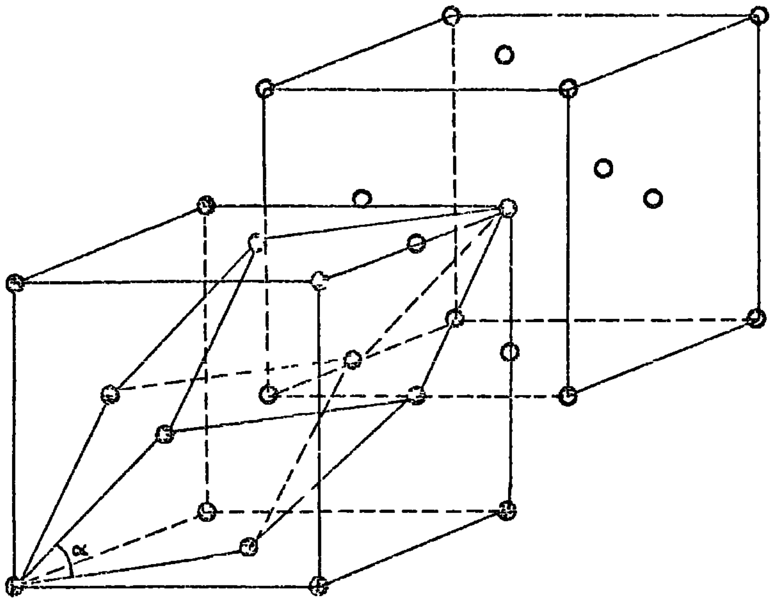

Figure 2.1 Two interpenetrating f.c.c. lattices showing the rhombohedral structure

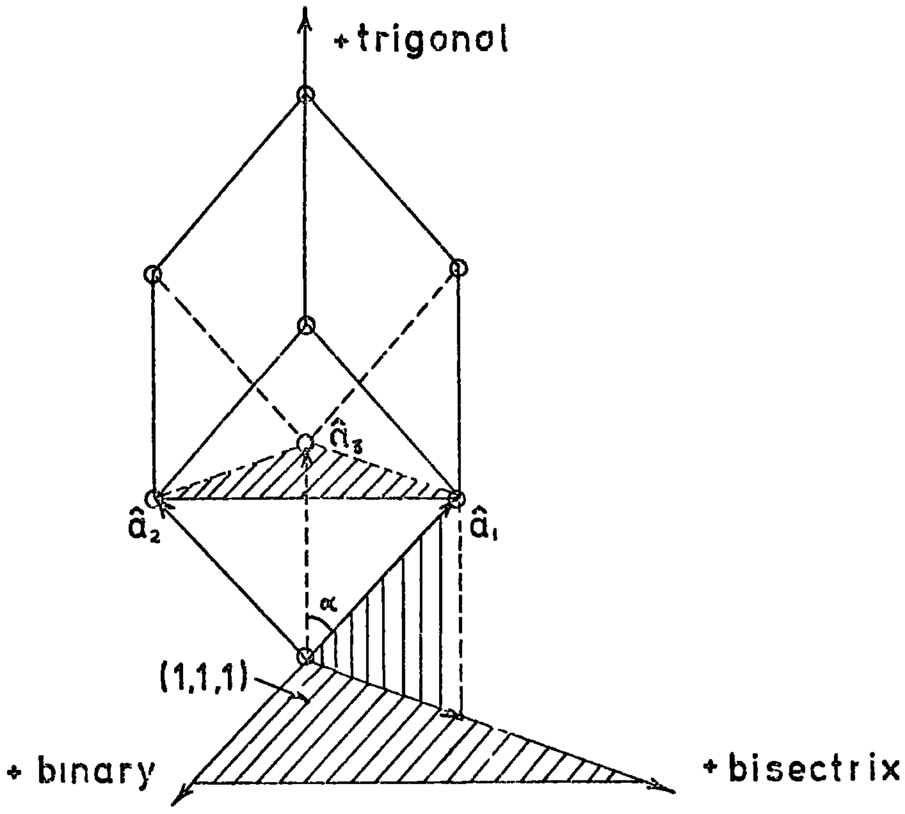

Figure 2.2 The crystallographic coordinates

2.2 Crystal Structure

Bismuth, antimony and the bismuth-antimony alloys all crystallise into a lattice with the rhombohedral, arsenic A7 crystal structure. This crystal structure may be regarded as a distortion of the simple cubic lattice. The distortion can be best illustrated by considering the simple cubic lattice to be composed of two interpenetrating face centred cubic lattices (Figure 2.1), the origin of the first sublattice is taken to be at (0,0,0) and the origin of the second to be at (2u,2u,2u). For the undistorted structure $u = 0.25$ and the angle α, between the unit vectors $\underline{a}_1$, $\underline{a}_2$, $\underline{a}_3$ is 60°. The two lattices are first displaced relative to each other along the body diagonal, thereby altering the value of u slightly from 0.25. The rhombohedral structure is then generated by a stretching of the lattice along the same body diagonal involved in the first displacement. This body diagonal becomes the trigonal, threefold axis of the crystal structure. The rhombohedral crystal parameters α and u of bismuth and antimony are summarised in Table 2.1. The trigonal system may also be described in the frame of the hexagonal lattice (see Cullity (1967) p.462)

An unambiguous orthogonal set of crystallographic coordinates is normally defined as shown in Figure 2.2 (Akgoz, Farley and Saunders 1972). The trigonal axis lies along the body diagonal of the primitive rhombohedral unit cell defined by the lattice translational vectors $\underline{a}_1$, $\underline{a}_2$, $\underline{a}_3$ The bisectrix axis is defined by the projection of any $\underline{a}_1$ on to the trigonal plane, the positive y axis is taken to be outward from the origin to the projection of $\underline{a}_1$. The coordinate system is completed by a positive binary axis.

	Bismuth(a)	Antimony(b)
Hexagonal Lattice Constants	a 4 645 Å c 11.862 Å	4.3084 Å 11.274 Å
Rhombohedral Parameters	u 0.2339 α 57.28°	0.2335 57.12°

References.

(a) Barrett (1960)

Cucka and Barrett (1962)

(b) Barrett, Cucka and Haefner (1963)

<u>Table 2.1</u> The Lattice Constants of pure bismuth and antimony at 298 K.

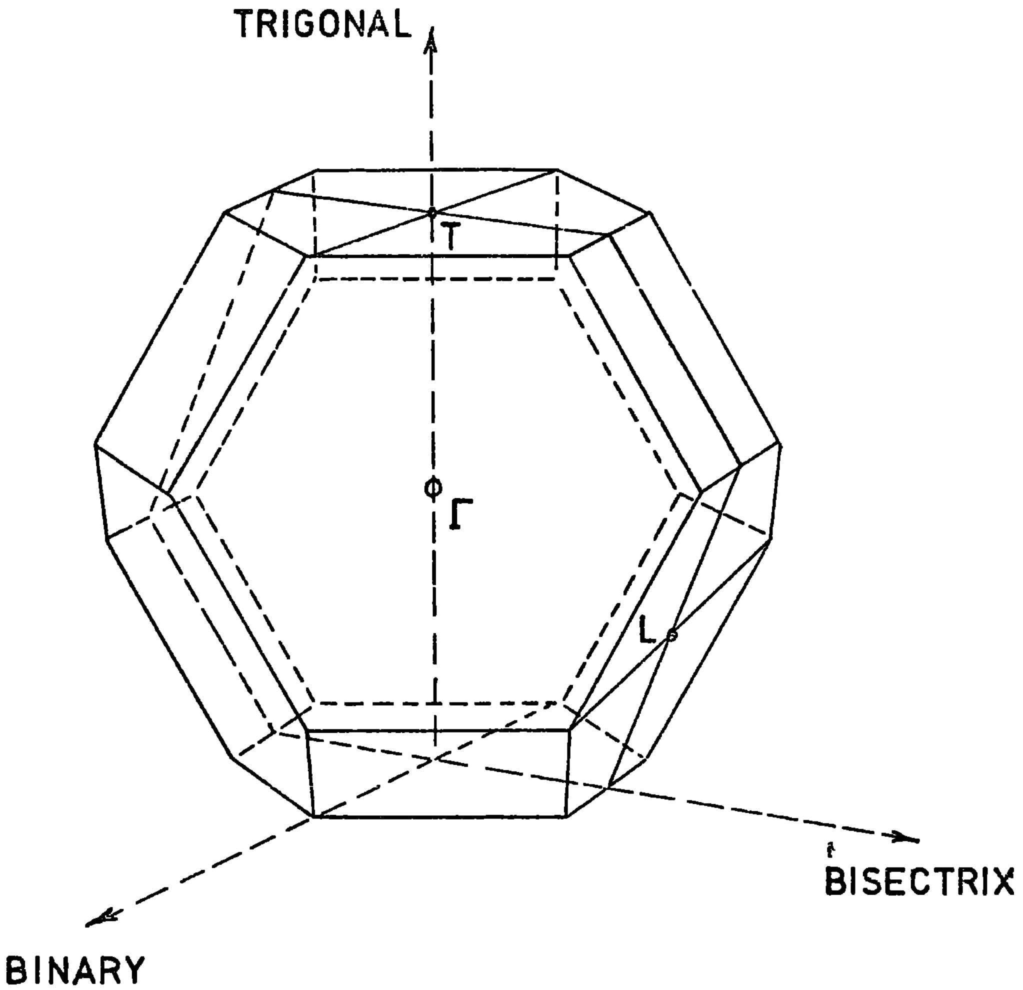

FIG 2.3 THE BRILLOUIN ZONE OF BISMUTH

Bismuth and antimony form solid solutions which crystallize in the rhombohedral structure over the entire range of composition. Cucka and Barrett (1962) have measured the lattice parameters in the range 0-29 at.% antimony and found that the variation is essentially linear.

2.3 The Band Structure of Bismuth and its Alloys

(a) Pure Bismuth

The band structure of bismuth is now well established (for a review see Dresselhaus 1970). The electron Fermi surface consists of three equivalent quasi ellipsoids centred at the La points, occupying $\sim 10^{-5}$ of the volume of the reduced Brillouin zone. The heavy hole Fermi surface comprises a single ellipsoid of revolution located at the T point of the reduced Brillouin zone. At 0 K the La-point electron pockets overlap the T-point hole band by about 38 meV producing a semimetal with a carrier population of 3.3×10^{17} cm^{-3} (Sumengen and Saunders 1972), the electron and hole concentrations are equal. The Fermi level is constrained towards the centre of the region of band overlap and is closer to the edge of that band containing the heavier carrier, i.e. the hole band edge, at 0 K the Fermi level in pure bismuth lies approximately 25 meV above the bottom of the L_s band edge (see Figure 2 4).

Each electron ellipsoid has one principal axis coincident with the crystallographic binary axis. The other two principal axes are tilted away from the bisectrix and trigonal directions by a tilt angle of approximate + 6°, the positive tilt angle is defined as a rotation about the binary +x axis which takes a vector along the +y axis towards the +z axis (see Figure 2.5). For a complete

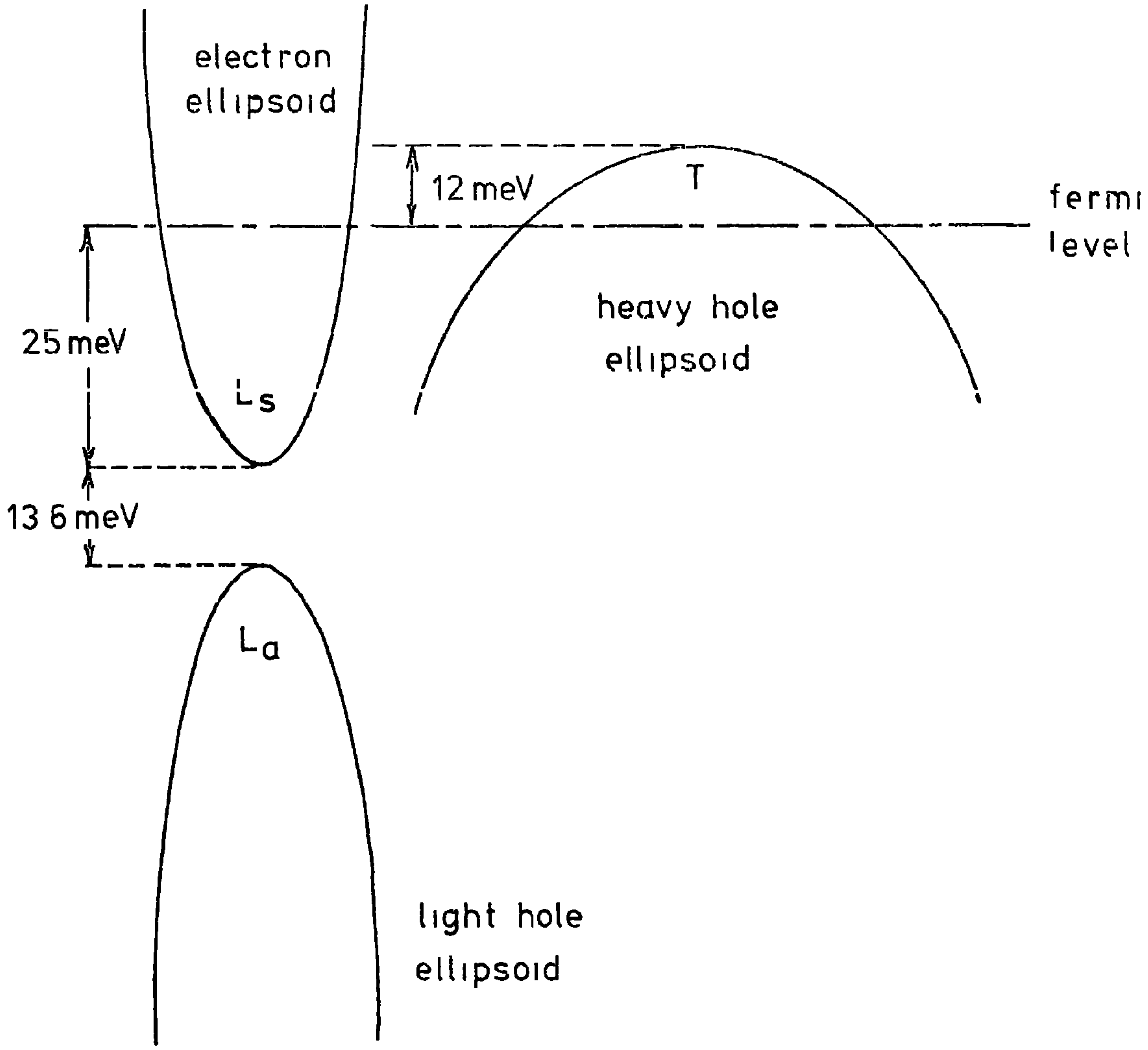

Figure 2.4 The band structure of pure bismuth at 4 2°K

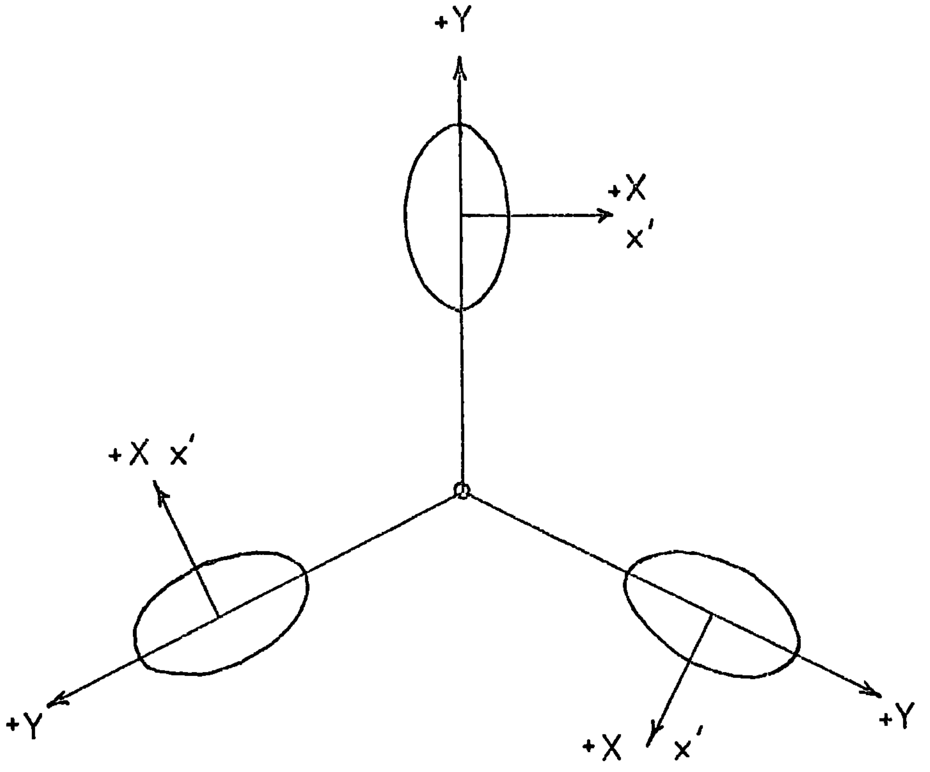

(a) XY plane

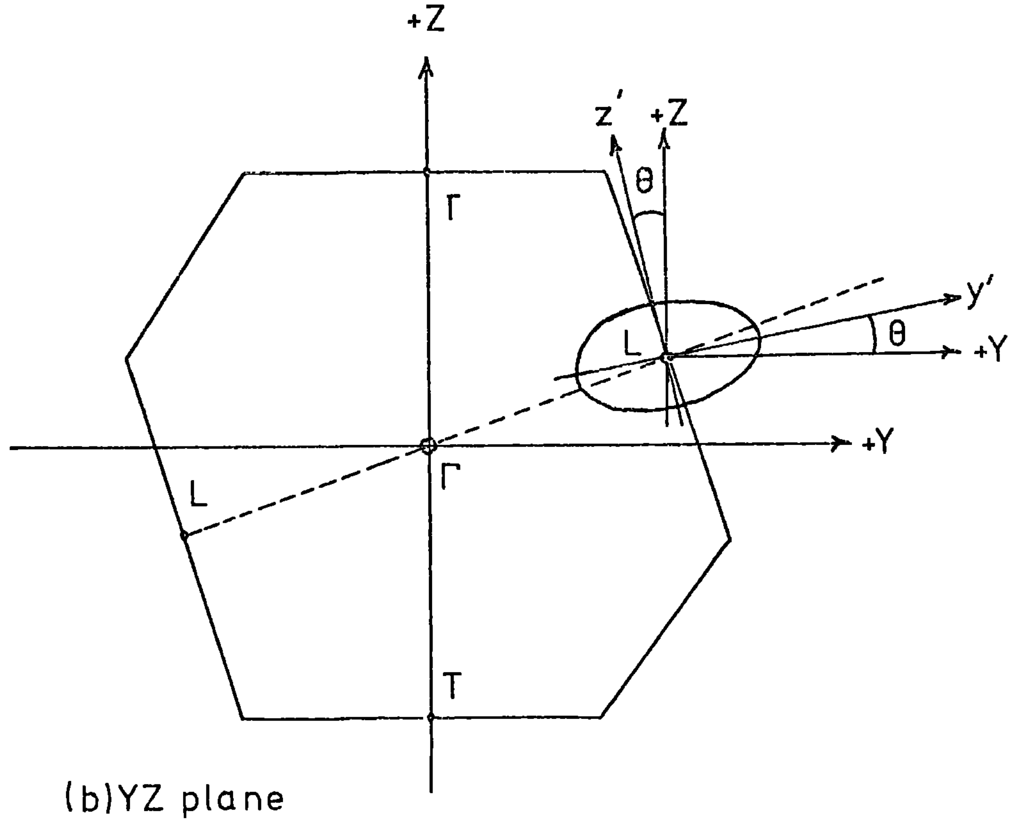

(b) YZ plane

Figure 2.5 Cross section of the Brillouin zone showing the tilt angle (θ) of the electron ellipsoids description of any electronic parameter associated with these ellipsoids, a total of four independent coefficients of the form

$$P^{(1)} = \begin{pmatrix} P_{11} & 0 & 0 \\ 0 & P_{22} & P_{23} \\ 0 & P_{23} & P_{33} \end{pmatrix} \tag{2.1}$$

are required, for example, $P^{(1)}$ may be the mobility, the effective mass or the deformation potential. The tilt angle of the electron ellipsoids, in terms of the general electronic parameter coefficients, is given by

$$\theta = \frac{1}{2}\tan^{-1}\frac{2P_{23}}{P_{22} - P_{33}} \tag{2 2}$$

If the form of the general parameter coefficients of equation 2.1 is assigned to one of the electron ellipsoids (superscript (1)) the form of the coefficient for the other two ellipsoids must be obtained by 120° rotations around the trigonal axis. Therefore

$$P^{(2)} = R^{+}_{120} \; P^{(1)} \; R^{+\,T}_{120} \tag{2.3}$$

and

$$P^{(3)} = R^{-}_{120} \; P^{(1)} \; R^{-\,T}_{120}$$

where

$$R^{+}_{120} = \begin{pmatrix} -\frac{1}{2} & \frac{\sqrt{3}}{2} & 0 \\ -\frac{\sqrt{3}}{2} & -\frac{1}{2} & 0 \\ 0 & 0 & 1 \end{pmatrix}, \quad R^{-}_{120} = \begin{pmatrix} -\frac{1}{2} & -\frac{\sqrt{3}}{2} & 0 \\ \frac{\sqrt{3}}{2} & -\frac{1}{2} & 0 \\ 0 & 0 & 1 \end{pmatrix}$$

and $R^{+\,T}_{120}$ refers to the transpose of R^{+}_{120} .

Since the hole Fermi surface consists of a single ellipsoid of revolution at the T point of the Brillouin zone the electronic components associated with it take the form

$$H = \begin{pmatrix} H_{11} & 0 & 0 \\ 0 & H_{11} & 0 \\ 0 & 0 & H_{33} \end{pmatrix} \qquad (2.4)$$

Lying about 13.6 meV (at 4.2 K, Vecchi and Dresselhaus 1974) below the La conduction band edge is a mirror image valence band edge (L_s band). The carriers in the L_s valence band are referred to as light holes, however, in pure bismuth at ordinary temperatures, their carrier density is low and their effects negligible.

The free carrier concentration increases as the temperature is raised, until at room temperature the carrier population is approximately 2.45 x 10^{18} cm^{-3} (Michenaud and Issi,1972) Thus, when the temperature increases, the tendency of the Fermi level in each electron valley to decrease is compensated by the thermal excitation of more carriers. Hence, while the number of carriers increases in the two bands, the Fermi level should stay at about the same position at all temperatures, the carriers in each band will be at least partially degenerate.

(b) Bismuth-Antimony Alloys

Jain (1959) and subsequent workers (Smith and Wolfe 1962, Brown and Silverman 1964, Dugué 1965, Chu and Kao 1970, Thomas and Goldsmid 1970, for a review see Goldsmid 1970) have shown that the addition of anitmony to bismuth causes a gradual decrease in the overlap energy between the La point electrons and the T point hole band, resulting in a transition from the semimetallic to the semiconducting state. This semimetal to semiconductor transition occurs at approximately 8 at.% antimony (Brandt and Svistova 1970). The recent work of a number of investigators has also shown that the L point energy gap decreases upon addition of antimony, with the result that the L point energy levels undergo a band inversion at some composition before the onset of the semiconducting state. This view is consistent with the theoretical calculation of Lin and Falicov (1966) which show that in pure antimony the L point conduction and valence bands have opposite symmetry to those in bismuth. The magnetoreflection data of Hebel and Smith (1964) led Golin (1968) to propose a model whose L point inversion occurs at 5.7 at.% antimony, after which the L point energy gap increases linearly with increasing antimony concentration. Tichovolsky and Mavroides (1969) from magnetoreflection data have found that the band inversion occurs at 4 at.% antimony, while Brandt (1969) observed the transition to be at approximately 8.5 at.% Sb, uncertainty of the nature of this band inversion still exists.

If there is a progressive change in the band edges with composition, the alloy must revert to the semimetallic state at a higher antimony concentration. The original work of Jain (1959) indicated that the semiconductor to semimetal transition occurred at a composition of approximately 40 at % antimony More recent studies indicate that the transition occurs at 22 at.% antimony (Wehrli 1968, Brandt et al 1970), the suggested cause is an overlap of a valence band at the H-point of the Brillouin zone and the

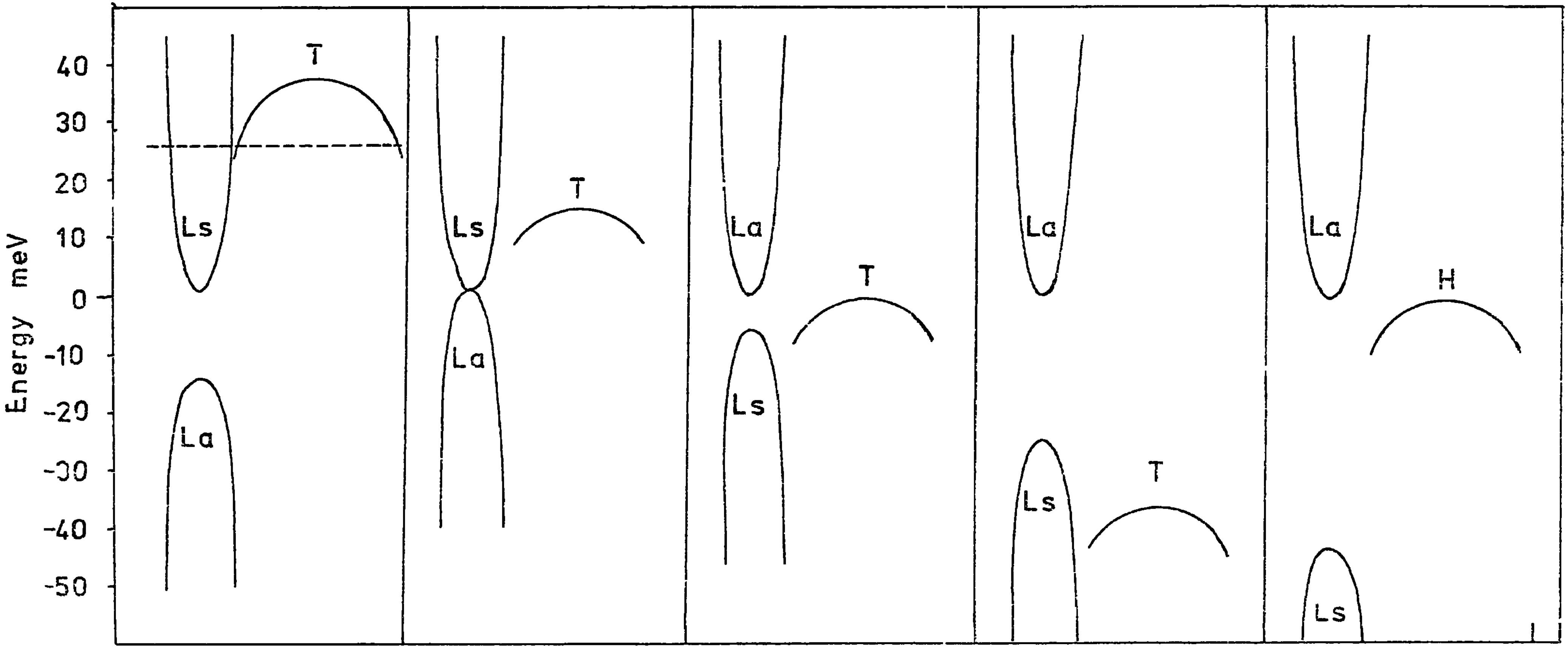

(a) Pure Bi (b) 5 At % Sb (c) 8 At % Sb (d) 15 At % Sb (e) 22 At % Sb

Figure 2 6 Band edge positions of the bismuth-antimony alloys

L_s point conduction band; in pure antimony semimetallic behaviour is a result of an overlap between the H-point hole ellipsoids and the L_s-point electron ellipsoids (Oktu and Saunders 1967). Apart from the galvanomagnetic data of Schnieder and Trinks (1972) (on 30 at.% antimony) and the magnetoreflection results of Apps (1974) (85-100 at.% antimony), little information exists on the band structure in the range of composition 22-100 at.% antimony.

The shape of the energy surfaces of the L and T point ellipsoids have been considered in detail (e.g. Lerner, Cuff and Williams 1968) in the range of composition 0-10 at % antimony. The results indicate that the L and T point pockets retain the shape characteristic of pure bismuth, the same dispersion relations may therefore be assumed.

(c) Donors and Acceptors in Bismuth

Many workers have investigated the effects of doping pure bismuth with elements from neighbouring columns of the periodic table (Noothoven van Goor 1971, G.A. Antcliffe and R T. Bate 1969, R.N. Bhargava 1967, N. Thompson 1936, Wiener 1962), in particular much study has been concentrated on the effects of tellurium (a donor) and tin (an acceptor) The dope densities spoil the intrinsic equality of the electron and hole populations; at high donor or acceptor concentrations only one type of carrier occurs. The addition of tin and tellurium in concentrations of less than 0.1 % is reported to leave the lattice constants practically unchanged (Cucka and Barrett 1962). Consequently it has been standard practice to assume that the rigid band model is applicable (i e. whilst the carrier populations change, the relative positions of the band edges remain constant). Early experiments on doped bismuth suffered from the uncertainty in ascertaining the exact level of doping, but the matter has now been resolved by Noothoven van Goor and Trum (1968) who have proved, with the aid of radioactive tracer analysis, that in bismuth tellurium is a monovalent donor and tin a monovalent acceptor.

The introduction of tellurium into the bismuth lattice increases the electron population in the L_s ellipsoids and decreases the heavy hole population in the T^-_{45} ellipsoid. Conduction electrons and holes can coexist as long as the dope is not heavy, but when 8×10^{17} donors are present (Noothoven van Goor 1971) the electrons are the only carriers, the hole band having been completely filled. Antcliffe and Bate (1966) have suggested that above 55 meV other electron bands exist (at the T point) and that these can become populated by up to 3% of the total electron population The existence of these additional electron bands has not, as yet, been fully confirmed.

The doping of bismuth with tin causes the number of L_s conduction electrons to fall and the hole population in the T^-_{45} level to increase Emptying of the conduction band requires 4×10^{18} acceptors cm^{-3} and at low temperatures only heavy holes exist. At higher temperatures thermal excitation of the electrons from the T point to the L_s band occurs. When the acceptor concentrations are large, there is an appearance of light holes in the valence band at the L point (R.T Bate, Einspruch and May 1969).

Donor and acceptor impurities in bismuth cannot give rise to localised states because of the strong screening of the impurity centres by the free carriers, so that the impurities remain ionized all the way down to temperatures below 4 2 K (Brownell and Hygh, 1967); i.e. the impurity carrier concentration will remain constant with temperature.

2.4 The Dispersion Relations

Shoenberg (1939) was the first to propose a dispersion relation for the Fermi energy surfaces of bismuth in which he assumed that the surfaces were both ellipsoidal and parabolic. The dispersion relation for the electron ellipsoids is given by

$$E = \frac{P_1^2}{2m_1} + \frac{P_2^2}{2m_2} + \frac{P_3^2}{2m_3} + \frac{P_2P_3}{m_4} \qquad (2.5)$$

where P_i ($i = 1,2,3$) are the momenta, m_j ($j = 1,2,3,4$) are the components of effective mass and E is the energy. The data can often be presented in terms of the inverse effective mass tensor $\overleftrightarrow{\alpha}$, where

$$\overleftrightarrow{\alpha} = \overleftrightarrow{m}^{-1} = \begin{pmatrix} \frac{1}{m_1} & 0 & 0 \\ 0 & \frac{m_3}{m_3m_2-m_4^2} & \frac{-m_4}{m_3m_2-m_4^2} \\ 0 & \frac{-m_4}{m_3m_2-m_4^2} & \frac{m_2}{m_3m_2-m_4^2} \end{pmatrix} \qquad (2.6)$$

The cross terms (i e. m_4) arise because two of the principal axes of the electron ellipsoids do not coincide with the crystal axes but are rotated by the tilt angle θ about the binary axis. It is usually more convenient to express the effective mass tensor in terms of a coordinate system in which $\overleftrightarrow{m}$ is diagonal (no cross terms) i.e.

$$\overleftrightarrow{m}' = \begin{pmatrix} m_1' & 0 & 0 \\ 0 & m_2' & 0 \\ 0 & 0 & m_3' \end{pmatrix} \tag{2.7}$$

The two effective mass tensors $\overleftrightarrow{m}'$ and $\overleftrightarrow{m}$ are related by a rotation $R(\theta)$ about the binary axis

$$\overleftrightarrow{m}' = R(\theta)\ \overleftrightarrow{m}\ R^T(\theta) \tag{2.8}$$

where

$$R(\theta) = \begin{pmatrix} 1 & 0 & 0 \\ 0 & \cos\theta & +\sin\theta \\ 0 & -\sin\theta & \cos\theta \end{pmatrix} \tag{2.9}$$

Thus the relationship between the coefficients of the two effective mass tensors is

$$\begin{aligned} m_1' &= m_1 \\ m_2' &= \frac{m_1 + m_3 + \left[(m_2 - m_3)^2 - 4m_4^2\right]^{\frac{1}{2}}}{2} \\ m'_3 &= \frac{m_2 + m_3 - \left[(m_2 - m_3)^2 - 4m_4^2\right]^{\frac{1}{2}}}{2} \end{aligned} \tag{2.10}$$

The ellipsoidal parabolic dispersion relation for the T point hole ellipsoid is

$$E = \frac{P_1^2 + P_2^2}{2M_1} + \frac{P_3^2}{2M_2} \qquad (2\ 11)$$

where M_1 and M_2 are the components of the effective mass tensor of the holes.

The Shoenburg model has been found adequate to describe the T point hole Fermi surface, however, it has failed to describe accurately the electron Fermi surface. Two different dispersion relations have been proposed to explain the departure from the ellipsoidal parabolic model. the ellipsoidal non-parabolic (ENP) model of Lax (1960) and the non-ellipsoidal non-parabolic model (NENP) of Cohen (1961). Non parabolic effects become important because of the strong interaction between the valence and conduction bands at the L points. The ellipsoidal non-parabolic dispersion relation is

$$\frac{P_1^2}{2m_1'(0)} + \frac{P_2^2}{2m_2'(0)} + \frac{P_3^2}{2m_3'(0)} = E\left(1 + \frac{E}{E_g}\right) \qquad (2.12)$$

where $m_i'(0)$ (i = 1,2,3) refer to the band edge effective mass components and E_g is the energy gap at the L point. This model then has an ellipsoidal Fermi surface but non-parabolic bands. The NENP model of Cohen (1961) modifies the dispersion relation still further by the inclusion of a term from the valence band

$$\frac{P_1^{\,2}}{2m_1'(0)} + \frac{P_2^{\,2}}{2m_2'(0)} + \frac{P_3^{\,2}}{2m_3'(0)} = E\left(1 + \frac{E}{E_g}\right) - \frac{1}{E_g}\left(\frac{P_2^{\,2}}{2m_2''(0)}\right)^2 \qquad (2.13)$$

where $m_2''(0)$ is the effective mass in the bisectrix direction at the top of the balence band, since the two bands are mirror images one can assume that $m_2' = m_2''$. The quartic term in P_2 gives rise to a Fermi surface which is distorted from an ellipsoid at large values of P_2.

The NENP dispersion relation represents a band having non-parabolic dispersion in the P_1 and P_3 directions and parabolic dispersion in the direction of P_2 However, as far as the band parameters are concerned, the difference between the Lax and the Cohen model is small. Experimentally it is difficult to differenciate between the two models because the dispersion relations reduce to the same equation over much of the Fermi surface. Moreover, in the region where they differ the effective mass is large and consequently very difficult to measure. Dinger and Lawson (1970) have recently reappraised previous cyclotron resonance data and conclude that the NENP model provides the best fit. In the present work the NENP model has been chosen.

2.5 The Density of States Function

For the ellipsoidal parabolic model, the density of states is ,

$$N^{(1)}(E) = \frac{4}{\pi^{1/2}}\left(\frac{2\pi m^*(EP)}{h^2}\right)^{3/2} E^{1/2} \qquad (2.14)$$

where $m^*(EP) = (m_1'm_2'm_3')^{1/3} m_o$, $m^*(EP)$ is the density of states effective mass, $m_i{}'$ ($i = 1,2,3$) are the Fermi level effective masses and m_o is the free electron mass. In the non-parabolic non-ellipsoidal model the density of states function must take into account the energy variation of the effective masses, where

$$\begin{aligned} m_1{}' &= m_1{}'(0) \left(1 + \frac{2E}{E_g}\right) \\ m_2{}' &= m_2{}'(0) \\ m_3{}' &= m_3{}'(0) \left(1 + \frac{2E}{E_g}\right) \end{aligned} \tag{2.15}$$

and $m_i{}'(0)$ ($i = 1,2,3$) are the effective mass components at the bottom of the conduction band The NENP density of states function therefore becomes

$$N^{(i)}(E) = \frac{4}{\pi^{\frac{1}{2}}} \left(\frac{2\ m^*(\mathrm{NENP})}{h^2}\right)^{3/2} E^{\frac{1}{2}} \left(1 + \frac{2E}{E_g}\right) \tag{2 16}$$

where $m^*(\mathrm{NENP}) = (m_1{}'(0)\ m_2{}'(0)\ m_3{}'(0))^{1/3}\ m_o$

2.6 Summary

This chapter has discussed the important features of the bismuth and bismuth-antimony band structures and has introduced the various dispersion relations used to describe the electron and hole Fermi surfaces. The calculation of the electron contribution to the elastic constants requires the evaluation of the density of states function, for which the appropriate electronic parameters are required. Chapter six will consider these points in greater detail.

CHAPTER 3

ULTRASONIC WAVE PROPAGATION IN THE RHOMBOHEDRAL STRUCTURE

3.1 Introduction

The strains normally encountered in ultrasonic experiments are infinitesimally small and calculations based upon classical linear elasticity, as reviewed by Love (1927), are normally valid. For the sake of completeness a brief outline description of elastic wave propagation as applied to the rhombohedral system is included here, for a comprehensive review the reader is referred to Hearmon (1961), Nye (1957). Truell, Elbaum and Chick (1969) and Musgrave (1970)

3.2 Definition of Stress and Strain

The stress tensor, with components σ_{ij}, is defined as the force per unit area in the x_i direction acting on an area normal to the x_j direction, σ_{ii} are normal (longitudinal) components and σ_{ij} $(i \neq j)$ are shear components. The deformation of a body is defined in terms of the variation of the displacement (u_1, u_2, u_3) with position (x_1, x_2, x_3) and there exist nine components of the form

$$\frac{\partial u_i}{\partial x_j} \quad (i, j = 1,3) \tag{3.1}$$

Two features need to be considered, namely strain within the media (extension per unit length) and body rotations, since a second rank tensor can be expressed as the sum of a symmetrical tensor $(T_{ij} = T_{ji})$ and an antisymmetrical tensor $(T_{ij} = -T_{ji})$, the strain tensor can be expressed as the symmetrical part, with components

$$\varepsilon_{ij} = \frac{1}{2}\left(\frac{\partial u_i}{\partial x_j} + \frac{\partial u_j}{\partial x_i}\right) \qquad (3.2)$$

and the rotation tensor can be expressed as the antisymmetric part, with components

$$\omega_{ij} = \frac{1}{2}\left(\frac{\partial u_i}{\partial x_j} - \frac{\partial u_j}{\partial x_i}\right) \qquad (3.3)$$

If the body is elastic, the relationship between stress and strain is linear and may be expressed by the familiar Hooke's Law. In an orthogonal cartesian coordinate system this law takes the form

$$\sigma_{ij} = C_{ijk\ell}\,\varepsilon_{k\ell} \qquad i,j,\ell,k = 1,2,3 \qquad (3.4)$$

and

$$\varepsilon_{ij} = S_{ijk\ell}\,\sigma_{k\ell} \qquad i,j,\ell,k = 1,2,3$$

where $C_{ijk\ell}$ and $S_{ijk\ell}$ are the elastic stiffness and compliance constants respectively, both are tensors of the fourth rank. In the generalised form of Hooke's Law there are 81 components of the elastic stiffness tensor. However, by considering the rotational and translational equilibrium conditions for an element of volume in the deformed state, it can be shown that the stress and strain tensors must be symmetric (i e $\sigma_{ij} = \sigma_{ji}$ and $\varepsilon_{ij} = \varepsilon_{ji}$), reducing the total number of independent stress and strain coefficients to six, this implies that since

$$C_{ijk\ell} = C_{jik\ell} = C_{ji\ell k} = C_{ij\ell k} \qquad (3.5)$$

the total number of independent elastic constants is reduced to 36. Furthermore, the restriction that the elastic potential is a function of thermodynamic state alone implies that

$$C_{ijk\ell} = C_{k\ell ij} \qquad (3\ 6)$$

This condition reduces the independent elastic constants to 21. Consideration of the crystal symmetry leads to the vanishing of some of the elastic constants and may lead to algebraic relations amongst the remainder, for example, for a complete description of the elastic behaviour of a cubic material only three constants are necessary (C_{11}, C_{12} and C_{44}).

For brevity and compactness, it is convenient to adopt the following contracted matrix notation.

$$11 = 1\ ,\quad 22 = 2\ ,\quad 33 = 3\ ,\quad 32,23 = 4\ ,\quad 13,31 = 5\ ,\quad 12,21 = 6\ ,$$

(for example, $C_{1132} = C_{14}$). The elastic constants may then be represented by a symmetric 6 x 6 matrix, with components C_{ij}, $i,j = 1,6$. In this notation Hooke's Law becomes

$$\sigma_i = C_{ij}\,\varepsilon_j \qquad (i,j = 1,2,3) \qquad (3.7)$$

and

$$\varepsilon_i = S_{ij}\,\sigma_j \qquad (i,j = 1,2,3)\ .$$

3 3 Elastic Constants of Bismuth

Bismuth and the bismuth-antimony alloys crystallise in a rhombohedral crystal structure, the crystallographic symmetry reduces the total number of independent elastic constants to six, the elastic constant matrix then taking the form

$$\begin{bmatrix} C_{11} & C_{12} & C_{13} & C_{14} & 0 & 0 \\ C_{12} & C_{11} & C_{13} & -C_{14} & 0 & 0 \\ C_{13} & C_{13} & C_{33} & 0 & 0 & 0 \\ C_{14} & -C_{14} & 0 & C_{44} & 0 & 0 \\ 0 & 0 & 0 & 0 & C_{44} & C_{14} \\ 0 & 0 & 0 & 0 & C_{14} & C_{66} \end{bmatrix}$$

where $C_{66} = [C_{11} - C_{12}]/2$

3.4 Equation of Motion

By considering the forces on opposite faces of an infinitesimally small parallelopipid (the element of volume) and by assuming that the body force components are zero, the equation of motion for an elastic material becomes

$$\frac{\partial \sigma_{ij}}{\partial x_j} = \rho \frac{\partial^2 u_i}{\partial t^2} \qquad (3.9)$$

where t is time and ρ is density. Substituting the stress-strain relationship (equations 3 2 and 3 4) in this expression gives

$$C_{ijk\ell}\left(\frac{\partial^2 u_\ell}{\partial x_k\, \partial x_j} + \frac{\partial^2 u_\ell}{\partial x_j\, \partial x_k}\right) = 2\rho \frac{\partial^2 u_i}{\partial t^2} \qquad (3.10)$$

Since $C_{ijk\ell}$ is symmetrical the expression reduces to

$$C_{ijk\ell} \frac{\partial^2 u_\ell}{\partial x_k \partial x_j} = \rho \frac{\partial^2 u_i}{\partial t^2} \qquad (3.11)$$

In any crystalline medium each direction of propagation can support three independent waves, each with a characteristic velocity and with particle displacements which are mutually orthogonal. Consequently, three solutions to the equation of motion in the form of plane travelling waves are sought ,

$$u_\ell = u_{o\ell} \exp i(\omega t - \underline{k}\ \underline{r}) \qquad \ell = 1,2,3 \qquad (3.12)$$

Each wave travels in the direction given by the propagation vector $\underline{k}$ (k_1,k_2,k_3), the magnitude and direction of the propagation vector are defined by

$$\underline{k} = \left(\frac{2\pi}{\lambda}\right)\hat{\underline{n}} = \left(\frac{\omega}{v}\right)\hat{\underline{n}} \qquad (3.13)$$

where λ is the wavelength, ω is the angular frequency, v is the phase velocity and $\hat{\underline{n}}(n_1,n_2,n_3)$ is the unit vector drawn normal to the wavefront.

By differentiating equation (3.12) and substituting into equation (3.11) the equation of motion becomes

$$C_{ijk\ell}\ u_{o\ell}\ n_k\ n_j = \rho v^2\ u_{oi} \qquad i = 1,2,3 \qquad (3.14)$$

For a particular crystallographic direction, defined by $\hat{\underline{n}}(n_1,n_2,n_3)$, the equation of motion will provide three solutions, one of which resembles a longitudinal (or compressional wave) and two of which resemble transverse waves (particle motion normal to the direction of propagation). A pure longitudinal plane wave is defined as one which has the particle motion in the direction of propagation, a pure transverse wave has its particle motion normal to the propagation direction In general, however, the solutions of the equation of motion are neither pure longitudinal nor pure transverse. Waves which have particle motions most closely resembling pure modes are referred to as either quasi-longitudinal or quasi-shear modes.

3.5 Solution of the Equation of Motion

For the rhombohedral system the equation of motion expands to give the following three equations

$$
\begin{aligned}
(L_{11} - \rho v^2)u_{o_1} &+ L_{12}u_{o_2} &+ L_{13}u_{o_3} &= 0 \\
L_{12}u_{o_1} &+ (L_{22} - \rho v^2)u_{o_2} &+ L_{23}u_{o_3} &= 0 \qquad (3.15) \\
L_{13}u_{o_1} &+ L_{23}u_{o_2} &+ (L_{33} - \rho v^2)u_{o_3} &= 0
\end{aligned}
$$

where the L_{ij}'s are the Christoffel coefficients

$$L_{11} = C_{11}\, n_1^2 + 2C_{14}\, n_2 n_3 + C_{44}\, n_3^2 + \frac{1}{2}\,(C_{11} - C_{12})$$

$$L_{12} = \frac{1}{2}\,(C_{11} + C_{12})\, n_1 n_2 + 2C_{14}\, n_1 n_3$$

$$L_{13} = 2C_{14}\, n_1 n_2 + (C_{13} + C_{44})\, n_1 n_3$$

$$L_{22} = C_{14}\, n_1^2 + (C_{13} + C_{44})\, n_2 n_3 - C_{14}\, n_2^2$$

$$L_{23} = C_{33}\, n_3^2 + C_{44}\, (n_1^2 + n_2^3)$$

$$L_{33} = C_{14}\, n_1^2 + (C_{13} + C_{44})\, n_2 n_3 - C_{14}\, n_2^2$$

For a complete determination of all the elastic constants a minimum of three crystallographic directions must be chosen. Measurements along the major crystallographic axes will yield all the elastic stiffness constants except C_{13} and the sign of C_{14}, the further data can be obtained from any direction except for those in the xy plane or along the z axis In the present work measurements were undertaken on [100], [001] and $[0,-\frac{1}{\sqrt{2}},\frac{1}{\sqrt{2}}]$ (or $[0,\frac{1}{\sqrt{2}},\frac{1}{\sqrt{2}}]$) samples, in the following sections the equation of motion for these propagation directions is solved, the notation used is consistent with that of Eckstein, Reneker and Lawson (1960).

(a) Propagation in the [001] Direction

For $n_1 = 0$, $n_2 = 0$, $n_3 = 1$, the Christoffel equations simplify to

$$
\begin{aligned}
&(i) && (C_{44} - \rho v^2)u_{o_1} = 0 \\
&(ii) && (C_{44} - \rho v^2)u_{o_2} = 0 \qquad (3\ 17) \\
&(iii) && (C_{33} - \rho v^2)u_{o_3} = 0
\end{aligned}
$$

Solution of these equations yields the velocities of a pure longitudinal (particle displacement vector parallel to the propagation direction) wave

$$\rho v_7^2 = C_{33} \qquad (3.18)$$

and a pure degenerate shear wave

$$\rho v_8^2 = C_{44} \qquad (3.19)$$

which may be polarised in any direction in the xy plane

(b) Propagation in the [100] Direction

For $n_1 = 1$, $n_2 = 0$, $n_3 = 0$ the Christoffel equations simplify to

$$\text{(i)} \qquad (C_{11} - \rho v^2) u_{o_1} = 0$$

$$\text{(ii)} \qquad [\tfrac{1}{2}(C_{11} - C_{12}) - \rho v^2] u_{o_2} + C_{14}\, u_{o_3} = 0 \qquad (3.20)$$

$$\text{(iii)} \qquad C_{14}\, u_{o_2} + (C_{44} - \rho v^2)\, u_{o_3} = 0$$

Solution of (i) yields the velocity of a pure longitudinal mode

$$\rho v_1^{\,2} = C_{11} \qquad (3.21)$$

Combination of (ii) and (iii) gives the velocity relationships for the two pure shear modes

$$\rho v_{2,3}^{\,2} = \frac{1}{2}\,[(C_{66} + C_{44}) \pm \{(C_{44} - C_{66})^2 + 4C_{14}^2\}^{\frac{1}{2}}] \qquad (3.22)$$

The direction of particle motion for each of the pure shear modes is given by

$$\tan \psi = \frac{u_{o_3}}{u_{o_2}} = -\left(\frac{C_{14}}{C_{44} - \rho v_{2,3}^2}\right) \qquad (3.23$$

where ψ is the angle the particle displacement vector makes with the xy plane.

(a) Propagation in the $[0, -\frac{1}{\sqrt{2}}, \frac{1}{\sqrt{2}}]$ Direction

For $n_1 = 0$, $n_2 = -\frac{1}{\sqrt{2}}$, $n_3 = \frac{1}{\sqrt{2}}$ the Christoffel equations reduce to

$$\text{(i)} \quad [-C_{14} + \tfrac{1}{2}C_{44} - \tfrac{1}{4}(C_{11} - C_{12}) - \rho v^2]\, u_{o_1} = 0$$

$$\text{(ii)} \quad [C_{14} + \tfrac{1}{2}C_{11} + \tfrac{1}{2}C_{44} - \rho v^2] u_{o_2} + [-\tfrac{1}{2}(C_{13} + C_{44}) - \tfrac{1}{2}C_{14}] u_{o_3} = 0$$

$$\text{(iii)} \quad [\tfrac{1}{2}C_{14} - \tfrac{1}{2}(C_{13} + C_{44})]\, u_{o_2} + [\tfrac{1}{2}C_{33} + \tfrac{1}{2}C_{44} - \rho v^2]\, u_{o_3} = 0$$

$$(3.24)$$

Expression (i) corresponds to a pure transverse wave whose velocity is given by

$$\rho v_{13}^2 = \frac{1}{2}(C_{66} + C_{44}) - C_{14} \tag{3.25}$$

Solution of (ii) and (iii) yields the velocity relationship for a quasi longitudinal and a quasi shear mode

$$2\rho v_{12,14}^2 = \frac{1}{2}(C_{11} + C_{33}) + C_{44} + C_{14} \pm \left\{ \left[\frac{1}{2}(C_{11} - C_{33}) + C_{14}\right]^2 + \left[C_{13} + C_{44} + C_{14}\right]^2 \right\}^{\frac{1}{2}} \tag{3.26}$$

The particle displacement direction is given by

$$\tan\psi = \frac{u_{o_3}}{u_{o_2}} = -\left[\frac{(C_{14} + C_{11/2} + C_{44/2} - \rho v_{12,14}^2)}{(-\frac{1}{2}(C_{13} + C_{44}) - \frac{1}{2}C_{14})}\right] \tag{3.27}$$

where ψ is the angle the particle displacement vector makes with the xy plane.

The relationship between the velocity and the elastic constants for the selected propagation directions is given in Table 3.1; the polarization vectors have been calculated from the data for pure bismuth at room temperature (the elastic constants are taken from Chapter 7).

3.6 The Energy Flux Vector

It is an experimental necessity to know the energy flux vector associated with the direction of propagation, since deviations of the energy flux from the propagation direction can result in the wave impinging on the sides of the specimen, giving rise to mode

Propagation Direction	Polarization Direction	Mode	Velocity	Relationship between velocity and elastic constants
[100]	[100]	Pure Longitudinal	V_1	$\rho V_1^2 = C_{11}$
[100]	[0,0.8594,0.5144]	Pure Shear	V_2	$\rho V_2^2 = \frac{1}{2}\left[(C_{66}+C_{44}) - \left((C_{44}-C_{66})^2+4C_{14}^2\right)^{\frac{1}{2}}\right]$
[100]	[0,0.5144,-0.0594]	Pure Shear	V_3	$\rho V_3^2 = \frac{1}{2}\left[(C_{66}+C_{44}) - \left((C_{44}-C_{66})^2+4C_{14}{}^2\right)^{\frac{1}{2}}\right]$
[001]	[001]	Pure Longitudinal	V_7	$\rho V_7^2 = C_{33}$
[001]	[cos θ , sin θ , 0]	Pure Degenerate Shear	V_8	$\rho V_8^2 = C_{44}$
$[0,\frac{1}{\sqrt{2}},\frac{1}{\sqrt{2}}]$		Quasi Longitudinal	V_9	$\rho V_9^2 = \frac{1}{2}\left[\frac{1}{2}(C_{11}+C_{33})+C_{44}-C_{14}+\left\{\left[\frac{1}{2}(C_{11}-C_{33})-C_{14}\right]^2+\left[C_{13}+C_{44}-C_{14}\right]^2\right\}^{\frac{1}{2}}\right]$
$[0,\frac{1}{\sqrt{2}},\frac{1}{\sqrt{2}}]$		Pure Shear	V_{10}	$\rho V_{10}^2 = \frac{1}{2}(C_{66}+C_{44})+C_{14}$
$[0,\frac{1}{\sqrt{2}},\frac{1}{\sqrt{2}}]$		Quasi Shear	V_{11}	$\rho V_{11}^2 = \frac{1}{2}\left[\frac{1}{2}(C_{11}+C_{33})-C_{44}-C_{14}-\left\{\left[\frac{1}{2}(C_{11}-C_{33})-C_{14}\right]^2+\left[C_{13}+C_{44}-C_{14}\right]^2\right\}^{\frac{1}{2}}\right]$
$[0,-\frac{1}{\sqrt{2}},\frac{1}{\sqrt{2}}]$	[0,-0.8421,0.3695]	Quasi Longitudinal	V_{12}	$\rho V_{12}^2 = \frac{1}{2}\left[\frac{1}{2}(C_{11}+C_{33})+C_{44}+C_{14}+\left\{\left[\frac{1}{2}(C_{11}-C_{33})+C_{14}\right]^2+\left[C_{13}+C_{44}+C_{14}\right]^2\right\}^{\frac{1}{2}}\right]$
$[0,-\frac{1}{\sqrt{2}},\frac{1}{\sqrt{2}}]$	[1,0,0]	Pure Shear	V_{13}	$\rho V_{13}^2 = \frac{1}{2}(C_{66}-C_{44})-C_{14}$
$[0,-\frac{1}{\sqrt{2}},\frac{1}{\sqrt{2}}]$	[0,0.5695,0.8421]	Quasi-Shear	V_{14}	$\rho V_{14}^2 = \frac{1}{2}\left[\frac{1}{2}(C_{11}+C_{33})+C_{44}+C_{14}-\left\{\left[\frac{1}{2}(C_{11}-C_{33})+C_{14}\right]^2+\left[C_{13}+C_{44}+C_{14}\right]^2\right\}^{\frac{1}{2}}\right]$

Table. 3.1

conversion and considerable error in the velocity measurements (Figure 3.1) Brugger (1965) has studied the effect of crystal symmetry on the energy flux vector, he concludes that for a pure longitudinal wave the energy flux vector is always parallel to the propagation direction; the same is true for a pure transverse wave propagated along a direction with a twofold, fourfold or sixfold symmetry or normal to a reflection plane.

Since in bismuth the x axis is of twofold symmetry, the pure longitudinal and the two pure shear modes will each have the energy flux vector parallel to the propagation direction, the same result is obtained for the pure longitudinal mode along the trigonal axis. Because the threefold symmetry along the z axis allows degenerate pure shear modes of arbitrary polarization to propagate, the deviation of the energy flux vector manifests itself in the phenomenon of internal conical refraction, as the particle displacement vector is rotated about the trigonal axis through 180° the energy flux vector rotates through 360°, thereby generating a cone of possible directions for energy flow (see Truell, Elbaum and Chick (1969 P.36). Propagation along the $[0, \frac{1}{\sqrt{2}}, \frac{1}{\sqrt{2}}]$ and $[0, -\frac{1}{\sqrt{2}}, \frac{1}{\sqrt{2}}]$ directions yields, in each case, one pure transverse mode polarized along the binary axis and two quasi-pure modes polarized in the yz plane, since none of these modes satisfy the conditions of Brugger, they must have energy flux vectors which deviate from the propagation direction. Pace and Saunders (1971) have calculated the energy flux deviations of the group VB semimetals for propagation directions in the zy plane, reference to their results has been made when considering the geometrical configuration of the samples.

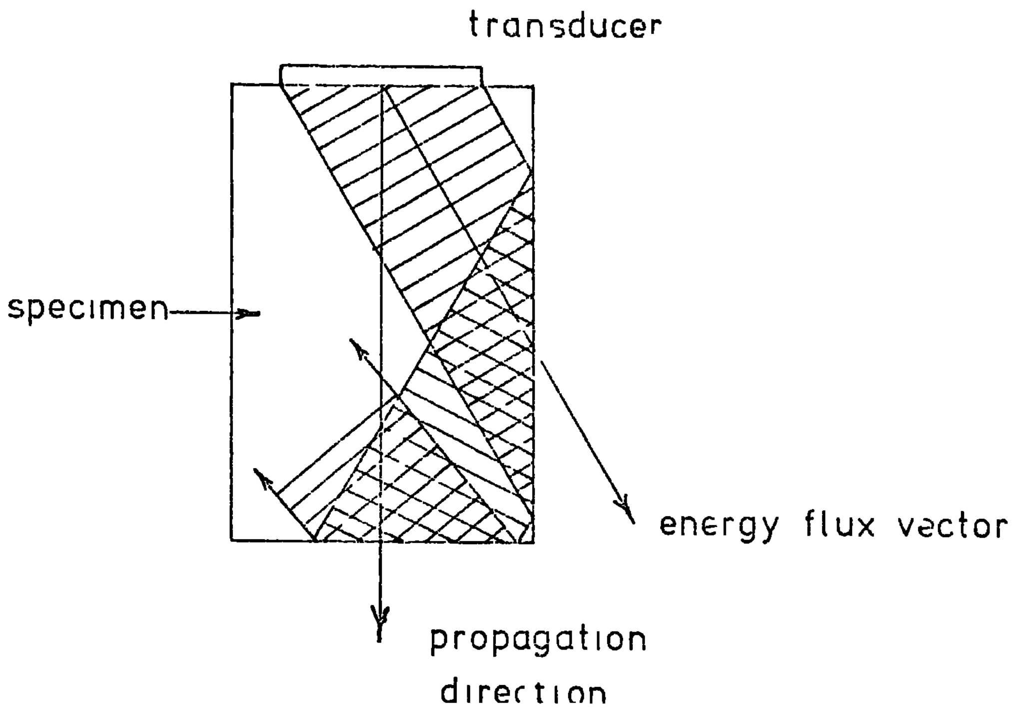

(a) Incorrectly shaped specimen giving rise to 'wall bounce' and mode conversion

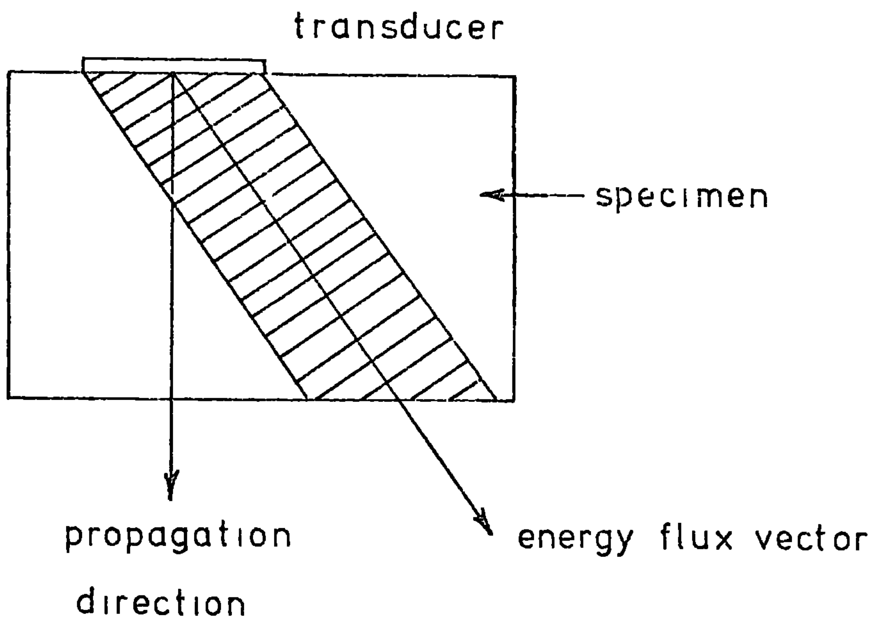

(b) Correctly shaped specimen

Figure 31

3.7 Adiabatic and Isothermal Elastic Constants

Mason (1947) has shown that there exists a difference between the adiabatic elastic constants, which apply to rapid loading, and the isothermal elastic constants, which refer to slow or static loading. The difference is given by

$$C^{A}_{ij} - C^{I}_{ij} = \frac{\alpha_i \alpha_j T_v}{C_v} \qquad (3.28)$$

where the superscripts A and I refer to the adiabatic and isothermal elastic constants respectively, α_i and α_j are the temperature coefficients of stress, T_v is the temperature and C_v is the specific heat at constant volume. In practice, the difference between the adiabatic and isothermal elastic constants is less than 1%. Under conditions of ultrasonic measurements the adiabatic elastic constants are obtained.

3.8 The Strain Energy

The strain energy is effectively the energy of deformation of a solid and many be related to the strain coefficients in the following manner ,

$$\phi = \phi_o + gC_{ij}\,\varepsilon_{ij} + \frac{1}{2}C_{ijk\ell}\,\varepsilon_{ij}\,\varepsilon_{k\ell} + \frac{1}{3}(C_{ijk\ell mn})\varepsilon_{ij}\,\varepsilon_{k\ell}\,\varepsilon_{mn} + \;\ldots \qquad (3.29)$$

where g is a constant, ε_{ij} are the strain components, ϕ_o is the strain energy before deformation and C_{ij}, $C_{ijk\ell}$, $C_{ijk\ell mn}$ are the first, second and third order elastic constants respectively. The strain energy before deformation is zero and if there is no static loading on the material the first two terms may be set to zero, reducing the strain energy function to

$$\phi = \frac{1}{2} C_{ijk\ell} \varepsilon_{ij} \varepsilon_{k\ell} + \frac{1}{3} C_{ijk\ell mn} \varepsilon_{ij} \varepsilon_{k\ell} \varepsilon_{mn} + \ldots \tag{3.30}$$

When the contracted matrix notation is used, the strain energy to second order in strain for the trigonal system is

$$\begin{aligned}\phi = {} & C_{11} \left(\frac{\varepsilon_{11}^2}{2} + \frac{\varepsilon_{22}^2}{2} + \varepsilon_{12}^2\right) + C_{12} \left(\varepsilon_{11}\varepsilon_{22} - \varepsilon_{12}^2\right) \\ & + \frac{1}{2} C_{33}\varepsilon_{33} + C_{44}\left(\varepsilon_{23}^2 + \varepsilon_{13}^2\right) \\ & + C_{14}\left(2\varepsilon_{11} \varepsilon_{23} + 4\varepsilon_{12} \varepsilon_{13} - 2\varepsilon_{22} \varepsilon_{23}\right) \\ & + C_{13}\left(\varepsilon_{11} \varepsilon_{33} + \varepsilon_{22} \varepsilon_{33}\right).\end{aligned} \tag{3.31}$$

In chapter five the comparison between the second order strain function and the electron free energy function derives the form of the electronic contribution to the elastic constants.

CHAPTER 4

EXPERIMENTAL TECHNIQUES

4.1 Crystal Growth

Since the original pioneering work of Jain (1959) considerable attention has been given to the growth of homogeneous single crystals of bismuth-antimony alloys. Reference to the phase diagram (Fig. 4.1a) indicates the problems involved in the growth of these solid solutions. The large temperature differences between the solidus and the liquidus (ΔT) suggest that constant composition alloys can best be grown by the repeated pass zone melting technique (Pfann 1958). The problem of constitutional supercooling (Tiller et al 1953) is greatly increased due to the large equilibrium segregation coefficient ($k_o = C_S/C_L$, where C_S and C_L are the solidus and liquidus concentrations respectively) and stringent precautions are necessary to eliminate the effect It has been shown that constitutional supercooling and its resultant solute segregation in the frozen alloy can only be avoided if the growth rate R is less than GD/ T, where G is the temperature gradient at the solid-melt interface and D is the diffusion coefficient of the minority component in the melt ($D = 2 \times 10^{5}$ cm^{2} sec^{-1} for Sb in Bi, Brown and Heumann 1964) Due to the low melting point of these alloys, large temperature gradients are difficult to achieve and as a result the growth rate must necessarily be small. Figure 4.1b shows the critical growth rate as a function of alloy composition, it can be assumed that crystals grown below the solid line show no inhomogeneity effects of constitutional supercooling.

The zone leveller used for the growth of the alloys is illustrated in Figure 4.2. The furnace comprised a toroidally

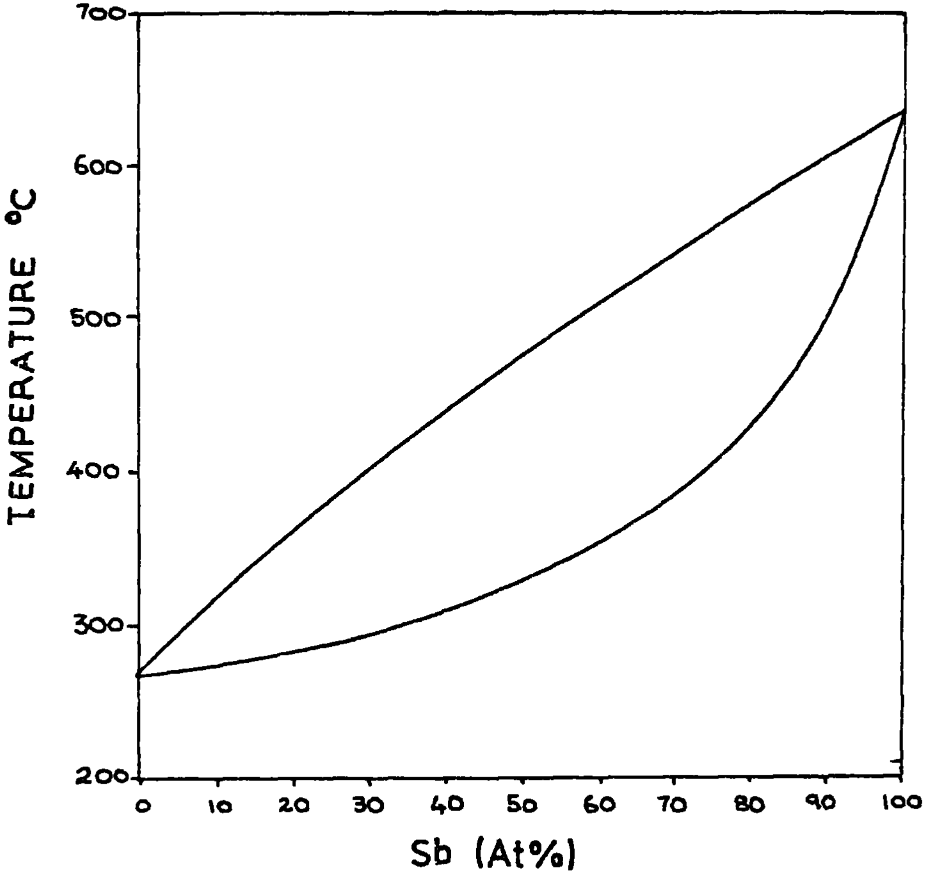

FIG 41a PHASE DIAGRAM OF THE Bi-Sb SYSTEM

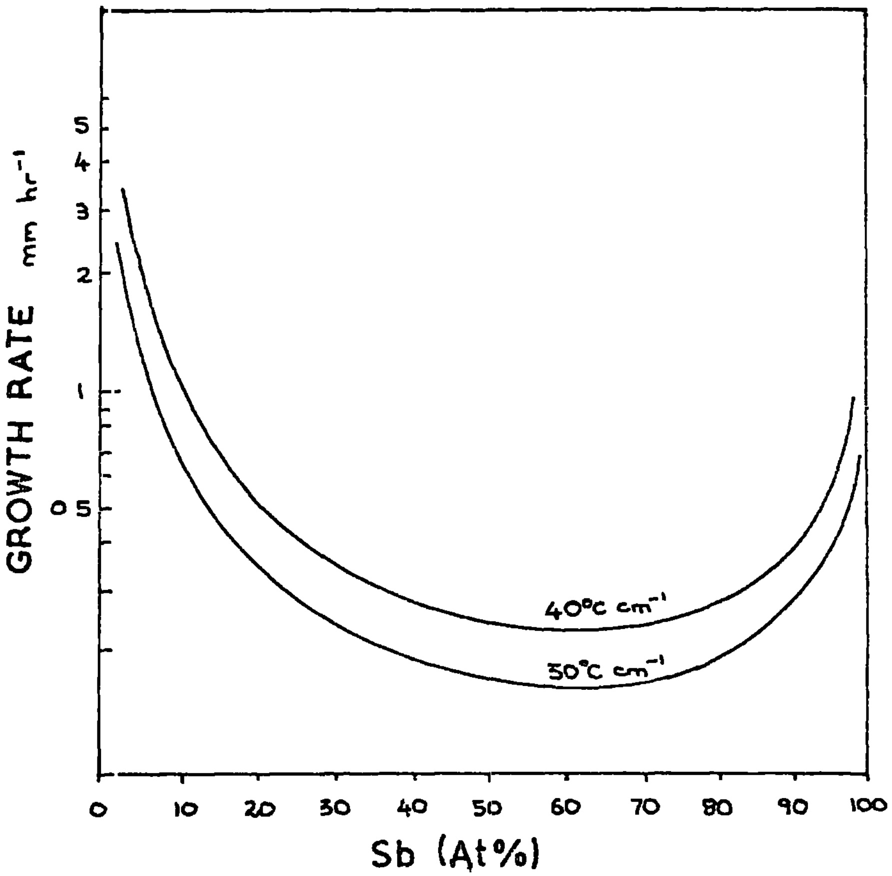

FIG 41b CRITICAL GROWTH RATE FOR VARIOUS TEMPERATURE GRADIENTS

wound Kanthal 'A' resistance wire heater powered by a stepless Eurotherm SR-10 temperature controller, the sensor for which was a Pt-Pt.Rh 13% thermocouple embedded deep in the heater assembly. To increase the temperature gradient, water cooled copper coils were mounted on either side of the furnace. The entire assembly was able to traverse along the bed by virtue of a screw thread driven by a variable speed motor (traversing speeds of 0.3 mm - 2.5 mm hr^{-1} were available). Crystals of approximate length 8 cm and semicircular cross section (diameter 2 cm) were grown in quartz boats coated with colloidal graphite, the circular cross section accommodated the thermal expansion of bismuth on freezing and the graphite coating prevented the alloy from sticking to the quartz. During the zone levelling process the crystal growth boats were encased in a 60 cm long, 3 cm diameter quartz tube, in which an inert atmosphere was provided by a controlled flow of oxygen-free nitrogen. The technique provided a temperature gradient of about $40^{o}C\ cm^{-1}$ at the solidus-liquidus interface (measured with a thermocouple embedded in the surface of the alloy).

Before the growth process, the high purity elements (99.9999% pure) were fused together in vacuo and raised to $700^{o}C$ to drive off volatile oxides, continuous shaking of the alloy promoted mixing. The frozen polycrystalline boule was then transferred to the quartz boat and melted within the zone leveller. Homogeneous single crystal growth was then accomplished by several zone passes Inspection of the alloys by chemical etching and x-ray analysis indicated that the entire charge was easily converted into single crystals and tended to grow in directions perpendicular to the trigonal direction, as observed and discussed on the basis of thermal conductivity by Yim and Dismukes (1967). During the growth process, which extended over several weeks, some oxidation

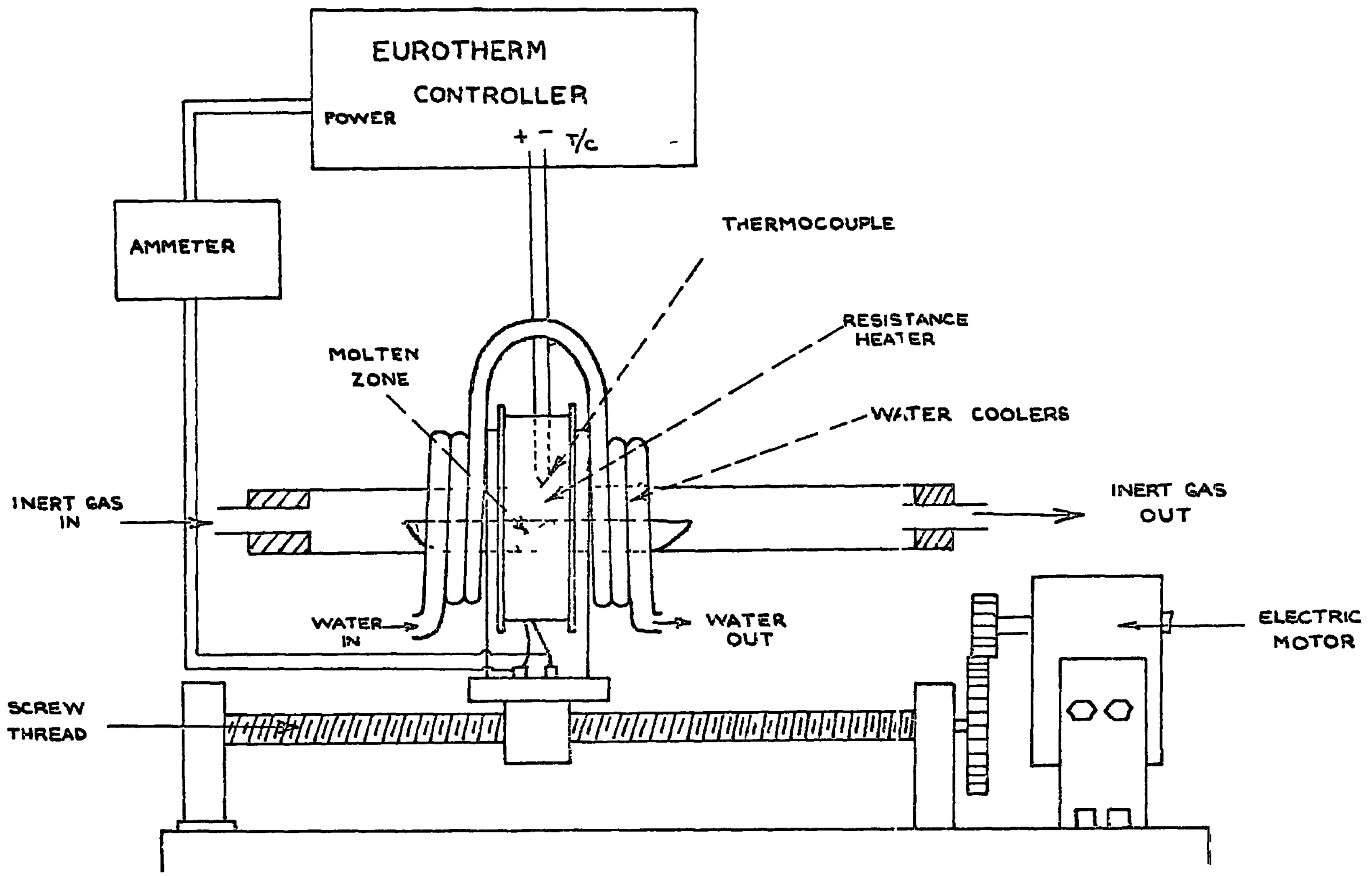

Figure 4 2 The zone leveller

occurred due to a small quantity of residual oxygen in the inert nitrogen. However, the oxidation was found to be insufficient to inhibit the growth of single crystals and could be readily removed by slight chemical etching with 30% Nitric acid.

Pure bismuth and crystals doped with tellurium were grown in the manner described above. The restriction on the growth rate could however be slightly relaxed, as the solidus-liquidus separation (ΔT) (Hansen 1958) is much less than in the antimony alloys.

4.2 Sample Preparation

The ultrasonic techniques employed here require samples with parallel opposite faces normal to a specified crystallographic direction. Crystallographic orientation of the as-grown crystals was accomplished by means of Laue back reflection x-ray photography. The cartesian co-ordinate system assigned to the rhombohedral lattice is described in Section 2.1. The trigonal axis was easily identified by the typical three-fold symmetry, the binary axis by the two-fold symmetry and the bisectrix axis by the reflection symmetry of the mirror plane. The sense of the bisectric (y) axis was recognised from its relationship with the trigonal (z) axis, the quadrant formed by the $+y$ and $+z$ axes contains a pseudo-threefold axis whilst that formed by the $-y$ and $+z$ axes contains a pseudo-fourfold axis.

Bismuth and its alloys with antimony cleave easily along the (001) planes To prevent damage to the material, all cutting and polishing was performed by a Servomet spark machine (Metals Research Ltd., Royston). The main advantage of this technique is that because the cutting action results from electrical spark erosion no mechanical stresses are induced by the pressure of a cutting tool Slight

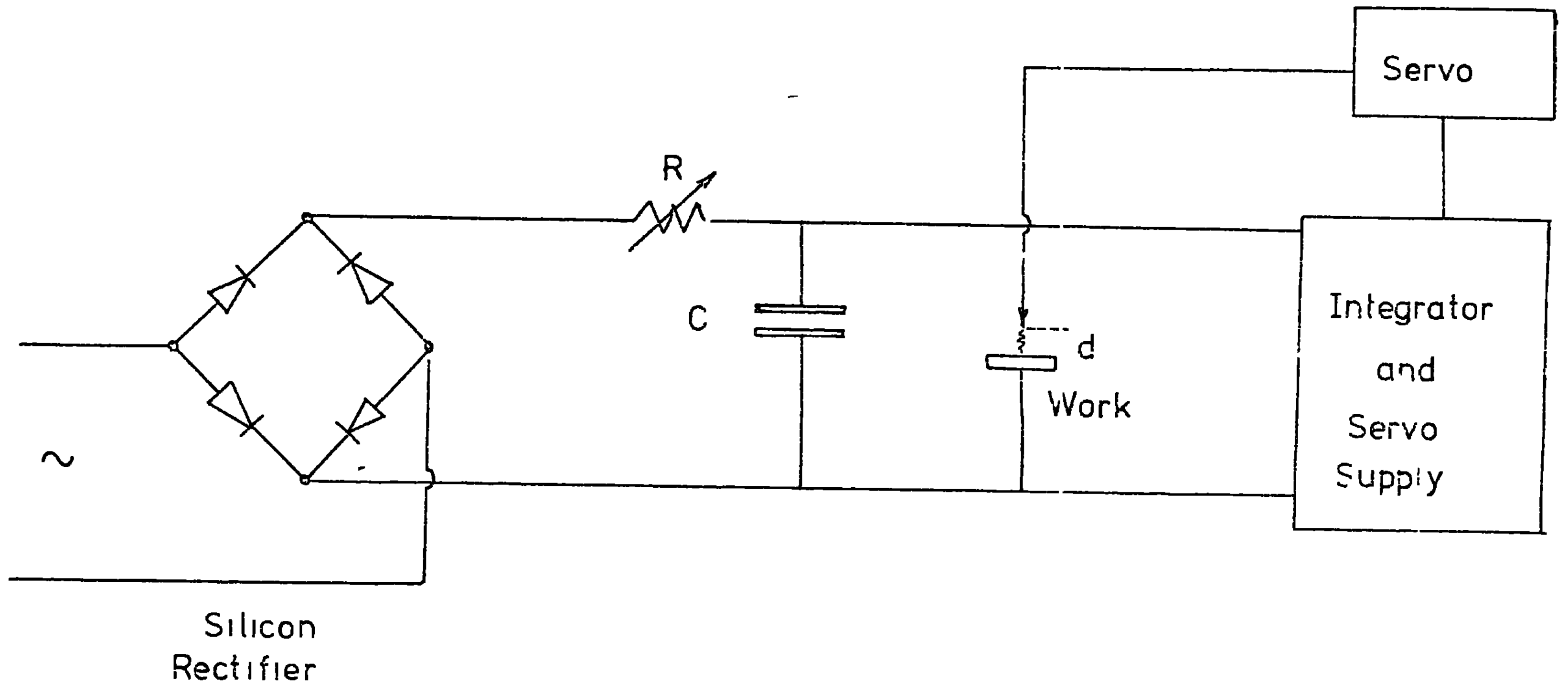

Fig 44 BLOCK DIAGRAM OF SPARK MACHINE

mechanical deformation occurs only at the sample interface, which can readily be removed by chemical etching. The Servomet spark machine produces a rapid succession of spark discharges between the tool and the work face, the entire machining area being immersed in a bath of kerosene (the dielectric). These sparks erode the work at a rate which can be controlled by the input energy The salient points of the operating principles are illustrated in Figure 4.4. A full wave bridge of silicon rectifiers smooths the mains voltage into a D.C. supply which is subsequently fed to a relaxation circuit comprising of a capacitor and a variable resistor. The capacitor, C, charges at a rate determined by the variable resistor until the dielectric breakdown is reached and an electrical discharge occurs across the gap. The capacitor then re-charges and the cycle is repeated A servo mechanism, controlled by the dielectric breakdown voltage, maintains the work tool at a constant value of d. The cutting tool was either a thin copper plate or a continuously moving tinned copper wire. Polishing was accomplished by a rapidly rotating flat copper disc Samples with end faces parallel to better than 10^{-4} radians and normal to within $\frac{1}{2}^{\circ}$ of the required crystallographic axis were readily produced using this technique.

4.3 Ultrasonic Velocity Measurements Between 4 2 K and 300 K

4.3a Pulse Echo Method

The pulse transit time methods are amongst the most accurate and sensitive techniques for the determination of the attenuation and velocity of stress waves within a solid, the basic principles will be described in detail.

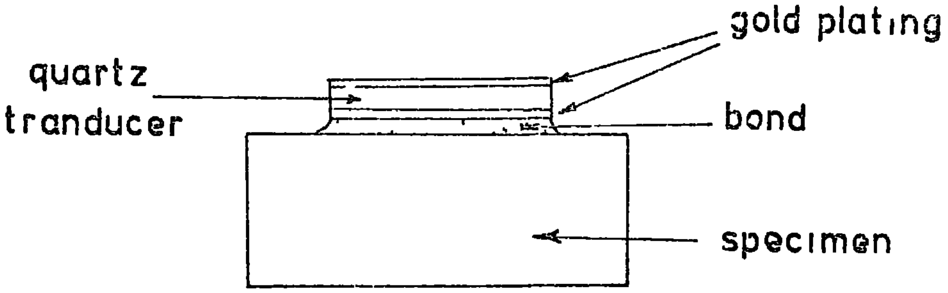

FIG 4 5 GOLD PLATED QUARTZ TRANSDUCER BONDED TO SPECIMEN

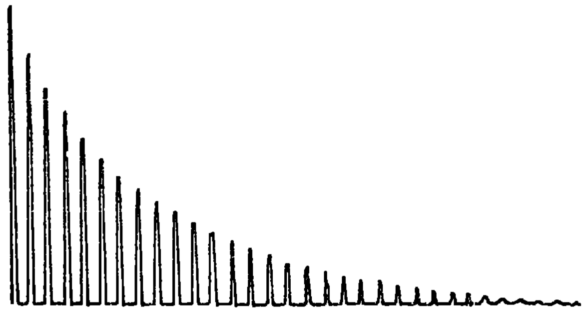

FIG 4 6 TYPICAL RECTIFIED ECHO PATTERN.

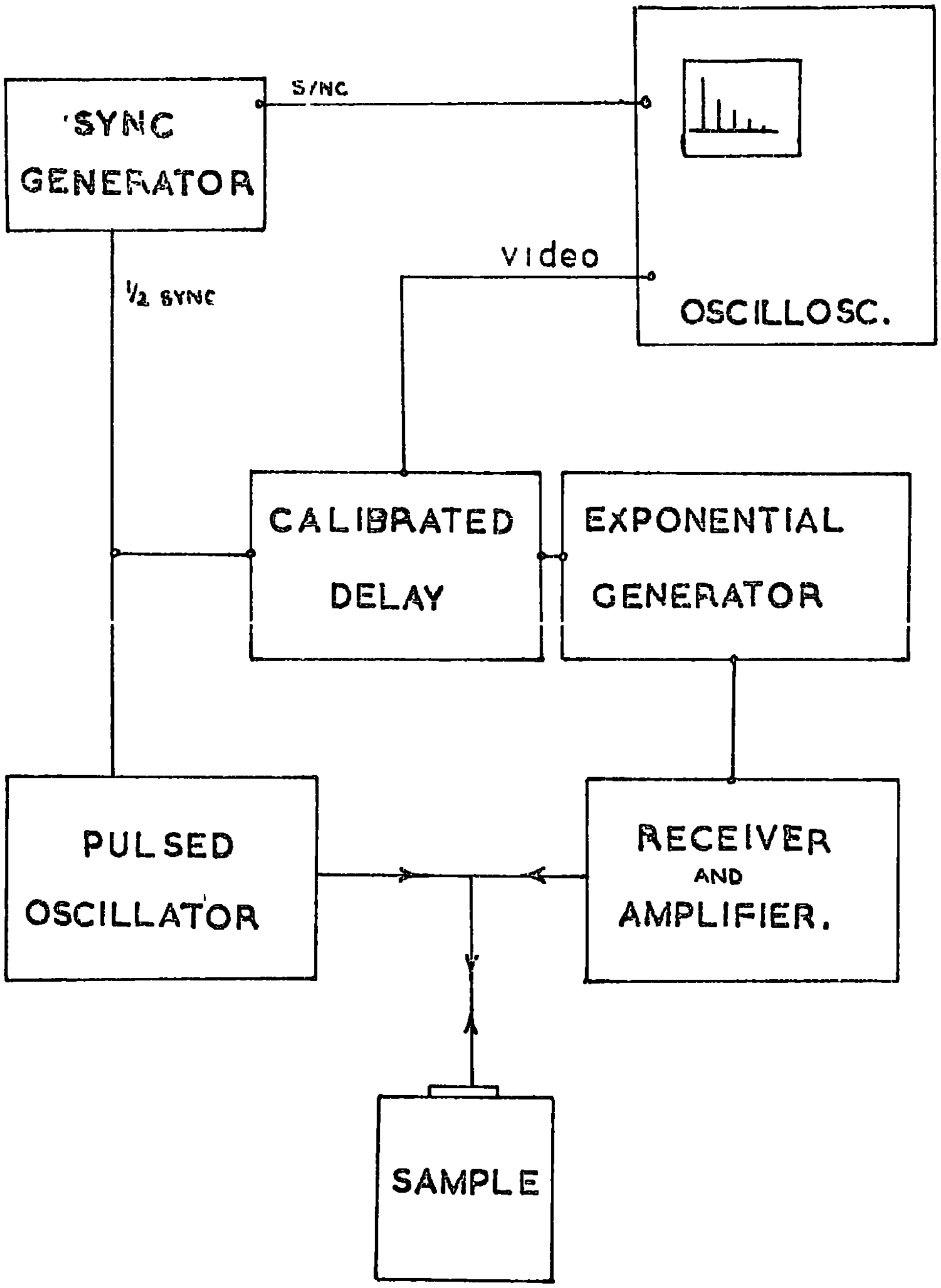

FIG 4 7 BLOCK DIAGRAM OF PULSE ECHO SYSTEM.

A short duration pulse of high frequency stress waves is introduced into a solid which has two accurately parallel faces (Figure 4.5), the stress wave is generated by the application of a high voltage electrical impulse to a gold plated piezoelectric transducer bonded to one of the normal surfaces of the material. Due to the high acoustic impedance mismatch at the surfaces, the stress wave is reflected at the lower interface and returns to the transducer-sample interface, here some of the acoustic energy is converted into electrical energy which is amplified by a receiver and displayed on an oscilloscope. The stress wave continues to travel through the material due to interface reflections, producing a sequence of multiple echoes, the decay of which is dependent upon the sound absorbing mechanisms of the sample. The time interval between successive echoes represents the velocity of ultrasonic wave propagation within the material.

The block diagram of a simple pulse echo system used in the present work is given in Figure 4.7. It consists of the model 6600 Matec pulse generator and amplifier and the model 1204A exponential generator, calibrated delay and master synchroniser The oscillator produces r f. pulses of a controlled duration (1 μs typically employed) at a repetition frequency determined by the master synchroniser (0-500 Hz). These r f. pulses are conveyed to the bonded piezoelectric transducer and the resultant set of echoes are amplified and rectified by the narrow band pass receiver, the rectified echoes are displayed on an oscilloscope to which an electronically synthesised exponential curve is added to facilitate the measurement of attenuation The time interval between successive echoes may be measured either by the calibrated delay or by the oscilloscope timebase

(b) Pulse Echo Overlap

The pulse echo overlap technique is based upon the pulse echo system, with the facility to superimpose any two selected, visually intensified echoes on an oscilloscope whose triggering rate is equal to the delay between the two chosen echoes. Critical adjustment of the triggering rate permits precise measurement of the transit time to 1 part in 10^4 (and under ideal conditions 1 part in 10^5).

The particular system used during the course of this work is illustrated in block form in Figure 4 8. The Bradley 235 signal generator is used to power the Matec 122A decade divider and double stroke generator The latter unit performs two functions (i) it provides two trigger sources, one equal to the signal generator frequency (Master Sync.) and the other a sub-multiple of 10^n $(n = 1,2,3)$ of the master frequency (divided sync). (ii) Secondly, the double delay stroke generates two, time variable 0-30 v square wave pulses which, when linked to the z-modulation of the oscilloscope permit the intensification of any two sections of the echo pattern. The divided sync. triggers the Matec 6000 r.f. pulse generator. Each trigger pulse creates an r.f. burst which is in turn transformed by the quartz transducer into a mechanical vibration within the crystal. Successive reflections are then detected by the transducer and amplified by the receiver, which then provides two types of output (i) the raw r.f. echoes amplified, (ii) the rectified r.f. echoes (referred to here as the video output), which are coupled via an exponential generator to an oscilloscope, where the attenuation can be measured manually The waveforms associated with the operation are illustrated in Figure 4 9.

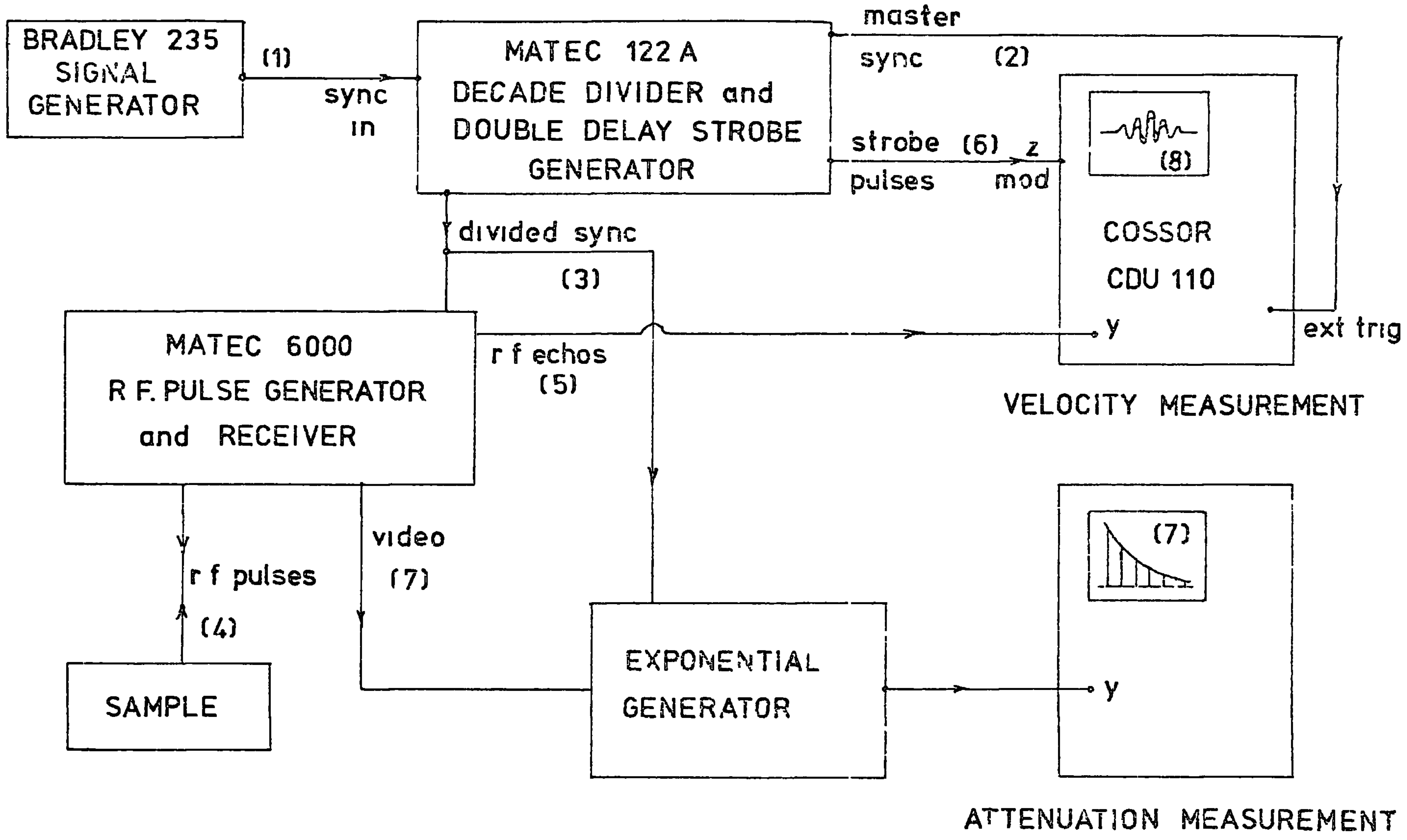

FIG 4.8 BLOCK DIAGRAM OF PULSE ECHO OVERLAP APPARATUS, the numbers in brackets refer to the waveforms shown in figure 4.9

(1) Signal Generator

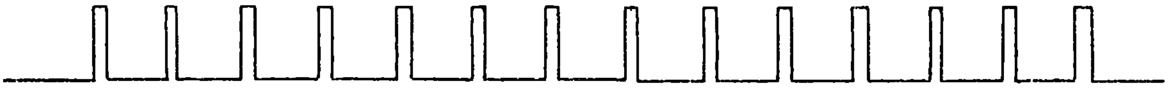

(2) Master Sync

(3) Divided Sync [-10]

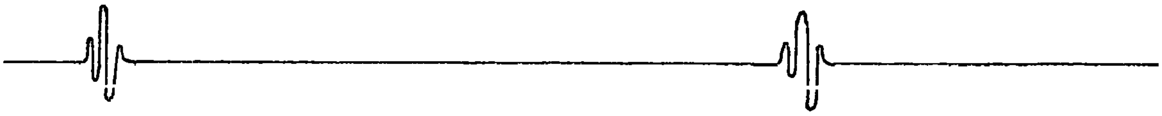

(4) R F Pulses to Sample

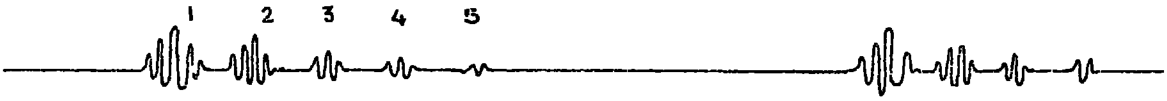

(5) R F Echoes

(6) Z Modulation - Intensification of Echoes 1 & 2

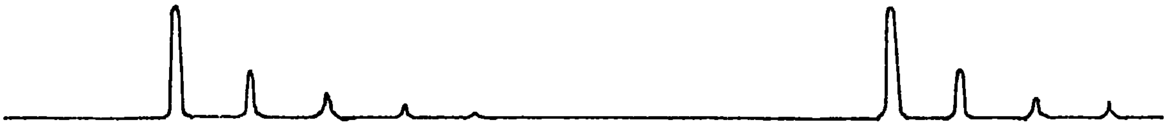

(7) Vidio Out

(8) Overlap of Echoes 1& 2

FIG 4 9 PULSE ECHO OVERLAP WAVEFORMS

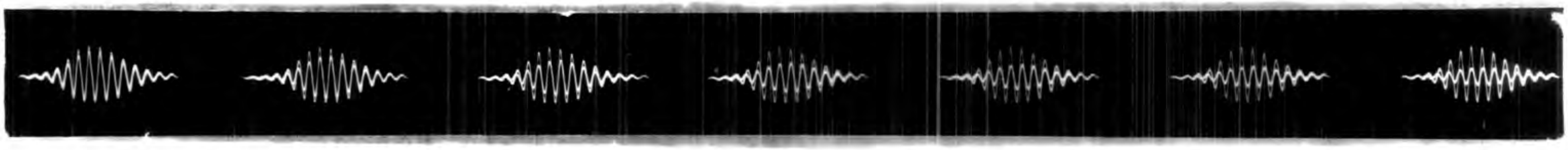

(a) Correct overlap

(b) Error of -1 r.f. cycle

(c) Error of +1 r.f. cycle

Figure 4.10: Cyclic Matching; overlap of the first echo with subsequent reflections

The raw r.f. echoes are first observed in their entirety by triggering the oscilloscope with the divided sync. Careful adjustment of the double delay stroke generator permits the intersifications (i.e. the brightness) of any two echoes. The oscilloscope brightness is then reduced until only the two selected echoes are visible. By triggering the oscilloscope with the master sync at a rate equivalent to the delay between the chosen echoes, the intensified regions may be overlapped. Critical adjustment of the signal generator will then provide cycle-to-cycle matching. Proper cyclic matching may be difficult for highly attenuating materials, but where four or more echoes are discernable the operation is straightforward.

Cyclic matching may be achieved by using a triggering rate that is assumed to be equivalent to the transit time between two successive echoes and intensifying the first echo in the display by the first strobe pulse. Time variation of the second strobe pulse permits the overlap of each echo upon the first. In the event of cyclic matching being in error by one cycle, this error will be multiplied by the transit time multiple and will become readily apparent as further echoes are overlapped (see Figure 4.10).

Measurement of velocity to 1 part in 10^4 is readily achieved, but it must be stressed that such a value is by no means the actual absolute velocity characteristic of the sample, corrections have to be applied due to the transducer and bond effects (see Section 4.3d).

(c) Transducers and Bonds

The generation and detection of ultrasound were effected by the use of gold plated quartz transducers produced commercially by Brookes Crystals (Ilminster) Ltd. X and Y cut transducers with fundamental resonant frequencies of 5, 10, 15 and 20 MHz and with diameters of 5 mm and 6 mm were used.

The resonant frequency of a transducer is determined by its thickness, the fundamental resonant frequency is given by d = λ/2, where d is the thickness and λ is the wavelength of sound in quartz at the resonant frequency. Odd harmonics of the transducer may be generated by applying higher r.f. frequencies which satisfy the conditions $f_n = (2n-1)f_o$ $(n = 1,2,3)$, where f_o is the fundamental frequency.

A large variety of viscous liquids have been used to bond quartz transducers to materials, a good review of which has been given by Farley (1973) For bonding to bismuth based alloys Nonaq Stopcock Grease has been found to be the most efficient. Reproducible bonds were formed by the gradual rotation of the transducer on to the grease coated surface of the material, bond thicknesses of 3 - 5 μm were thus readily produced The Nonaq bond performed well at all temperatures in the range 4.2 - 300 K.

(d) Transit Time Errors

In the pulse echo method it is standard practice to regard the transit time at the measured delay between the peaks of two consecutive echoes. Essentially the pulse echo overlap technique method gives the time delay between two corresponding r f. cycles. Although it appears experimentally that the transit time can be measured to a precision of 1 part in 10^4, owing to the transducer loading effect the true transit time within the sample is smaller than the electronically measured transit time

An investigation of the behaviour of ultrasonic waves incident on a boundary between two dissimilar materials requires the calculation of the reflection and transmission coefficients, which are derived from the acoustic impedances of the respective materials. The acoustic impedance is defined as:-

$$Z = \rho v \,, \tag{4.1}$$

where v is the velocity of sound propagation and ρ is the density. The reflection coefficient of a wave incident normal to a boundary is given by

$$R = \frac{Z_2 - Z_1}{Z_2 + Z_1} \,, \tag{4 2}$$

and the transmission coefficient is

$$T = \frac{2Z_1}{(Z_2 + Z_1)} \,, \tag{4.3}$$

where Z_1 and Z_2 are the acoustic impedances of the materials containing the incident and transmitted waves respectively

At the free end of the sample the acoustic impedance mismatch from sample to air is effectively infinite ($Z_1 >> Z_2$). the reflectivity is total (R = - 1) But, at the transducer end of the sample the situation is far more complex, a gold plated quartz transducer is bonded to the specimen with a suitable bonding agent, consequently there are four interfaces Since the thickness of the bond and the gold plating together (10 µm) are very much less than the thickness of the transducer (0 15 - 0 6 mm) they can, to a first approximation, be ignored, and the interface can be considered to be purely between the quartz and the sample.

Thus, for ultrasonic wave incident from the sample the reflection and transmission coefficients take the form (see Figure 4.11)

$$R_1 = \frac{Z_S - Z_Q}{Z_S + Z_Q} \qquad T_1 = \frac{2Z_S}{Z_S + Z_Q} , \tag{4.4}$$

and for waves incident from the transducer ,

$$R_2 = \frac{Z_Q - Z_S}{Z_S + Z_Q} \qquad T_2 = \frac{2Z_Q}{Z_S + Z_Q} , \tag{4.5}$$

where Z_S and Z_Q are the acoustic impedances of the sample and quartz respectively. Figure 4.12 gives the calculated reflection and transmission coefficients between quartz and bismuth for the ultrasonic velocities encountered in the present work

Thus when an acoustic wave crosses the sample-quartz interface part of it is reflected and part is transmitted. The transmitted part is then totally reflected from the free end of the transducer and on reaching the interface from the opposite direction part is reflected and the transmitted part combines with the original reflection in the sample. The ultrasonic wave continues to be reflected back and forth within the transducer thereby producing an output pulse which differs in shape from the input pulse The relative amplitude of a wave entering the sample after n round trip reflections in the transducer is simply

$$\begin{aligned} A_n &= - T_1 T_2 R_2^{n-1} \\ &= T_1 T_2 \frac{R_2^{\,n}}{R_1} \\ &= \frac{4Z_S Z_Q}{(Z_S + Z_Q)(Z_S - Z_Q)} \; R_2^{\,n} \end{aligned} \tag{4.6}$$

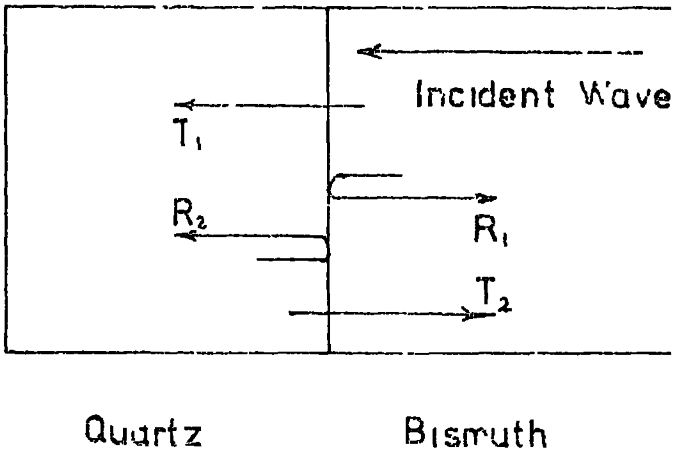

Figure 4.11 The quartz–bismuth interface

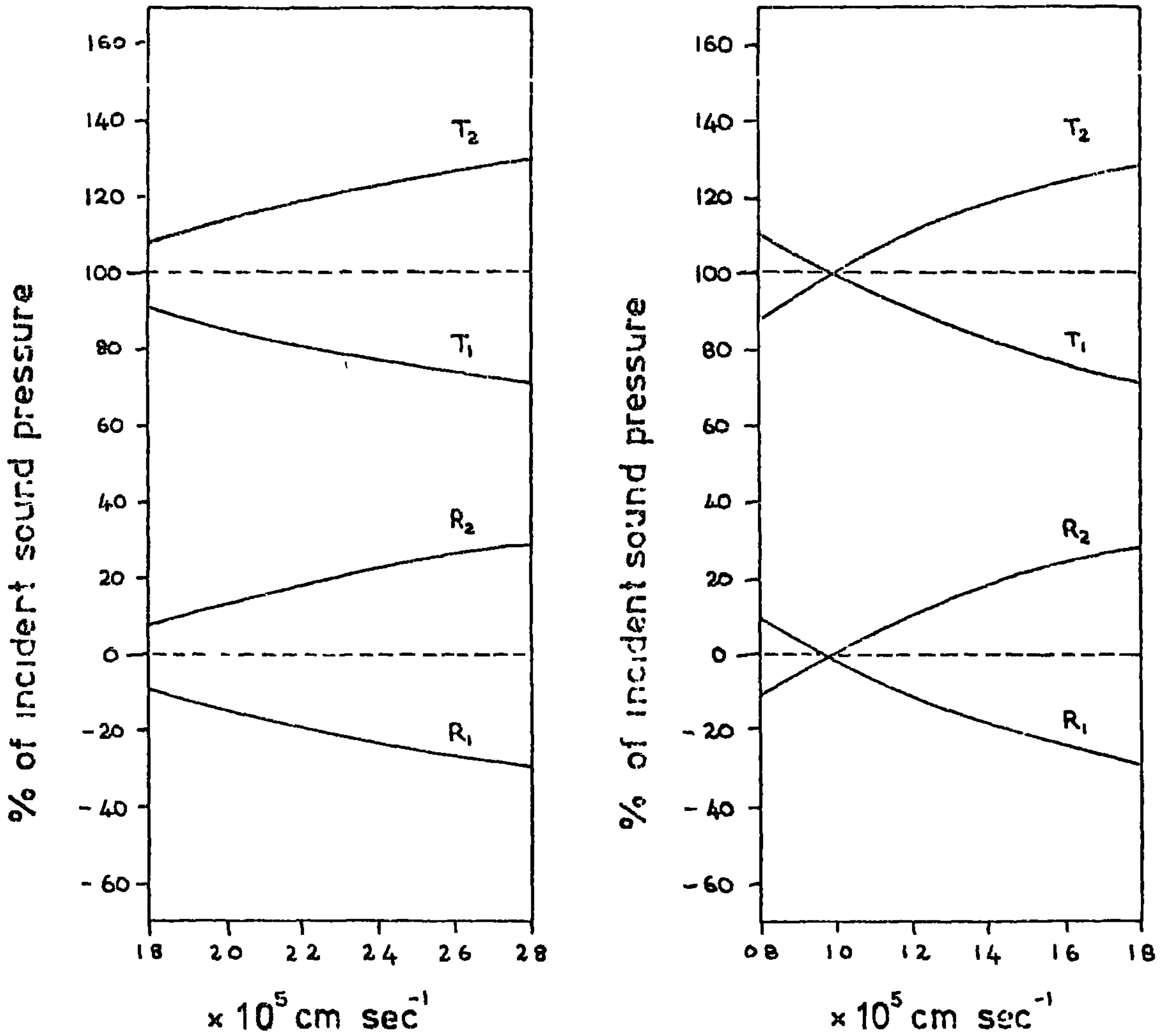

(a) longitudinal waves (b) shear waves

Figure 4.12 The reflection and transmission coefficients between quartz and bismuth

The wave will be delayed by a time interval $n\tau$, where τ refers to the transit time within the transducer. If the incident wave function is denoted by $i(t)$, the reflected function $r(t)$ will be

$$r(t) = R_1\, i(t) + \sum_{n=1}^{\infty} R_2^{\,n}\, i(t + n\ ) \tag{4.7}$$

Lenkkeri and Lahteenkorva (1973) have solved this equation by assuming that the input pulse has the form of a Gaussian wave packet $i(t) = \exp(^{-t^2}/a^2)$, where a refers to the pulse width. If the input pulse $i(t)$ has a maximum at $t = 0$, the negative time coordinate of the maximum of $r(t)$ will represent the time delay δ. At the maximum of $g(t)$, $dg/dt = 0$ and $t = \delta$, differentiation of equation 4.7 yields

$$R_1\, \delta = \beta \sum_{n=1}^{\infty} R^n \exp\left[-n\tau\ (n\tau - 2t\delta)/_{a^2}\right] (n\tau - \delta)\ . \tag{4.8}$$

The apparent transit time delay δ may therefore be calculated by numerical solution of the above equation. The delay is found to be independent of the pulse width a for $a > 0\ 5$ μs. To a good approximation the time delay may be obtained by assuming that $a^2 \gg n\tau(n\tau - 2\delta)$, with the result that

$$\delta \approx \tau \cdot \frac{Z_Q}{Z_S} \tag{4.9}$$

The variation of the transit time plotted against the thickness of the transducer should therefore produce a plot which is essentially linear An extrapolation of this plot to zero transducer thickness derives the hypothetical transit time corresponding to a lossless transducer The intercept value can be considered to

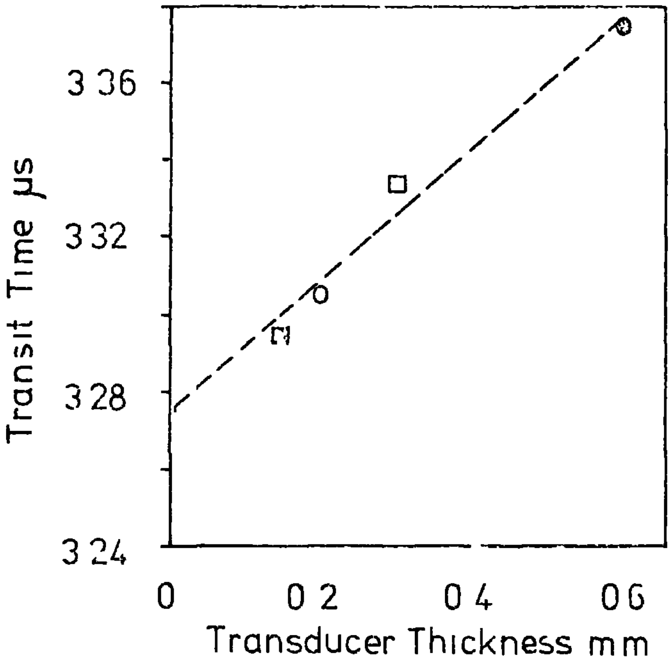

(a) $V_L = 2.548 \times 10^5$ cm sec^{-1}

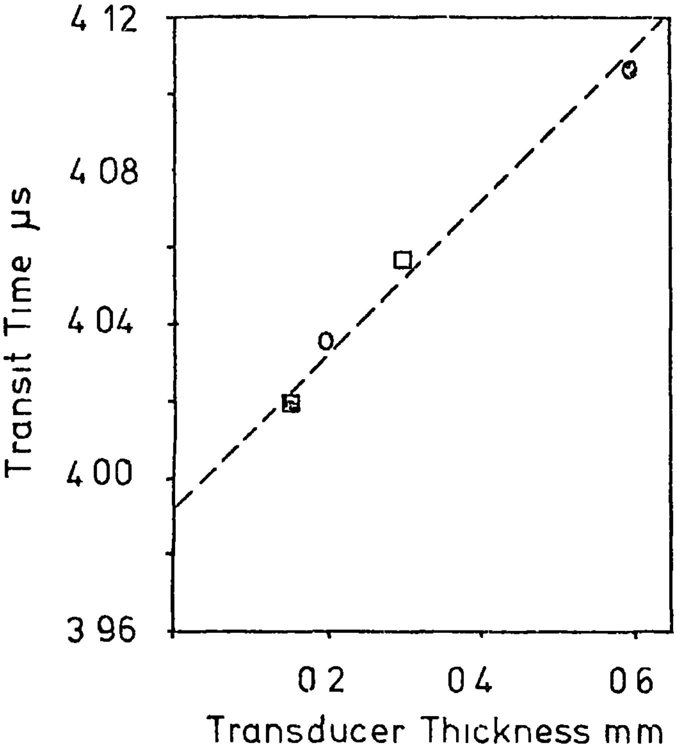

(b) $V_L = 1.968 \times 10^5$ cm sec^{-1}

Figure 4.13 Typical extrapolation plots to derive the unpeturbed transit time

⊙ 5MHz, □ 10MHz, ○ 15MHz, ▨ 20MHz

represent the true transit time within the material. This technique has been verified experimentally by Kammer (1964).

During the course of this work all the ultrasonic velocity measurements were performed with different thicknesses of transducer (5, 10, 15 and 20 MHz fundamental resonant transducers were chosen) and the extrapolated value was assumed to be the unperturbed transit time. Typical extrapolation plots are shown in Figure 4.13. The transit time errors derived from these plots were found to correspond closely with the theoretical predictions and it was concluded that this method could yield the true transit time to within 0 015 µs.

4.4 Measurement of Temperature Dependence

(a) The Cryostat

Measurements in the temperature range 4.2 K to 300 K were accomplished using a conventional glass dewar system (see Figure 4 14). The cryostat assembly consisted of two double walled glass dewars and employed liquid nitrogen and helium refrigerants The interspace vacuum was monitored using a Pirani head and gauge (Edwards speedivac gauge B5, head type M6A). The dewar inner space included a Pirani gauge and a mercury manometer, a mercury protection valve was also incorporated to protect the dewar from accidental pressure build up.

The frame of the sample holder was constructed of thin walled stainless steel tubing to reduce heat leakage Electrical leads for the temperature sensors were taken through the tubing and lead out through a neoprene vacuum seal at the top of the holder. The ultrasonic coaxial line was constructed from a solid core of stainless steel sheathed in a thick walled teflon tube, electrical

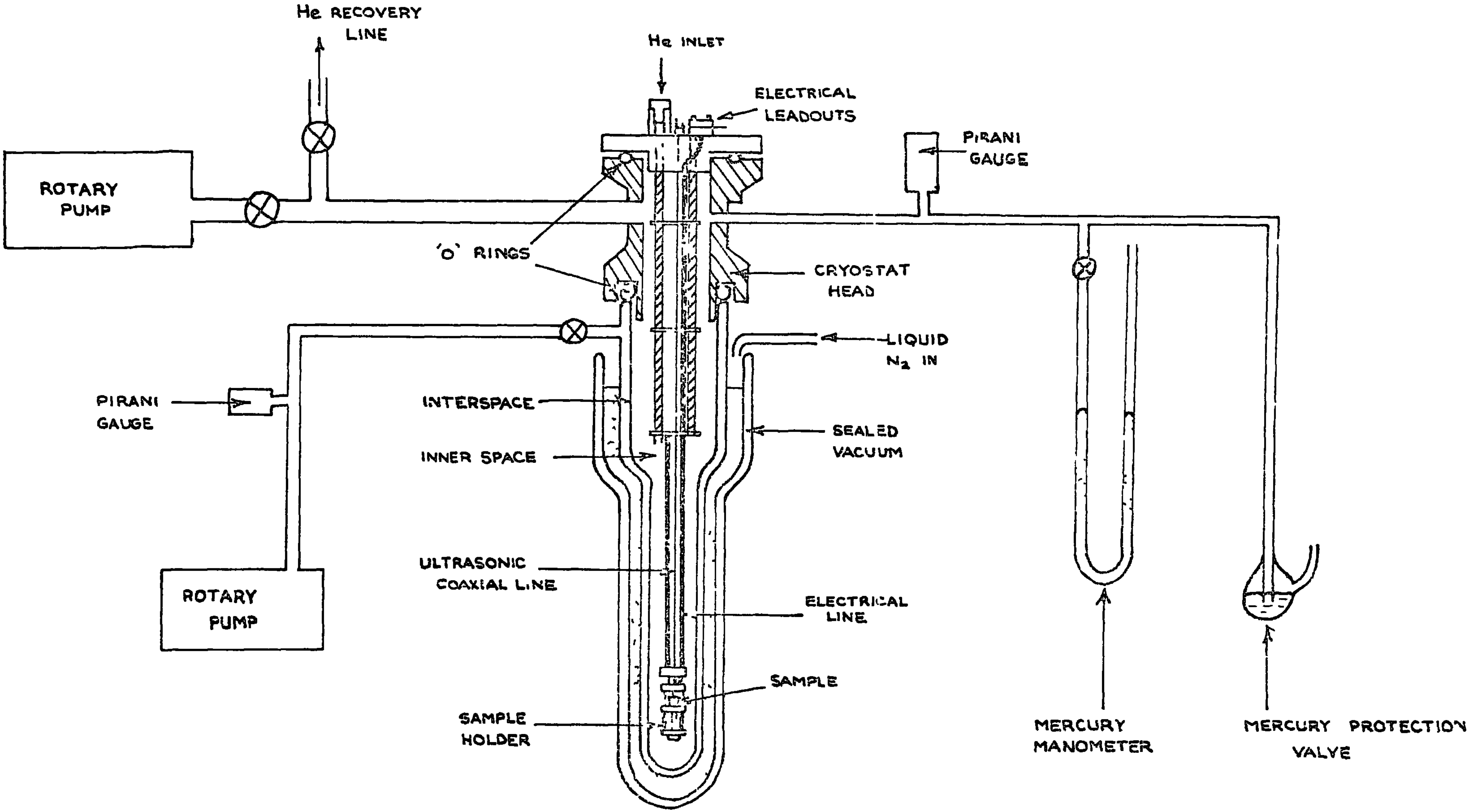

Figure 414 The cryostat system

connection to the transducer was made by a spring loaded, copper centre contact.

Ultrasonic measurements were usually taken whilst the sample was being cooled. The rate of cooling was determined by the quality of the interspace vacuum and by the atmosphere of the inner dewar. Before cooling was begun, the inner space of the helium dewar was usually filled with dry helium gas (at atmospheric pressure) in order to provide good heat exchange within the system and to facilitate the later transfer of liquid helium. With an interspace vacuum better than 0.1 torr the time of cooling from 300 K to 80 K was approximately 3 hours. Refrigeration of the system from 80 K to 4.2 K was achieved by the steady transfer of cold helium gas. Careful control of the transfer rate permitted a fine degree of control over the cooling rate Rapid fluctuations of temperature were avoided by monitoring the temperature with a thermocouple linked to a digital potentiometer, measurements were only taken under steady conditions. To achieve the final temperature of 4.2 K it was usually necessary to inject a small quantity of liquid helium. Thus, with great care, the total amount of liquid helium used could be restricted to 1.5 litres.

(b) Temperature Measurement

The measurement of temperature within the cryostat assembly was accomplished by means of an Oxford Instruments digital temperature controller. The sensor for the unit was a cryogenic linear temperature sensor (CLTS), consisting of a fine resistive grid of nickel and manganin. For ease of operation, the CLTS was permanently mounted on the sample holder in close proximity (within 5 mm) to the specimen

The operation of the CLTS is essentially that of the four probe potentiometric method. The unit provides the CLTS with a constant current and then compares the developed voltage with an internally generated reference voltage The characteristic voltage of the sensor as a function of temperature is generated by a millivolt D.C. amplifier, whose gain is varied in segments using resistor networks, in the range 0 K to 100 K it is approximated by 10 K linear steps and is treated as linear in the range 100 K to 300 K. The CLTS voltage is compared to the characteristic voltage by a differential network and the error voltage produced modulates the digital output. The reading accuracy was found to be ± 1 K.

CHAPTER 5

THE KEYES MODEL

5.1 Introduction

It is well established that the free carriers in a semiconductor (or for that matter a semimetal) can have profound effects on the elastic properties of the materials The free carriers referred to here are those which occupy either the conduction or valence bands and take part in normal electrical conduction Bruner and Keyes (1961) have shown that in germanium the addition of 2.8×10^{19} cm^{-3} arsenic donors decreases the elastic constant C_{44} by 5 5% whilst the elastic constant $(C_{11} - C_{12})/2$ remains essentially unchanged. Similar results have been obtained for silicon by Einspruch and Czavinszky (1963) and by Hall (1967) in which $(C_{11} - C_{12})/2$ is changed rather than C_{44}. This difference between the behaviour of silicon and germanium can be explained on the basis of the symmetry of their electronic band structures, a shear strain along a <111> axis destroys the symmetry of the valleys in germanium, whereas a shear strain along a <100> axis does not. The reverse is true in silicon The impurity atoms, which alter the carrier concentration, may also have an effect upon the elastic constants. The relative changes in the elastic behaviour are usually of the same order of magnitude as the atomic fraction of impurity (Huntingdon, 1958), whereas in these semiconductors the relative changes can be two orders of magnitude greater than the impurity concentration.

An insight into the free electron contribution may be gained by considering a two dimensional structure consisting of a four fold degenerate conduction band, as illustrated in Figure 5 1 In

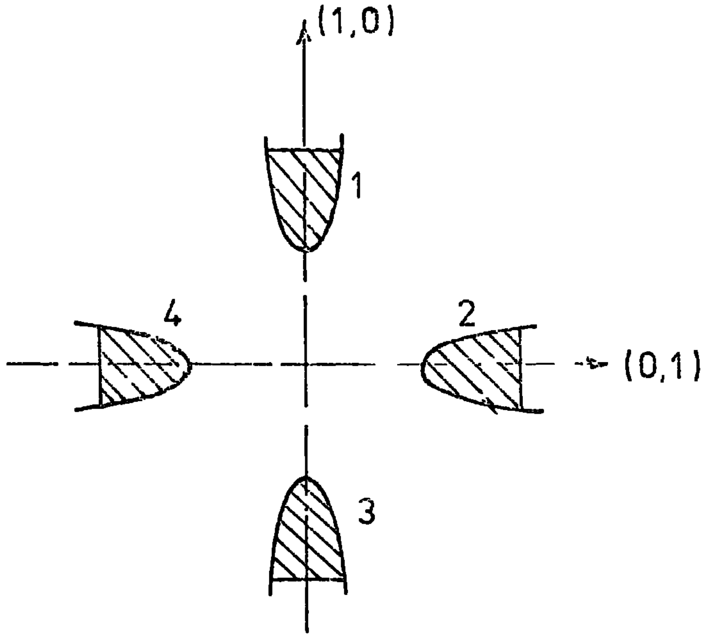

(a) No strain

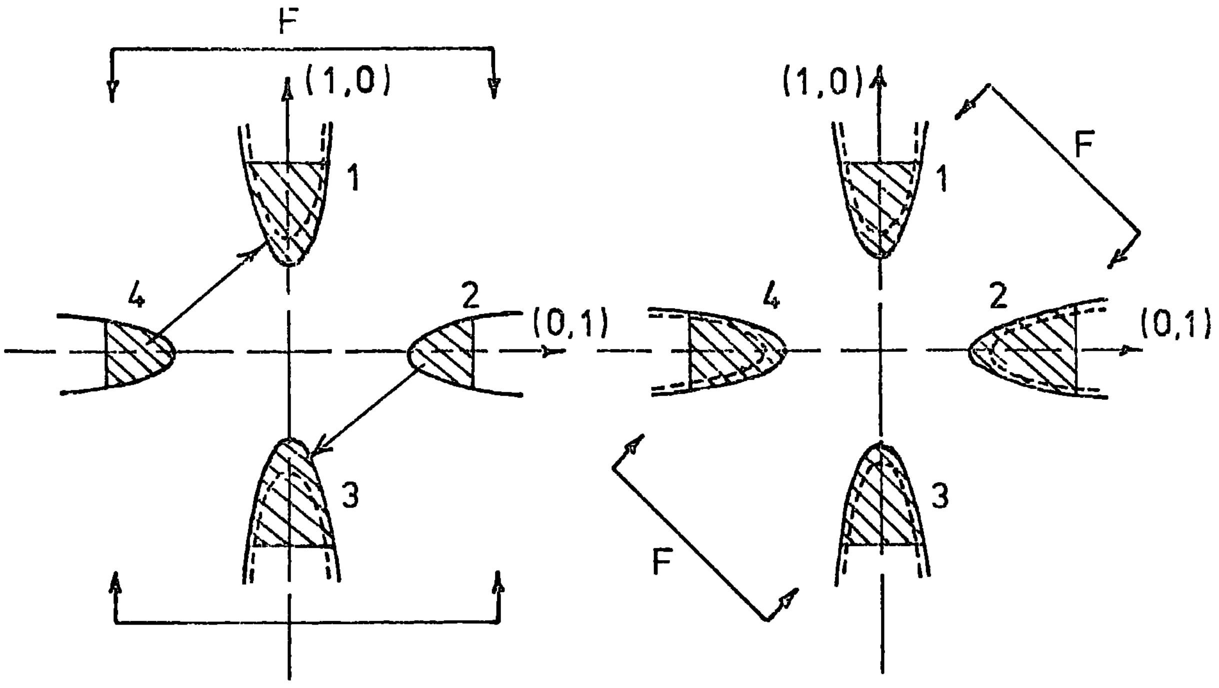

(b) (1,0) strain (c) (1,1) strain

Figure 5.1 Fourfold degenerate conduction band – demonstrating the effect of strain on the electron distribution the absence of strain the energy of each valley is equivalent and the electron population is distributed evenly amongst the four degenerate bands (Fig. 5.1a). A strain in the (1,0) direction (Fig. 5.1b) will cause valleys 1 and 3 to decrease in energy, to attain equilibrium, the electrons are forced to redistribute themselves. Since the electron redistribution minimises the free energy in the strained crystal, some of the work needed to strain the crystal is recovered and the effective elastic constant is decreased. A strain component in the (1,1) direction (Fig. 5.1c) would shift all the valleys by the same energy, as there is no net energy difference between the valleys, the electrons cannot redistribute themselves and no minimisation of electronic free energy takes place.

On the basis of thermodynamics and statistical mechanics Keyes (1961 and 1967) has developed a theory which reasonably quantitatively explains the electronic effects in silicon and germanium. The model predicts that electronic effects should be present in multivalley semiconductors, but a knowledge of the deformation potential constants is necessary before the electronic contribution to the elastic constants can be calculated. Pratt and Das (1970) have observed the effect of the $L_6^+ - L_6^-$ band inversion on the temperature dependence of the elastic constant C_{44} of $Pb_{0.5}Sn_{0.5}Te$ and have interpreted their results on the basis of the Keyes' model. Houston and Strakna (1964) found a large variation in the elastic constant of SnTe as a function of carrier concentration but since the band structure has not been fully resolved it has not been possible to interpret the findings on the basis of the Keyes model.

The rest of this chapter is devoted to the extension of the Keyes model to derive the form of the electronic contributions for the bismuth band structure. Since the deformation potential constants have been measured experimentally by Walther (1968) and by Inoue and Tsuji (1967) it is possible to calculate the theoretical magnitudes of these contributions in bismuth.

5.2 Band edge energy changes

The assumption is made that the strain shifts a band in energy without altering any associated physical parameters, such as the effective mass or the deformation potential In view of the small mechanical strains involved in ultrasonic experiments this rigid band model should be quite an accurate approximation. The change in energy of a band edge under the influence of a mechanical strain is given by a double contraction of the deformation potential tensor over the strain tensor,

$$W^{(1)} = \sum_{k,\ell} D_{k\ell}\, \varepsilon_{k\ell} \qquad (5.1)$$

where $D_{k\ell}$ is the deformation potential and $\varepsilon_{k\ell}$ is the strain component The solution of the equation of motion of an ultrasonic wave (see Section 3.4) takes the form of a plane travelling wave

$$u = u_o \exp i(\omega t - \underline{k} \cdot \underline{r}) \qquad (5.2)$$

where $\underline{u}$ is the particle displacement vector, $\underline{k}$ the direction of propagation and ω the angular frequency It should be emphasised that, except for certain pure mode directions, the displacement $\underline{u}$ is not parallel to the propagation direction $\underline{k}$. The strain tensor $\varepsilon_{k\ell}$ is the symmetrical part of that tensor which describes the deformation of the body and comprises two partial differentials ,

$$\varepsilon_{k\ell} = \frac{1}{2}\left(\frac{\partial u_k}{\partial x_\ell} + \frac{\partial u_\ell}{\partial x_k}\right) \tag{5.3}$$

where u_k, u_ℓ are the components of the displacement vector and x_k and x_ℓ are the components of the position vector $\underline{x}$. For an infinitesimal strain equation (5 3) may be approximated to,

$$\varepsilon_{k\ell} = \frac{1}{2}\left[u_k k_\ell + u_\ell k_k\right] \tag{5.4}$$

Since the deformation potential tensors are symmetric ($D_{k\ell} = D_{\ell k}$) , the expression for the band edge energy change may be approximated as,

$$W^{(i)} \simeq \sum_{k\ell} D_{k\ell}\, u_k\, k_\ell \tag{5.5}$$

The deformation potential tensors $I^{(i)}$ associated with the electron ellipsoids can be written in the general form (see eqn. 2 3)

$$L^{(1)} = \begin{pmatrix} L_{11} & 0 & 0 \\ 0 & L_{22} & L_{23} \\ 0 & L_{23} & L_{33} \end{pmatrix}$$

$$L^{(2)} = \begin{pmatrix} \frac{1}{4}(L_{11}+3L_{22}), & +\frac{\sqrt{3}}{4}(L_{11}-L_{22}), & \frac{\sqrt{3}}{2}L_{23} \\ +\frac{\sqrt{3}}{4}(L_{11}-L_{22}), & \frac{1}{4}(3L_{11}+L_{22}), & -\frac{1}{2}L_{23} \\ +\frac{\sqrt{3}}{2}L_{23} & , -\frac{1}{2}L_{23} & , L_{33} \end{pmatrix} \tag{5.6}$$

$$L^{(3)} = \begin{pmatrix} \frac{1}{4}(L_{11}+3L_{22}), & -\frac{\sqrt{3}}{4}(L_{11}-L_{22}), & -\frac{\sqrt{3}}{2}L_{23} \\ -\frac{\sqrt{3}}{4}(L_{11}-L_{22}), & \frac{1}{4}(3L_{11}+L_{22}), & -\frac{1}{2}L_{23} \\ -\frac{\sqrt{3}}{2}L_{23} & , -\frac{1}{2}L_{23} & , L_{33} \end{pmatrix}$$

and the deformation potential tensor T of the hole ellipsoid as

$$T = \begin{pmatrix} T_{11} & 0 & 0 \\ 0 & T_{11} & 0 \\ 0 & 0 & T_{33} \end{pmatrix} \tag{5.6a}$$

The shift in energy of each of the four carrier ellipsoids may be calculated by using equation 5.5. Table 5.1 gives the energy change of each of the carrier ellipsoids for sound propagation along the [100], [001] and $[0, \frac{-1}{\sqrt{2}}, \frac{1}{\sqrt{2}}]$ crystallographic

Propagation Vector $\underline{k}$	Velocity	Polarisation Vector $\underline{u}$	Band Index	Band Edge Energy Change $W^{(i)} = \sum_{k\ell} D_{k\ell} u_k k_\ell$
$\begin{bmatrix} 1 \\ 0 \\ 0 \end{bmatrix}$	V_1	$\begin{bmatrix} 1 \\ 0 \\ 0 \end{bmatrix}$	1	L_{11}
			2,3	$\frac{1}{4}(L_{11} + 3L_{22})$
			4	T_{11}
	V_2	$\begin{bmatrix} 0 \\ 0.859 \\ 0.514 \end{bmatrix}$	1	0
			2,3	$\pm \frac{\sqrt{3}}{2} [0.429[L_{11} - L_{22}] + 0.514 L_{23}]$
			4	0
	V_3	$\begin{bmatrix} 0 \\ 0.514 \\ -0.859 \end{bmatrix}$	1	0
			2,3	$\pm \frac{\sqrt{3}}{2} [0.257 [L_{11} - L_{22}] - 0.859 L_{23}]$
			4	
$\begin{bmatrix} 0 \\ 0 \\ 1 \end{bmatrix}$	V_7	$\begin{bmatrix} 0 \\ 0 \\ 0 \end{bmatrix}$	1	L_{33}
			2,3	L_{33}
			4	T_{33}
	V_8	$\begin{bmatrix} \cos\theta \\ \sin\theta \\ 0 \end{bmatrix}$	1	L_{23}
			2,3	$\frac{1}{2}[\pm\sqrt{3}\cos\theta - \sin\theta]L_{23}$
			4	0
$\begin{bmatrix} 0 \\ -\frac{1}{\sqrt{2}} \\ \frac{1}{\sqrt{2}} \end{bmatrix}$	V_{12}	$\begin{bmatrix} 0 \\ -0.842 \\ 0.569 \end{bmatrix}$	1	$\frac{1}{\sqrt{2}}(+0.842 L_{22} + 0.569 L_{33} - 1.411 L_{23})$
			2,3	$\frac{1}{\sqrt{2}}(+0.211 [3L_{11} + L_{22}] + 0.569 L_{33} + 0.705 L_{33})$
			4	$\frac{1}{\sqrt{2}}(0.842 T_{11} + 0.569 T_{33})$
	V_{13}	$\begin{bmatrix} 1 \\ 0 \\ 0 \end{bmatrix}$	1	0
			2,3	$\frac{1}{\sqrt{2}} (\frac{\sqrt{3}}{2} L_{23} - \frac{\sqrt{3}}{4} (L_{11} - L_{22}))$
			4	0
	V_{14}	$\begin{bmatrix} 0 \\ 0.569 \\ 0.842 \end{bmatrix}$	1	$\frac{1}{\sqrt{2}}(-0.569 L_{22} + 0.842 L_{33} - 0.273 L_{33})$
			2,3	$-\frac{1}{\sqrt{2}}(-0.145 [3L_{11} + L_{22}] + 0.842 L_{33} - 0.136 L_{23})$
			4	$\frac{1}{\sqrt{2}}(-0.569 T_{11} + 0.842 T_{33})$

Table 5.1 Energy Changes for the Carrier Ellipsoids.

Band Indexes 1,2, and 3 are the electron ellipsoids and 4 is the hole ellipsoid directions, the particle displacement vectors are those calculated for pure bismuth at room temperature (see Table 3.1). These calculations demonstrate the important feature that sound propagation in any direction in the bismuth crystals will produce changes in band edge energies. Moreover, as a consequence of the three fold symmetry the electron ellipsoids can only be perturbed identically when a longitudinal sound wave is propagated along the trigonal direction, therefore energy differentials will exist between the electron Fermi pockets for all directions of sound propagation other than for the longitudinal trigonal pure mode. A redistribution of carriers in pure bismuth may be accomplished by two distinct processes. Energy differentials between the three L-point electron ellipsoids will promote the transfer of electrons between the valleys to attain equilibrium. These transitions will be referred to here as L→L point transitions. A stress that induces a change in the L - T point overlap energy will either create more carriers (increase the overlap) or will initiate electron-hole recombination with an accompanying decrease in the carrier population. This effect will be referred to as an L→T point transition. In high purity bismuth both the L→L and the L→T point transitions could occur, however, in the case of highly donor (tellurium) doped bismuth the L→L point transition must be the dominant mechanism since Noothoven van Goor and Trum (1971) have shown that when 8×10^{17} cm^{-3} donors are present the electrons are the only carriers, the hole band having been completely filled. The application here of the Keyes model to the electronic band structure of bismuth will make the assumption that only L→L point transitions occur and that the energy shift of T point hole ellipsoid does not influence the carrier density

5.3 Application of the Keyes model to the electron band structure of bismuth

As in equation (5.1), the change in energy of an electron pocket in the presence of a mechanical deformation is denoted by

$$W^{(i)} = \sum_{k,\ell} L_{k\ell}\,\varepsilon_{k\ell} \tag{5.7}$$

Band edge energy changes may modify the Fermi level from its equilibrium value, E_{F_o}, by an amount α, so that $E_F = E_{F_o} + \alpha$ represents the new location of the Fermi level. The electronic free energy of the electrons in a valley (i) is given by the expression (which is derived in Appendix 1)

$$F_e^{(i)} = n^{(i)} E_F + kT \int_{E^{(i)}}^{\infty} N^{(i)}(E) \log \left[1 - f(E,E_F)\right] dE \tag{5.8}$$

where $F_e^{(i)}$ is the electronic free energy, $N^{(i)}(E)$ is the density of states function, $f(E,E_F)$ is the Fermi-Dirac probability function, $n^{(i)}$ is the number of electrons and $E^{(i)}$ is the minimum band edge energy. The Fermi-Dirac probability function is

$$f(E,E_F) = \left[1 + \exp \frac{E - E_F}{kT}\right]^{-1} \tag{5.9}$$

and the total population of electrons in valley (i) is

$$n^{(i)} = \int_{E^{(i)}}^{\infty} N^{(i)}(E)\, f(E,E_F)\, dE \tag{5.10}$$

The expression for the free energy may be expanded by using a Taylor Series expansion of $\log\,[1 - f(E,E_F)]$ in powers of $(W^{(i)} - \alpha)$ and derivatives of $f(E,E_{F_o})$. Since the band energies are modified by $W^{(i)}$ (i.e. $E \rightarrow E - W^{(i)}$) and the Fermi level is altered by α (i.e. $E_F = E_{F_0} + \alpha$), the logarithmic term in the free energy becomes

$$\log\Big[\, 1 - f(E,E_F)\Big] = \log\Big[1 - (1 - \exp\Big[(E - E_{F_0}) - (W^{(i)} - \alpha)\Big]/kT)^{-1}\Big] \qquad (5.11)$$

Since $\partial(\log\big[1 - f(E,E_{F_0})\big])/\partial E = f(E,E_{F_0})/kT$, the series expansion is

$$\log\Big[1 - f(E,E_F)\Big] = \log\Big[1 - f(E,E_{F_0})\Big]$$

$$+ (W^{(i)} - \alpha)\ f(E,E_{F_0})/kT + \frac{(W^{(i)} - \alpha)^2}{2kT} \quad \frac{\partial f(E,E_{F_0})}{\partial E}$$

$$+ \frac{(W^{(i)} - \alpha)^3}{6kT} \quad \frac{\partial^2 f(E,E_{F_0})}{\partial E} + \ . \ . \qquad (5.12)$$

The total electron free energy is obtained by a summation over all three valleys ,

$$F_e = \sum_{i=1}^{3} F_e^{(i)} = \sum_{i=1}^{3} \Bigg[n^{(i)} (E_{F_0} + \alpha) + kT \int_{E^{(i)}}^{\infty} N^{(i)}(E)$$

$$\Big[1 - \log f(E,E_{F_0})\Big]\ dE + (W^{(i)} - \alpha) \int_{E^{(i)}}^{\infty} N^{(i)}(E)\ f(E,E_{F_0})\ dE$$

$$+ \frac{1}{2} (W^{(i)} - \alpha)^2 \int_{E^{(i)}}^{\infty} N^{(i)}\ (E)\ \frac{\partial f(E,E_{F_0})\ dE}{\partial E} + \frac{1}{6} (W^{(i)} - \alpha)^3 \int_{E^{(i)}}^{\infty} N^{(i)}(E)$$

$$\frac{\partial^2 f(E,E_{F_0})}{\partial E^2}\ dE + \ .... \Bigg] \qquad (5.13)$$

The fourth term in the expansion is quadratic in strain and will make a contribution to the second-order elastic constants, $\partial f(E,E_{F_o})/\partial E$ is a negative delta function and consequently the function

$$\beta^{(i)} = -\int_{E^{(i)}}^{\infty} N^{(i)}(E)\,\frac{\partial f(E,E_{F_o})}{\partial E}\,dE \qquad (5.14)$$

is essentially the effective density of states at the Fermi surface concerned in the redistribution The fifth term in the expansion is third order in strain and leads to a contribution to the third order elastic constants, a solution to this term will not be pursued here.

Since the assumption is made that only L → L point transitions occur, the total number of electrons remains constant. From this criterion, the shift α in the fermi level can be determined. The change in population of valley (i) is

$$\Delta n^{(i)} = (W^{(i)} - \alpha)\,\beta^{(i)} \qquad (5.15)$$

To fulfil the condition of constant electron population

$$\sum_{i=1}^{3} \Delta n^{(i)} = 0 = \sum_{i=1}^{3} (W^{(i)} - \alpha)\,\beta^{(i)},$$

therefore

$$\sum_{i=1}^{3} W^{(i)}\beta^{(i)} - \alpha\sum_{i=1}^{3}\beta^{(i)} = 0 \qquad (5.16)$$

and the change in Fermi level is

$$\alpha = \frac{\sum_{i=1}^{3} W^{(i)}\beta^{(i)}}{\sum_{i=1}^{3}\beta^{(i)}} \qquad (5.17)$$

Substitution of (5.17) into (5.13) yields the following expression for the total electron free energy to second order in strain ,

$$F_e = N E_{F_o} + kT \sum_{i=1}^{3} \left[\int_{E^{(i)}}^{\infty} N^{(i)} (E) \log \left[1 - f(E,E_{F_o}) \right] dE \right]$$

$$+ \sum_{i=1}^{3} n^{(i)} W^{(i)} + \sum_{i=1}^{3} - \frac{1}{2} \left[W^{(i)} - \frac{\sum_{j=1}^{3} W^{(j)} \beta^{(j)}}{\sum_{j=1}^{3} \beta^{(j)}} \right]^2 \beta^{(i)} \qquad (5.18)$$

where the total electron population $N = \sum_{i=1}^{3} n^{(i)}$.

The first two terms

$$N E_{F_o} + kT \sum_{i=1}^{3} \int_{E^{(i)}}^{\infty} N^{(i)} (E) \log \left[1 - f(E,E_{F_o}) \right] dE \qquad (5.19) ,$$

represent the electronic free energy in the absence of strain. The third term is linear in strain and represents the effect of dilational strain on the electronic energy. Expansion of the fourth term which is quadratic in the strain yields

$$F_e = \sum_{j=1}^{3} - \frac{1}{2} \left[W^{(i)^2} - 2W^{(i)} \frac{\sum_{j=1}^{3} W^{(j)} \quad ^{(j)}}{\sum_{j=1}^{3} \beta^{(j)}} + \frac{\left(\sum_{j=1}^{3} W^{(j)} \quad ^{(j)} \right)^2}{\left(\sum_{j=1}^{3} \beta^{(j)} \right)^2} \right] \beta^{(i)}$$

(5.20)

$$= \frac{\frac{1}{2} \sum_{i=1}^{3} \sum_{j=1}^{3} \left[W^{(i)^2} \beta^{(i)} \beta^{(j)} - 2W^{(i)} W^{(j)} \beta^{(i)} \beta^{(j)} - W^{(i)} W^{(j)} \beta^{(i)} \beta^{(j)} \right]}{\sum_{j=1}^{3} \beta^{(j)}}$$

$$= \frac{\frac{1}{2} \sum_{i=1}^{3} \sum_{j=1}^{3} \left(\frac{1}{2} W^{(i)^2} + \frac{1}{2} W^{(j)^2} - W^{(i)} W^{(j)} \right) \beta^{(i)} \beta^{(j)}}{\sum_{j=1}^{3} \beta^{(j)}}$$

$$= \frac{\frac{1}{4} \sum_{i=1}^{3} \sum_{j=1}^{3} \left(W^{(i)} - W^{(j)} \right)^2 \beta^{(i)} \beta^{(j)}}{\sum_{i=1}^{3} \beta^{(j)}} \tag{5.21}$$

Since from equation (5.14) $\beta^{(i)} = \beta^{(j)}$, the quadratic free energy term reduces to

$$F_e = -\frac{1}{12} \sum_{i=1}^{3} \sum_{j=1}^{3} \left(W^{(i)} - W^{(j)} \right)^2 \beta^{(i)} \tag{5.22}$$

This equation clearly shows that there will only be a free electron energy contribution to the second order elastic constants if there exists an energy differential between at least two of the electron ellipsoids, otherwise, if the band edges remain constant or are perturbed identically, the contribution will be zero, since

$$\sum_{i=1}^{3} \sum_{j=1}^{3} \left(W^{(i)} = W^{(j)} \right)^2 = 0 \tag{5.23}$$

The general form of the free energy obtained here is identical to that derived by Keyes (1967) which he subsequently applied to the ellipsoidal and parabolic band structures of cubic silicon and germanium. For the first time, a solution of the Keyes model to the band structure of rhombohedral bismuth will be presented.

The dispersion relation that best describes the electron Fermi surface in bismuth is that of the non-ellipsoidal non-parabolic (N.E.N.P.) band model, originally developed by Cohen (1961) The density of states function is ,

$$N^{(i)}(E) = \frac{4}{\pi^{\frac{1}{2}}}\left(\frac{2\pi m^*}{h^2}\right)^{3/2} E^{\frac{1}{2}}\left(1 + \frac{2E}{Eg}\right) \tag{5.24}$$

where m* is the band edge effective mass, h is Planck's constant and Eg is the L-point energy gap The electron density of a valley is therefore

$$n^{(i)} = \frac{4}{\pi^{\frac{1}{2}}}\left(\frac{2\pi m^*}{h^2}\right)^{3/2} \int_0^\infty E^{\frac{1}{2}}\left(1 + \frac{2E}{Eg}\right)\left[1 + \exp\frac{E - E_{F_0}}{kT}\right]^{-1} dE \tag{5.25}$$

Introducing the well known Fermi-Dirac function (Macdougall and Stoner 1939)

$$F_k(\eta) = \int_0^\infty \frac{x^k}{1 + \exp(x - \eta)}\, dx \tag{5.26}$$

where x = E/kT and $\eta = E_{F_0}/kT$, the electron density reduces to

$$n^{(i)} = \frac{2}{\pi^{1/2}} N_c \left[F_{1/2}(\eta) + \frac{2kT}{E_g} F_{3/2}(\eta) \right] \qquad (5.27)$$

where

$$N_c = 2\left(\frac{2\pi m^* kT}{h^2}\right)^{3/2} \qquad (5.28)$$

The effective density of states concerned in the electron redistribution $\beta^{(i)}$ becomes

$$\beta^{(i)} = \frac{4}{\pi^{1/2}} \left(\frac{2\pi m^*}{h^2}\right)^{3/2} \int_0^\infty E^{1/2} \left(1 + \frac{2E}{E_g}\right) \frac{\partial}{\partial E} \left[1 + \exp \frac{E - E_{F_o}}{kT}\right]^{-1} dE$$

$$= \frac{2}{\pi^{1/2}} \left(\frac{N_c}{kT}\right) \left[F'_{1/2}(\eta) + \frac{2kT}{E_g} F'_{3/2}(\eta) \right] \qquad (5.29)$$

where

$$F'_{1/2}(\eta) = \frac{\partial}{\partial \eta} F_{1/2}(\eta)$$

and

$$F'_{3/2}(\eta) = \frac{\partial}{\partial \eta} F_{3/2}(\eta) \qquad (5.30)$$

To facilitate numerical calculation, the derivatives of the Fermi Dirac integrals may be transformed into a non derivative form by the following relationships ,

$$F'_k(\eta) = k\, F_{k-1}(\eta) \qquad (5.31)$$

Since

$$F'_{1/2}(\eta) = 1/2\, F_{-1/2}(\eta) \qquad (5.32)$$

and

$$F'_{3/2}(\eta) = 3/2\, F_{1/2}(\eta) \qquad (5.33)$$

the effective density of states transforms to

$$\beta^{(i)} = \pi^{-1/2} N_c (kT)^{-1} \left[F_{-1/2}(\eta) + \frac{6kT}{E_g} F_{1/2}(\eta) \right] \qquad (5.34)$$

To complete the evaluation of the second order electronic contribution it is necessary to calculate the energy change of each ellipsoid in the presence of a mechanical strain and to expand the summation

$$\sum_{i=1}^{3} \sum_{j=1}^{3} \left(W^{(i)} - W^{(j)}\right)^2 \qquad (5.35)$$

The change in energy of each electron pocket is given by a double contraction of the deformation potential tensor over the strain tensor. Since the strain tensor is symmetrical, it has six independent components

$$\varepsilon = \begin{pmatrix} \varepsilon_{11} & \varepsilon_{12} & \varepsilon_{13} \\ \varepsilon_{12} & \varepsilon_{22} & \varepsilon_{23} \\ \varepsilon_{13} & \varepsilon_{23} & \varepsilon_{33} \end{pmatrix} \qquad (5.36)$$

Application of equations (5.7a) and (5.6) gives the form of the band edge energy changes ,

$$\begin{aligned} W^{(1)} &= \sum_{k\ell} L^{(1)}_{k\ell}\, \varepsilon_{k\ell} \\ &= L_{11}\, \varepsilon_{11} + L_{22}\, \varepsilon_{22} + 2L_{23}\, \varepsilon_{23} + L_{33}\, \varepsilon_{33} \end{aligned}$$

$$\begin{aligned} W^{(2)} &= \sum_{k\ell} L^{(2)}_{k\ell}\, \varepsilon_{k\ell} \\ &= 1/4\, (L_{11} + 3L_{22})\, \varepsilon_{11} + \frac{\sqrt{3}}{2}\, (L_{11} - L_{22})\, \varepsilon_{12} + \sqrt{3}\, L_{23}\, \varepsilon_{13} \\ &\quad + 1/4\, (3L_{11} + L_{22})\, \varepsilon_{22} - L_{23}\, \varepsilon_{23} + L_{33}\, \varepsilon_{33} \qquad (5.38) \end{aligned}$$

$$\begin{aligned} W^{(3)} &= \sum_{k\ell} L^{(3)}_{k\ell}\, \varepsilon_{k\ell} \\ &= 1/4\, (L_{11} + 3L_{22})\, \varepsilon_{11} - \frac{\sqrt{3}}{2}\, (L_{11} - L_{22})\, \varepsilon_{12} - \sqrt{3}\, L_{23}\, \varepsilon_{13} \\ &\quad + 1/4\, (3L_{11} + L_{22})\, \varepsilon_{22} - L_{23}\, \varepsilon_{23} + L_{33}\, \varepsilon_{33} \qquad (5.39) \end{aligned}$$

Expansion of the summation in the free energy yields six non zero components

$$\begin{aligned} \sum_{i=1}^{3} \sum_{j=1}^{3} \left(W^{(i)} - W^{(j)} \right)^2 &= \left(W^{(1)} - W^{(2)} \right)^2 + \left(W^{(2)} - W^{(1)} \right)^2 \\ &+ \left(W^{(1)} - W^{(3)} \right)^2 + \left(W^{(3)} - W^{(1)} \right)^2 + \left(W^{(2)} - W^{(3)} \right)^2 + \left(W^{(3)} - W^{(2)} \right)^2 \end{aligned} \qquad (5.40)$$

Due to the similarity in the first four components these will be summed collectively:

$$W^{(2)} - W^{(1)} = {}^{3}/_{4}(L_{22} - L_{11})\varepsilon_{11} + {}^{\sqrt{3}}/_{2}(L_{11} - L_{22})\varepsilon_{12} + \sqrt{3}\, L_{23}\, \varepsilon_{13} + {}^{3}/_{4}(L_{11} - L_{22})\varepsilon_{22} - 3L_{23}\, \varepsilon_{23}$$

$$W^{(1)} - W^{(2)} = {}^{3}/_{4}(L_{11} - L_{22})\varepsilon_{11} - {}^{\sqrt{3}}/_{2}(L_{11} - L_{22})\varepsilon_{12} - \sqrt{3}\, L_{23}\, \varepsilon_{13} + {}^{3}/_{4}(L_{22} - L_{11})\varepsilon_{22} + 3L_{23}\, \varepsilon_{23}$$

$$W^{(3)} - W^{(1)} = {}^{3}/_{4}(L_{22} - L_{11})\varepsilon_{11} - {}^{\sqrt{3}}/_{2}(L_{11} - L_{22})\varepsilon_{12} - \sqrt{3}\, L_{23}\, \varepsilon_{13} + {}^{3}/_{4}(L_{11} - L_{22})\varepsilon_{22} - 3L_{23}\, \varepsilon_{23}$$

$$W^{(1)} - W^{(3)} = {}^{3}/_{4}(L_{11} - L_{22})\varepsilon_{11} + {}^{\sqrt{3}}/_{2}(L_{11} - L_{22})\varepsilon_{12} + \sqrt{3}\, L_{23}\, \varepsilon_{13} + {}^{3}/_{4}(L_{22} - L_{11})\varepsilon_{22} + 3L_{23}\, \varepsilon_{23}$$

Therefore $\left(W^{(2)} - W^{(1)}\right)^2 + \left(W^{(1)} - W^{(2)}\right)^2 + \left(W^{(3)} - W^{(1)}\right)^2 - \left(W^{(1)} - W^{(3)}\right)^2$

$$= {}^{9}/_{4}(L_{11} - L_{22})^2\, \varepsilon_{11}^2 + 3(L_{11} - L_{22})^2\, \varepsilon_{12}^2 + 12L_{23}^2\, \varepsilon_{13}^2 + {}^{9}/_{4}(L_{11} - L_{22})^2\, \varepsilon_{22}^2 + 36L_{23}^2\, \varepsilon_{23}^2$$

$$- {}^{9}/_{2}(L_{11} - L_{22})^2\, \varepsilon_{22}\, \varepsilon_{11} + 18(L_{11} - L_{22})\, L_{23}\, \varepsilon_{11}\, \varepsilon_{23} + 12\, [L_{11} - L_{22}]\, L_{23}\, \varepsilon_{12}\, \varepsilon_{13}$$

$$- 18(L_{11} - L_{22})\, L_{23}\, \varepsilon_{22}\, \varepsilon_{23} \tag{5.41}$$

Summation of the last two components of equation (5.40) yields

$$\left(W^{(3)} - W^{(2)}\right)^2 + \left(W^{(2)} - W^{(3)}\right)^2 = 24L_{23}^2\,\varepsilon_{13}^2 + 6(L_{11} - L_{22})^2\,\varepsilon_{12}^2 + 24(L_{11} - L_{22})L_{23}\,\varepsilon_{12}\,\varepsilon_{13} \qquad (5\ 42)$$

The total summation therefore becomes

$$\sum_{i=1}^{3}\sum_{j=1}^{3}\left(W^{(i)} - W^{(j)}\right)^2 = 18\Big[{}^1/_4\,(L_{11} - L_{22})^2\left(\frac{\varepsilon_{11}^2}{2} + \frac{\varepsilon_{22}^2}{2} + \varepsilon_{12}^2\right) - {}^1/_4\,(L_{11} - L_{22})^2\,(\varepsilon_{11}\varepsilon_{22} - \varepsilon_{12}^2) + 2L_{23}^2(\varepsilon_{13}^2 + \varepsilon_{23}^2) + {}^1/_2\,(L_{11} - L_{22})L_{23}\,(2\varepsilon_{11}\varepsilon_{23} + 4\varepsilon_{12}\varepsilon_{13} - 2\varepsilon_{22}\varepsilon_{23})\Big] \qquad (5.43)$$

The elastic strain energy of a trigonal crystal to terms of second order in strain has been shown (see Section 3 8) to be

$$\Phi = C_{11}\left(\frac{\varepsilon_{11}^2}{2} + \frac{\varepsilon_{22}^2}{2} + \varepsilon_{12}^2\right) + C_{12}\,(\varepsilon_{11}\varepsilon_{22} - \varepsilon_{12}^2) + C_{44}\,(\varepsilon_{13}^2 + \varepsilon_{23}^2) + C_{14}\,(2\varepsilon_{11}\varepsilon_{23} + 4\varepsilon_{12}\varepsilon_{13} - 2\varepsilon_{22}\varepsilon_{23}) \qquad (5.44)$$

Comparison of the elastic strain energy with that of the electron free energy shows that the elastic constants C_{11}, C_{12}, C_{14} and C_{44} will possess electronic contributions. The magnitude of these contributions will be (from equation 5.22 and 5.34)

$$\begin{aligned}
\Delta C_{11} &= -{}^{9}/_{2}\,(L_{11} - L_{22})^2\ \gamma \\
\Delta C_{12} &= +{}^{9}/_{2}\,(L_{11} - L_{22})^2\ \gamma \\
\Delta C_{14} &= -12\,(L_{11} - L_{22})L_{23}\ \gamma \\
\Delta C_{44} &= -36\ L_{23}^2\ \gamma
\end{aligned} \qquad (5.45)$$

where

$$\begin{aligned}
\gamma &= \beta/_{12} \\
&= \frac{\pi^{-1/2}}{12} N_c (kT)^{-1} \left[F_{-1/2}(\eta) + \frac{6kT}{E_g} F_{1/2}(\eta) \right]
\end{aligned} \qquad (5.46)$$

The deformation potentials have been measured experimentally by Walther (1968) and by Inoue and Tsuji (1967) and have been calculated using a pseudopotential method by Katsuki (1969). The numerical values obtained are presented in Table 6.4. Substitution of the deformation potentials into equation 5.45 indicates that, in the presence of a strain, C_{11} and C_{44} will be reduced, whilst C_{12} and C_{14} will be increased in magnitude. At first sight this might appear paradoxical, since we might expect a lowering of all the elastic constants. However, in reality, we must expect a lowering of some of the effective elastic constants ($C = \rho V_i^2$, where C may be a combination of second order elastic constants, see Table 3.1), but not necessarily a reduction of all the second order elastic constants. In the rhombohedral structure there are only three modes with a simple velocity-elastic constant relationship, i.e.

$$\begin{aligned}
\rho V_1^2 &= C_{11} \\
\rho V_7^2 &= C_{33} \\
\rho V_8^2 &= C_{44}
\end{aligned} \qquad (5.47)$$

The present theory predicts a lowering of V_1 and V_8, consistent with our expectations. But other directions of propagation present a far more complex picture (Table 3.1), since C_{12} always appears as a negative constant, an increase in C_{12} will decrease the effective elastic constants, (N.B. C_{12} in silicon also increases, Hall (1966)), a change in C_{14} may either raise or reduce the effective elastic constants and therefore an increase in C_{14} is consistent with the argument. The computations in Chapter 6 will show that the electronic contributions should decrease all the measured ultrasonic velocities, apart from the longitudinal trigonal pure mode ($\rho V_7^2 = C_{33}$).

CHAPTER 6

ELECTRON BAND PARAMETERS AND COMPUTATION OF THE ELECTRON CONTRIBUTION TO THE ELASTIC CONSTANTS

6.1 Introduction

To calculate the electronic contributions to the elastic constants as a function of temperature, a knowledge of the electronic parameters is required, i.e. the carrier concentration, the L point energy gap, the effective masses and the deformation potentials. Fortunately, we have been able to obtain the experimental data for these parameters from the literature. The magnitudes of the electronic parameters of pure bismuth at 4.2 K are now well established values for the effective masses have been obtained by a number of different experiments, among them those based on cyclotron resonance, quantum oscillations and optical reflectivity, the deformation potentials have been deduced from magnetoacoustic experiments, the L point energy gap from magnetoreflection and the carrier concentration has been derived from galvanomagnetic measurements. As the temperature is increased from 4.2 K the electron relaxation time decreases rapidly and the condition for cyclotron resonance and quantum oscillation ($\omega\tau >> 1$) breaks down. Thus, at higher temperatures, transport properties and magnetoreflection measurements have to be relied upon for the necessary information Previously, in the absence of quantitative data, it has been standard practice to assume that the effective masses and the L point energy gap remain constant with temperature, however, recent magnetoreflection studies (Vecchi and Dresselhaus 1974) have indicated that this assumption is grossly inaccurate.

This chapter reviews the measurements which have been carried out on bismuth and on the bismuth-antimony alloys, in the light of this knowledge a justification of the parameters used in the present work is made. Finally, the electronic contributions to the elastic constants, as predicted by the model in chapter five, are presented.

6.2 Band Parameters of Pure Bismuth

(a) At 4.2 K

The Fermi surface effective masses of pure bismuth at 4.2 K, measured by a variety of experimental techniques, are collected in Table 6.1, the effective masses m_1', m_2', m_3' refer to those measured at the Fermi level. The density of states effective mass in the ellipsoidal parabolic model of Shoenberg is given by

$$m^* \text{ (EP)} = (m_1' \; m_2' \; m_3')^{1/3} \qquad (6\ 1)$$

In the non-ellipsoidal non-parabolic model (see Chapter 2, page 15) the dispersion (E-k) curves corresponding to m_1' and m_3' are non-parabolic, whilst that corresponding to m_2' is parabolic. The band edge effective masses for the NENP model are derived from the electron Fermi level effective masses by the relations

$$m_1'(0) = m_1' / (1 + \frac{2E_F}{E_g})$$

$$m_2'(0) = m_2' \qquad (6.2)$$

$$m_3'(0) = m_3' / (1 + \frac{2E_F}{E_g}) \qquad (6.3)$$

Experimental Technique	Fermi level masses			Density of states effective mass			Reference
	m_1'	m_2'	m_3'	m*(EP)	m*(ENP)	m*(NENP)	
1. de Haas-van Alphen	0.00239	2.53	0.0245	0.053	0.012	0.020	Shoenberg (1939)
2. Cyclotron resonance	0.00598	1.01	0.0099	0.039	0.009	0.015	Aubrey and Chambers (1957)
3. Cyclotron resonance	0.00877	1.79	0.0213	0.069	0.016	0.026	Galt et al (1959)
4. Infrared absorption	0.00752	1.70	0.0110	0.052	0.012	0.020	Boyle and Brailsford (1960)
5. de Haas-van Alphen	0.00495	1.16	0.0141	0.043	0.009	0.016	Weiner (1962)
6. Cyclotron resonance	0.00617	1.31	0.0115	0.045	0.010	0.017	G.E. Smith et al (1963)
7. Reinterpretation of 3 & 4	0.00709	1.71	0.0114	0.052	0.012	0.019	Kao (1963)
8. Shubnikov-de Haas	0.00840	1.75	0.0097	0.052	0.012	0.019	Jain and Koenig (1962)
9. Resistance Oscillations	0.00521	1.21	0.014	0.045	0.0103	0.016	G.E. Smith, Baraff and Rowell (1964)

Table: 6.1

Thus, the NENP band edge density of states effective mass is

$$m^*(\text{NENP}) = m^*(\text{E.P}) \Big/ \left[1 + \frac{2E_F}{E_g}\right]^{2/3} \qquad (6.4)$$

Since, in the ENP model of Lax the effective masses are non-parabolic in all directions, the band edge ENP density of states effective mass is

$$m^*(\text{ENP}) = m^*(\text{EP}) \Big/ \left[1 + \frac{2E_F}{E_g}\right] \qquad (6.5)$$

Thus, if the Fermi level and the L point energy gap are known, the band edge effective masses may be calculated using either (6.4) or (6.5). There is now general agreement that the Fermi level lies 25 meV above the conduction band minima and that the L point gap is 13.6 meV (Vecchi and Dresselhaus 1974). Dinger and Lawson (1970) have reappraised the experimental results of both Kao (1963) and Edelman and Khaikin (1966) and have concluded that the NENP is a more accurate description of the electron Fermi surface. In the present study the NENP model was employed, the band edge density of states effective mass was computed from the results of Smith, Baraff and Rowell (1964) to be 0.016 free electron masses. Table 6.1 presents the density of states effective masses calculated from the various reported Fermi surface experiments.

(b) As a function of Temperature

Michenaud and Issi (1972) have resolved the temperature variation of the carrier population; Figure 6.1 shows that the carrier concentration is approximately constant below liquid nitrogen temperatures (3.3×10^{17} cm^{-3} at 4.2 K), but at higher temperature it increases rapidly (2.45×10^{18} cm^{-3} at 290 K). Recently

Vecchi and Dresselhaus (1974) have overcome the problems of making magnetoreflection experiments at higher temperatures and have measured the temperature dependence of some of the L point band edge parameters. They give the temperature variation of the L point gap as

$$E_g = 13.6 + (2.1 \times 10^{-3})\ T + (2.5 \times 10^{-4})\ T^2\ \text{eV} \qquad (6.6)$$

Thus, the L point energy gap increases with temperature with the result that the electron bands should become more parabolic. Vecchi and Dresselhaus also measured the temperature variation of some of the inverse cyclotron masses β*, but since they only present the results for three cyclotron masses (light binary, heavy bisectrix and light bisectrix) it is not possible to derive the temperature dependence of all the effective mass components. To utilise their results, it is necessary to make a number of simplifying assumptions, the data is presented in the form of the inverse cyclotron mass β*, where

$$\beta^* = \beta_o \frac{m_o}{m_c^*} \qquad (6.7)$$

and

$$\beta_o = \frac{e\,h}{m_o c}$$

where β_o is twice the Bohr magnetron, m_c^* is the cyclotron mass, e is electron charge, h is Plank's constant and c is the velocity of light. The relationship between the cyclotron effective mass and the band edge effective masses is

$$m_c^* = \left(\frac{(\mathrm{DET}\ \overleftrightarrow{m})}{(\hat{\underline{h}} \cdot \overleftrightarrow{m} \cdot \hat{\underline{h}})} \right)^{\frac{1}{2}} m_o \tag{6.8}$$

where $\underline{h}$ is a unit vector in the direction of the external magnetic field and $\overleftrightarrow{m}$ is

$$\overleftrightarrow{m} = \begin{pmatrix} m_1(0) & 0 & 0 \\ 0 & m_2(0) & m_4(0) \\ 0 & m_4(0) & m_3(0) \end{pmatrix} \tag{6.9}$$

For the three orientations measured by Vecchi and Dresselhaus, we obtain

(i) light binary

$$m_c^*(\ell bn) = 2\left(\frac{m_1(m_2m_3 - m_4^2)}{m_1 + 3m_2} \right)^{\frac{1}{2}} \tag{6.10}$$

(ii) light bisectrix

$$m_c^*(\ell bx) = \left(\frac{m_1(m_2m_3 - m_4^2)}{m_2} \right)^{\frac{1}{2}}$$

(iii) heavy bisectrix

$$m_c^*(hbx) = 2\left(\frac{m_1(m_2m_3 - m_4^2)}{3m_1 + m_2} \right)^{\frac{1}{2}}$$

Inspection of these equations reveals that only solutions to m_1, m_2 and m_3/m_4 are possible, however, attempts at a direct solution failed because m_2 is much larger than m_1 Since to calculate the density of states band edge effective mass we require solutions in which the effective mass is diagonal, $\overleftrightarrow{m}$, diagonalization will now be carried through. The two effective mass tensors are related by a rotation R(θ) about the binary axis

$$\overleftrightarrow{m} \quad = \quad R(\theta) \ \ \overleftrightarrow{m'} \ R^{T}(\theta) \qquad (6.11)$$

where

$$R(\theta) \quad = \quad \begin{pmatrix} 1 & 0 & 0 \\ 0 & \cos\theta & -\sin\theta \\ 0 & \sin\theta & \cos\theta \end{pmatrix}$$

and θ is the tilt angle of the electron ellipsoid. Solution of equation 6.11 yields the relationships between the components of the two effective mass tensors,

$$\begin{aligned} m_1 &= m_1' \\ m_2 &= m_2' \cos^2\theta + m_3' \sin^2\theta \\ m_3 &= m_2' \sin^2\theta + m_3' \cos^2\theta \\ m_4 &= (m_2' - m_3') \cos\theta \sin\theta \end{aligned} \qquad (6.12)$$

and

$$(m_2 m_3 - m_4^2) \quad = \quad m_2' \, m_3'$$

The three cyclotron masses therefore become

(i) light binary

$$m_c^*(\ell bn) \quad = \quad 2\left[\frac{m_1' \, m_2' \, m_3'}{m_1' + 3\left[m_2' \cos^2\theta + m_3' \sin^2\theta\right]}\right]^{\frac{1}{2}}$$

(ii) light bisectrix (6.13)

$$m_c^*(\ell bx) \quad = \quad \left[\frac{m_1' \, m_2' \, m_3'}{\left[m_2' \cos^2\theta + m_3' \sin^2\theta\right]}\right]^{\frac{1}{2}}$$

(iii) heavy bisectrix

$$m_c^*(hbx) \quad = \quad 2\left[\frac{m_1' \, m_2' \, m_3'}{3m_1' + (m_2' \cos^2\theta + m_3' \sin^2\theta)}\right]^{\frac{1}{2}}$$

Assuming that the tilt angle is known, a solution for $\overleftrightarrow{m}'$ should be possible, the tilt angle at 4.2 K has been reported to be $6^\circ 20' \pm 15'$ (Edelman and Khaikin 1966). However, a small variation in the assumed tilt angle would produce wide variations in the calculated effective masses. Moreover, the assumption that the tilt angle is independent of temperature is not necessarily valid, (indeed the galvanomagnetic data of Michenaud and Issi (1972) indicates that the tilt angle increases with temperature). Thus a solution which is independent of the tilt angle is desirable. Since the tilt angle is small,

$$m_2' \cos^2\theta \simeq m_3' \sin^2\theta \qquad (6.14)$$

and because

$$m_2' \gg m_1' \qquad (6.15)$$

the cyclotron equations may be simplified to

$$\begin{aligned} m_c^*(\ell bn) &= 2\left[\frac{m_1'\ m_3'}{3}\right]^{\frac{1}{2}} \\ m_c^*(\ell bx) &= \left[m_1'\ m_3'\right]^{\frac{1}{2}} \qquad (6\ 16) \\ m_c^*(hbx) &= 2\left[m_1'\ m_3'\right]^{\frac{1}{2}} \end{aligned}$$

Therefore, to a first approximation, the results of Vecchi and Dresselhaus give the temperature variation of $m_1'\ m_3'$. This is not an unreasonable conclusion since for the geometrical orientations used in their experiments the contribution for m_2' is small. Table 6.2 compares the cyclotron masses obtained at 4.2 K by Vecchi and Dresselhaus with those calculated on the basis of the simplified equations (6 16) using the experimental data of other workers, the correspondence is good

Reference	Band Edge Effective Masses			$\left[m_1' m_3'\right]^{\frac{1}{2}}$	$2\left[m_1' m_3'\right]^{\frac{1}{2}}$	$2\left[\frac{m_1' m_3}{3}\right]^{\frac{1}{2}}$
	m_1'	m_2'	m_3'			
1. Snoenberg (1939)	0.000511	2.53	0.00523	0.0016	0.0032	0.0018
2. Aubrey and Chambers (1959)	0.00217	1.01	0.00212	0.0016	0.0032	0.0018
3. Galt et al (1959)	0.00187	1.79	0.00455	0.0029	0.0060	0.0033
4. Boyle and Brailsford (1960)	0.00161	1.70	0.00236	0.0019	0.0038	0.0021
5. Weiner (1962)	0.00158	1.16	0.00302	0.0022	0.0044	0.0025
6. G.E. Smith et al (1963)	0.00132	1.31	0.00259	0.0018	0.0036	0.0021
7. Kao (1963)	0.00152	1.71	0.00244	0.0019	0.0038	0.0022
8. Jain and Koenig (1962)	0.00179	1.75	0.00208	0.0019	0.0038	0.0022
9. Smith, Baraff and Rowell (1964)	0.00114	1.21	0.00299	0.0018	0.0036	0.0021
11. Vecchi and Dresselhaus (1974)	-	-	-	0.0017	0.0032	0.0018

Table 6.2

The assumption is made that in the NENP model m_2' is parabolic and does not vary with temperature. Consequently the temperature variation of the light bisectrix electrons given by Vecchi and Dresselhaus

$$\beta^*(\ell bx) = 7.06 - (2.2 \times 10^{-2})T + (7.4 \times 10^{-6})T^2$$

will directly give the temperature dependence of the NENP density of states effective mass as

$$m_B = (m_1'(0)\ m_2'(0)\ m_3'(0))^{1/3}\ (\Delta\beta^*)^{2/3}$$

$$= m_D(0)\ (\Delta\beta^*)^{2/3}$$

where

$$\Delta\beta^* = 7.06/(7.06 - (2.2 \times 10^{-2})T + (7.4 \times 10^{-6})T^2)$$

and $m_i'(0)$ $i = 1,2,3$ refer to the band edge masses at 0 K

6.3 The Fermi level in pure and donor doped bismuth

In the previous section all the electronic parameters necessary for the calculation of the Fermi level in bismuth as a function of temperature were introduced The Fermi level is computed from the Fermi-Dirac equation which defines the total electron concentration (see equation 5 27)

$$N = 2\left(\frac{2\pi\, m_B kT}{h^2}\right)^{3/2} \left[F_{1/2}(\eta) + \frac{2kT}{E_g} F_{3/2}(\eta)\right]$$

where

$$F_k(\eta) = \int_0^\infty \frac{x^k\, dx}{\exp(x - \eta) + 1}$$

and

$$E_F = \eta kT$$

$$E = xkT$$

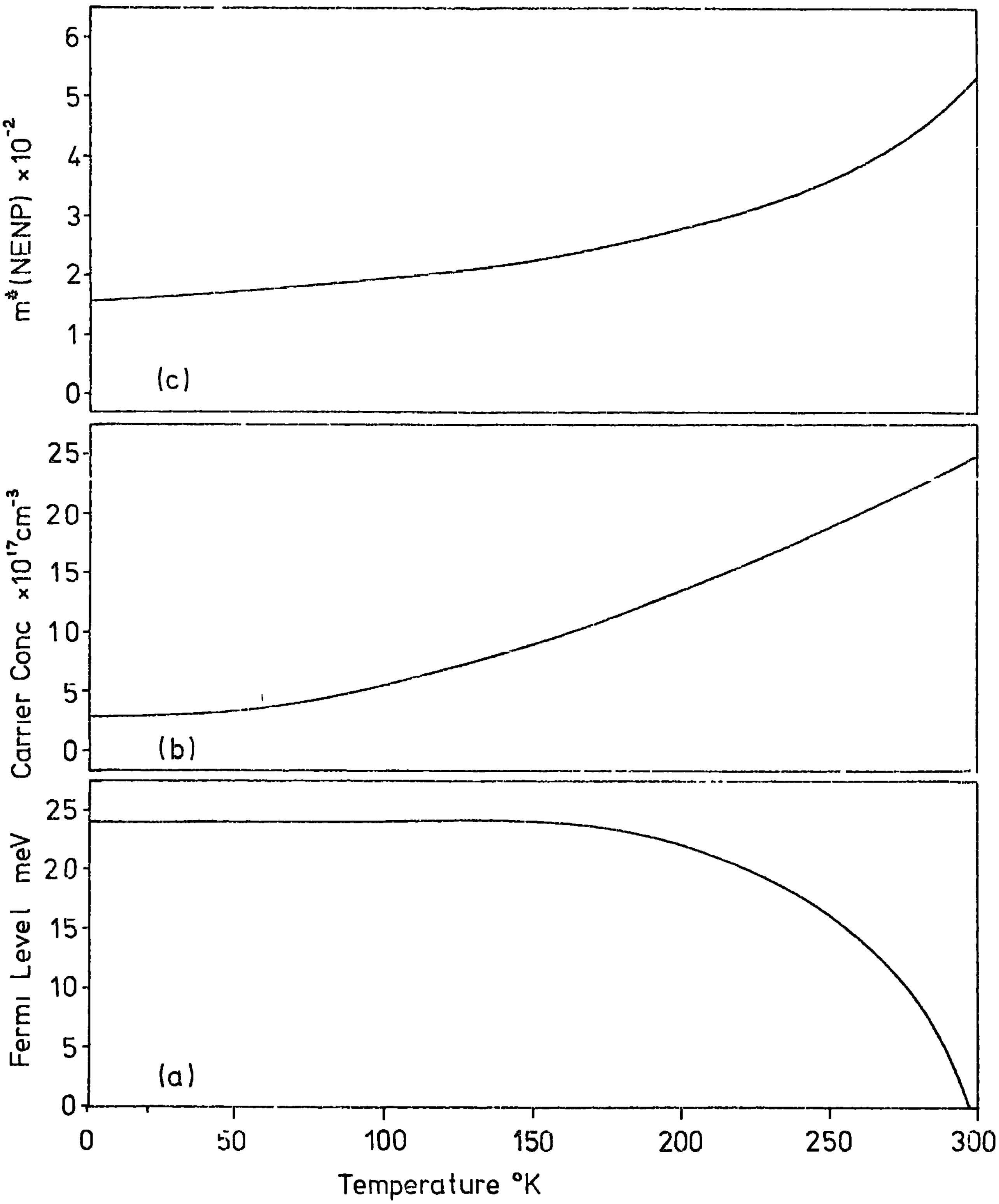

Fig 6 1 Temperature variation of the electron parameters of pure bismuth (a) Fermi level (b) carrier concentration (c) NENP band edge effective mass

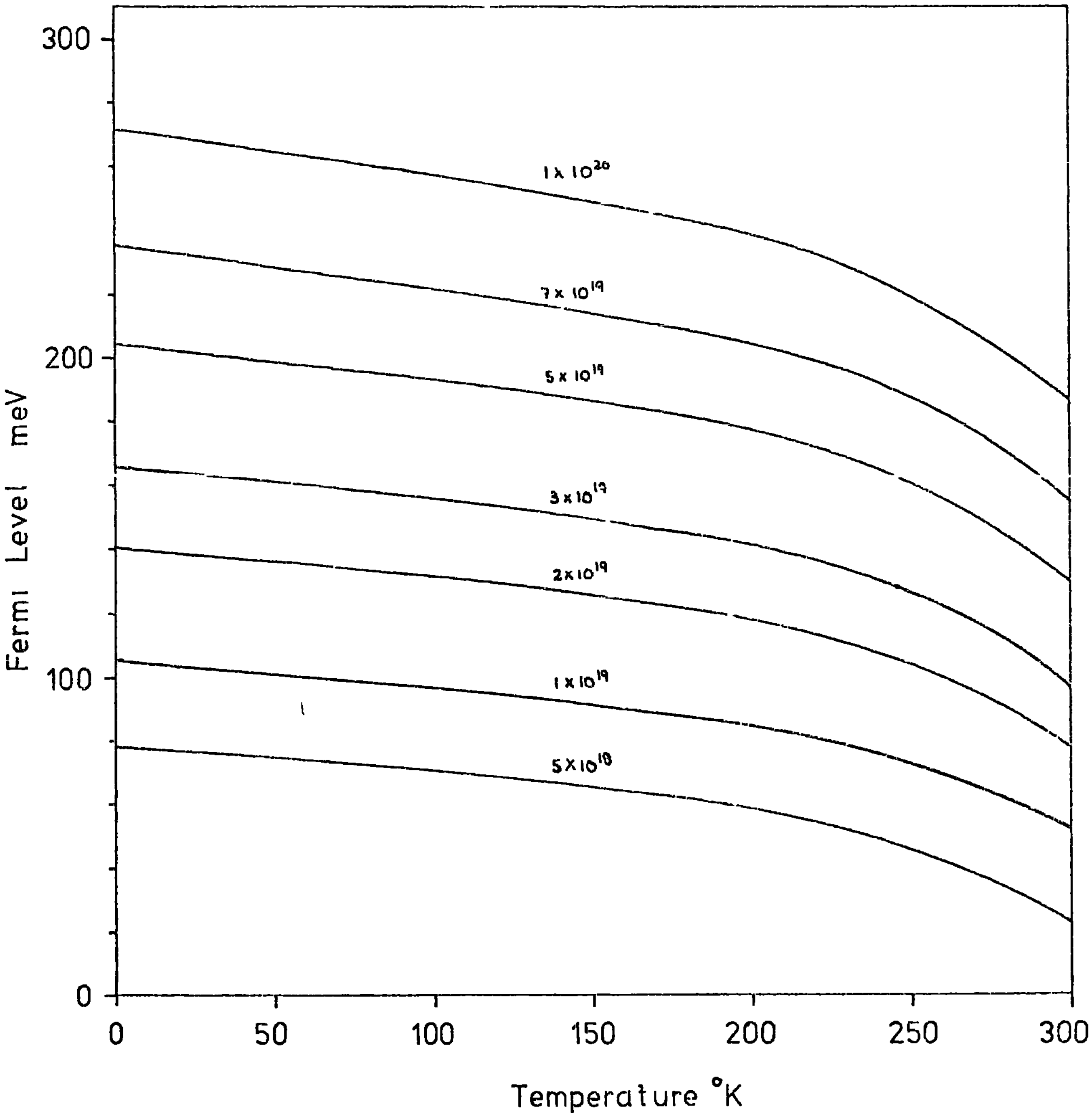

Fig 6 2a The electron Fermi level as a function of temperature for electron concentrations in the range $5\times10^{18}\,\mathrm{cm}^{-3}$ - $1\times10^{20}\,\mathrm{cm}^{-3}$

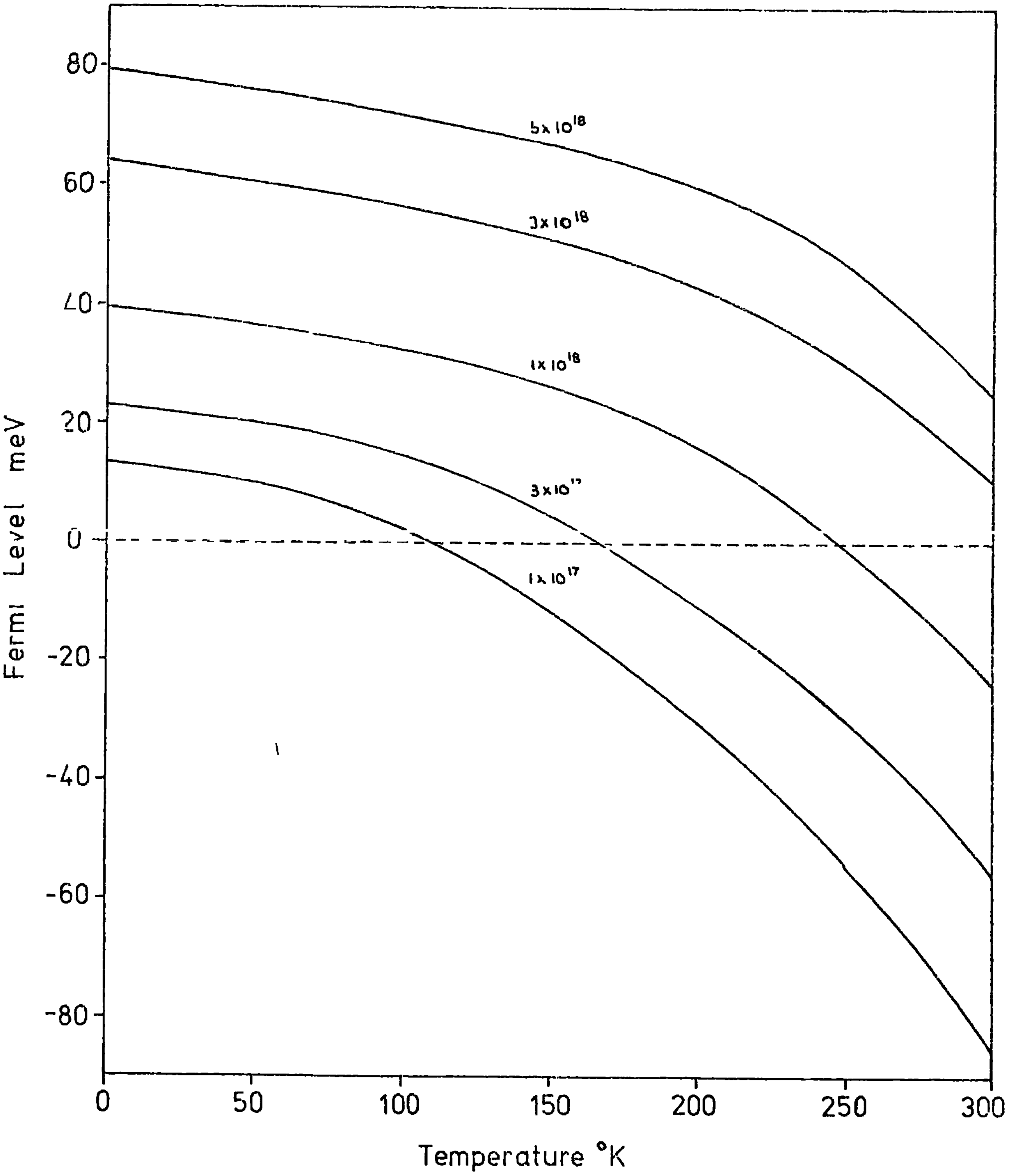

Fig 6 2 b The electron Fermi level of bismuth as a function of temperature for electron concentrations in the range $1\times10^{17}\,cm^{-3}$ - $5\times10^{18}\,cm^{-3}$

The method of computation of the Fermi Dirac integrals $F_k(\eta)$ is described in the appendix.

The Fermi level of pure bismuth calculated as a function of temperature is shown in Figure 6.1c, it remains more or less constant over the temperature range 0-200 K and then decreases slightly as the temperature approaches 300 K. The increasing electron population is thus counteracted by the increase of the effective mass. This is in contradiction to the work of Lerner and Martin (1972) who, having assumed that the effective masses and the L point energy gap remain constant, concluded that the Fermi level should increase monotonically with temperature.

When bismuth is doped with a donor the electron concentration is increased while the band edge parameters remain constant When more than 10^{19} cm^{-3} donors are present the electron concentration can be considered to be independent of temperature. Figure 6.2 shows the variation of the Fermi level for various electron concentrations, the Fermi level decreases with temperature for all concentrations.

6.4 Band parameters of bismuth-antimony alloys

(a) Carrier Concentration

The carrier concentrations of 4.2 K of pure bismuth-antimony alloys in the composition range 0-15 at.% antimony have been reported by numerous authors. As antimony is added to bismuth the decrease in the overlap between the L point and the T point ellipsoids will cause a gradual decrease in the carrier population. In the semimetallic region (0-8 at.% antimony) there will always be a finite carrier population at 0 K resulting from the band overlap However, when the alloy becomes semiconducting, the carrier concentration at low temperatures will be predominantly governed by the presence of any donor or acceptor impurities Table 6 3 collects some of the reported carrier concentrations for the bismuth-antimony alloys considered here. The large scatter of the reported values reflects the problems associated with impurities. To a good approximation, the carrier concentration at 4.2 K decreases monotonically from 3.3×10^{17} cm^{-3} for pure bismuth to approximately 1×10^{14} cm^{-3} for 10 at.% antimony.

At higher temperatures thermal excitation will increase the population of carriers, in view of the small band gap energies involved at 300 K the carrier concentration is of the same order of magnitude as that of pure bismuth, Ivanov and Popov (1964) have measured the number of carriers in 10 at.% alloy to be 1.29×10^{18} cm^{-3} at 300 K compared to 2.48×10^{18} cm^{-3} in pure bismuth. Jain (1959), who worked on crystals of doubtful homogeneity, also observed that the carrier populations of all the alloys at room temperature were of similar magnitude.

(b) Band edge parameters of bismuth-antimony

Measurements of cyclotron resonance for the bismuth-antimony alloys carried out within the semimetallic range (Kao et al, 1964, G E Smith, 1962, Herman et al (1974)) show that in general the Fermi level effective mass values decrease with the addition of antimony. Magnetoreflection results have indicated that the energy gap at the L point first decreases, goes to zero at an antimony concentration of about 4 at % and then increases again with increasing antimony concentration. Recently, Chao, Chu and Kao (1974) have reported a Shubnikov-de Haas study of 0-3 at.%

Reference	at.% Antimony	Electron concentration at 4.2 K cm^{-3}
(a)	0.0	3.3×10^{17}
(f)	0.68	2.7×10^{17}
(c)	0.95	1.7×10^{17}
(b)	2.00	1.1×10^{17}
(f)	2.90	1.1×10^{17}
(g)	5.0	1.39×10^{17}
(c)	6.0	7.77×10^{14}
(d)	7.8	2.0×10^{14}
(d)	9.0	9×10^{14}
(c)	9.0	4.4×10^{13}
(c)	11.2	1.5×10^{15}
(c)	15.0	9×10^{13}
(e)	15.0	4.7×10^{15}

References

(a) Saunders and Sümengen (1972)

(b) Jacobson (1973)

(c) Brandt, Dittman and Ponomerev (1972)

(d) Lerner, Cuff and Williams (1968)

(e) Brown and Silverman (1964)

(f) Chao, Chu and Kao (1974)

(g) Thomas and Goldsmid (1970)

Table 6.3 Electron concentration of the bismuth-antimony alloys at 4.2 K.

antimony alloys in which they propose a non-linear variation of the band parameters in the vicinity of the L point gapless region, this is to be expected since, if the NENP model still holds in the gapless region the effective masses must become very small or the Fermi level must increase.

Measurements carried out in the semiconducting region at liquid helium temperatures suffer from the effects of impurities (evidenced by the large scatter in the reported carrier concentrations). Consequently one must question the validity of any interpretation which depends upon results taken from different groups, for example, Oelgart and Herrmann (1973) calculate the band edge effective masses of n-type semiconducting bismuth antimony alloys by taking the Fermi energy from Lerner, Cuff and Williams (1968).

The extension of the results to room temperature suffer from the absence of experimental data Although the approximate variation of the carrier density as a function of temperature is known (Jain, 1959), there is no precise information regarding the effective masses or the L point energy gap. Lerner and Martin (1972) attempted some band edge calculations on bismuth-antimony alloys using parameters derived from various cyclotron and galvanomagnetic measurements and suggested an approximate temperature dependence for the gap at the L point, however, they ignored any temperature variation of the effective masses.

In view of the fact that the variation of all the important parameters in these alloys still remains somewhat unclear, it was decided that to calculate an approximate magnitude of the electronic contribution to the elastic constant at room temperature, the following assumptions would have to be made (i) the carrier concentration at room temperature decreases monotonically from 2.48 x 10^{18} cm^{-3} for pure bismuth to 1 x 10^{18} cm^{-3} for a 10 at.% antimony alloy, (ii) the L point energy gap remains constant with composition, (iii) the band edge mass is the same as that of pure bismuth.

6.5 The Deformation Potentials

The deformation potentials of pure bismuth measured at liquid helium temperatures by Walther (1968) and by Inoue and Tsuji (1967) and calculated by Katsuki (1969) are given in Table 6.4. Since, at present, the deformation potentials can only be obtained through magnetoacoustic experiments, no information regarding the temperature dependence is available and consequently temperature independent deformation potentials must be assumed. Likewise, in the absence of data for the bismuth-antimony alloys, the potentials must also be considered to be constant with composition.

6.6 Computation of the Electronic Contributions to the Elastic Constants

(a) Basis

The electronic contributions to the elastic constants were shown in chapter five to be,

	Walther (1968)	Katsuki (1969)	Isque and Tsuji (1967)
L_{11}	-2.2	-1.7	-2.1
L_{22}	5.9	5.0	5.3
L_{23}	1.5	1.1	-
L_{33}	-1.7	-3.8	-1.7
T_{11}	1.2	1.1	1.1
T_{33}	-1.2	-2.5	-1.2

Table 6.4 The Deformation Potentials (eV) of Bismuth.

$$\Delta C_{11} = -9/2\ (L_{11} - L_{22})^2\ \nu$$

$$\Delta C_{12} = 9/2\ (L_{11} - L_{22})^2\ \nu$$

$$\Delta C_{14} = -12\ (L_{11} - L_{22})\ L_{23}\ \nu$$

$$\Delta C_{44} = -36\ L_{23}^2\ \nu$$

where

$$\nu = \frac{\pi^{-\frac{1}{2}}}{12} \cdot 2 \left(\frac{2\ m^*(\mathrm{NENP})kT}{h^2} \right)^{3/2} \left[F_{-\frac{1}{2}}(\eta) + \frac{6kT}{E_g} F_{\frac{1}{2}}(\eta) \right]$$

Utilising the band edge parameters discussed in the previous sections, the electronic contributions were computed both as a function of temperature and carrier concentration. The computer programme is reproduced in the appendix.

(b) Bismuth

Figure 6.3 presents the theoretical electronic contributions to the elastic constants C_{11}, C_{12}, C_{14} and C_{44} of bismuth (at 4.2 K) calculated as a function of carrier concentration The magnitude of the electronic component increases with the free electron density but for the pure material it is relatively small in comparison to the absolute values of the elastic constants, for example, a carrier population of 3 x 10^{19} cm^{-3} is required to produce a measurable change of 1% in C_{11} (C_{11} = 69 3 x 10^{10} dyne cm^{-2} at 4.2 K). Thus, to obtain a satisfactory experimental verification of the effect, ultrasonic measurements on highly donor doped crystals must be performed Figure 6 4 gives the temperature variation of the electronic contribution for various electron concentrations, the electronic contribution increases slightly with temperature, as a consequence

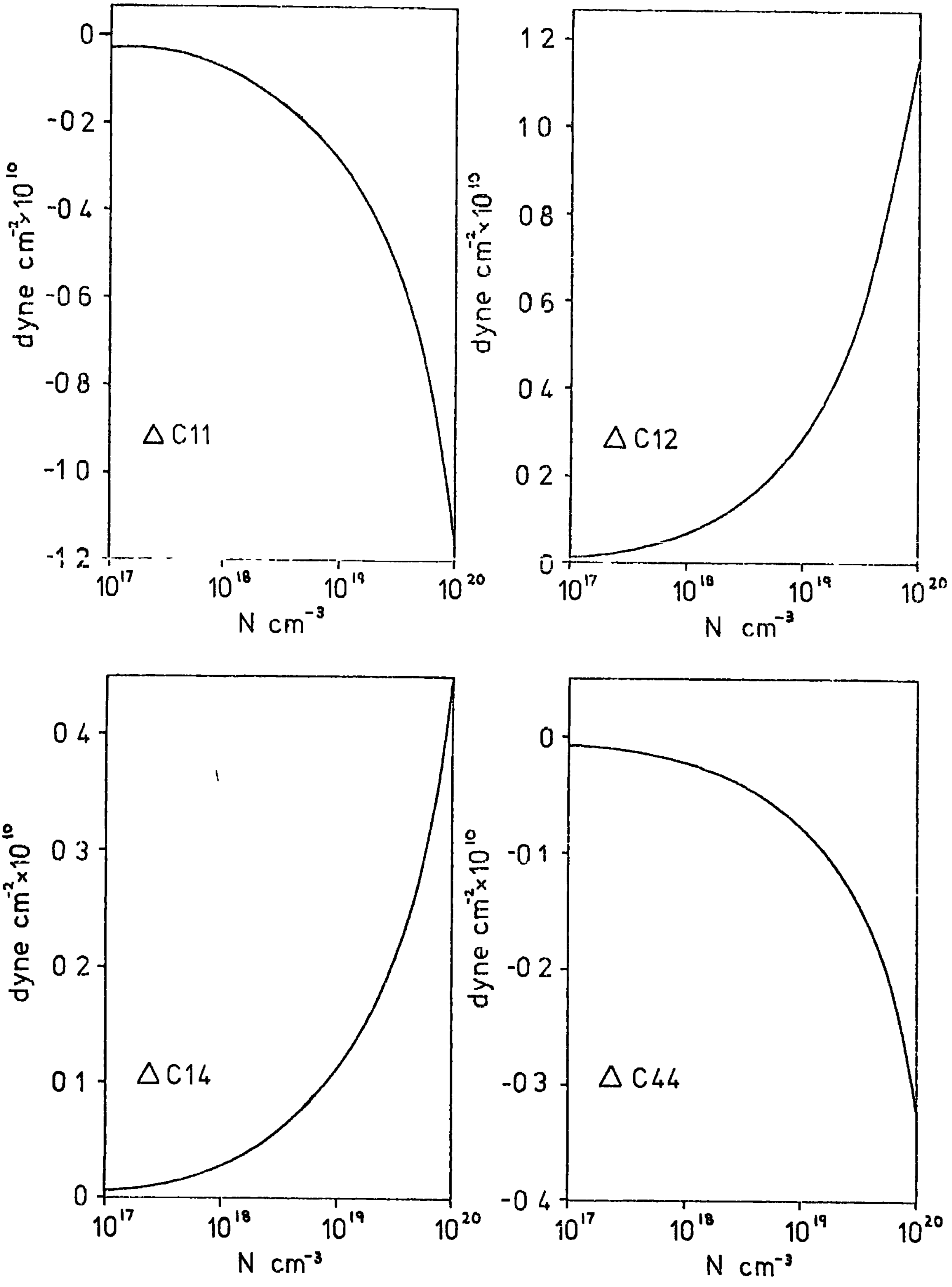

Fig 6 3 Electronic contributions to the elastic constants of bismuth at 4 2 K as a function of electron concentration (theoretical calculation)

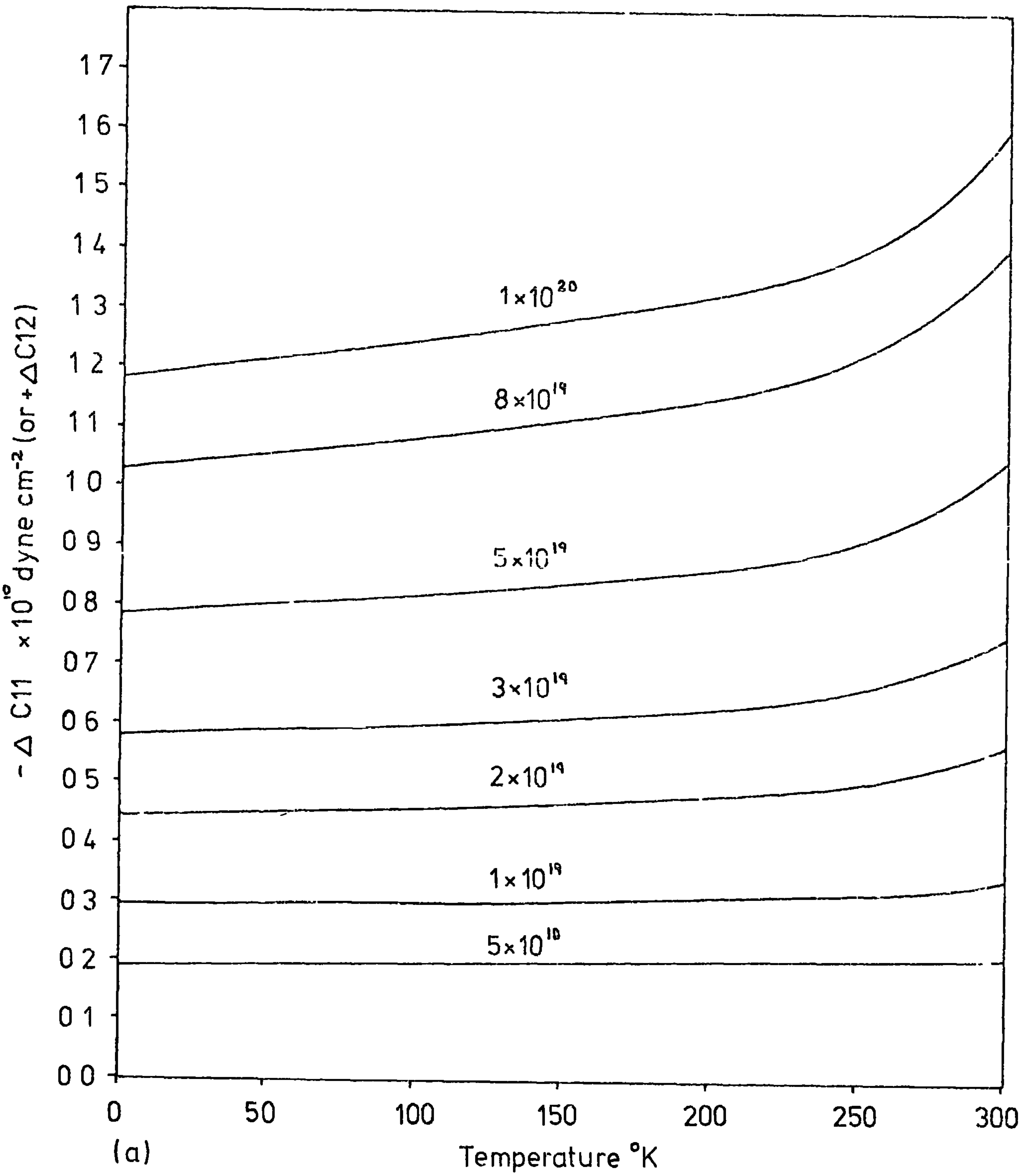

Figure 6 4 The theoretical temperature variation of (a) $-\Delta C11$ and $+\Delta C12$ (b) $+\Delta C14$ and $-\Delta C44$ for various electron concentrations (cm^{-3})

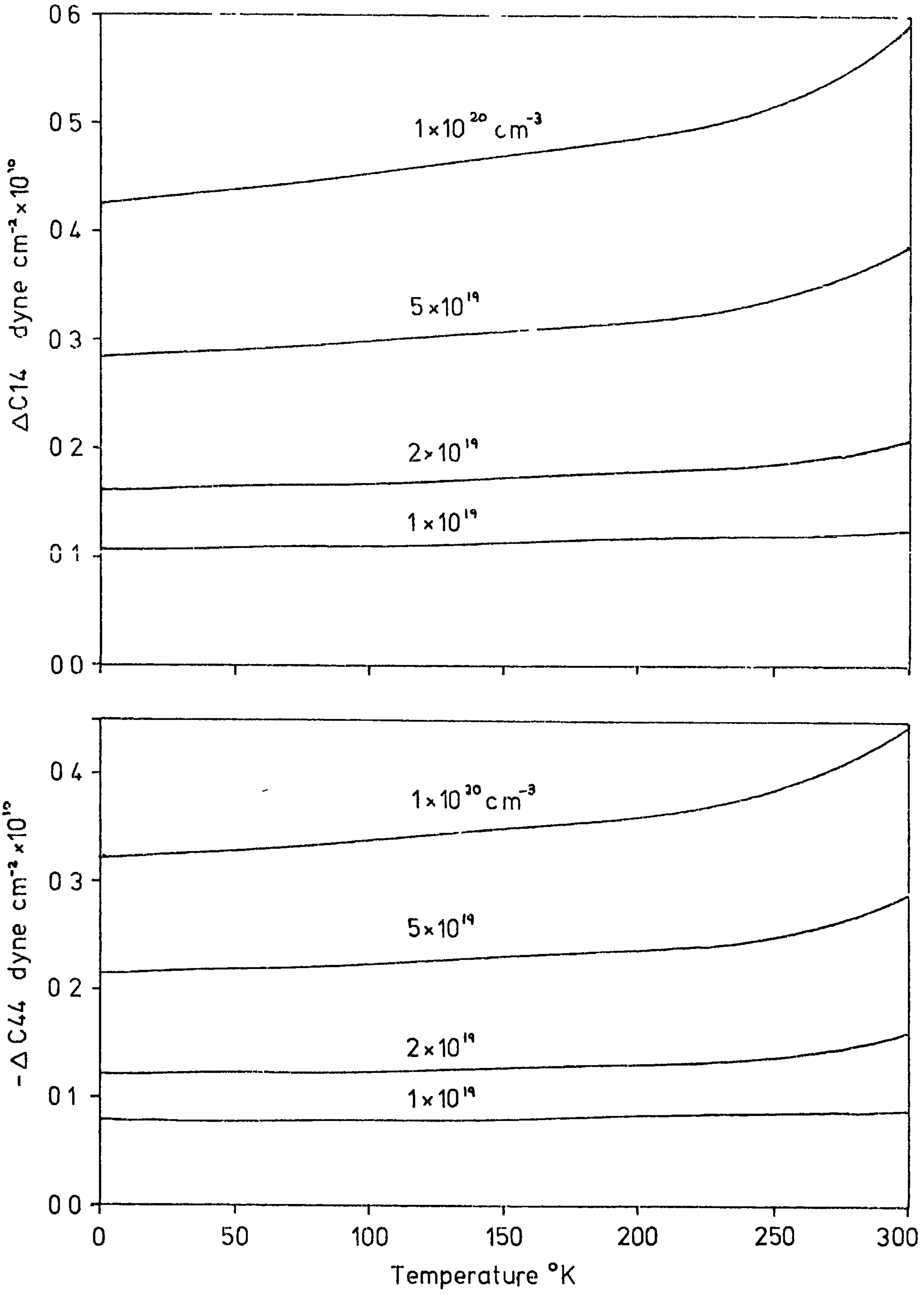

Figure 6 4 (b) + ΔC14 and - ΔC44

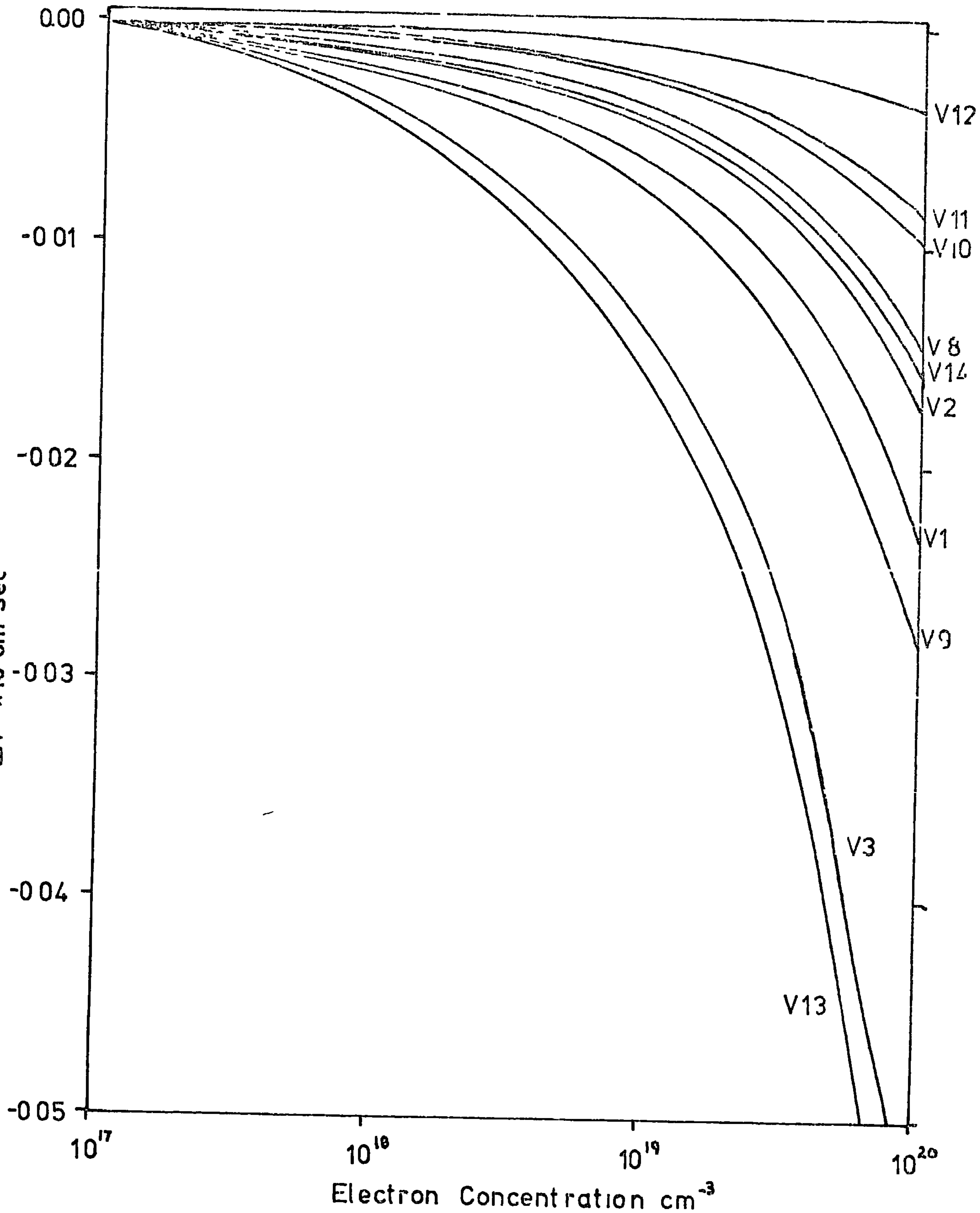

Figure 6.5 The theoretical electronic contribution to the room temperature ultrasonic velocities

of the large temperature variation of the band edge effective masses. The Keyes model predicts that the electron redistribution reduces the free energy and hence the effective elastic constants should be decreased for all directions of propagation (other than for the trigonal pure mode). The change in the velocities for the propagation directions discussed in chapter three have been computed for various electron concentrations. Figure 6.5 verifies that all the ultrasonic velocities are decreased as the electron population increases.

(c) Bismuth-antimony

The room temperature electronic contributions to the elastic constants of intrinsic bismuth-antimony alloys in the composition range 0-10 at.% antimony are presented in Table 6.5, the assumptions made are those discussed in Section 6.4a. The computation clearly shows that the electronic effect is so small as to be virtually insignificant. Moreover, because it has been assumed that the band edge parameters remain constant with composition, the theoretically calculated electronic contribution should be larger than is actually the case, the experimental evidence shows that the band edge parameters decrease with the addition of antimony.

6.7 Summary

In this chapter the band parameters necessary for the calculation of the electronic contributions have been detailed. The computations have shown that for the intrinsic materials the electronic contributions should be negligible However, the effect should be observable in highly donor doped crystals of bismuth.

At % Antimony	ΔC_{11}	ΔC_{12}	ΔC_{14}	ΔC_{44}
	$\times 10^{10}$ dyne cm^{-2}			
0	-0.113	+0.113	+0.042	-0.031
3	-0.098	+0.098	+0.036	-0.027
5	-0.085	+0.085	+0.031	-0.023
7	-0.077	+0.077	+0.028	-0.021
10	-0.045	+0.045	+0.018	-0.014

Table 6.5 The room temperature electronic contributions to the elastic constants of the bismuth-antimony alloys.
(For comparison the elastic constants of pure bismuth are ,

$C_{11} = 63.4$, $C_{12} = 24.5$, $C_{13} = 24.9$

$C_{14} = 7.28$, $C_{44} = 11.5$,

$C_{33} = 37.9 \times 10^{10}$ dyne cm^{-2})

Chapter seven gives the results of ultrasonic measurements on the bismuth-antimony alloys and chapter eight reports the results for donor doped bismuth. A more precise discussion of the experimentally observable electronic effect is reserved for these latter chapters.

CHAPTER 7

THE ELASTIC CONSTANTS OF THE BISMUTH-ANTIMONY ALLOYS

7.1 Introduction

The results of ultrasonic velocity measurements on single crystal bismuth-antimony alloys in the range of composition 0-10 at % are presented both as a function of composition and of temperature. From these measurements the elastic stiffness and elastic compliance constants have been derived. The polycrystalline moduli are deduced from the single crystal constants and contrasted with the existing data on aggregate material.

7.2 a Room Temperature Ultrasonic Velocities

The as-grown crystals were orientated to an accuracy of $\frac{1}{2}^{\circ}$ by the conventional Laue back reflection technique and specimens having rectangular shapes were then machined by the spark erosion process, the final surfaces being flat and parallel to 1 part in 10,000. The sample dimensions were 3-5 mm in thickness, with a cross-sectional area of at least 1 cm^2. For a complete determination of all the elastic constants three directions of propagation were required (i) the (001) axis gave C_{33} and C_{44}, (ii) the (100) axis C_{11}, C_{12} and the magnitude of C_{14}, (iii) the $(0, -\frac{1}{\sqrt{2}}, \frac{1}{\sqrt{2}})$ direction C_{13} and the sign of C_{14}. The relationship between the various modes and the elastic constants is outlined in Table 3.1, the notation used is consistent with the nomenclature of Eckstein, Reneker and Lawson (1960).

Quartz piezoelectric transducers were bonded to the specimens with Nonaq stopcock grease and the ultrasonic transit times were measured at room temperature (290 K) using the pulse echo overlap technique. Corrections for the transducer transit time (see Section 4.3d) were evaluated by measuring the ultrasonic velocity as a function of transducer thickness and extrapolating the values so obtained to zero transducer thickness The (001) and (100) longitudinal modes were readily excited and distinguishable as were the two shear modes in the (100) direction. The degenerate shear mode along the trigonal axis proved to be the most difficult to propagate and considerable patience had to be exercised before a clean and exponential echo train was obtained; cooling of the sample produced extremely sharp and well defined echoes. Propagation of ultrasonic waves in the YZ direction presented no difficulties, although, due to their similar velocities, care had to be taken to differentiate between the pure and the quasi-pure shear modes. In general, for all modes, the Nonaq bond appeared to stiffen when cooled from room temperature to 0°C, producing an apparent, but small decrease in the attenuation, however, no anomalies were observed in the ultrasonic velocities

Figure 7.1 gives the ultrasonic velocities as a function of composition for the eight modes studied here. There is an increase in all the experimentally measured velocities as antimony is added to bismuth.

The principal errors in the velocity measurements are. (i) the uncertainty in the measurement of the apparent transit time, i.e instrumentation error, (ii) the determination of the correction for the effective transit time in the transducer, (iii) misorientation of the sample, (iv) uncertainty in the length measurement, (v) diffraction Since the pulse echo overlap technique can measure

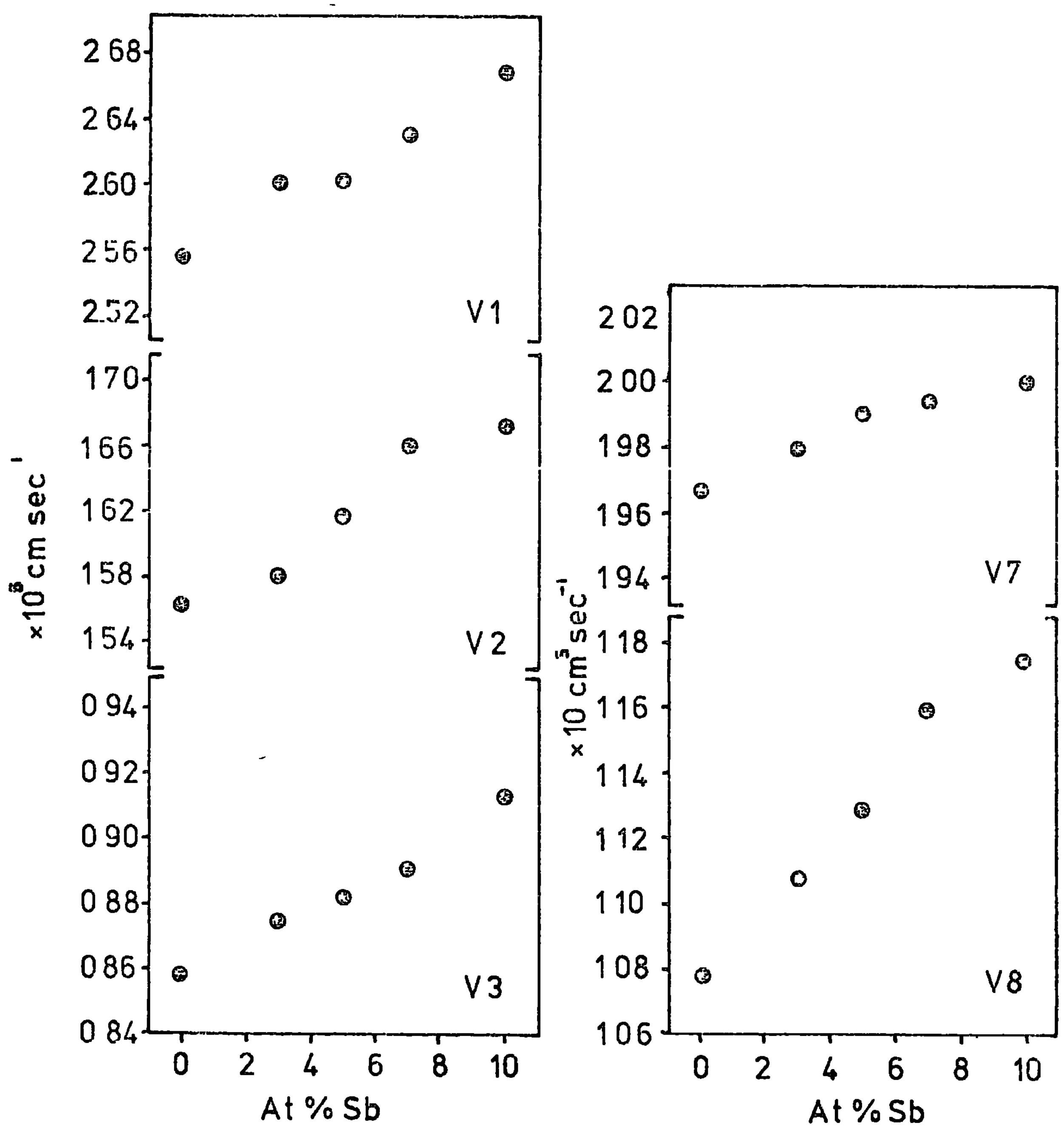

[a] (100) Velocities

[b] (001) Velocities

Figure 7.1 The ultrasonic velocities as a function of antimony concentration (290°K)

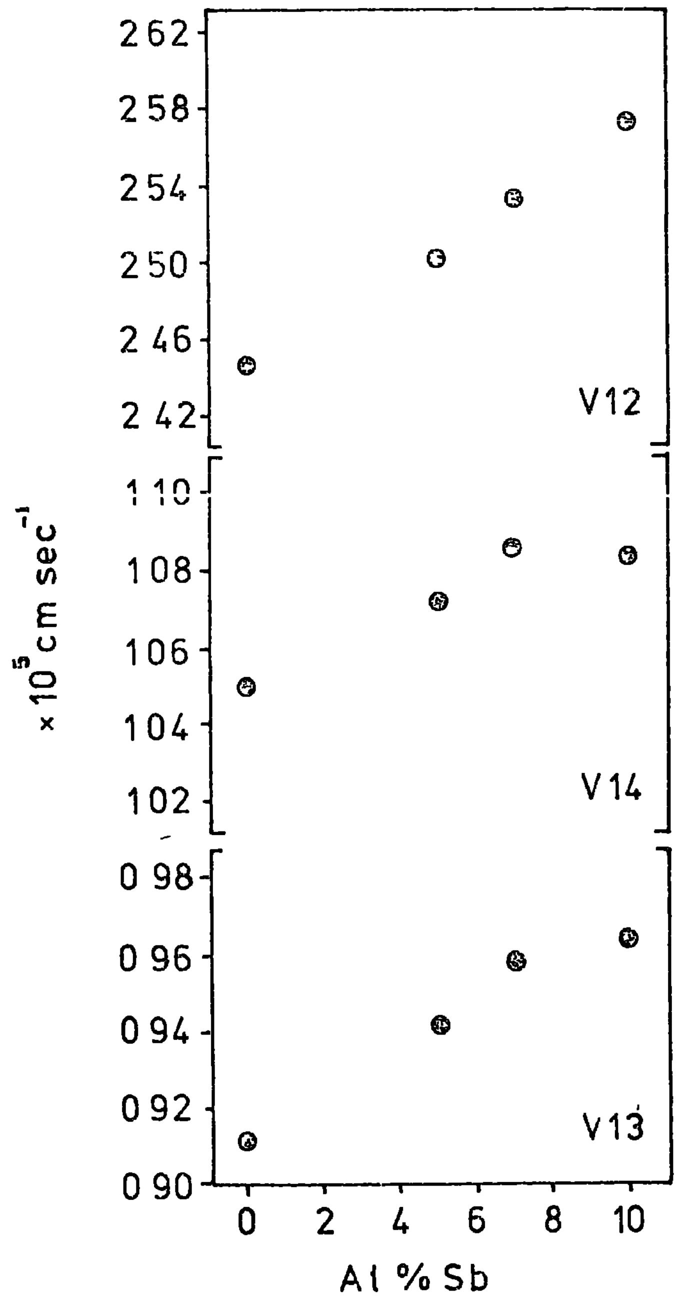

Figure 7 1 [c] (0,-1/√2,1/√2) Velocities the apparent transit time to an accuracy of 1 part in 10^4, this error can be neglected. The uncertainty in the determination of the effective transit time within the transducer is estimated to be at most 0.015 µs, thus, this error is dependent on both the velocity of propagation and on the thickness of the sample. De Bretteville et al (1966) have shown, following the method of Waterman (1959), how to calculate the velocity errors due to misorientation for the particular modes in rhombohedral crystals, for a misorientation of 1° the errors for V_1, V_2, V_3 and V_7 will be less than 0.01% and for V_7, V_{12}, V_{13} and V_{14} less than 0.1%. The specimen dimensions were measured, using a dial gauge, to an accuracy of 0.03%. Papadakis (1966) has shown that, for the frequencies used here, the effect of diffraction is less than 0.05%. Thus the total uncertainty limits are approximately 0 4% for longitudinal velocities and 0.2% for the shear wave velocities

7.2b The Elastic Constants at Room Temperature

Only the elastic constants C_{11}, C_{33} and C_{44} can be obtained from single velocity measurements in pure mode directions, the constants C_{12}, C_{13} and C_{14} must be deduced from a combination of velocity measurements The method of least-mean-squares has been employed to compute the entire set of elastic constants for each composition (see Pace and Saunders 1970). Initially each of the effective elastic constants is calculated from an approximated set of C_{ij}'s, divided by the corresponding experimental value and compared to unity to compute the parameter SUMSQ

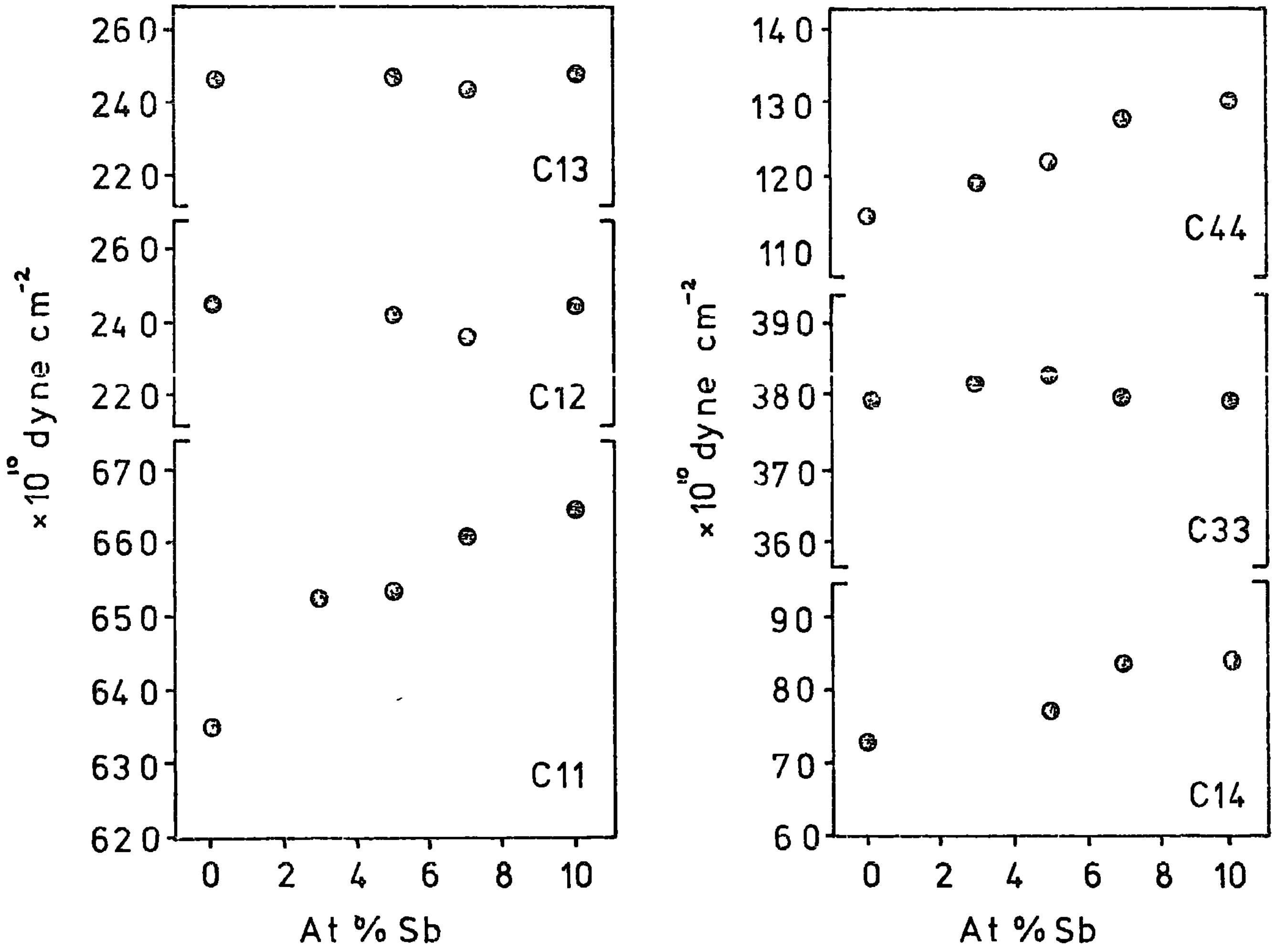

Figure 7.2 The elastic constants as a function of antimony concentration (at 290°K)

$$\mathrm{SUMSQ} = \sum_{\substack{i=1,2,3,7,8\\12,13,14}} \left[\frac{\text{CALULATED } \rho v_i^{2}}{\text{MEASURED } \rho v_i^{2}} - 1.0 \right]^2$$

SUMSQ is then minimised by a cyclic adjustment of the elastic constants. The computer program and its mode of operation are given in Appendix 3. The densities of the samples were obtained by the displacement method of Archimedes. The computed elastic constants as a function of composition are given in Figure 7.2. The errors in the elastic constants were estimated by using the least-mean-squares programme and adjusting the measured velocities to their experimental limits of accuracy. The elastic constants C_{11}, C_{14} and C_{44} are observed to increase monotonically with composition, while C_{12}, C_{13} and C_{33} remain approximately constant. The constants show an approximate agreement with Vegard's Law if they are extrapolated to pure antimony (Epstein and De Bretteville (1964) have measured the elastic constants of pure antimony at 300 K to be $C_{11} = 99.4$, $C_{12} = 30.9$, $C_{13} = 26.4$, $C_{14} = 21.6$, $C_{33} = 44.5$, $C_{44} = 39.5 \times 10^{10}$ dyne cm^{-2}), an extrapolation over such a small composition range must however be treated with extreme caution. The elastic constants of pure bismuth at room temperature obtained here compare favourably to the results of Eckstein, Reneker and Lawson (1960) and Kammer, Cardinal, Vold and Gliskman (1972). Table 7.1 compares these three sets of data. As in the present work, both Eckstein et al and Kammer et al made corrections for the effective transit time in the transducer, Eckstein et al used the empirical procedure of determining the transit time with and without a dummy transducer on the opposite face of the sample,

Elastic Constant	T K	This Work	Eckstein, Lawson and Reneker (1960)	Kammer et al (1972)
c_{11}	4.2	69.25	68.7	-
	80	68.18	68.6	-
	290	63.39 ± 0.4	63.7	63.5
c_{12}	4.2	24.48	23.7	-
	80	24.49	23.8	-
	290	24.52 ± 0.3	24.9	24.7
c_{13}	4.2	25.37	-	-
	80	25.41	-	-
	290	24.90 ± 0.4	24.7	24.5
c_{14}	4.2	8.40	8.44	
	80	8.12	8.05	
	290	7.28 ± 0.1	7.17	7.23
c_{33}	4.2	40.41	40.6	
	80	39.93	40.6	
	290	37.90 ± 0.3	38.2	38.1
c_{44}	4.2	13.55	12.9	
	80	13.09	12.7	
	290	11.51 ± 0.15	11.23	11.3
c_{66}	4.2	22.39	22.5	
	80	21.85	22.4	
	290	19.44 ± 0.4	19.41	19.4

Table 7.1. The elastic constants of pure bismuth at 4.2 K, 78 K and 290 K, comparison with the work of Eckstein, Lawson and Reneker (1960) and Kammer, Cardinal, Vold and Glicksman (1972).

while Kammer et al measured the transit time as a function of transducer thickness. Thus, in all three studies, the principal error has been reduced to a minimum. Both these groups measured the ultrasonic velocities of fourteen modes of propagation and therefore, although their electronic techniques were not as sophisticated as used in the present work, they were able to reduce their errors by having a large number of redundant terms.

7.3 Temperature Dependences

The temperature variation of most of the modes was measured with the pulse echo overlap technique in the range 4 2-290 K The results are presented in Figures 7.3 to 7.10 An interesting finding is that the temperature dependence of the ultrasonic velocities is essentially unaltered by alloying; Figures 7.11-7.13 present the velocity data as V(T)/V(290) and demonstrate that the temperature variation is independent of composition. The degree of scatter of the experimental points reflects the accuracy of the technique. The pulse echo overlap method is sensitive to a velocity variation of 1 part in 10^4, the transit time was continuously monitored and measurements recorded in at least five degree intervals. Some error might be introduced if the transit time correction for the perturbation of the transducer were to change with temperature. To check this, the corrections were evaluated both at room temperature and at liquid nitrogen and found to be essentially identical, thus it was concluded that the transit time correction was temperature independent Furthermore, the fact that the temperature dependences of the ultrasonic velocities of all the bismuth-antimory alloys are identical attests to this assumption. The sample thicknesses, although similar, were not identical and thus the percentage transit time corrections were different for each specimen Any change in the correction factor would thus have reflected itself in the temperature dependence. Based upon this simple evidence, the temperature dependences measured here are believed to be of high precision.

The least-mean-squares programme was used to obtain values of the elastic constants at a series of temperatures down to 4 2 K. The ultrasonic path length and the density were corrected for change with temperature by use of the two coefficients of thermal expansion of pure bismuth given by White (1972). Values of the elastic constants at temperatures between 4.2 K and 290 K are given in Table 7.2 and shown graphically in Figures 7.14-7.16. Apart from C_{12}, the constants vary linearly with temperature approaching a maximum at 0 K with zero slope - the usual behaviour found to crystalline materials. Within the limits of experimental accuracy, the constant C_{12} is observed to be independent of temperature Eckstein et al measured all the elastic constants apart from C_{13} at 4.2 K to 78 K, making corrections for thermal expansion from the data of Erfling (1939), in general, the present findings substantiate their measurements. However, the temperature dependences obtained here are accurate to 1 in 10^5 for C_{11}, C_{33} and C_{44} and 1% for the indirectly measured constants C_{12}, C_{13} and C_{14} Kammer et al (1972) determined the adiabatic stiffness constants at a number of discrete temperatures ranging from room temperature to the melting point, and made corrections to the sonic path length and density by using the thermal expansion data of Cave and Holroyd (1960) Thus, the present results complete the data for pure bismuth over the entire range of temperature extending from 4 2 K to the melting point

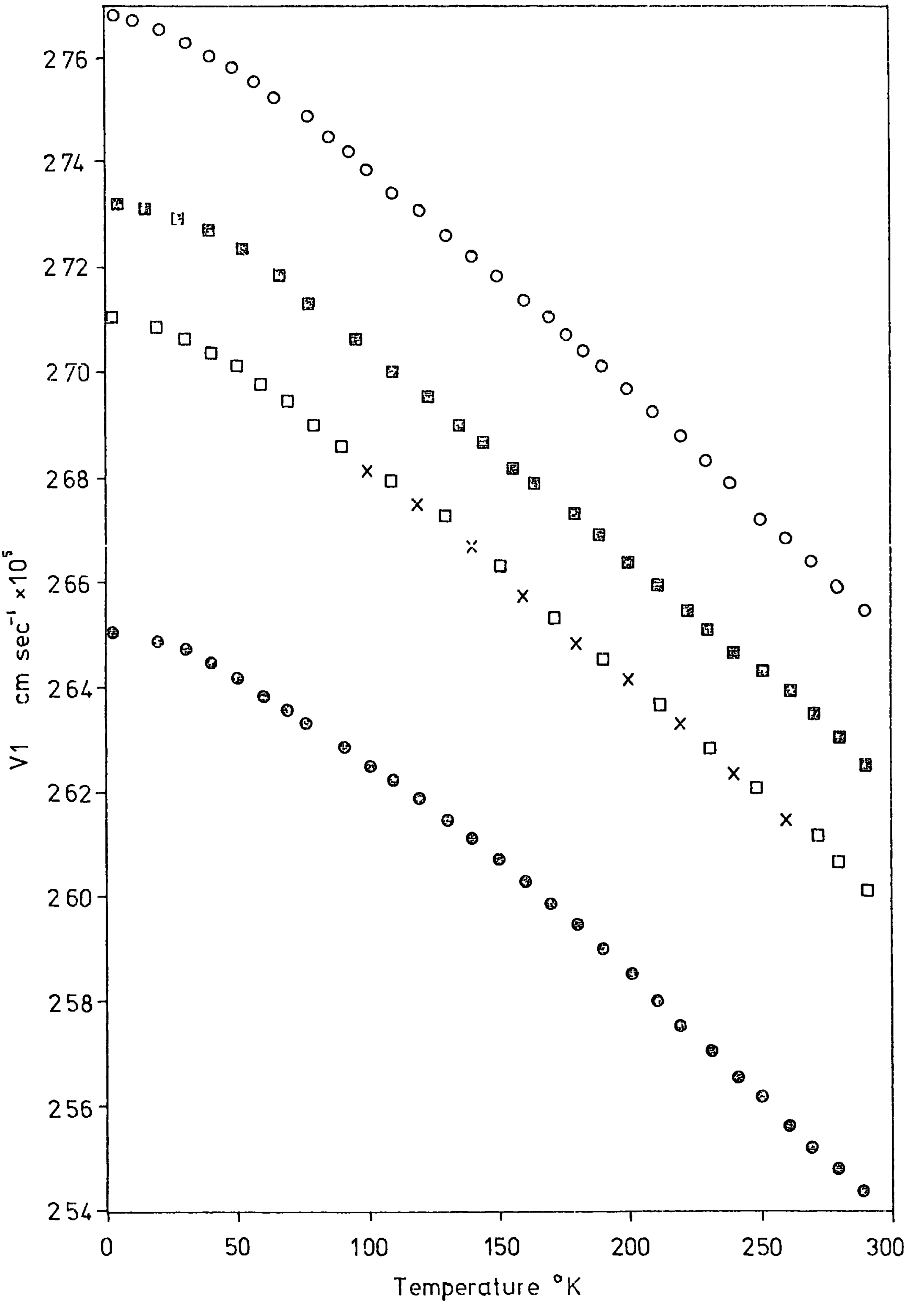

Figure 73 The temperature variation of V1

● pure bismuth, × 3at%, □ 5at% ▨ 7at%, ○ 10at% antimony

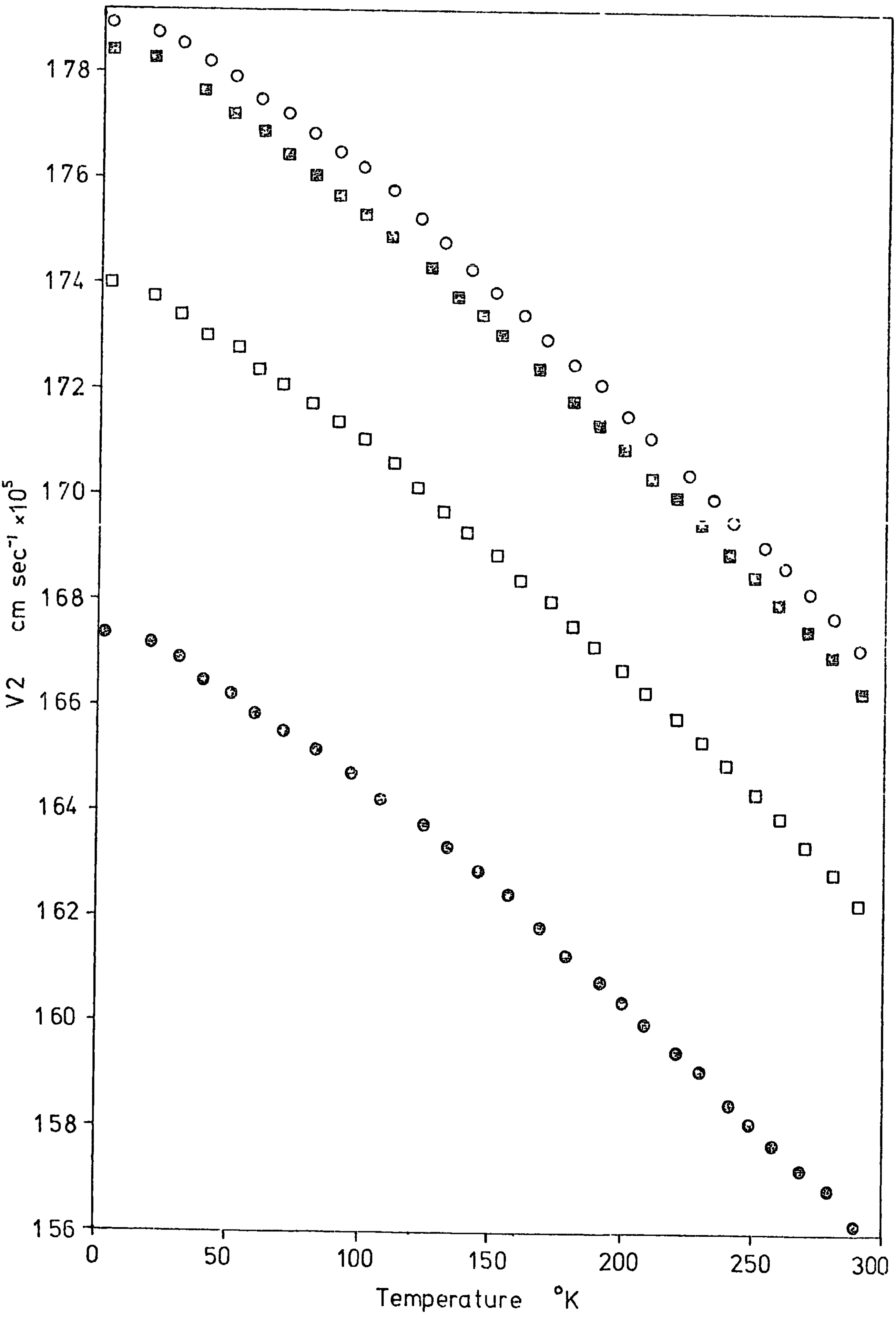

Figure 7 4 The temperature variation of V2

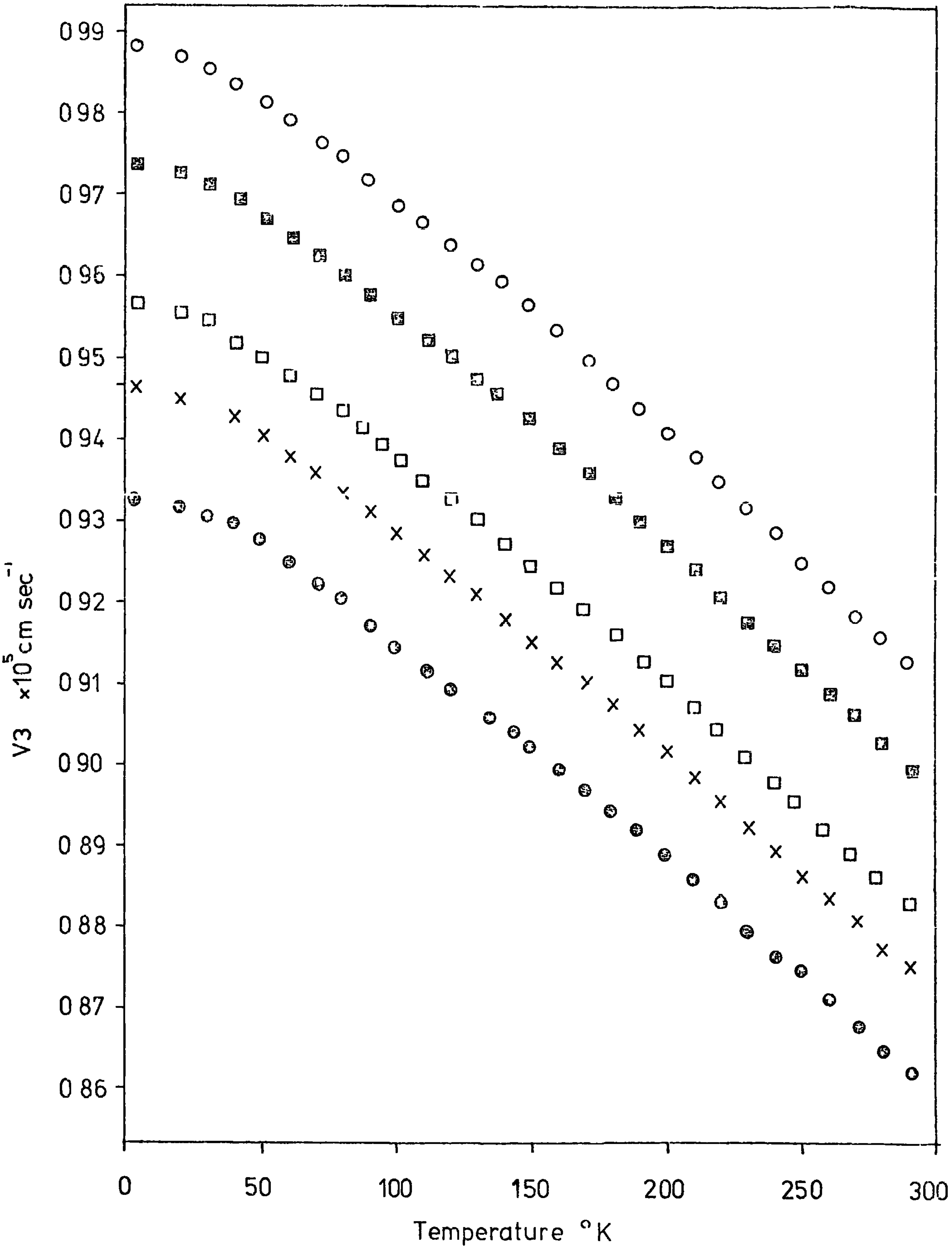

Figure 75 The temperature variation of V3

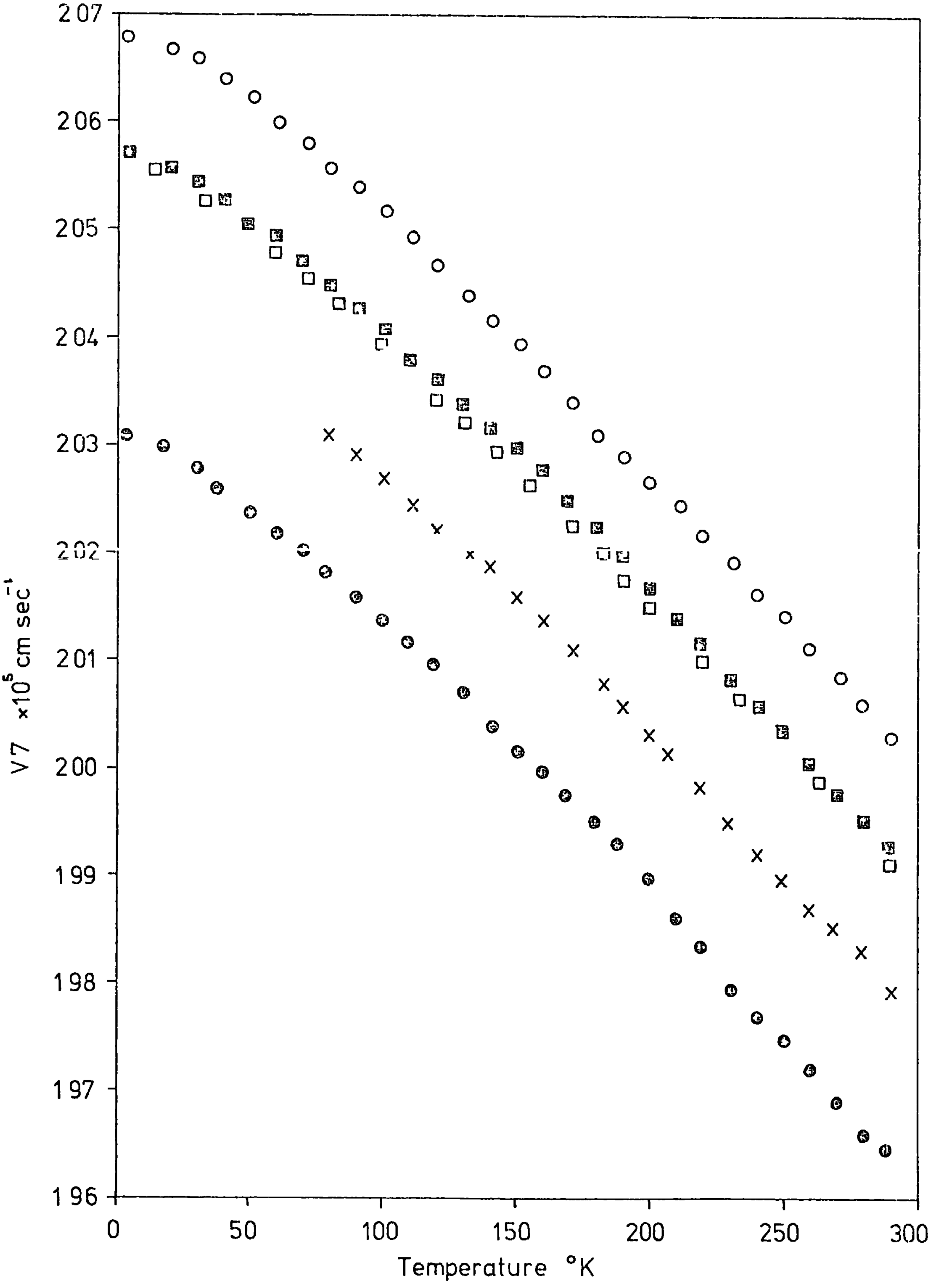

Figure 76 The temperature variation of V7

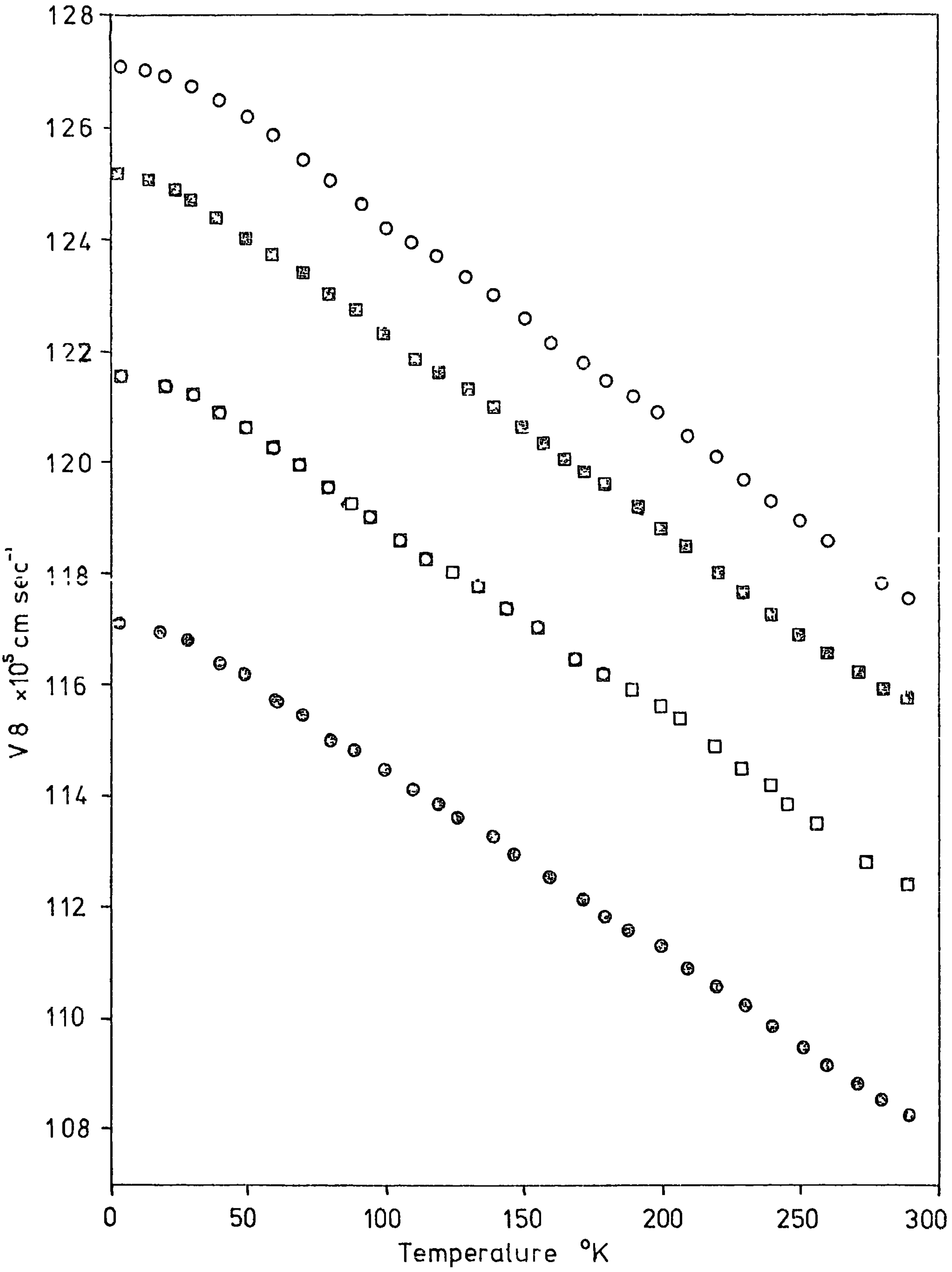

Figure 7 7 The temperature variation of V8

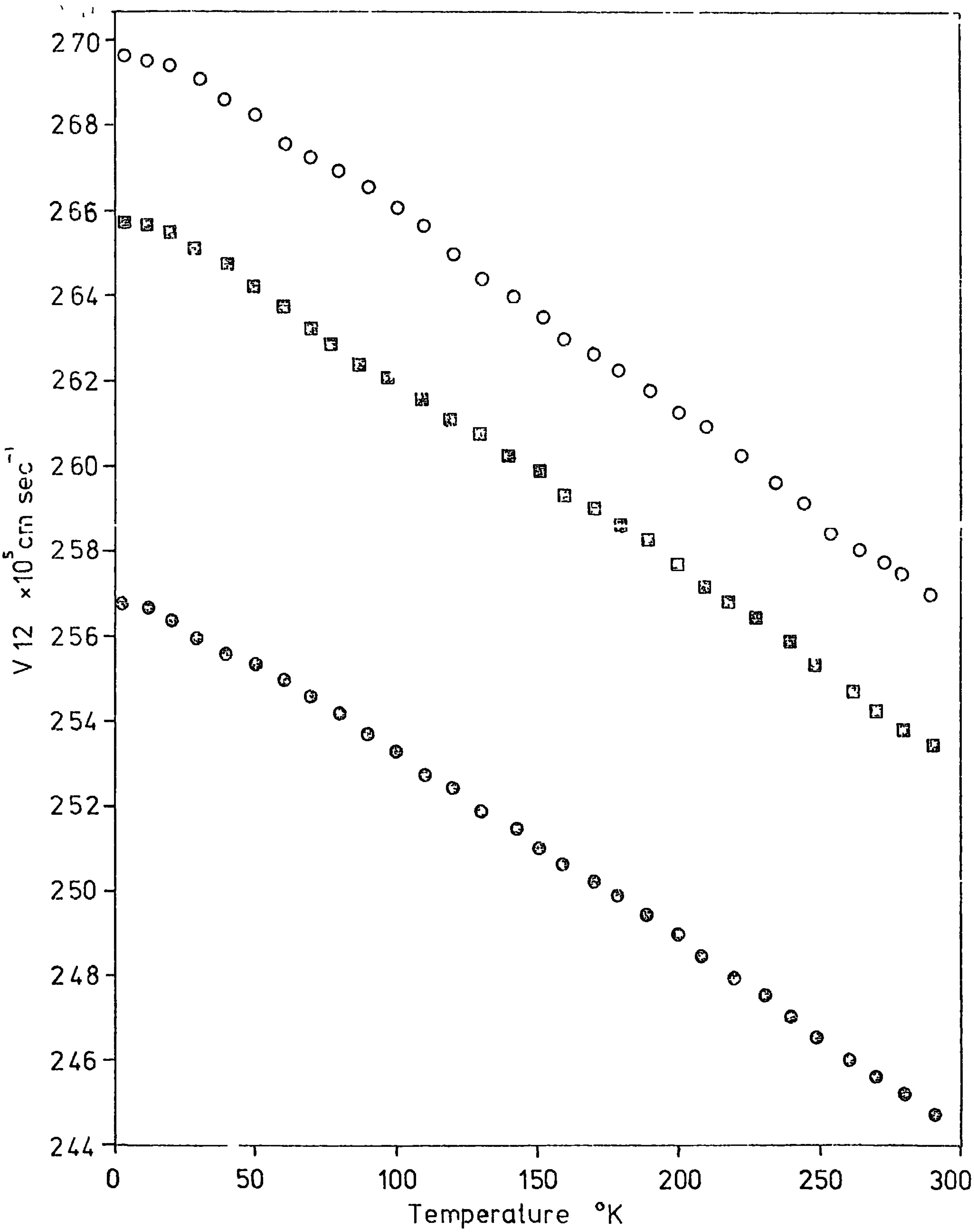

Figure 7 8 The temperature variation of V12

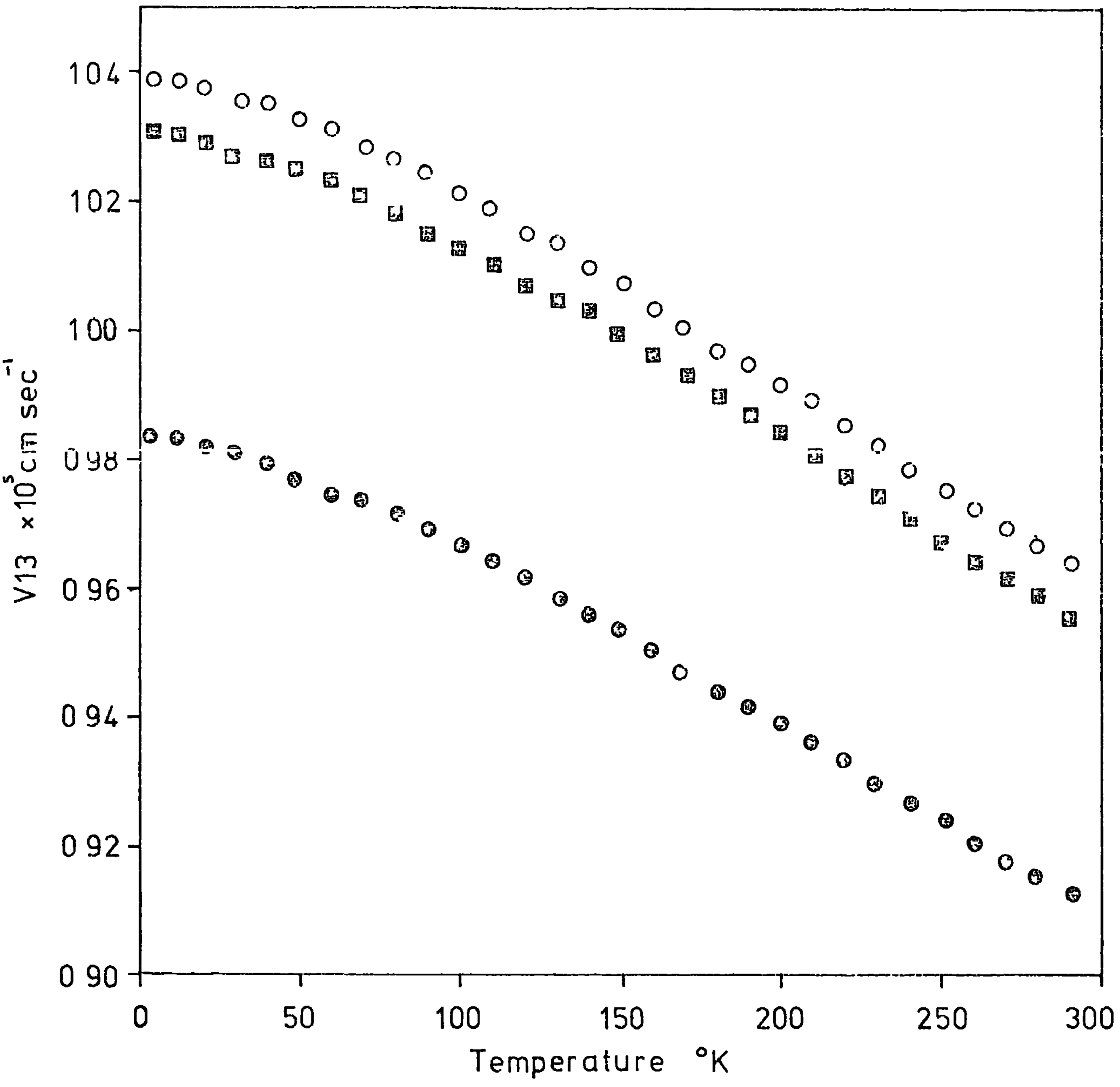

Figure 7 9 The temperature variation of V13

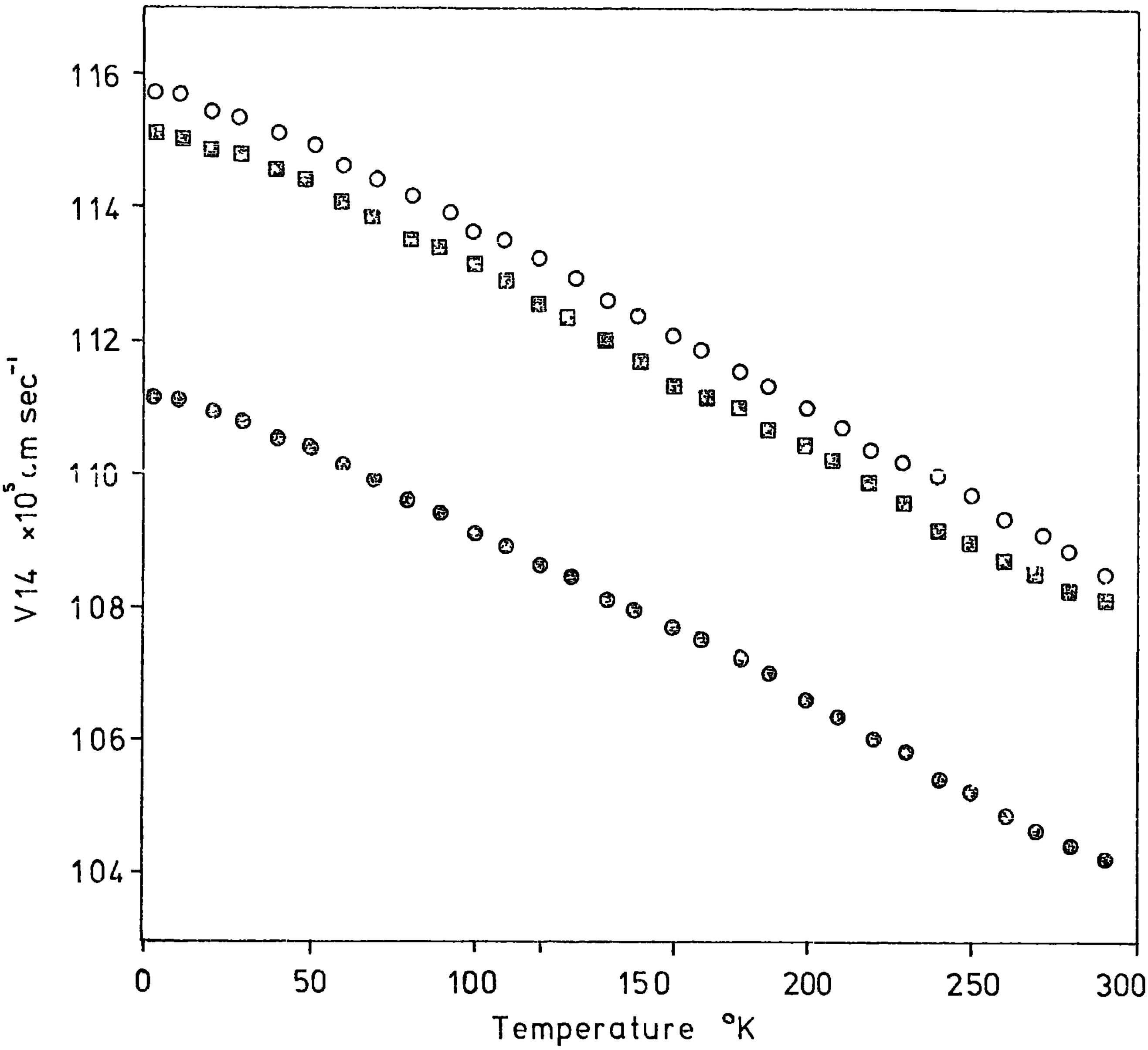

Figure 710 The temperature dependence of V14

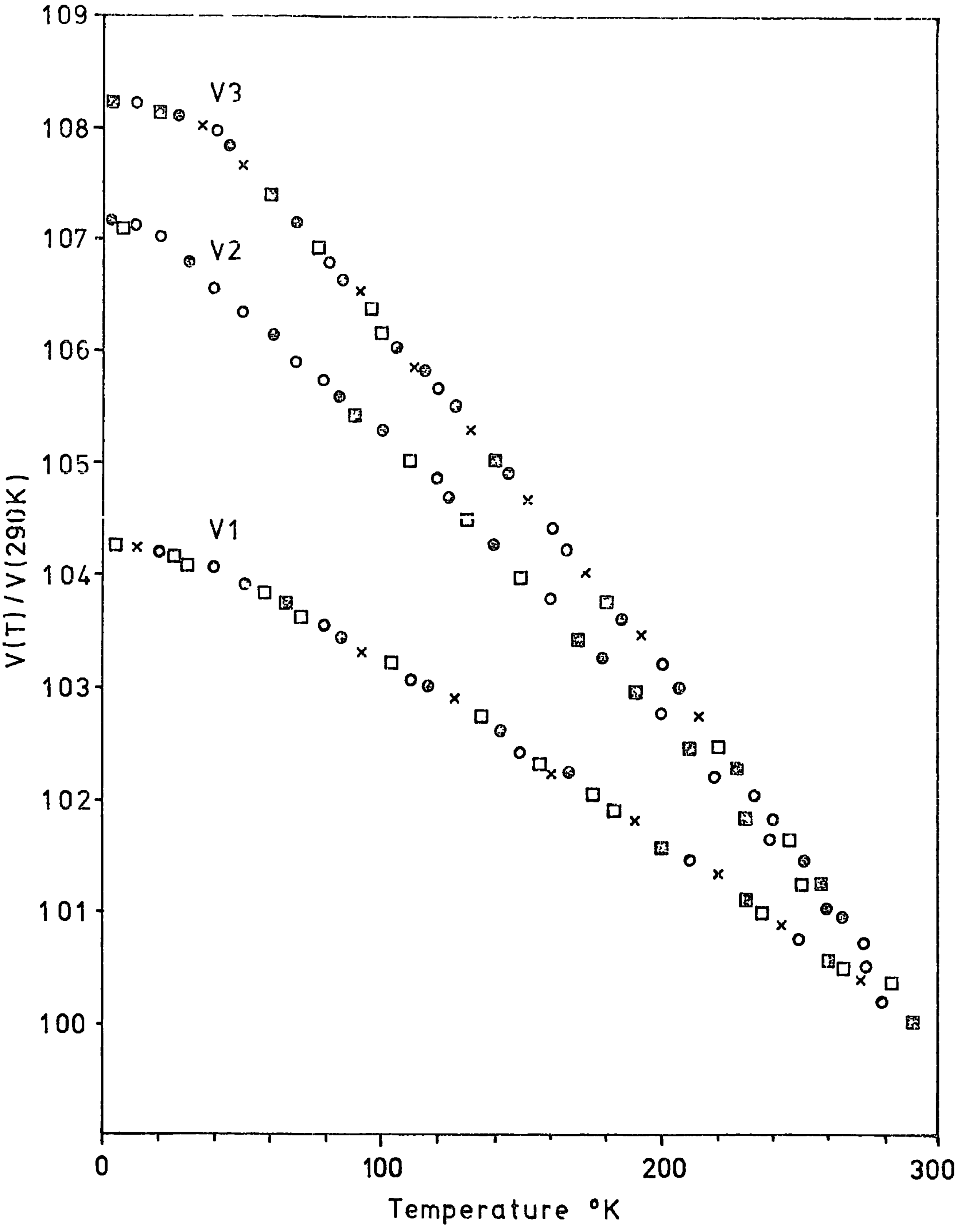

Figure 7.11 Normalised temperature dependence of the ultrasonic velocities, (100) direction

⊛ pure bismuth, x 3at% Sb, □ 5at% Sb, ▨ 7at% Sb, ○ 10at% Sb

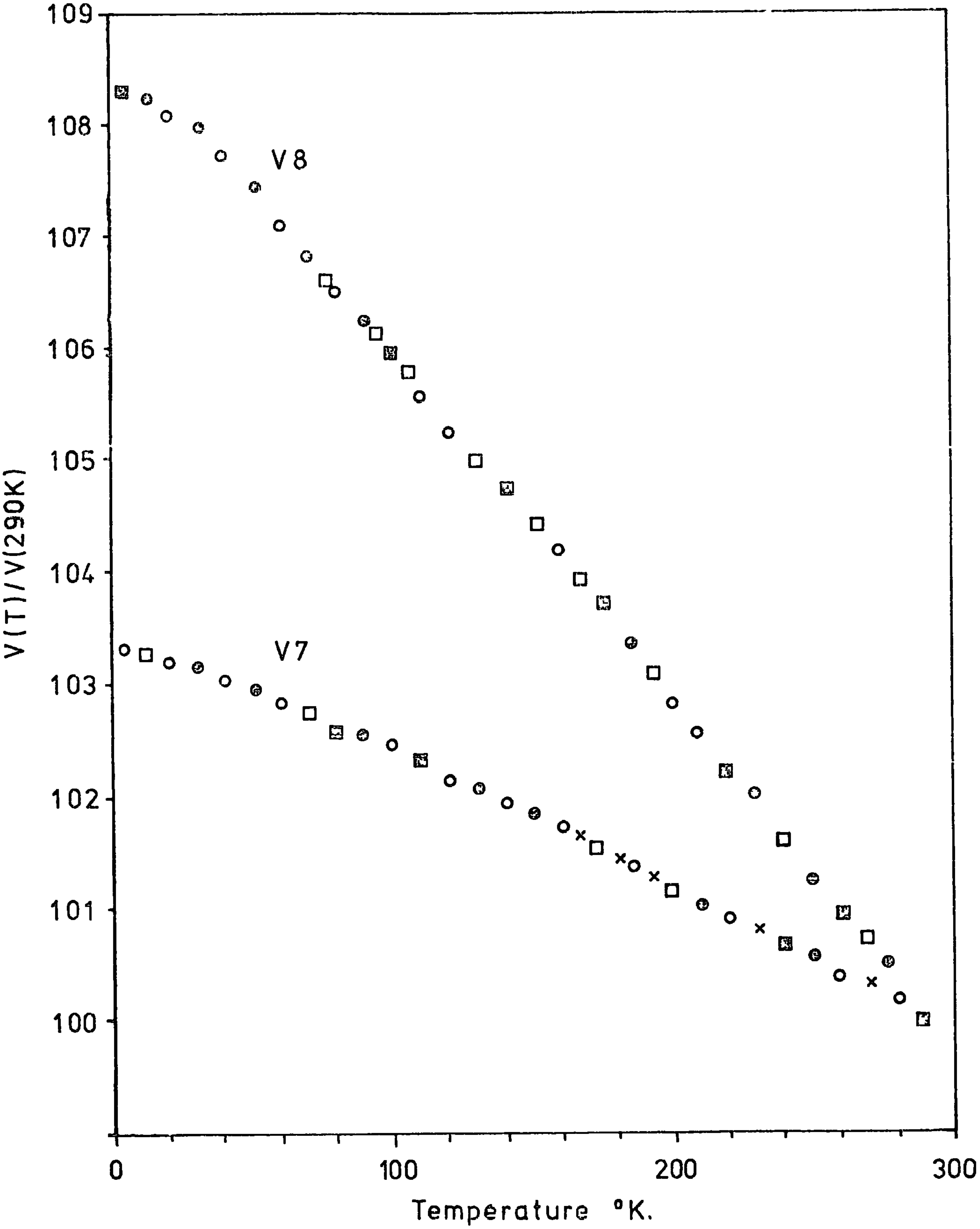

Figure 712 Normalised temperature dependence of the ultrasonic velocities, (001) direction

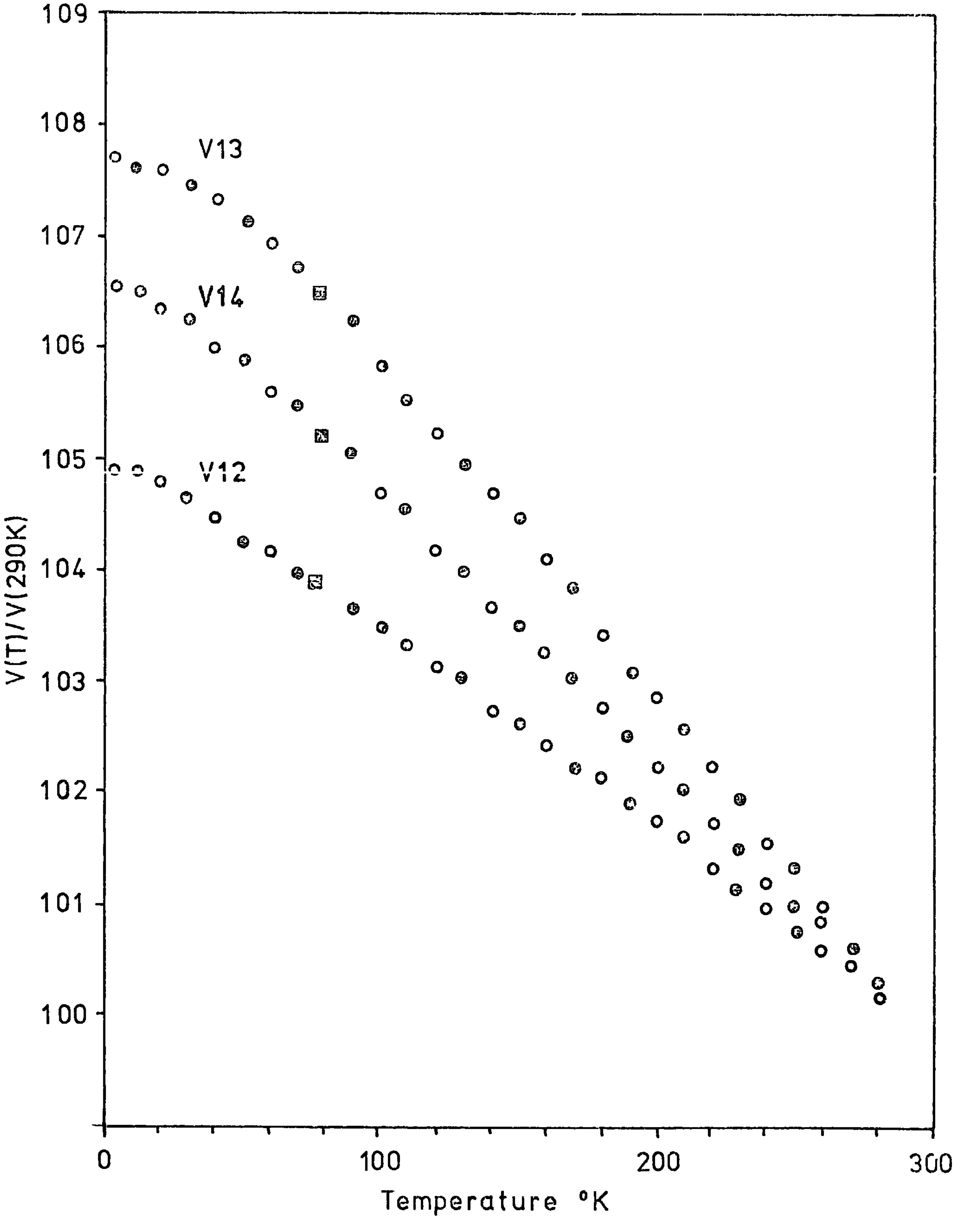

Figure 7 13 Normalised temperature dependence of the ultrasonic velocities, (0, 1/√2, 1/√2) direction

Temperature °K	Atomic Percent Antimony			
	0	5	7	10
290	63.39	65.28	66.07	66.80
280	63.68	65.48	66.11	66.90
260	64.20	66.02	66.72	67.57
240	64.63	66.44	67.16	68.10
220	65.04	66.86	67.67	68.54
200	65.59	67.38	68.14	68.91
180	65.96	67.81	68.52	69.46
160	66.44	68.33	69.06	69.89
140	66.84	68.75	69.43	70.28
120	67.32	69.21	69.85	70.83
100	67.70	69.70	70.30	71.21
80	68.18	70.15	70.72	71.66
60	68.54	70.46	71.13	71.98
440	68.84	70.86	71.55	72.31
20	69.14	71.06	71.82	72.68
4.2	69.25	71.24	71.95	72.80

(a) Temperature Dependence of C_{11}

Temperature °K	Atomic Percent Antimony			
	0	5	7	10
290	24.52	24.30	23.56	24.41
280	24.71	24.30	23.40	24.42
260	34.56	23.95	23.37	24.45
240	24.52	23.87	23.47	24.42
220	24.43	23.76	23.21	24.35
200	24.52	23.85	23.18	24.38
180	24.49	23.78	23.17	24.39
160	24.48	23.80	23.16	24.36
140	24.48	23.80	23.21	24.45
120	24.51	23.76	23.26	24.39
100	24.45	23.86	23.36	24.34
80	24.49	23.86	23.35	24.35
60	24.53	23.96	23.34	24.33
40	24.55	23.85	23.26	24.48
20	24.56	23.96	23.31	24.46
4.2	24.48	23.89	23.34	24.42

(b) Temperature Dependence of C_{12}

Table 7.2: The Temperature Dependence of the Elastic Constants (in units of 10^{10} dyne cm^{-2}).

Temperature o K	Atomic Percent Antimony			
	0	5	7	10
290	24.90	24.80	24.40	24.69
280	24.95	24.80	24.40	24.72
260	25.08	24.84	24.53	24.75
240	25.10	24.85	24.52	24,75
220	25.10	24.83	24.57	24.77
200	25.15	24.93	24.63	24.81
180	25.18	24.90	24.62	24.82
160	25.25	24.96	24.71	24.85
140	25.29	25.01	24.64	24.85
120	25.33	25.02	24.70	24.89
100	25.32	25.11	24.66	24.92
80	25.41	25.11	24.67	24.95
60	25.37	25.11	24.76	24.96
40	25.39	25.07	24.71	24.98
20	25.41	25.08	24.70	24.97
4.2	25.37	25.07	24.67	24.99

(c) Temperature Dependence of C_{13}

Temperature o K	Atomic Percent Antimony			
	0	5	7	10
290	7.28	7.80	8.30	8.30
280	7.29	7.85	8.30	8.35
260	7.41	8.01	8.44	8.40
240	7.51	8.11	8.57	8.50
220	7.58	8.20	8.66	8.60
200	7.67	8.26	8.73	8.65
180	7.74	8.37	8.84	8.76
160	7.81	8.44	8.89	8.81
140	7.88	8.52	9.00	8.91
120	7.98	8.63	9.08	9.00
100	8.07	8.68	9.17	9.12
80	8.12	8.78	9.22	9.15
60	8.20	8.83	9.32	9.26
40	8.27	8.93	9.43	9.36
20	8.36	8.99	9.48	9.46
4.2	8.40	9.03	9.58	9.50

(d) Temperature Dependence of C_{14}

Temperature ° K	Atomic Percent Antimony			
	0	5	7	10
290	37.9	38.27	37.91	37.93
280	37.95	38.38	38.12	38.04
260	38.14	38.53	38.25	38.23
240	38.33	38.73	38.43	38.43
220	38.55	38.95	38.68	38.65
200	38.77	39.21	38.92	38.87
180	38.95	39.36	39.11	39.03
160	39.18	39.58	39.36	39.37
140	39.35	39.75	39.45	39.45
120	39.55	39.96	39.69	39.64
100	39.74	40.20	39.84	39.83
80	39.92	40.36	40.09	39.99
60	40.07	40.52	40.24	40.15
40	40.22	40.63	40.40	40.31
20	40.36	40.79	40.51	40.43
4.2	40.41	40.83	40.57	40.47

(e) Temperature Dependence of C_{33}

Temperature ° K	Atomic Percent Antimony			
	0	5	7	10
290	11.51	12.22	12.84	13.09
280	11.61	12.27	12.91	13.15
260	11.75	12.43	13.04	13.28
240	11.92	12.61	13.23	13.53
220	12.08	12.78	13.41	13.66
200	12.23	12.92	13.57	13.84
180	12.38	13.10	13.77	14.03
160	12.50	13.23	13.87	14.13
140	12.68	13.41	14.07	14.33
120	12.83	13.57	14.21	14.50
100	12.97	13.69	14.38	14.73
80	13.09	13.85	14.52	14.79
60	13.25	13.99	14.72	14.99
40	13.40	14.18	14.87	15.20
20	13.50	14.29	14.98	15.31
4.2	13.55	14.31	15.04	15.37

(f) Temperature Dependence of C_{44}

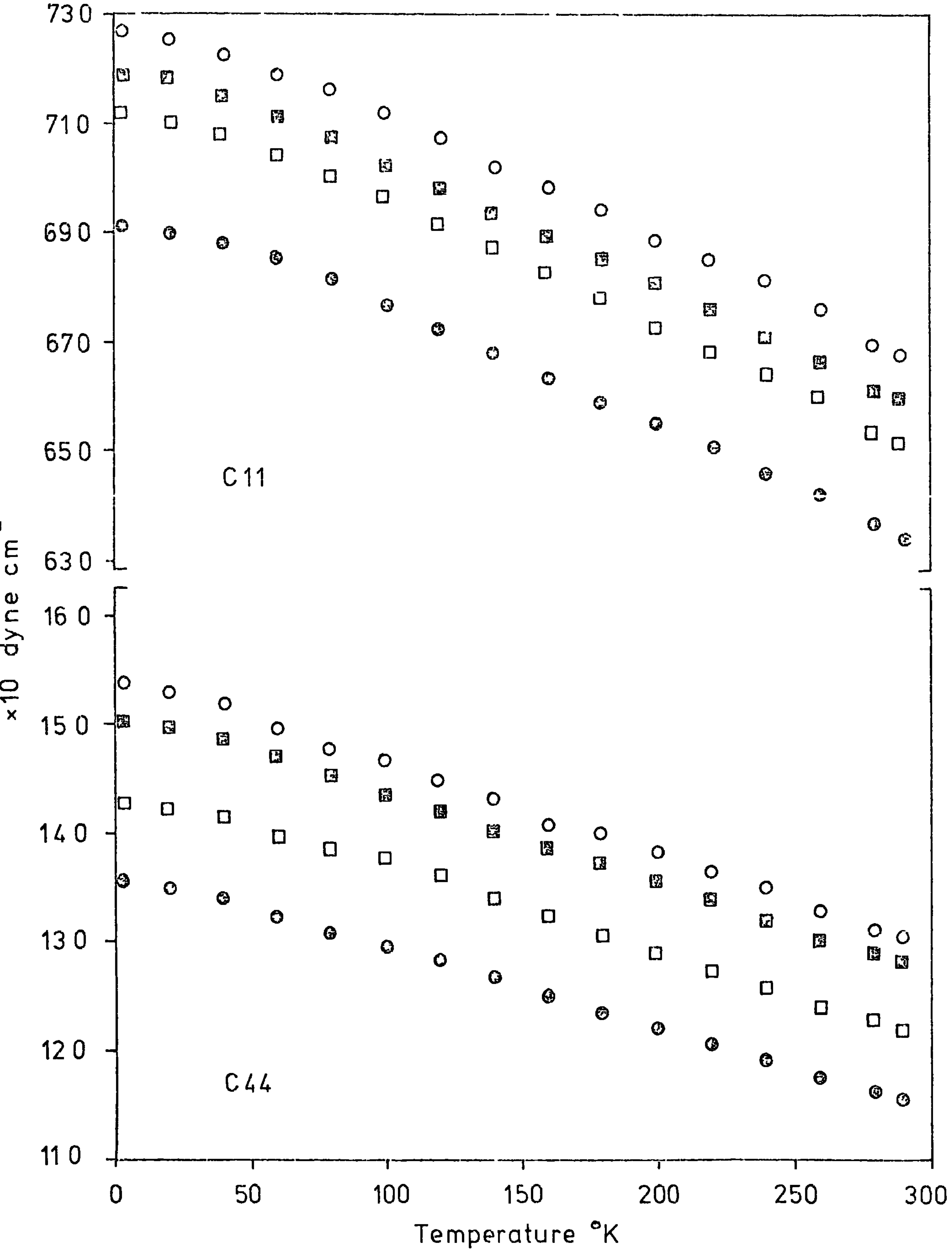

Figure 7.14 Temperature variation of the elastic constants C11 and C44

◎ pure bismuth, □ 5 at% Sb, ▨ 7 at% Sb, ○ 10 at% Sb

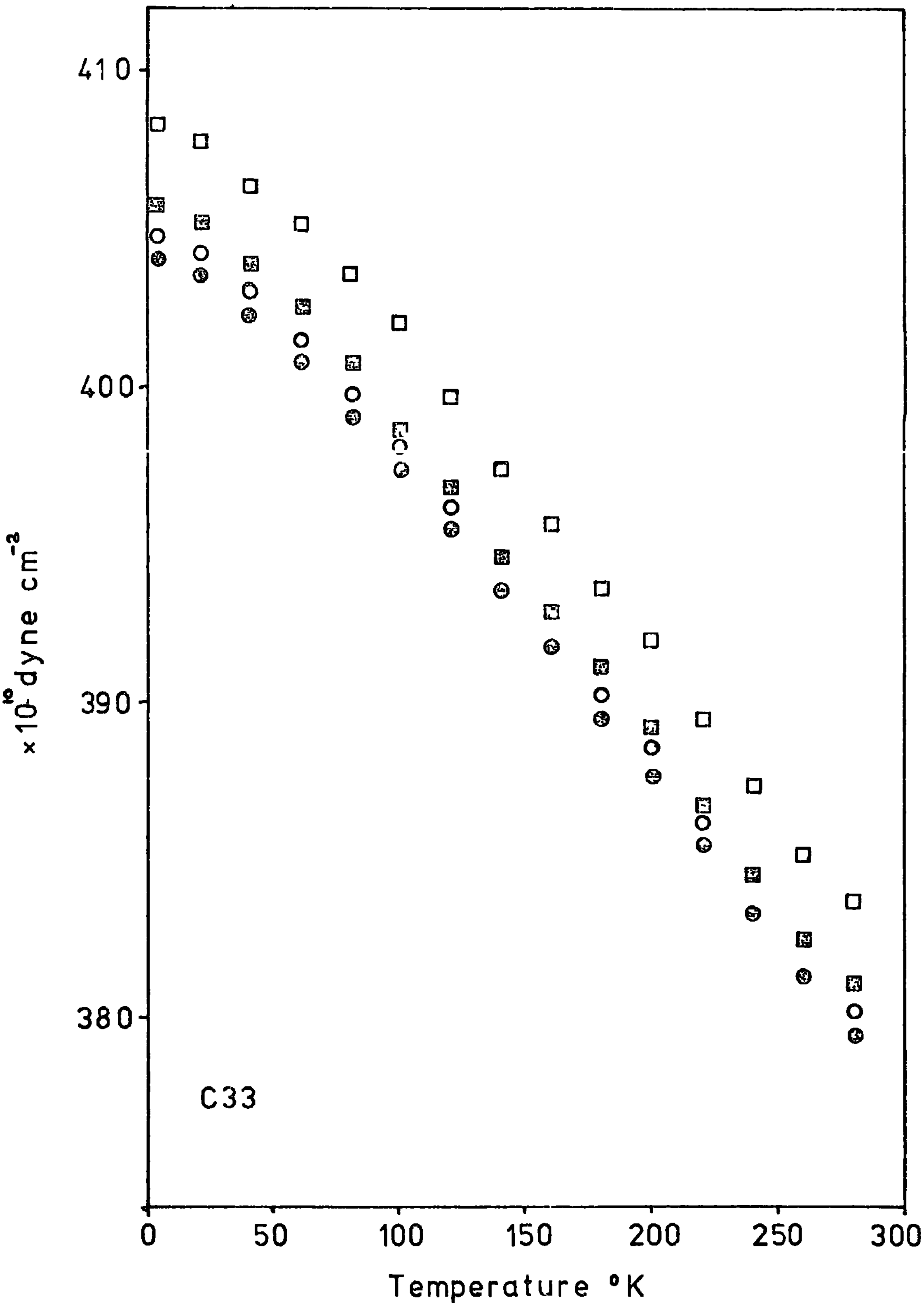

Figure 715 Temperature variation of the elastic constant C33

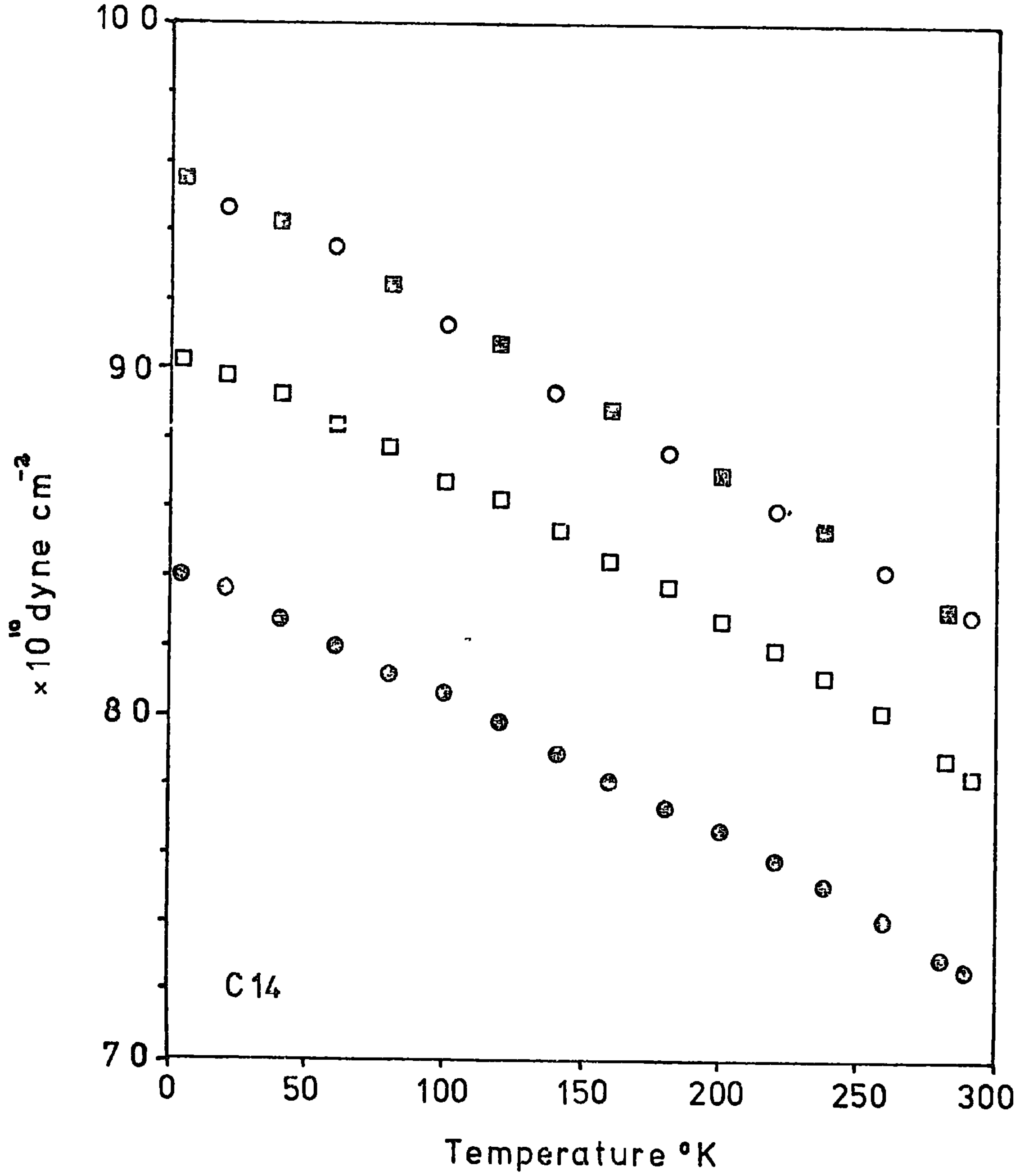

Figure 7.16 Temperature variation of the elastic constant C14

7.4 The Elastic Compliances

Often, it is more convenient to relate the response of a body directly to a particular stress. The elastic compliance tensor is given by

$$\varepsilon_i = S_{ij}\,\sigma_j \qquad (7.1)$$

The transformation between the elastic stiffness and compliance tensor is affected by ,

$$S_{ij} = (-1)^{i+j}\,\Delta^c_{ij}/\Delta^c \qquad (7.2)$$

where Δ^c is the determinant of the C_{ij} terms and Δ^c_{ij} is the minor of the element C_{ij}. Expansion of (7.2) gives the relationship between the coefficients of the two tensors as

$$\begin{aligned}
S_{11} &= (C_{33}/M + C_{44}/N)/2 \\
S_{12} &= (C_{33}/M - C_{44}/N)2 \\
S_{13} &= -C_{13}/M \\
S_{14} &= -C14/M \\
S_{33} &= (C_{11} + C_{12})/M \\
S_{44} &= (C_{11} - C_{12})/N \\
S_{66} &= 2(S_{11} - S_{12})
\end{aligned} \qquad (7.3)$$

$$\begin{aligned}
\text{where} \quad M &= C_{33}(C_{11} + C_{12}) - 2C_{13}^{\,2} \\
N &= C_{33}(C_{11} - C_{12}) - 2C_{14}^{\,2}
\end{aligned}$$

The computed temperature dependences of the elastic compliances are presented in Figures 7.17-7.19. As expected, the elastic compliances increase with temperature.

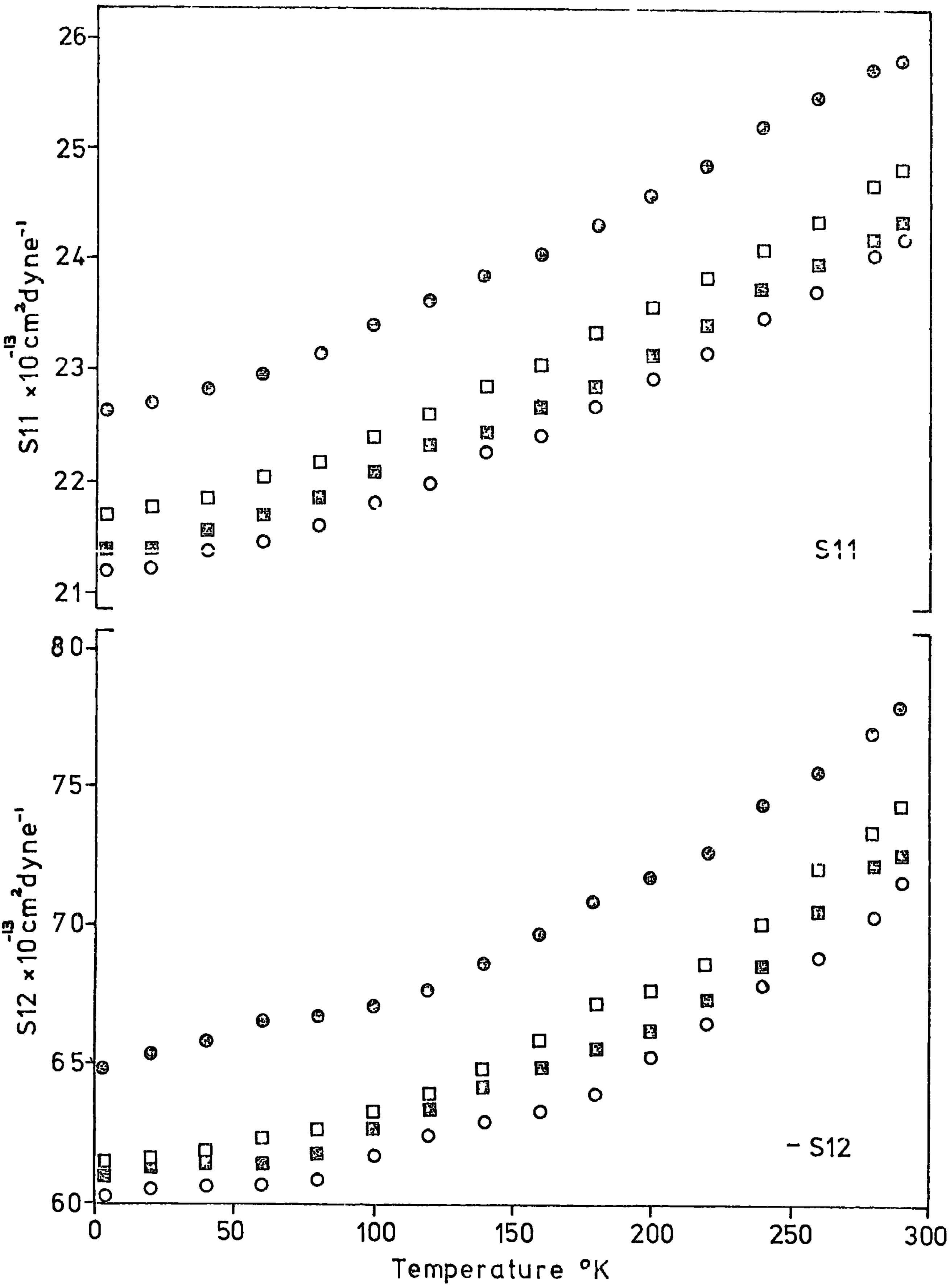

Figure 717 – 719 The temperature variation of the elastic compliance constants

⊙pure bismuth, □5at%Sb, ▨7at%Sb, ○10at%Sb

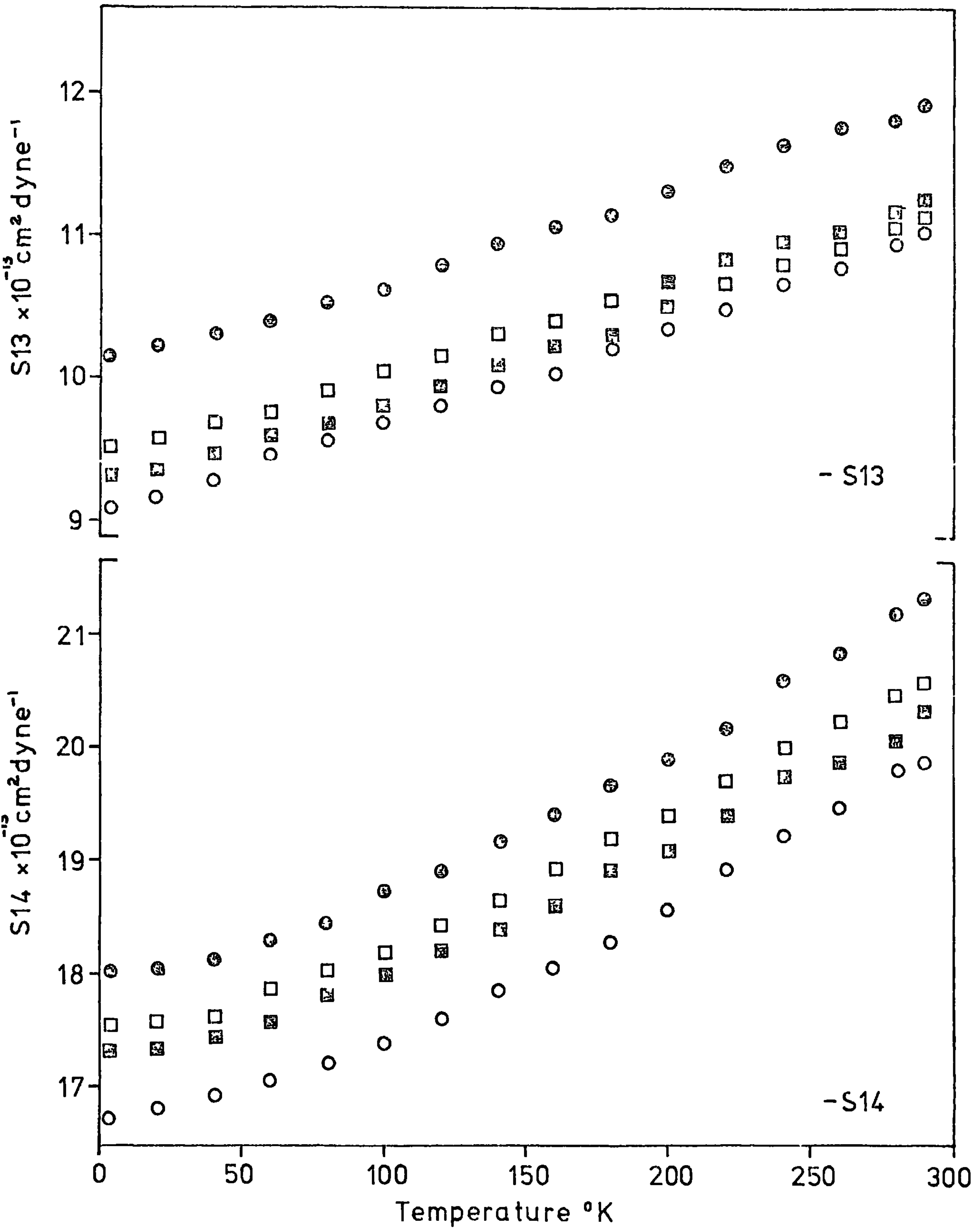
12
11
10
9
S13 ×10^{-13} cm^2 dyne^{-1}
− S13
21
20
19
18
17
S14 ×10^{-13} cm^2 dyne^{-1}
−S14
0
50
100
150
200
250
300
Temperature °K

Figure 718

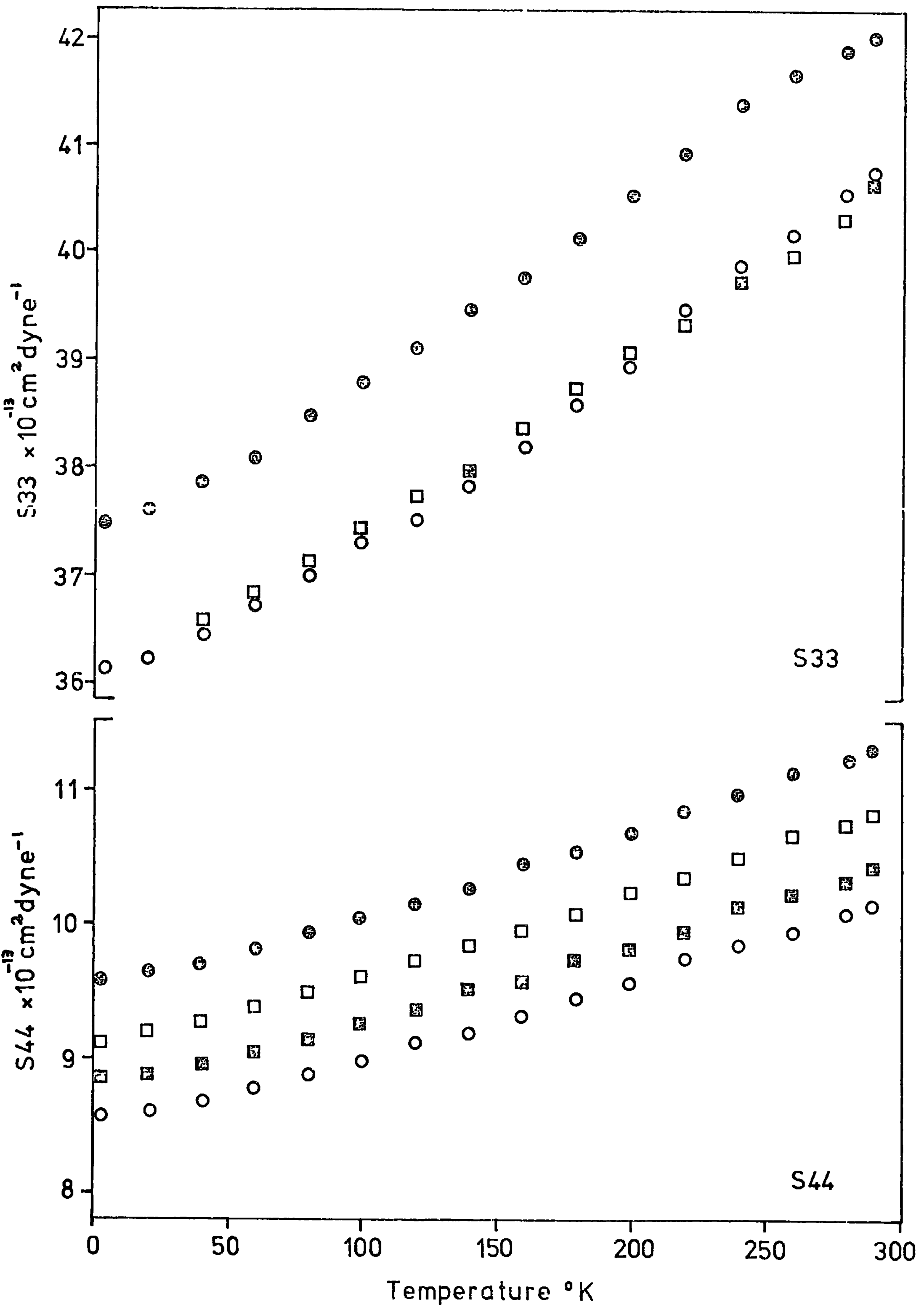
42
41
40
39
38
37
36
S33 ×10⁻¹³ cm² dyne⁻¹
S33
11
10
9
8
S44 ×10⁻¹³ cm² dyne⁻¹
S44
0
50
100
150
200
250
300
Temperature °K

Figure 7.19

7.5 The Polycrystalline Moduli

The results obtained here indicate that there are no strange anomalies in the elastic behaviour of the bismuth-anitmony alloys in the range of composition 0-10 at.% antimony. This is in complete contradiction to the work of Gopinathan and Padmini (1974) on polycrystalline alloys, in which they observed very large changes in the elastic moduli, both as a function of composition and temperature. These workers attempt to explain qualitatively their observations on the basis of a change in the electronic contribution to the elastic constants and on the complex variation of the lattice parameter as determined by Jain (1959). The present work has shown that the electronic contribution is so small, as to be insignificant, while the lattice parameters (0-29 at.% antimony) have been very carefully measured by Cucka and Barrett (1962) and shown to vary linearly with composition.

To facilitate a more direct comparison between the present findings and the data of Gopinathan and Padmini (1974), the elastic constants obtained here are transformed into the elastic moduli for a polycrystalline aggregate. Hill (1952) showed that the values of the elastic moduli for a polycrystalline material lie between those calculated from the two classical approximations of Voigt (1928) and Reuss (1929), the Voigt method averages over all lattice directions using the assumption that the strain is uniform throughout the aggregate, while the Reuss method assumes that the stress is uniform throughout the aggregate, the Voigt moduli are larger than the Reuss moduli. Both methods are slightly inaccurate, but the average of the values obtained is in good agreement with the experimental evidence (see Hearmon 1961, p.44). For the rhombohedral structure the equations for the shear moduli (G = V_S^2, where V_S is the polycrystalline shear velocity) are

$$G_V = \frac{1}{15}((2C_{11} + C_{33}) - (C_{12} + 2C_{13}) + 3(2C_{44} + C_{66}))$$

$$G_R = 15/(4(2S_{11} + S_{33}) - 4(S_{12} + 2S_{13}) + 3(2S_{44} + S_{66}))$$

and for the bulk moduli

$$K_V = \frac{1}{9}((2C_{11} + C_{33}) + 2(C_{12} + 2C_{13}))$$

$$K_R = 1/((2S_{11} + S_{33}) + 2(S_{12} + 2S_{13}))$$

where the subscripts V and R refer to the Voigt and Reuss approximations respectively. In both approximations the bulk moduli are equivalent ($K_V = K_R$).

For the bismuth-antimony alloys it can be assumed that, like other materials, the actual shear modulus is

$$G = (G_V + G_R)/2$$

The Young's modulus E, Poisson's ratio σ, compressibility B and the longitudinal modulus L (L = ρV_L^2, where V_L is the longitudinal velocity of the aggregate) are calculated from the following formulae,

$$\frac{1}{E} = \frac{1}{3G} + \frac{1}{9K}$$

$$\sigma = (E - 2G)/2G$$

$$L = E\left[\frac{1 - \sigma}{(1 + \sigma)(1 - 2\sigma)}\right]$$

$$B = 1/K .$$

The longitudinal and shear moduli and the compressibility as a function of composition are given in Figure 7.20, the results obtained by Gopinathan and Padmini (1974) are also plotted. The differences between the two sets of data are very striking. Not only do these workers observe a pronounced minima in the moduli at 5% at % antimony, but their longitudinal modulus for pure bismuth is only half of that obtained here. Their data suggests that they measured a longitudinal velocity for pure bismuth which is less than the slowest longitudinal velocity in single crystal material. Furthermore, they incorrectly related the longitudinal velocity to Young's modulus, i.e. their quoted Young's modulus is in fact the longitudinal modulus. Gopinathan and Padmini measured their ultrasonic velocities using the composite oscillator method, originally developed by Balmuth (1934), at a frequency of 110 kHz. In a subsequent paper they report various ultrasonic studies on bismuth single crystals, using the same technique they measure the z axis velocities to be (i) longitudinal 1.470 x 10^5 cm sec^{-1} (1 968 x 10^3 cm sec^{-1} measured here) and (ii) shear 0.703 x 10^5 cm sec^{-1} (1.083 x 10^5 cm sec^{-1}). The deviations (from the results obtained here) for their longitudinal and shear velocities are 25% and 42% respectively, yet they quote their measurements as accurate to a few parts in a thousand, and the modulus values accurate to one percent Thus, assuming that they used bismuth and single crystals, their technique must be accurate not to a few parts in a thousand, but to 2 parts in ten. Bearing in mind that their errors are so extreme, it is interesting to note that their quoted polycrystalline Young's modulus (which they incorrectly related to $E = \rho V_L^2$) and shear modulus for pure bismuth

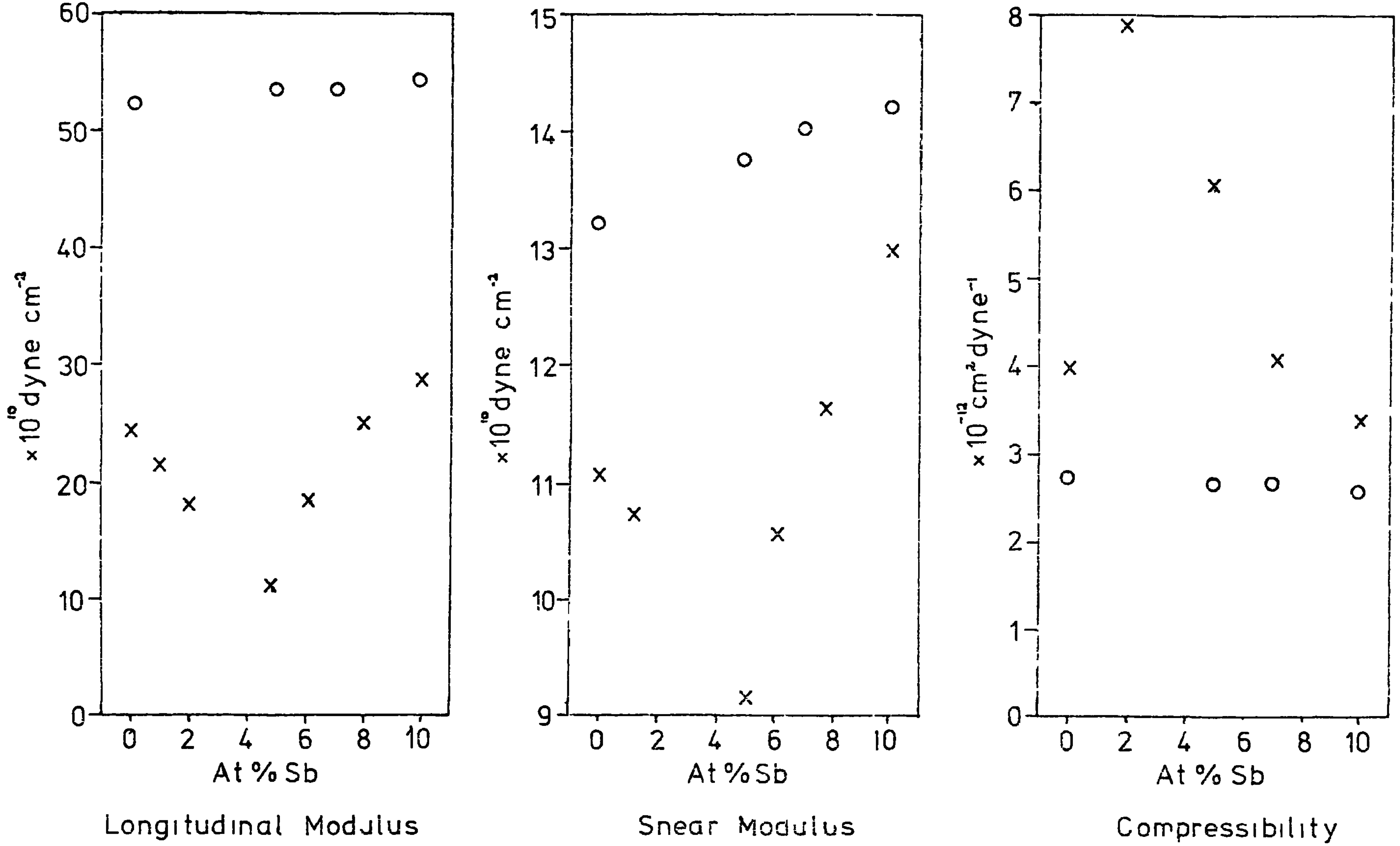

Figure 7.20 The polycrystalline moduli

o Present work - calculated from single crystal elastic constants

x Gopinathan and Padmini (1974a)

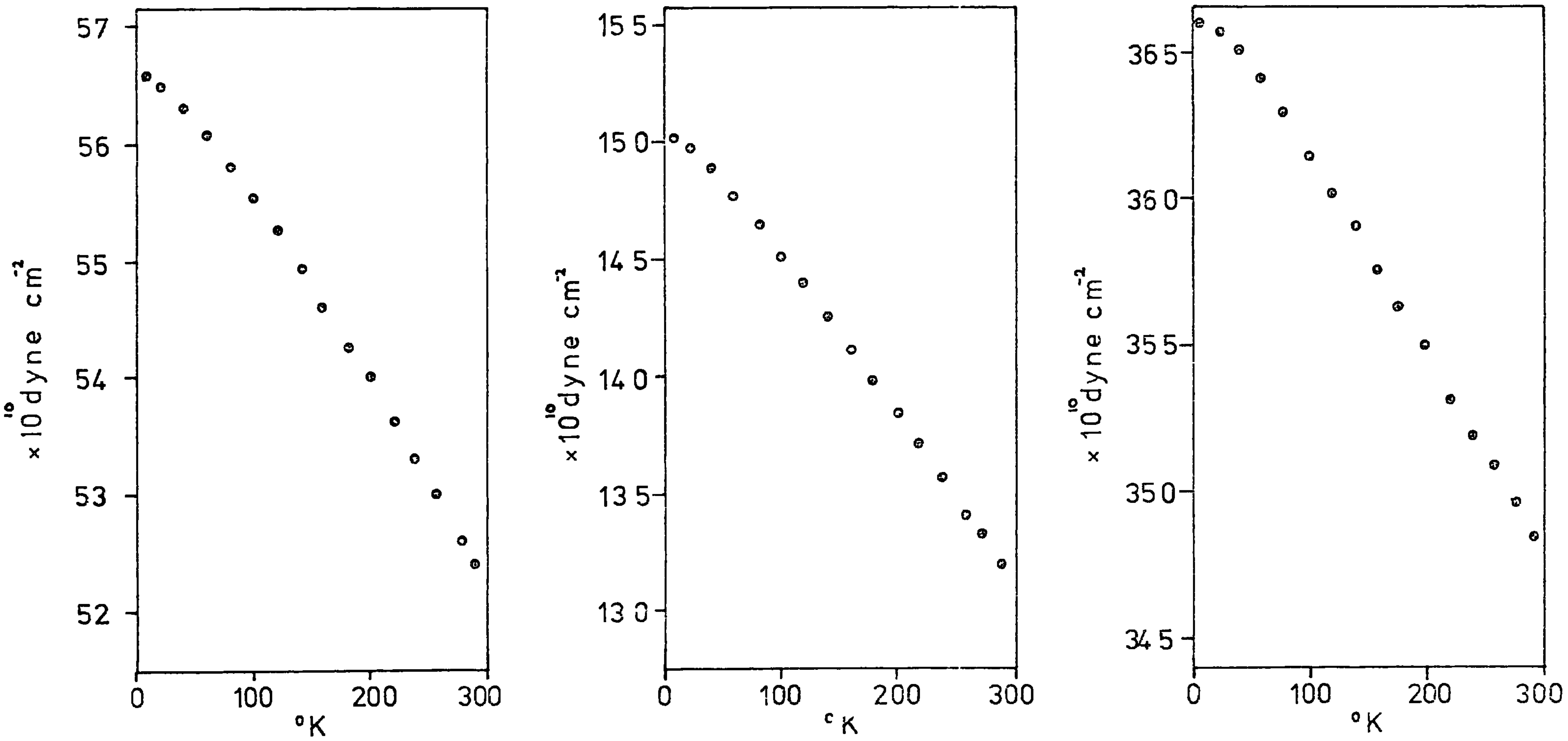

(i) Longitudinal Modulus (ii) Shear Modulus (iii) Young's Modulus

Figure 721 The temperature dependence of the polycrystalline moduli of pure bismuth – calculated from the single crystal elastic constants (which they correctly related to $G = \rho V_S^2$) agree to within 0.3% and 0.1% of those quoted in Hearmon (p 44, 1961). In view of their compounded experimental and theoretical errors, this coincidence is remarkable. These workers then go on to point out a perfect correlation between the variation of the lattice parameter (as measured by Jain 1959) as a function of antimony concentration with Young's Modulus (obtained from V_L^2). The maxima and minima in both properties occur at the same composition Yet, these workers are apparently unaware of the careful and accurate measurements of Cucka and Barrett (1962) of the lattice parameters and atomic positional parameters of the bismuth-antimony alloys which demonstrate that the lattice constants vary linearly with composition in the range 0-30 at.% antimony. In the composition range considered here Gopinathan and Padmini also incorrectly related the decrease in the L-T point band overlap to the decrease in velocity, throughout the paper these workers have assumed that the electronic contribution increases the elastic constants, whereas here it has been shown from the Keyes model that the reverse is true and also that the effect is negligible. Since Gopinathan and Padmini have made so many basic experimental, theoretical and interpretive errors no further discussion will be pursued here

7.6 Measurements of Ultrasonic Attenuation

Although they were not of primary interest, ultrasonic attenuation measurements were taken simultaneously with the velocity measurements Furthermore, to ensure accurate velocity measurements it was important to ensure that the sequence of multiple echoes remained exponential whilst the temperature was varied.

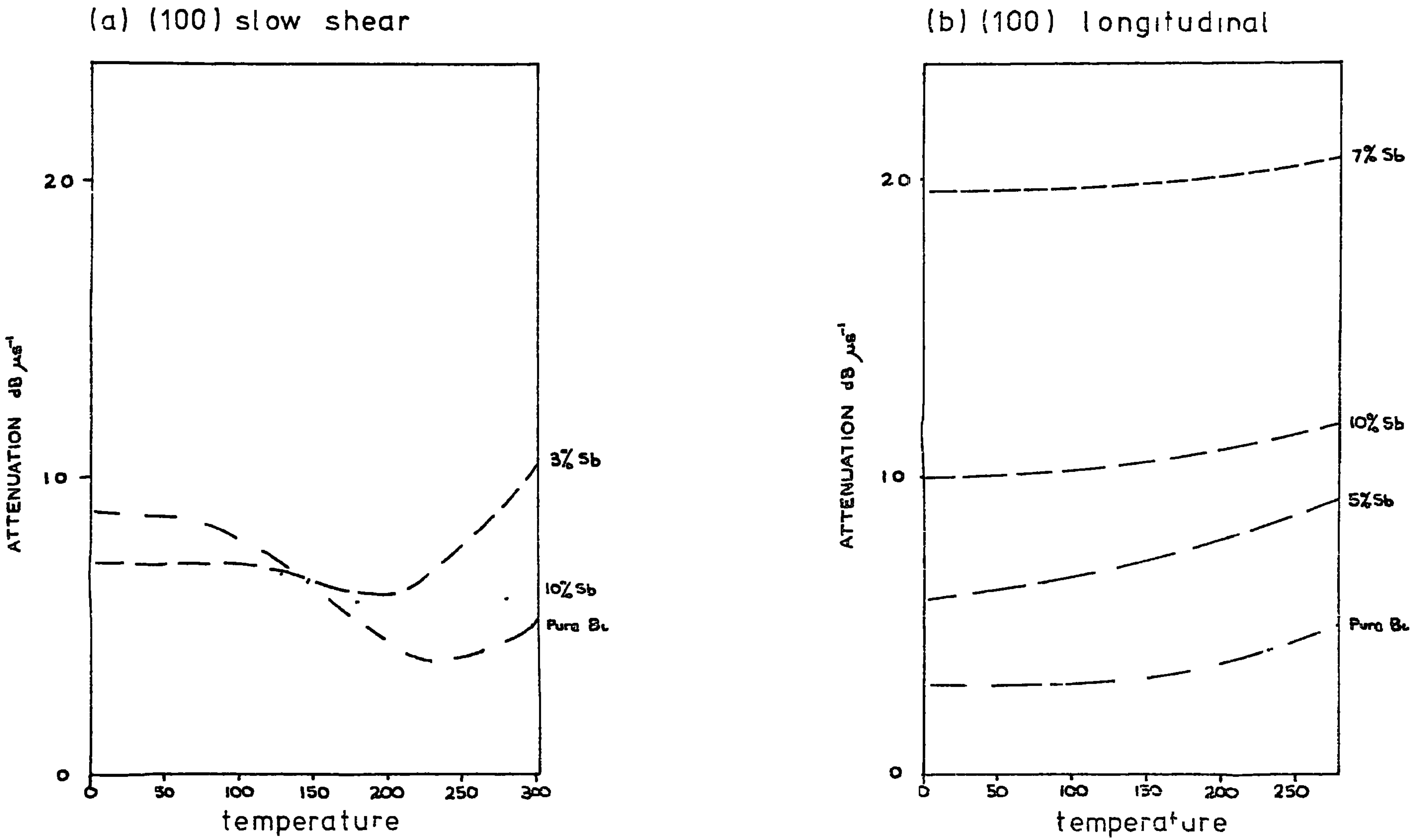
(a) (100) slow shear

(b) (100) longitudinal

Figure 7 22 Typical attenuation measurements

In general, the attenuation decreased with decreasing temperature and there was no evidence of any pronounced effects. No overall dependence with composition could be ascertained; typical results obtained are shown in Figure 7.22. The attenuation measurements could not always be readily reproduced. There are probably two main reasons for the behaviour of the attenuation: (i) the Nonaq band is lossy (Farley 1974, Maynell 1972) and the attenuation within it might vary with temperature, (ii) the prepared sample must necessarily have a thin ($\sim 100\ \mu$) layer of polycrystalline material on each of the two parallel faces (a result of the machining process), this layer may have a dominating influence on the apparent attenuation. Therefore, unless the machining process is identical for all samples (and this is difficult to achieve), a direct comparison of the absolute attenuation coefficients is not easy. Augeri and Freedman (1967) have commented on this very point and have shown that the presence of this layer does introduce a significant excess attenuation. To obtain reliable acoustic attenuation measurements they propose a technique which utilises a combination of mechanical grinding and electropolishing. The polycrystalline layer should however have a negligible effect on the velocity measurements.

7.7 The Debye Temperature

The elastic constant and density data at low temperature were used by Dr. G A. Saunders to calculate the Debye temperature θ_D from

$$\theta_D = \left(\frac{9N}{4\pi}\right)\frac{h}{k} \Bigg/ \left(\int \left[\frac{1}{v_1^{\,3}} + \frac{1}{v_2^{\,3}} + \frac{1}{v_3^{\,3}}\right] \frac{d\Omega}{4\pi}\right)^{\frac{1}{3}}$$

where h and k are Plancks and Boltzmann's constants respectively, N is Avogadro's number and V_i are th eigenvalues of the Christoffel equations. The integral over the solid angle $d\Omega$ has been approximated by a sum taken 10288 points each subtending on equal solid angle $\Delta\Omega$ (= 1.218 x 10^{-3} steradians). Values of θ_D obtained for pure bismuth and 10 at.% antimony are 121 ± 1 K and 128 ± 1 K respectively Separation of the specific heat of bismuth into lattice and electronic contributions has proved to be rather difficult because the Debye temperature is small and the electrons in this semimetal with a small band overlap contribute little to the low temperature specific heat. However, accurate measurements by Collam, Krusuis and Pickett (1969) gave a best fit to an expression of the form $\gamma T + BT + AT^{-2}$ of

$$C_p = (8.5 \pm 2.5)T + (1120 \pm 50)T^3 + (0.0064 \pm 0.002)T^{-2}\ \mu J/mole\ K^2$$

with the result that the electronic contribution (γT) to the specific heat is in good agreement with that calculated (γ = 7.1 μJ/mole K) from the ellipsoidal model of the Fermi surface, thus removing the apparent discrepancies observed by other workers. The T^3 dependent lattice contribution to the specific heat gives a Debye temperature of 120.3 ± 1.5 K in excellent agreement with Phillips (1960) determination and the 121 ± 1 K obtained here from the elastic constants. Previous calculations (Anderson 1965) of the Debye temperature from elastic constant data have obtained 106 K (Eckstein, Reneker and Lawson) and 118 K (Bridgman 1924).

There is no available specific heat data with which to compare the θ_D calculated from the elastic constant data of the bismuth-antimony alloys. However, the increase of the Debye temperature to

128 K for the 10 at % alloy is consistent with the θ_D of 184 K for pure antimony calculated by Anderson (1965) from the isothermal constants of Bridgman (1924).

7.8 Discussion

The ultrasonic measurements on the bismuth-antimony alloys in the range of composition 0-10 at.% antimony have shown that the elastic constants vary monotonically with composition and, contrary to the results of Gopinathan and Padmini (1974) exhibit no anomalous behaviour This confirms the theoretical studies of chapters five and six, which have shown that, although the electronic band structure undergoes some rather drastic changes, the electronic contributions to the elastic constants are negligible.

Despite the abundance of literature reporting the elastic constants of various elements, compounds and alloys, little information regarding the elastic behaviour of comparable crystalline solid solutions is available. Araki and Tanaka (1972) have measured the elastic stiffness constants of the selenium-tellurium system which, like the bismuth-antimony alloys, also form an uninterrupted series of solid solution. They found that the variation of the elastic constants was essentially linear over the entire range of composition. Grison (1951) has shown that the unit cell dimensions of the selenium-tellurium system with composition depart only slightly from linearity Since this system crystallises in the hexagonal structure, it bears resemblance to the rhombohedral structure of the bismuth-antimony alloys. The present finding that the elastic constants of the bismuth-antimony alloys show approximate agreement with Vegard's Law are thus, in essence, supported by the results of Araki and Tanaka

CHAPTER 8

THE ELASTIC CONSTANTS OF BISMUTH DOPED WITH TELLURIUM

8.1 Introduction

The computations at the end of Chapter 6 have shown that, in highly donor doped bismuth, an electronic contribution to certain elastic constants should be observable, the theory predicts that an increase in the free electron density should decrease C_{11}, C_{66} and C_{44} and increase C_{12} and C_{14}. A programme was evolved to attempt an experimental verification of the effect.

Single crystals of bismuth doped with tellurium were grown by the zone levelling technique and ultrasonic samples were prepared in the manner described for the bismuth-antimony alloys Since Noothoven van Goor and Trum (1969) have shown that tellurium is a monovalent donor in bismuth, it was assumed that each tellurium atom contributed one electron to the ellipsoids at the L point. The complete set of elastic constants was measured for crystals with electron concentrations of approximately 10^{19} cm^{-3} and 10^{20} cm^{-3} (the exact tellurium and electron concentrations are given in Table 8.1), for brevity these will be referred to here as T19 and T20 respectively.

The T19 crystal was cut and polished into samples with parallel faces normal to the (100), (010), (001) and $(0,-\frac{1}{\sqrt{2}}, \frac{1}{\sqrt{2}})$ crystallographic directions, the measured room temperature ultrasonic velocities and the velocity-elastic constant relationships are summarised in Table 8 2. The T20 crystal was cut into samples with faces normal to the (100), (001) and $(0, \frac{1}{\sqrt{2}}, \frac{1}{\sqrt{2}})$ crystallographic directions, the ultrasonic velocities measured at room temperature are given in Table 8.3 The same corrections for the perturbation

Sample	% Wt. Te	% At Te	Electron cm^{-3} Concentration
T_{19}	0.024	0.039	1.11×10^{19}
T_{20}	0.262	0.428	1.21×10^{20}

Table 8.1. The densities of the bismuth doped tellurium samples.

Propagation Direction	Mode	Room Temperature Velocity x 10^5 cm $\sec^{-1}$	Relationship between Velocity and Elastic Constants
[100]	Pure Longitudinal	2.529	$\rho V_1{}^2 = C_{11}$
[100]	Pure Shear	1.547	$\rho V_2{}^2 = \frac{1}{2}\ (C_{66} + C_{44}) + ((C_{44} - C_{66})^2 + 4C_{14}{}^2)^{\frac{1}{2}}]$
[100]	Pure Shear	0.835	$\rho V_3{}^2 = \frac{1}{2}[(C_{66} + C_{44}) - ((C_{44} - C_{66})^2 + 4C_{14}{}^2)^{\frac{1}{2}}]$
[010]	Shear	2.549	$\rho V_4{}^2 = \frac{1}{2}[(C_{11} + C_{44}) + ((C_{44} - C_{11})^2 + 4C_{14}{}^2)^{\frac{1}{2}}]$
[010]	Longitudinal	1.385	$\rho V_5{}^2 = (C_{11} - C_{12})/2$
[010]	Shear	1 022	$\rho V_6{}^2 = \frac{1}{2}[(C_{11} + C_{44}) - ((C_{44} - C_{11})^2 + 4C_{14}{}^2)^{\frac{1}{2}}]$
[001]	Pure Longitudinal	1.968	$\rho V_7{}^2 = C_{33}$
[001]	Degenerate Shear	1.074	$\rho V_8{}^2 = C_{44}$
$[0, -\frac{1}{\sqrt{2}}, \frac{1}{\sqrt{2}}]$	Quasi Longitudinal	2.429	$\rho V_{12}{}^2 = \frac{1}{2}[\frac{1}{2}(C_{11} + C_{33}) + C_{44} - C_{14} + \{[\frac{1}{2}(C_{11} - C_{33}) + C_{14}]^2 + [C_{13} + C_{44} + C_{14}]^2\}^{\frac{1}{2}}]$
$[0, -\frac{1}{\sqrt{2}}, \frac{1}{\sqrt{2}}]$	Pure Shear	0.873	$\rho V_{13}{}^2 = \frac{1}{2}(C_{66} + C_{44}) - C_{14}$
$[0, -\frac{1}{\sqrt{2}}, \frac{1}{\sqrt{2}}]$	Quasi Shear	1.044	$\rho V_{14}{}^2 = \frac{1}{2}[\frac{1}{2}(C_{11} - C_{33}) + C_{44} + C_{14} - \{[\frac{1}{2}(C_{11} - C_{33}) + C_{14}]^2 + [C_{13} + C_{44} + C_{14}]^2\}^{\frac{1}{2}}]$

Table 8.2: Room Temperature Ultrasonic Velocities of T19.

Propagation Direction	Mode	Room Temperature Velocity $\times 10^5$ cm sec^{-1}	Relationship between Velocity and Elastic Constants
[100]	Pure Longitudinal	2.503	$\rho V_1{}^2 = C_{11}$
[100]	Pure Shear	1.527	$\rho V_2{}^2 = \frac{1}{2}[(C_{66}+C_{44}) + ((C_{44}-C_{66})^2 + 4C_{14}{}^2)^{\frac{1}{2}}]$
[100]	Pure Shear	0.828	$\rho V_3{}^2 = \frac{1}{2}[(C_{66}+C_{44}) - ((C_{44}-C_{66})^2 + 4C_{14}{}^2)^{\frac{1}{2}}]$
[001]	Pure Longitudinal	1.961	$\rho V_7{}^2 = C_{33}$
[001]	Degenerate Shear	1.088	$\rho V_8{}^2 = C_{44}$
$[0,\frac{1}{\sqrt{2}},\frac{1}{\sqrt{2}}]$	Quasi Longitudinal	2.053	$\rho V_9{}^2 = \frac{1}{2}[\frac{1}{2}(C_{11}-C_{33}) + C_{44} - C_{14} + \{[\frac{1}{2}(C_{11}-C_{33}) - C_{14}]^2 + [C_{13}+C_{44}-C_{14}]^2\}^{\frac{1}{2}}]$
$[0,\frac{1}{\sqrt{2}},\frac{1}{\sqrt{2}}]$	Pure Shear	1.509	$\rho V_{10}{}^2 = \frac{1}{2}(C_{66}+C_{44}) + C_{14}$
$[0,\frac{1}{\sqrt{2}},\frac{1}{\sqrt{2}}]$	Quasi Shear	1.128	$\rho V_{11}{}^2 = \frac{1}{2}[\frac{1}{2}(C_{11}+C_{33}) + C_{44} - C_{14} - \{[\frac{1}{2}(C_{11}-C_{33}) - C_{14}]^2 + [C_{13}+C_{44}-C_{14}]^2\}^{\frac{1}{2}}]$

Table 8.3: Room Temperature Ultrasonic Velocities of T20.

of the transducer, as detailed in 7.3 and 4.3, were made The velocity errors are of the same magnitude discussed for the bismuth-antimony alloys. Table 8.4 compares the ultrasonic velocities for both samples with those measured for pure bismuth. In general the addition of tellurium causes a decrease in the ultrasonic velocities, consistent with the theoretical prediction of the Keyes model (see Figure 6.6), however, the changes in many of the velocities are still within the limits of uncertainty.

8.2 The elastic constants at room temperature

The elastic constants at room temperature were compiled by the method of least-mean-squares described in Section 7.2, the derived values are given in Table 8.5 and compared to the theoretical magnitude of the electronic contribution calculated from the Keyes model. For both samples a change in most of the elastic constants has been observed. For T19 the changes in the elastic constants from that of pure bismuth are just within the limits of experimental uncertainty, while for T20 the changes in C_{11}, C_{12} and C_{66} are larger than the error limits (the error in the change in the measurement of each individual constant). Moreover, the overlying trend is for C_{11} and C_{66} to decrease and for C_{12} to increase with the tellurium concentration, as predicted by the Keyes model, the numerical change (not percentage change) of each of these constants is approximately the same. The variation of C_{33} is negligible, lying well within the uncertainty limits of pure bismuth. The changes observed in the elastic constants C_{13}, C_{14} and C_{44} remain somewhat unclear. C_{44} decreases for T19 and increases for T20 C_{13} decreases by 2%: C_{14} increases marginally with the tellurium concentration.

	Pure Bismuth	T19	T20
V_1	2.548	2.529	2.503
V_2	1.561	1.547	1.527
V_3	0.862	0.835	0.828
V_4	-	2.549	-
V_5	-	1.385	-
V_6	-	1.022	-
V_7	1.965	1.968	1.961
V_8	1.083	1.074	1.088
V_9	-	-	2.053
V_{10}	-	-	1.509
V_{11}	-	-	1.128
V_{12}	2.448	2.429	-
V_{13}	0.9130	0.873	-
V_{14}	1.043	1.044	-

Table 8.4 Comparison of the Room Temperature Velocities (x 10^5 cm sec^{-1}) .

	Pure Bismuth	T19			T20		
		Experimental		Theoretical	Experimental		Theoretical
		C_{ij}	δC_{ij}	ΔC_{ij}	C_{ij}	δC_{ij}	ΔC_{ij}
C_{11}	63.4 ± 0.4	62.7	-0.7 ± 0.8	-0.35	61.4	-2.0 ± 0.8	-1.55
C_{12}	24.5 ± 0.3	25.1	+0.6 ± 0.6	+0.35	25.5	+1.0 ± 0.6	+1.55
C_{13}	24.9 ± 0.4	24.6	-0.3 ± 0.8	0.0	24.3	-0.6 ± 0.8	0.0
C_{14}	7.28± 0.1	7.28	0.0 ± 0.2	+0.13	7.42	+0.14± 0.2	+0.57
C_{33}	37.9 ± 0.3	37.9	0.0 ± 0.6	-0.0	37.7	-0.2 ± 0.6	0.0
C_{44}	11.5 ± 0.15	11.3	-0.2 ± 0.3	-0.09	11.6	+0.1 ± 0.3	-0.43
C_{66}	19.44± 0.4	18.80	-0.65± 0.8	-0.35	17.96	-1.5 ± 0.8	-1.55

Table 8.5: The Elastic Constants (x 10^{10} dyne cm^{-2}) at room temperature;

C_{ij} is the theoretical electronic contribution.

In view of the experimental uncertainties, it is concluded that only the elastic constants C_{11}, C_{12}, C_{66} and C_{33} are observed to vary in the manner predicted by the Keyes model. The changes in the elastic constants C_{13}, C_{14} and C_{44} have not been verified experimentally. Since, to obtain an electron concentration of 10^{20} cm^{-3}, it has been necessary to introduce 0.4 at.% tellurium into the bismuth lattice, some of the variation of the elastic behaviour could presumably be due to the presence of impurity atoms The changes in C_{11} and C_{12} are 3 - 5%, which is barely an order of magnitude larger than the atomic fraction of impurity. In comparison, the addition of 0 4 at % antimony causes a 0.5% change in C_{11} (based upon extrapolation of the data in Chapter 7) while C_{12} and C_{33} change to a negligible extent. On this basis one may plausibly argue that the electrons are the dominant mechanism in the change of the elastic constants found here for tellurium doped bismuth. The only other reported work concerned with the effects of impurities on the elastic properties of bismuth is the ultrasonic study of Gopinathan and Padmini (1974b) on polycrystalline bismuth doped with tin, in which they observe a most pronounced dependence of the elastic moduli with composition. However, since these workers have made the same fundamental errors as in their paper on the bismuth-antimony alloys (for a discussion of this point see Section 7 5), a comparison with their work will be omitted here.

8 3 The Compressibilities and Young's Modulus

A knowledge of the complete set of elastic tensor coefficients permits the determination of a material's response to any applied stress system. Particularly important in relating theoretically the interatomic binding forces and elasticity are the bulk modulus, the volume compressibility and the linear compressibilities. The volume compressibility (its inverse is the bulk modulus) is the measure of dilation under hydrostatic pressure and for rhombohedral crystals is given by

$$\beta_v = 2(S_{11} + S_{12}) + 2S_{13} + S_{33} \qquad (8.1)$$

where S_{ij}'s are the compliances, (the transformation for which has been given in 7.4). The linear compressibility of a crystal is the relative decrease in length of a line when subjected to unit hydrostatic pressure, it has two components, one parallel to the trigonal axis,

$$\beta_z = 2S_{13} + S_{33} \qquad (8.2)$$

and the other normal to the trigonal direction

$$\beta_{xy} = (S_{11} + S_{12}) + S_{13} \qquad (8.3)$$

Theoretically, since the electronic contribution to the elastic compliances is such that

$$\delta S_{11} = -\delta S_{12}\ , \qquad \delta S_{13} = 0\ , \qquad \delta S_{33} = 0 \qquad (8\ 4)$$

there should be no electronic effect on the compressibilities. This is the same result found by workers on silicon and germanium in which only very small changes in the bulk modulus were observed Table 8 6 shows that the compressibilities measured here decrease slightly with the addition of tellurium, but are within the limits of uncertainty.

In view of the complex crystal structure of bismuth, it is interesting to consider the Young's Modulus surface change due to the electronic contribution The Young's modulus is defined as the ratio

	s_{11}	s_{12}	s_{13}	s_{14}	s_{33}	s_{44}	s_{66}
Pure Bismuth	25.6	-8.0	-11.1	-21.3	39.1	114.0	67.4
T19	26.7	-8.8	-11.6	-22.8	41.5	117.9	70.9
T20	27.9	-9.9	-11.6	-24.2	41.5	117.2	75.7

Table 8.6(a) The Elastic Compliance Constants in units of 10^{-13} cm^2 dyn^{-1} .

	Linear		Volume
	β_z	β_{xy}	β_v
Pure Bismuth	16.9 ± 1.5	6.58 ± 0.7	52.2 ± 2.5
T19	18.2	6.28	54.0
T20	18.3	6.40	54.3

Table 8.6(b) The Linear and Volume Compressibilities in units of 10^{-13} cm^2 dyn .

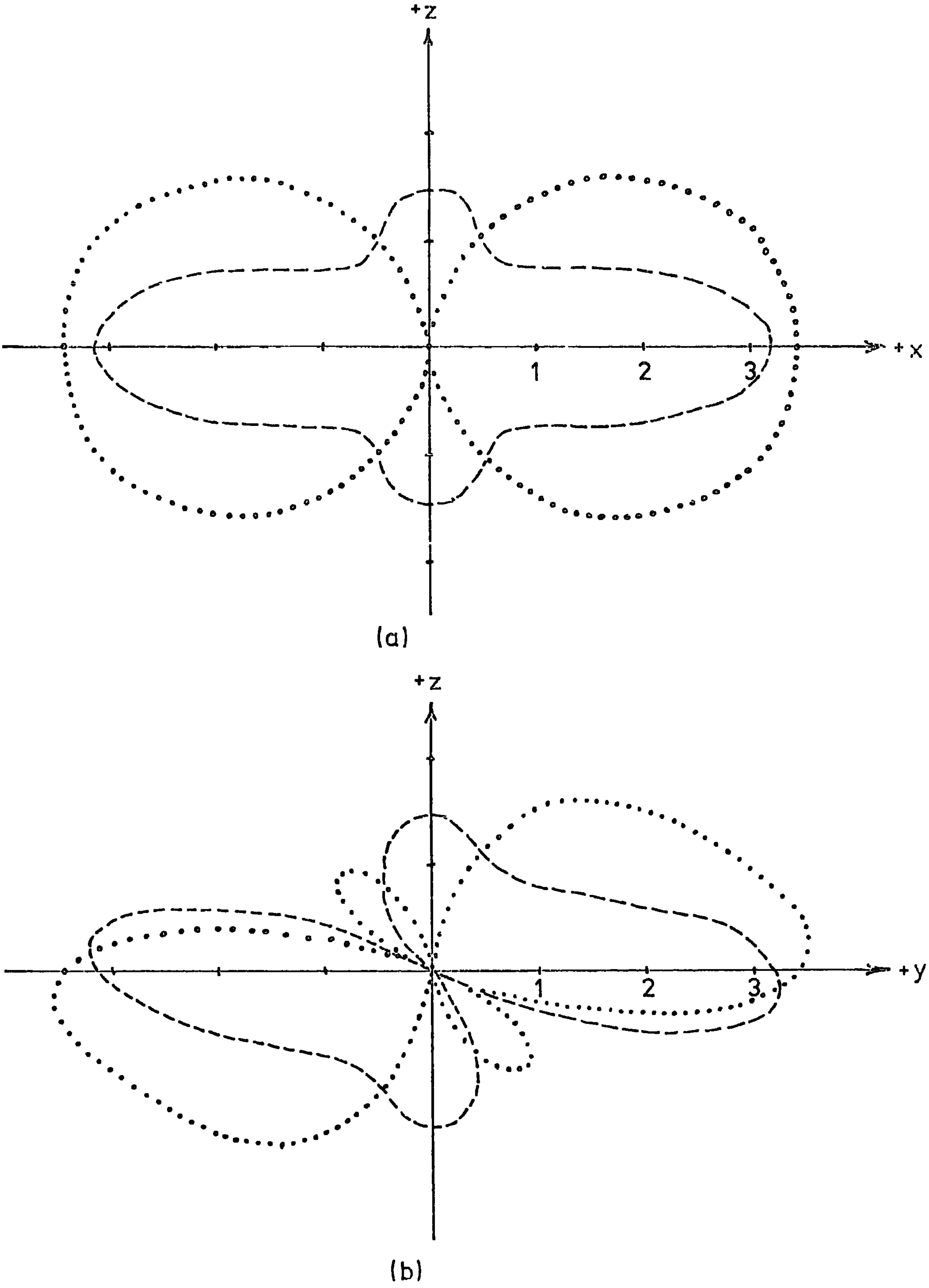

(a)

(b)

Figure 8.1 Cross sections of the change in Youngs modulus surface (a) xz plane, (b) yz plane ($\times 10^{11}$ dyne cm^{-2})
----- experimental T20 · · · theoretical N=10^{20} cm^{-3}

of the longitudinal stress to the longitudinal strain, its orientation dependence for rhombohedral crystals is given by

$$YM = (S'_{11})^{-1} = \left[(1-\ell_3^{\,2})^2 S_{11} + \ell_3^{\,4} S_{33} + \ell_3^{\,2}(1-\ell_3^{\,2})(2S_{13}+S_{44}) + 2\ell_2\ell_3(3\ell_1^{\,2}-\ell_2^{\,2})S_{14}\right]^{-1} \qquad (8.5)$$

where (ℓ_1,ℓ_2,ℓ_3) is the unit vector in the direction of the longitudinal stress. The orientation dependence of Young's modulus in pure bismuth was first reported by Gunton and Saunders (1972) Figure 8.1 presents the change in Young's modulus in the XY and XZ crystallographic planes.

8.4 The Temperature Dependence

The temperature dependence of five of the velocities of propagation were measured (V_1, V_2, V_3, V_7 and V_8), sufficient to obtain the temperature dependence of all the elastic constants bar C_{13}, the normalised ultrasonic velocities V(T)/V(290 K) are presented in Figures 8 2-8.6. An interesting finding is that, as for the bismuth-antimony alloys, there is no measurable deviation in the temperature variation of the ultrasonic velocities from that of pure bismuth. The least mean-squares program was used to compute the elastic constants at a series of temperatures down to 4 2 K, the temperature dependences obtained are given in Figure 8.7. As demonstrated by the normalised velocity curves, the temperature variation of most of the elastic constants appears to be virtually independent of the tellurium concentration However, for the tellurium doped samples the elastic constant C_{12} (which is temperature independent for pure bismuth) increased slightly as the

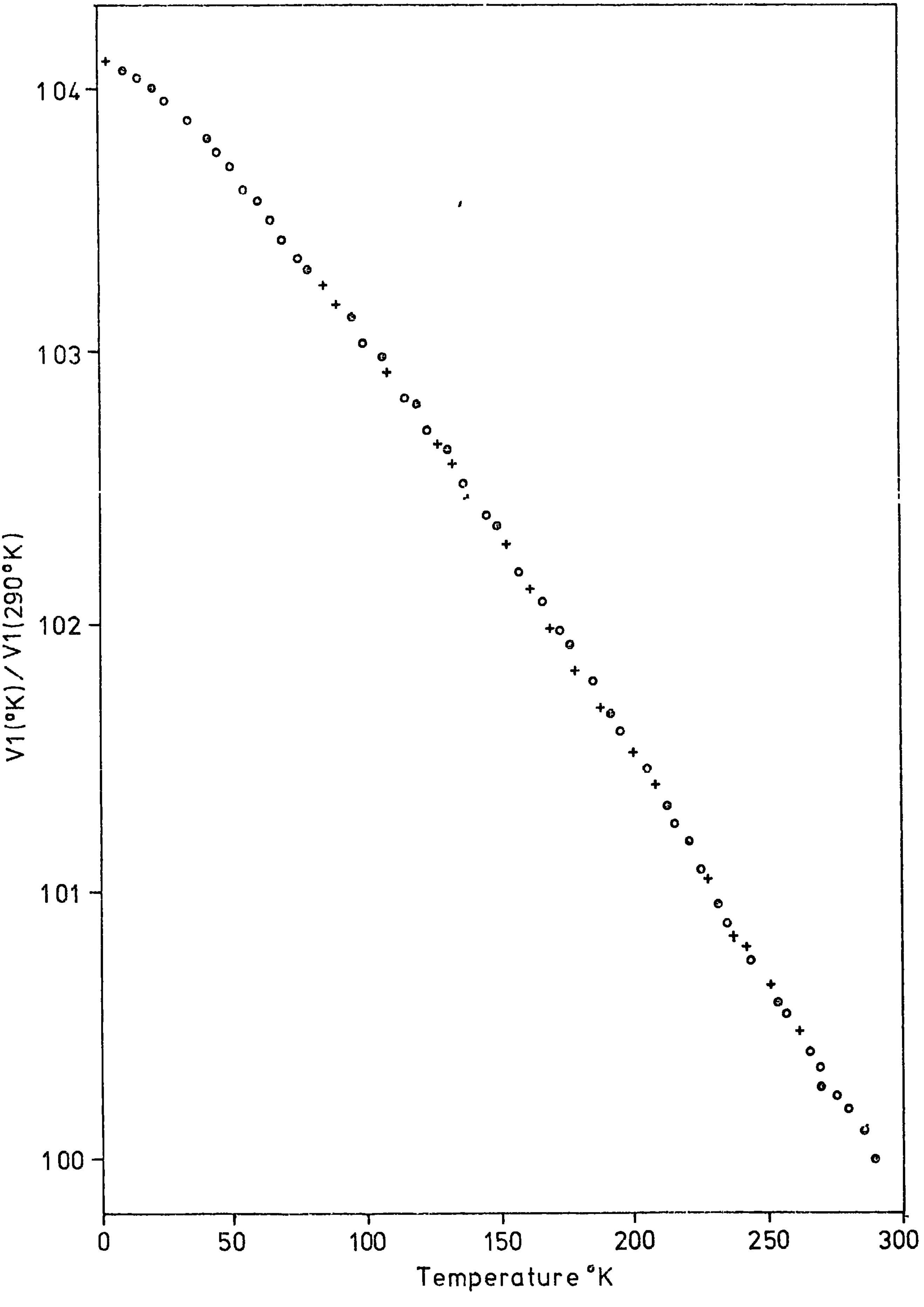

Figure 8 2 Normalised temperature dependence of V1 ◦ pure bismuth, + T19, ◦ T20

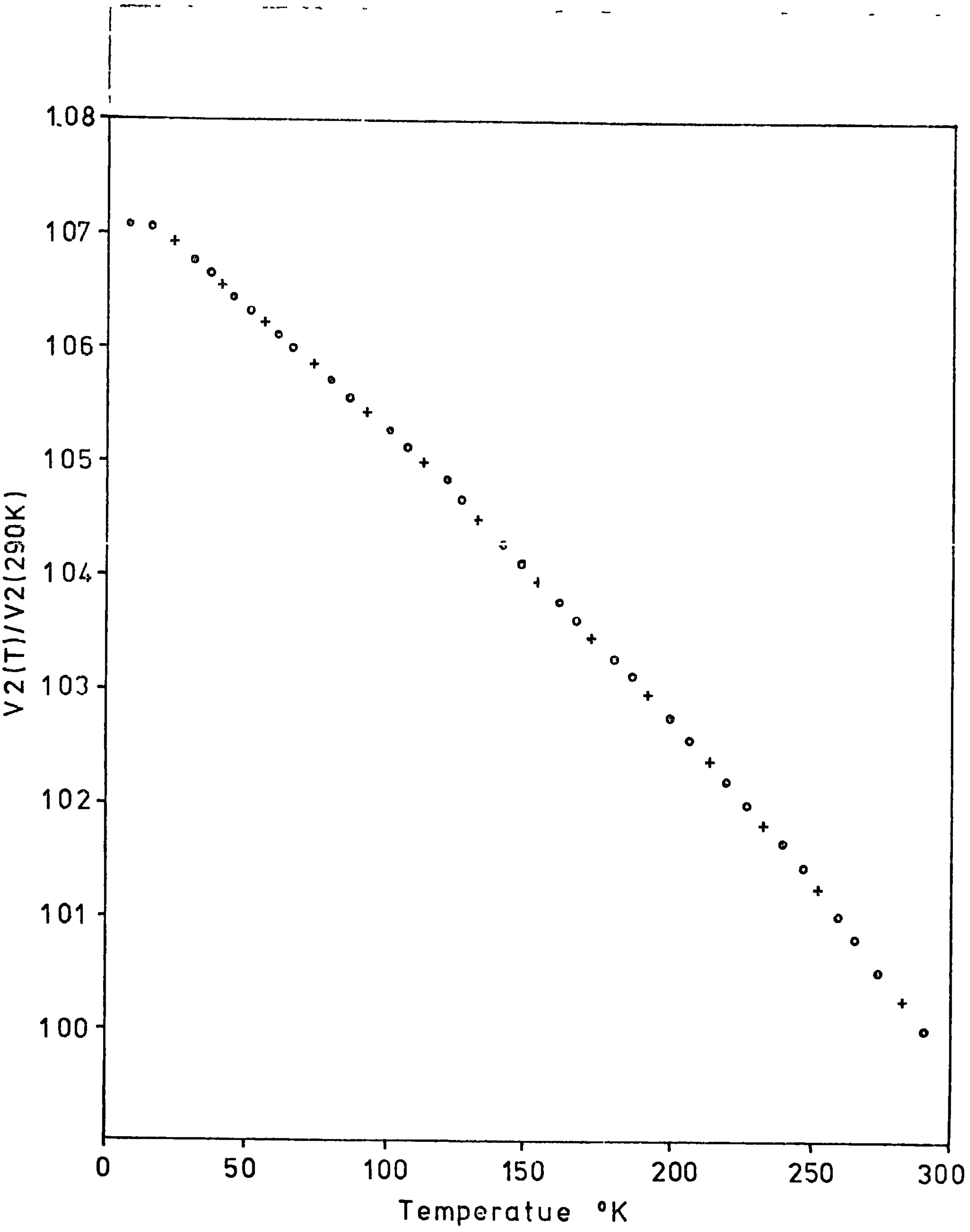

Figure 83 Normalised temperature dependence of V2

⊙ pure bismuth, + T19, ∘ T20

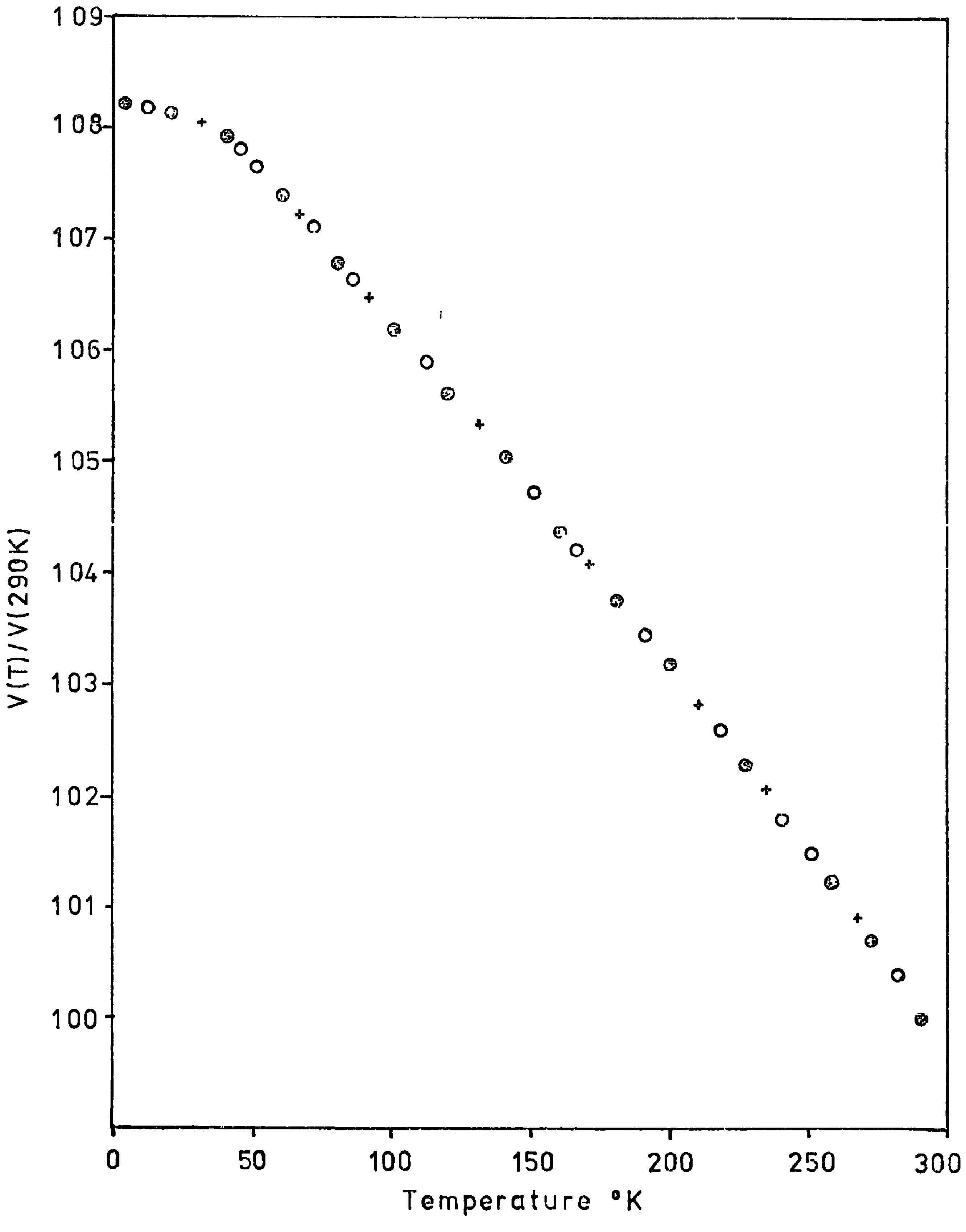

Figure 8 4 Normalised temperature dependence of V3

⊛ pure bismuth, + T19, o T20

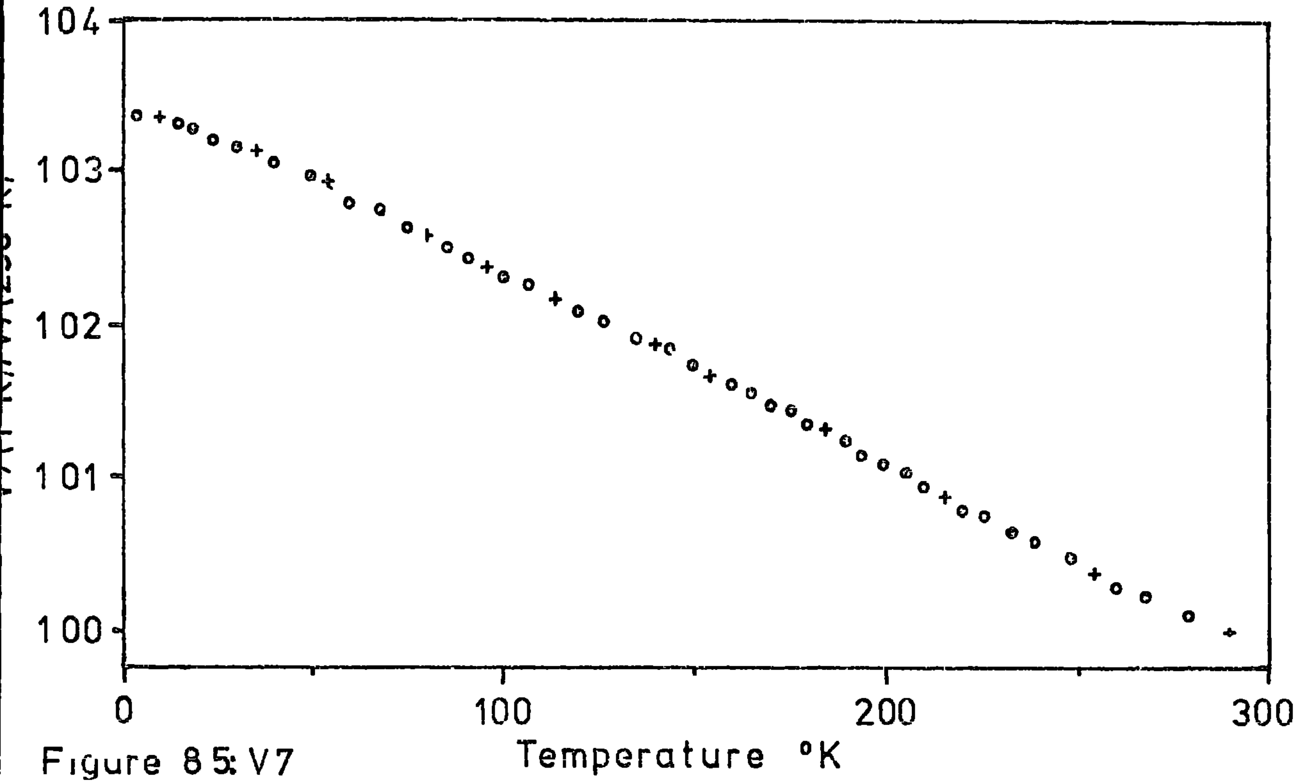

Figure 85: V7

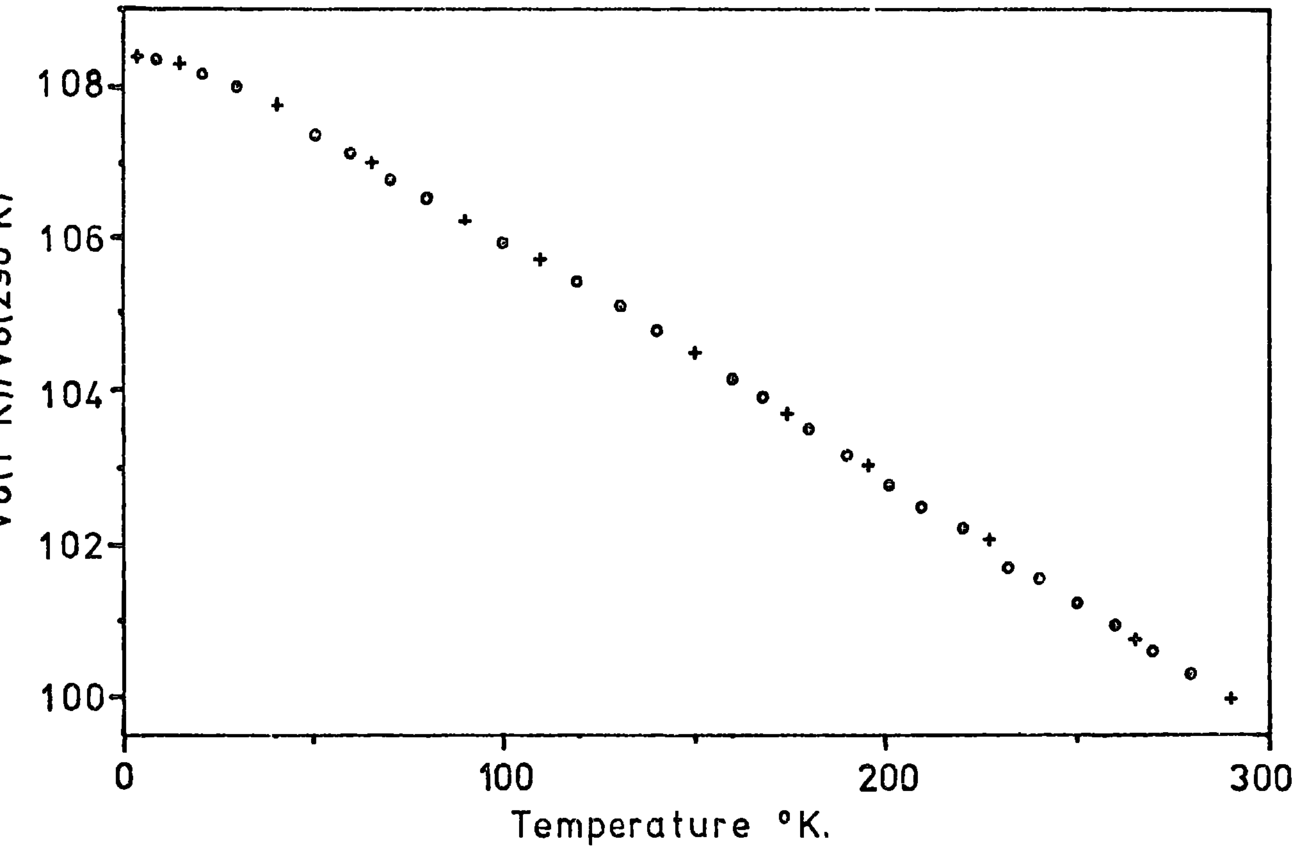

Figure 86 Normalised temperature dependence of V8

∘ pure bismuth, + T19; ∘ T20

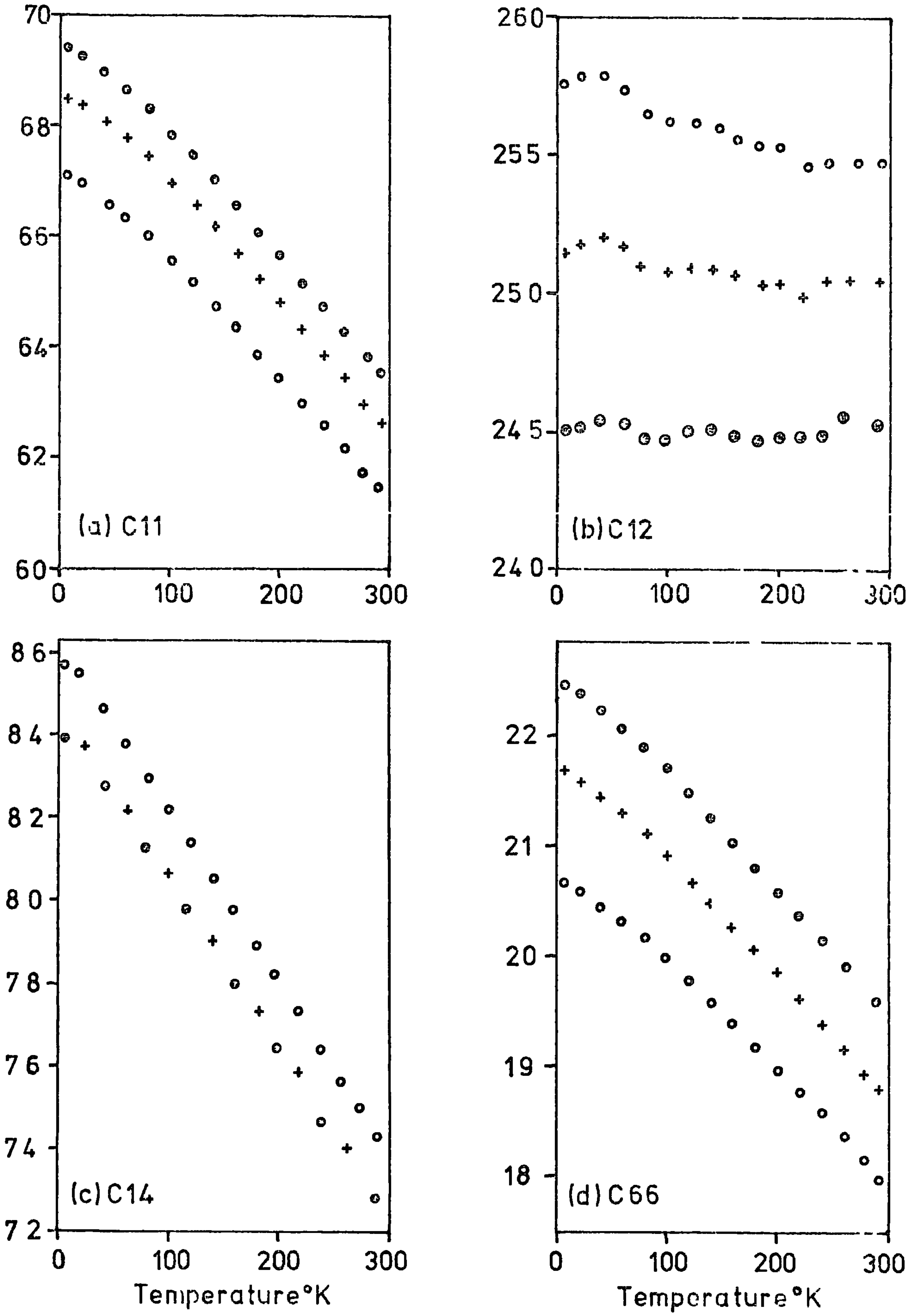

Figure 8.7 The temperature dependence of the elastic constants C11, C12, C14, C66, C33, C44 ($\times 10^{10}$ dyne cm^{-2})
⊙⊙⊙⊙⊙ pure bismuth, +++++ T19, ○○○○○ T 20

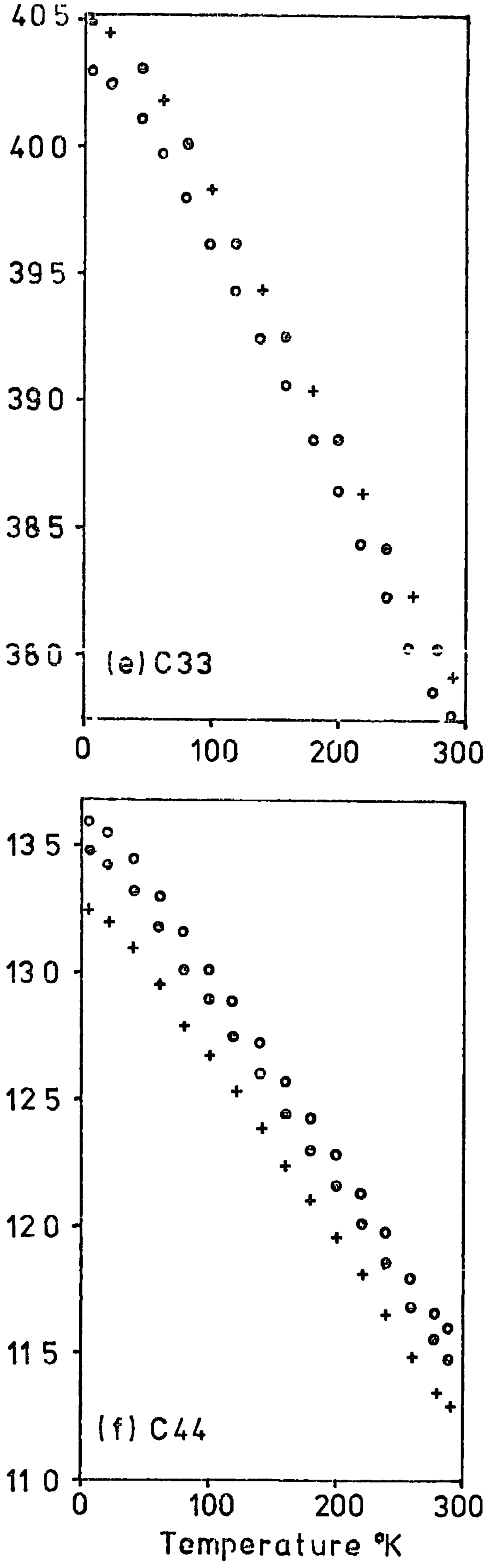

Figure 87 (cont)

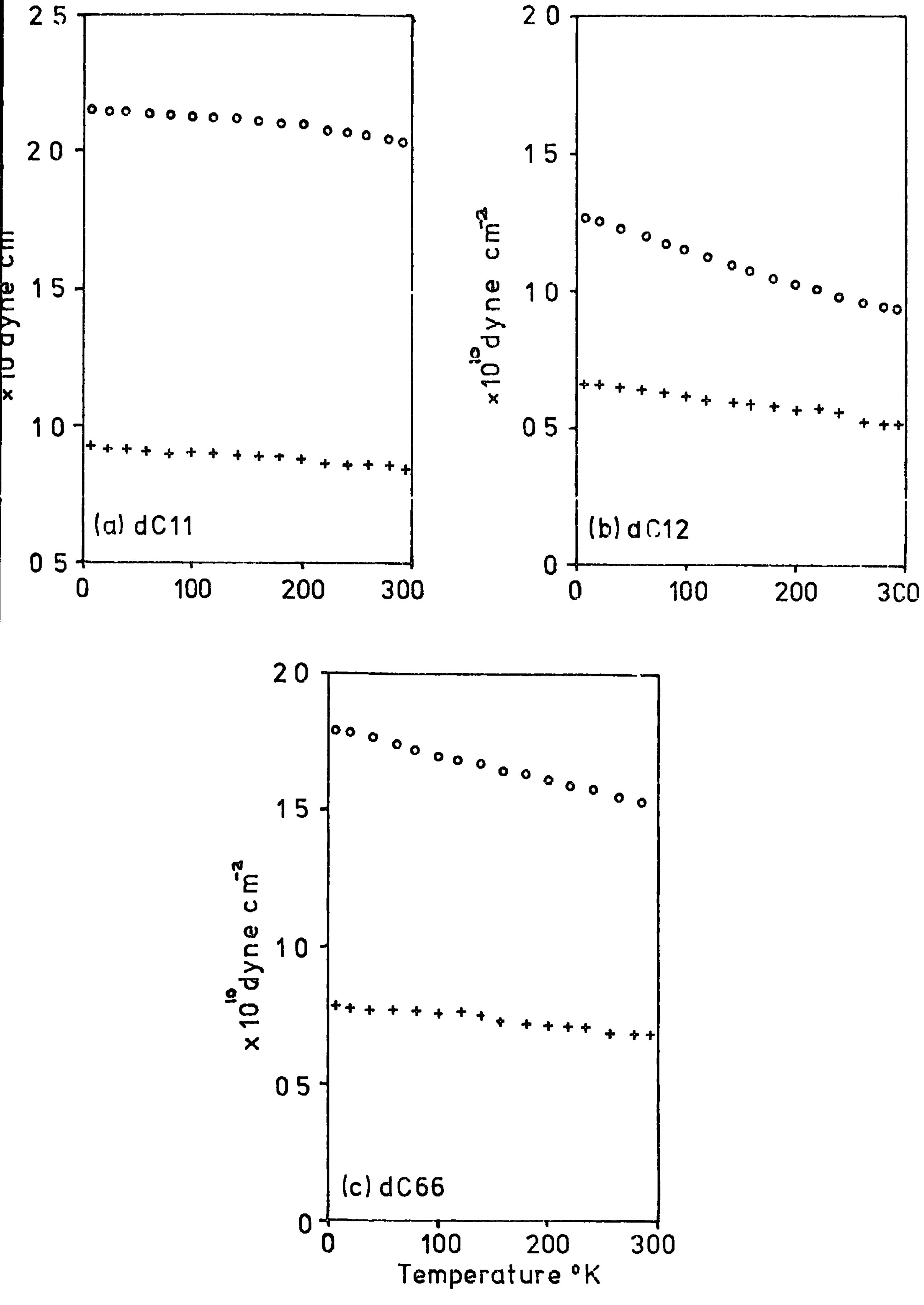

Figure 8 8 The temperature dependence of the change in the elastic constants C11, C12 and C66 from that of pure bismuth

+++++ T19, ooooo T20

temperature is decreased. The corresponding changes in the elastic constants C_{11}, C_{12}, C_{66}, C_{14} and C_{44} are given in Figure 8.8, the changes are larger at lower temperatures and take the approximate form

$$\frac{\delta C(T\ K)}{\delta C(290\ K)} \simeq \frac{C(T\ K)}{C(290\ K)}$$

for all the constants, apart from C_{12}

8.5 The Temperature Variation of the Band Edge Effective Mass and of the Deformation Potentials

Figure 6.4 shows that the theoretical electronic contribution previously calculated from the Keyes model increases slightly with temperature (30% from 4 2 K to room temperature for a carrier concentration of 10^{20} cm^{-3}). This is in contradiction to the present finding of a decreasing electronic contribution with temperature. When comparing the experimental results with the calculations of chapter 6, it must be remembered that the temperature variation of the band edge effective masses were only approximated from the data of Vecchi and Dresselhaus (1974) and, although their results are of high precision at lower temperatures (below 100 K), the extension of these parameters to higher temperatures is only based on two data points taken at 200 K and 280 K Moreover, the Fermi level of pure bismuth calculated from these parameters (see Figure 6 1) exhibits a rather strange dependence, remaining constant in the range 0 - 180 K and then decreasing rapidly to reach the conduction band edge at approximately room temperature, this implies that the material must become semiconducting at higher temperatures. Furthermore, the assumption that the deformation potentials are temperature independent is not necessarily valid. Indeed, the work of Balslev (1966) has shown that the deformation potentials of silicon at 295 K differ slightly from those obtained at ~80 K (E_u = 9.2 eV at 295 K, 8.6 eV at 80 K). In view of the large temperature variation of all the other parameters, both electronic and elastic, it would not be surprising to find a large variation of the deformation potentials of bismuth. Unfortunately, there is no independent way of separating the temperature dependence of the deformation potentials from that of the effective masses. Two distinct approaches will be made here to resolve the temperature variation of the elastic constants. Firstly, by assuming the deformation potentials to be temperature independent, the temperature dependence of the effective masses will be derived and contrasted with those approximated from the results of Vecchi and Dresselhaus (1974). Secondly, the effective masses of Vecchi and Dresselhaus will be assumed accurate and the temperature dependence of the deformation potentials will be deduced.

Before proceeding, it is important to realise that the form of the electronic contribution cannot modify all the elastic constants in such a way as to be temperature independent. Since

$$|\Delta c_{11}| = |\Delta c_{12}| = |\Delta c_{66}| \tag{8.6}$$

and

$$\frac{c_{11}(T\ K)}{c_{11}(290\ K)} \neq \frac{c_{12}(T\ K)}{c_{12}(290\ K)} \neq \frac{c_{66}(T\ K)}{c_{66}(290\ K)} \tag{8.7}$$

there must be some variation in the temperature dependence of the elastic constants from that of pure bismuth, however, it might be so small as to be experimentally indistinguishable.

Since the temperature variation of C_{11} was observed to be independent of the electron concentration, the temperature dependence of the band edge effective mass was deduced making the following assumptions· (i) the deformation potentials remain constant, (ii) the band edge effective mass, the Fermi level and the calculated electronic contribution at 4.2 K are accurate, (iii) the temperature variation of the L point energy gap as measured by Vecchi and Dresselhaus is accurate. The electronic contribution calculated at 4.2 K was then extrapolated over the entire temperature range to give a temperature dependence of C_{11} consistent with the experimental measurements. From a combination of the equations which define the carrier concentration (see equation 5.24) and the electronic contributions (see equation 5.45), the Fermi level and the effective masses were calculated over the entire range of temperature. The Fermi level was deduced from

$$F_e = -9(L_{11} - L_{22})^2 N.(24\ kT)^{-1} \frac{\left[F_{-\frac{1}{2}}(\eta) + \frac{6kT}{E_g} F_{\frac{1}{2}}(\eta)\right]}{\left[F_{\frac{1}{2}}(\eta) + \frac{2kT}{E_g} F_{\frac{1}{2}}(\eta)\right]} \qquad (8.8)$$

and the effective mass from

$$m^* = \pi^{\frac{1}{2}} N/(6N_c \left[F_{\frac{1}{2}}(\eta) + \frac{2kT}{E_g} F_{\frac{1}{2}}(\eta)\right]) \qquad (8.9)$$

The variation of the Fermi level and the band edge effective mass for a carrier population of 10^{20} cm^{-3} calculated from the temperature dependence of C_{11} is given in Figure 8.9, the Fermi level increases slightly with temperature, as does the effective mass. The effective mass deduced from these computations was then used to recompute the electronic contributions to the elastic constants both as a function of temperature and electron concentration, the electronic contributions obtained at 4.2 K and room temperature are presented in

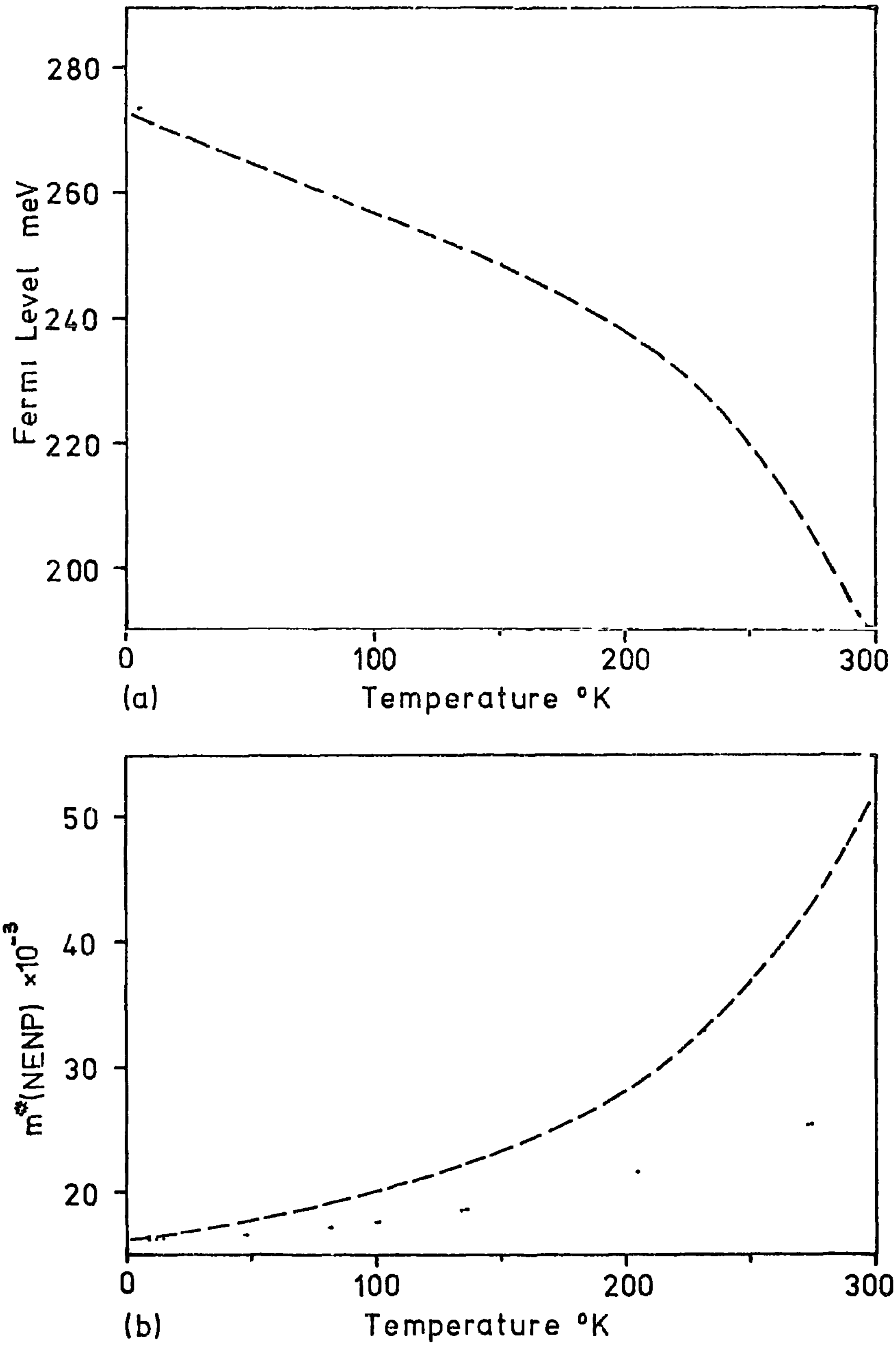

Figure 8.9 Temperature variation of the band edge density of states effective mass and of the Fermi level for $N=10^{20}cm^{-3}$

·· - Derived assuming temperature independent deformation potentials

-----Calculated from the data of Vecchi and Dresselhaus (1974)

Elastic Constant	Donor cm^{-3} Concentration	x 10^{10} dyne cm^{-2}				$\sqrt{\frac{C_{ij}(4.2\ K)}{C_{ij}(290\ K)}}$	$\sqrt{\frac{C_{ij}(4.2\ K)}{C_{ij}(290\ K)}}$
		ΔC_{ij}		C_{ij}			
		4.2 K	290 K	4.2 K	290 K		
C_{11}	0	0	0	69.25	63.39	1.092	1.045
	1 x 10^{19}	-0.296	-0.241	68.95	63.15	1.092	1.045
	5 x 10^{19}	-0.777	-0.711	68.47	62.67	1.092	1.045
	1 x 10^{20}	-1.177	-1.085	68.07	62.31	1.092	1.045
C_{14}	0	0	0	8.40	7.28	1.154	1.074
	1 x 10^{19}	+0.109	+0.089	8.51	7.37	1.155	1.075
	5 x 10^{19}	+0.288	+0.264	8.69	7.54	1.152	1.073
	1 x 10^{20}	+0.436	+0.402	8.83	7.68	1.150	1.072
C_{44}	0	0	0	13.55	11.51	1.177	1.085
	1 x 10^{19}	-0.081	-0.066	13.46	11.44	1.177	1.085
	5 x 10^{19}	-0.213	-0.195	13.34	11.31	1.179	1.086
	1 x 10^{20}	-0.323	-0.298	13.23	11.21	1.179	1.086
C_{66}	0	0	0	19.44	22.39	1.152	1.072
	1 x 10^{19}	-0.296	-0.241	22.09	19.20	1.151	1.073
	5 x 10^{19}	-0.777	-0.711	21.61	18.73	1.154	1.074
	1 x 10^{20}	-1.177	-1.085	21.21	13.36	1.155	1.074

Table 8.7: The theoretical temperature dependence of the elastic constants calculated using the derived temperature variation of the band edge effective mass (see Figure 8.7)

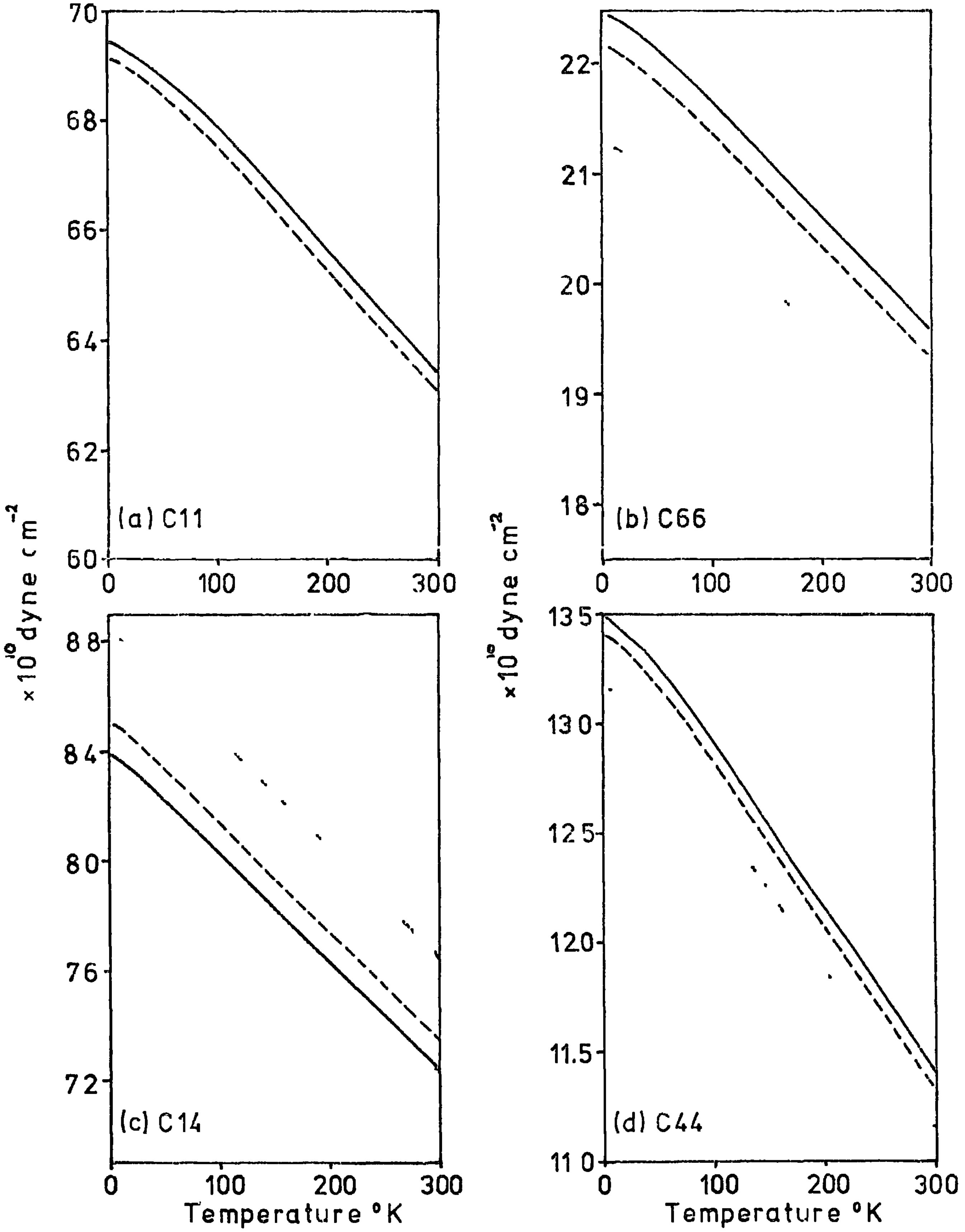

Figure 8.10. Theoretical temperature dependence of the elastic constants – calculated using the derived temperature variation of the effective mass

—— pure bismuth, ----- $N=10^{19}$ cm^{-3}, ·· ··· · $N=10^{20}$ cm^{-3}

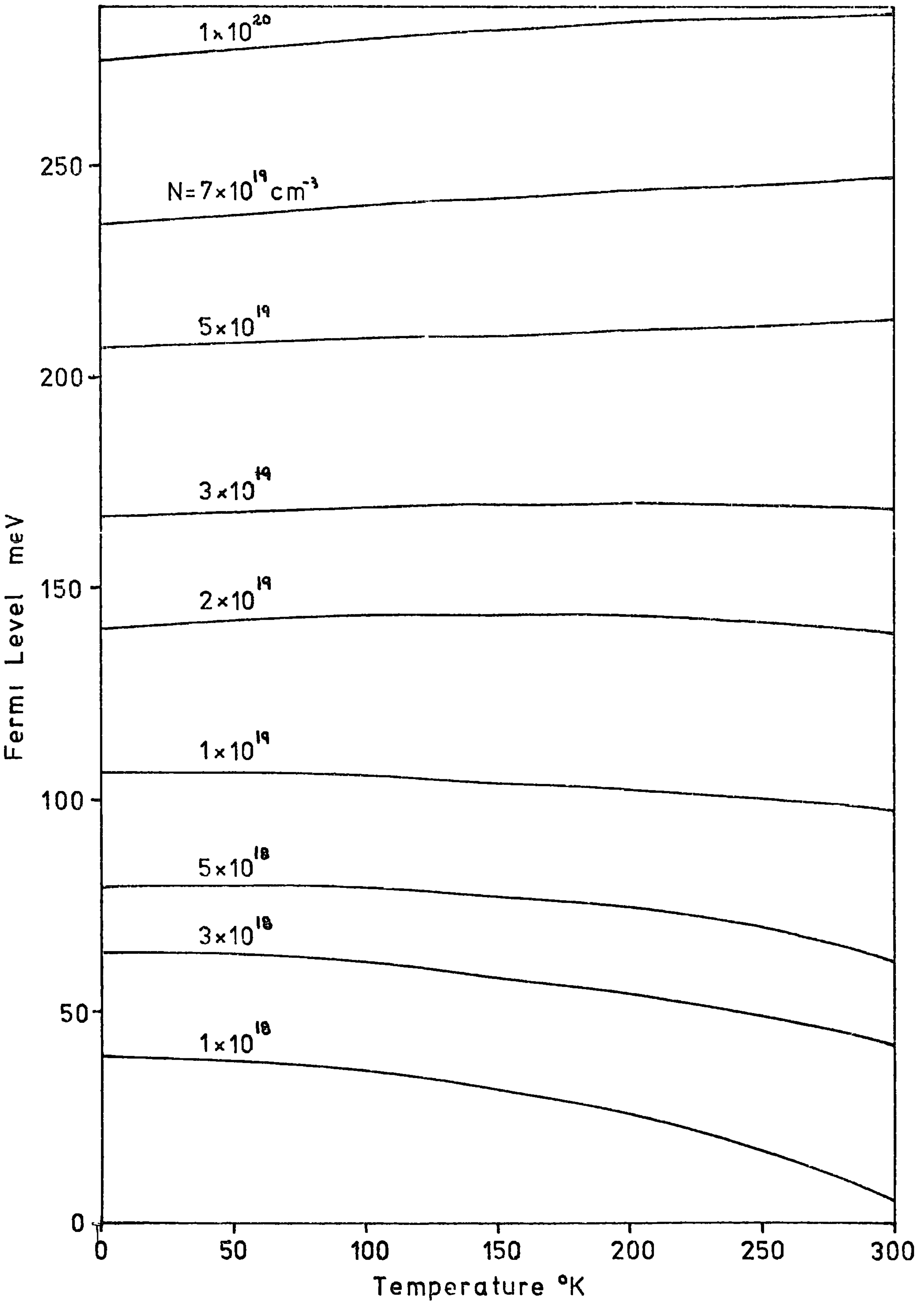

Figure 8.11 Temperature variation of the Fermi level for various electron concentrations – calculated using the derived effective mass (see Figure 8.9b)

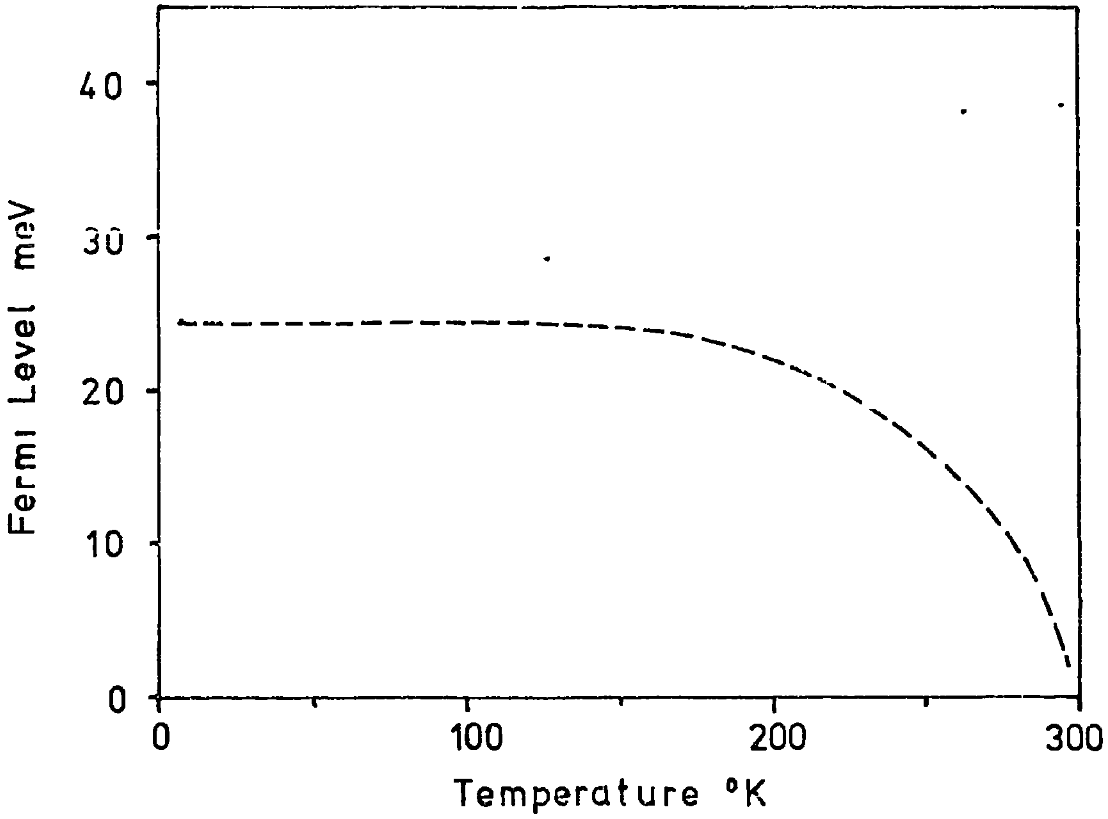

Figure 8.12 The temperature dependence of the electron Fermi level in undoped bismuth

· Calculated using the derived temperature variation of the effective mass (see figure 8.9 b)

---- Calculated from the data of Vecchi and Dresselhaus (1974)

Table 8.7. The interesting finding is that the temperature dependence of all the elastic constants are, within the limits of experimental uncertainty, effectively independent of the electron density. Thus, although there is a slight deviation in the temperature dependence of the elastic constants from that of pure bismuth, it is experimentally unobservable. Figure 8.10 compares the theoretical temperature dependence with the experimentally measured temperature dependence of the elastic constants C_{11}, C_{66}, C_{44} and C_{14}.

Thus, by fitting the electronic parameters to the temperature dependence of the elastic constants, the behaviour of the Fermi level and the band edge effective masses have been deduced The variation of the Fermi level for various electron concentrations is given in Figure 8.11, above carrier densities of 2×10^{19} cm^{-3} the Fermi level increases slightly with temperature, whereas for concentrations of less than 2×10^{19} cm^{-3} it decreases with temperature. However, if the effects of thermal excitation are included, the Fermi level rises slightly with temperature for all donor concentrations (at 290 K the carrier density of pure bismuth is 2.3×10^{18} cm^{-3}). Figure 8.12 presents the Fermi level of pure bismuth as a function of temperature (the carrier concentration is taken from Michenand and Issi, 1972). It can be seen that the Fermi level rises from 25 meV at 4 2 K to 36 meV at 290 K, in contrast to the decreasing Fermi level calculated from the data of Vecchi and Dresselhaus.

The temperature dependence of the band edge effective mass obtained here deviates rather strongly, especially at higher temperatures, from the results of Vecchi and Dresselhaus, thus it was felt that the observed temperature dependence of the elastic constants was more likely to be a consequence of a variation in the deformation potentials.

Using the temperature dependence of the band edge effective mass of Vecchi and Dresselhaus, the temperature dependence of the deformation potentials $(L_{11} - L_{22})$ and L_{23} were calculated to fit the observed variation in the elastic constants The following assumptions were made (i) the band edge effective mass, the deformation potentials, the Fermi level and the calculated electronic contribution at 4.2 K were accurate, (ii) the temperature variation of the band edge effective mass and of the L point energy gap were those derived from Vecchi and Dresselhaus (1974). Figure 8.13 shows the temperature dependence of the deformation potentials $(L_{11} - L_{22})$ and L_{23} calculated from the temperature variation of the elastic constants of T20, the potentials change by approximately 20% from 4 2 K to 300 K

8 6 Summary

In this chapter it has been shown that the addition of tellurium to bismuth causes changes in the elastic constants which are consistent with the electronic contributions to the elastic constants predicted by the theoretical extension of the Keyes model The temperature variation of the elastic moduli has been shown to be effectively independent of the free electron density, in marked contrast to that obtained by other workers on silicon and germanium (Hall 1967), in which the electron contribution is 2 - 4 times larger at 4 2 K than at 300 K. Indeed, the temperature variation of the electronic contribution to the elastic constants of silicon and germanium can be so large at lower temperatures that the elastic constants can increase (rather than decrease) with temperature. The results obtained here for bismuth doped with tellurium and for the bismuth-antimony alloys indicate that it is not possible to control the temperature dependence of the elastic constants

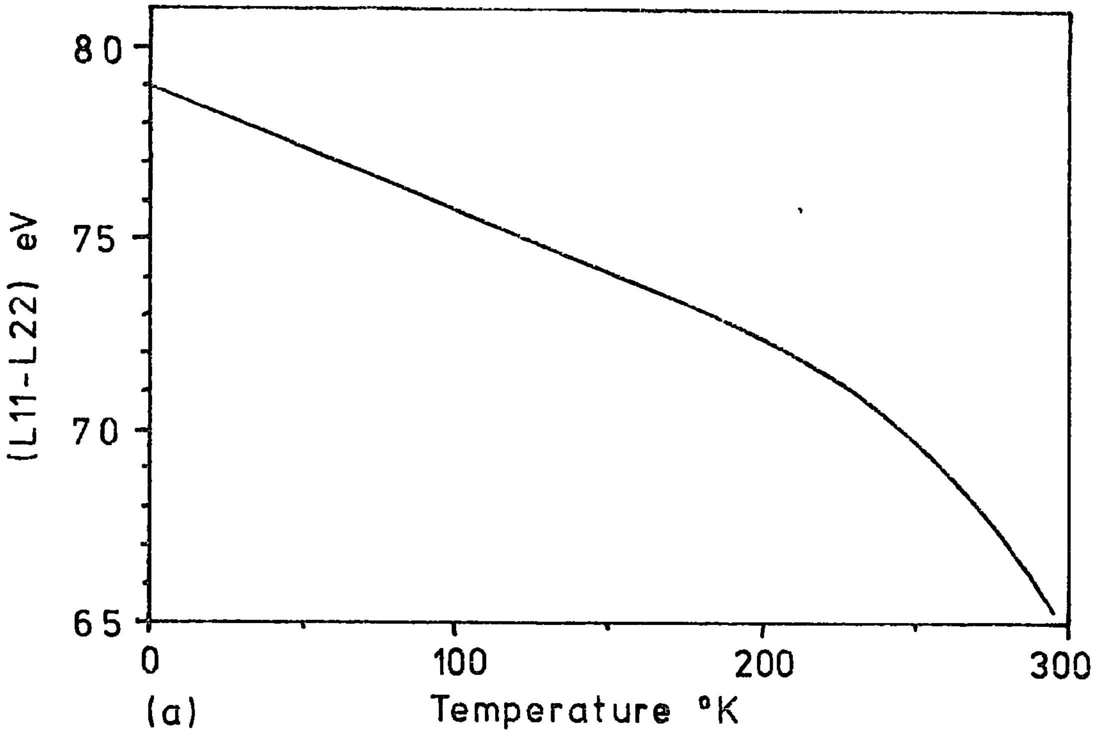

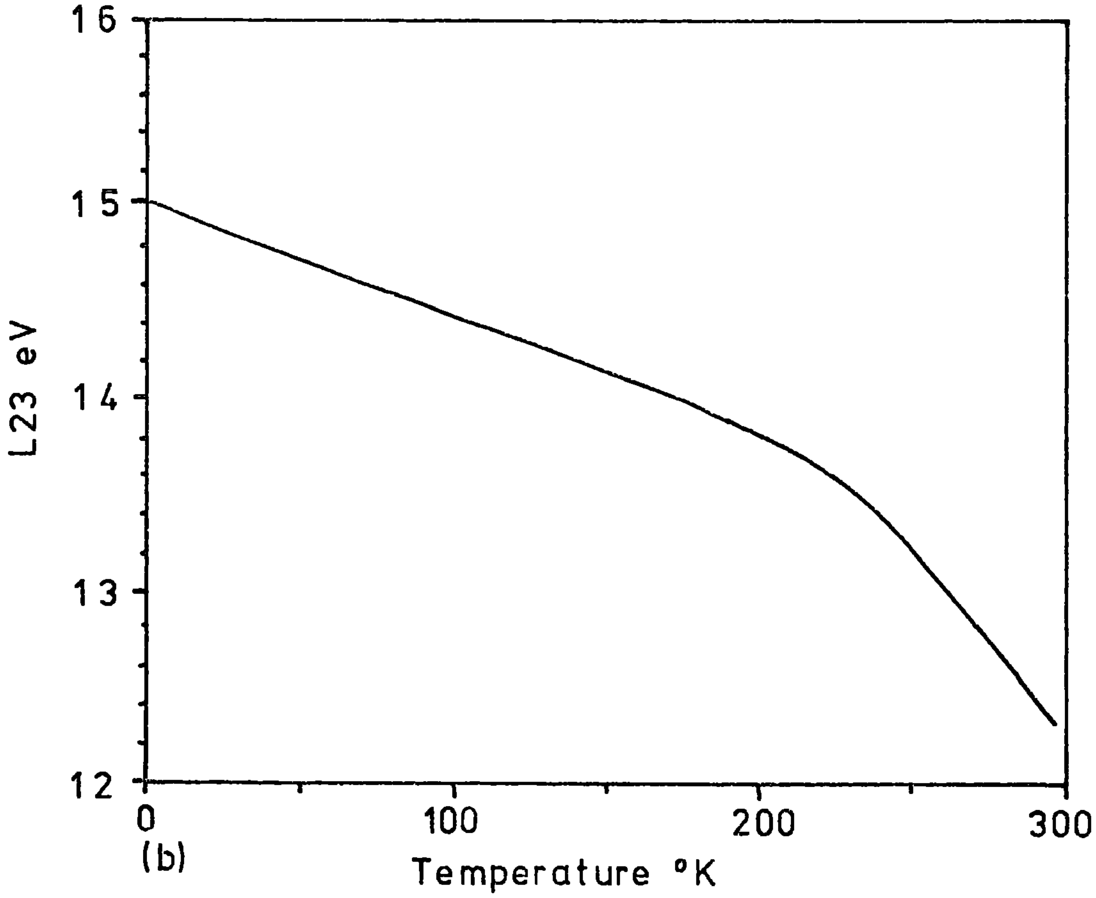

Figure 8 13 The temperature variation of the deformation potentials – calculated using the effective mass data of Vecchi and Dresselhaus (1974)

Thus, even though the observed change in the elastic constants may in part be due to the impurity atoms, the electronic contributions to the elastic constants of bismuth must have a temperature dependence which is, in effect, independent of the carrier concentration. Furthermore, it has been demonstrated that, by a suitable adjustment of the temperature variation of either the deformation potentials or of the band edge effective mass, the theoretical electronic contribution can predict the observed temperature dependence to a high precision; however, it is felt that the observations are best explained by a temperature variation of the deformation potentials.

APPENDIX 1

CALCULATION OF THE FREE ENERGY

In Fermi Dirac statistics the electrons are assumed to occupy N levels with energies ε_1, ε_2 .... ε_N, each of these levels having g_1, g_2 . g_N states. The states in each energy level are assumed to contain n_j electrons (a maximum of one electron per state is allowed), consequently n_j states are full and $g_j - n_j$ states are empty. The total electron concentration is ,

$$n = \sum_j n_j \qquad \text{(A1.1)}$$

and the total energy of all the electrons is

$$U = \sum_j n_j \varepsilon_j \qquad \text{(A1.2)}$$

Since the electrons are indistinguishable, they cannot be identified by number and therefore an exchange of state can only be considered if an occupied state is exchanged with an unoccupied state. Therefore the ways or permuting the thermodynamic probability for one energy level ε_j is given by

$$W_j = \frac{g_j!}{n_j!\,(g_j! - n_j!)} \qquad \text{(A1.3)}$$

The total thermodynamic probability is

$$W = \prod_j W_j = \prod_j \frac{g_j!}{n_j!\,(g_j! - n_j!)} \qquad \text{(A1.4)}$$

The electronic free energy is related to the total energy U and the entropy S by the function

$$F = U - TS \qquad \text{(A1.5)}$$

The entropy is given by ,

$$S = k\ln W_{MAX} \tag{A1.6}$$

The thermodynamic probability will be a maximum when dW/dnj = 0. However W is a difficult function to differentiate and it is more convenient to differenciate with respect to ℓn W. Using Sterling's approximations ,

$$\ln n_j! = n_j \ln n_j - n_j$$

$$\frac{d\ln n_j!}{dn_j} = \ln n_j \tag{A1.7}$$

it can be shown that

$$\ln W = \sum_j \left[g_j \ln g_j - n_j \ln n_j - (g_j - n_j) \ln(g_j - n_j) \right] \tag{A1.8}$$

$$= \sum_j \left[n_j(\ln(g_j - n_h) - \ln n_j) + g_j\left[\ln g_j - \ln(g_j - n_j)\right]\right] \tag{A1.9}$$

Using the method of the Lagrange undetermined multipliers the summation Z is constructed ,

$$Z = \ln W + a(n - \sum_j n_j) + b \left[U - \sum_j n_j \varepsilon_j \right] \tag{A1.10}$$

which when differentiated with respect to n_j must obviously be equal to zero

$$\frac{dZ}{dn_j} = 0 = -\ln n_j + \ln(g_j - n_j) - a - \beta\varepsilon_j \tag{A1 11}$$

The solution to the above equation is found to be

$$n_j = g_j/(1 + \exp(a + \beta\varepsilon_j)) \qquad (A1.12)$$

which is easily recognised to be the Fermi-Dirac probability function where

$$a = -\xi/kT \quad \text{and} \quad \beta = \frac{1}{kT} \qquad (A1.13)$$

Substitution of equations A1(11,12 and 13) into A1.19 yields

$$\ell n\, W_{MAX} = -\sum_j n_j / kT + \sum_j n_j \frac{\varepsilon_j}{kT}$$

$$+ \sum_j g_j \left[\ell n g_j - \ell n \left[g_j \left(1 - \frac{1}{1 + \exp\left(\frac{E - \xi}{kT}\right)}\right)\right]\right]$$

therefore

$$\ell n\, W_{MAX} = -\sum_j n_j\, \xi/_{kT} + \sum_j n_j \frac{\varepsilon_j}{kT} - \sum_j g_j\, \ell n \left[1 - f(E,\xi)\right] \qquad (A1.14)$$

where

$$f(E,\xi) = \left[1 + \exp \frac{E - \xi}{kT}\right]^{-1} \qquad (A1.15)$$

The electronic free energy therefore takes the form

$$F = \sum_j n_j\, \xi + \sum_j kT\, g_j\, \ell n \left[1 - f(E, \xi)\right] \qquad (A1.16)$$

g_j is essentially the density of states $N^{(i)}$ (E) and therefore the free energy of the electrons in a valley (i) is given by

$$F^{(i)} = n^{(i)}\, \xi + kT \int_0^\infty N^{(i)} (E)\, \ell n \left[1 - f(E, \xi)\right] dE \qquad (A1.17)$$

APPENDIX 2

THE COMPUTER PROGRAM FOR THE EVALUATION OF THE ELECTRONIC CONTRIBUTION TO THE ELASTIC CONSTANTS

Fermi-Dirac statistics frequently require the evaluation of integrals which have the form ,

$$F_k(\eta) = \int_0^\infty \frac{x^k \, dx}{\exp(x - \eta) + 1}$$

especially for the values $k = -\frac{1}{2}, \frac{1}{2}$ and $\frac{3}{2}$.

Macdougall and Stoner (1939) have shown how these integrals should be evaluated for all values of η. They have tabulated the numerical values of these integrals in the range $-4 < \eta < 20$ and have derived series representations for those integrals with $\eta > 20$ and $\eta < 0$. In the computer program presented here the methods of Macdougall and Stoner (1939) have been utilised.

$F_k(\eta)$ for $\eta < 0$

When $\eta \leqslant 0$ and $k > -1$

$$F_k(\eta) = \Gamma(k+1) \sum_{r=1}^{\infty} (-1)^{r-1} \exp(r\eta)/r^{k+1}$$

where $\Gamma(k+1)$ is a gamma function For $k = \frac{1}{2}, \frac{1}{2}$ and $\frac{3}{2}$ the gamma functions are

$$\Gamma(1) = \sqrt{\pi} , \quad \Gamma(2) = \sqrt{\pi}/2, \quad \Gamma(3) = 3\sqrt{\pi}/4$$

Summation of only three terms are necessary to achieve an absolute accuracy of better than 10^{-6}.

$F_k(\eta)$ for $-4 \leqslant \eta \leqslant 20$

For the range $-4 \leqslant \eta \leqslant 20$ the Fermi-Dirac integrals were obtained from the tabulated results of Macdougall and Stoner. Intermediate values were computed by interpolation.

$F_k(\eta)$ for $\eta > 20$

When $\eta \gg 1$

$$F_k(\eta) = \frac{\eta^{k+1}}{k+1} \left\{ 1 + \sum_{r=1}^{n} a_{2r} \eta^{-2r} \right\}$$

where a_{2r} is a zeta function Summation of the first six terms of the assymptotic series was necessary to achieve a precision of 10^{-6}.

Nomenclature of Computer Program

NEW	=	η	
FNNP2	=	$F_{\frac{1}{2}}(\eta)$	
FKNP32	=	$F_{\frac{3}{2}}(\eta)$	
FKNN2	=	$F_{-\frac{1}{2}}(\eta)$	
BOLTZ	=	k	Boltzman's Constant
PLANK	=	h	Plank's Constant
FASS	=	m_o	Free electron mass
NO	=	N	Electron Concentration
MASS	=	m^*(NENP)	Band Edge Effective mass
FEM	=	E_F	Fermi Level
EGG	=	E_g	L-point energy gap
BET	=		Temperature Dependence of mass
C(7)	=	C_{ij}	Elastic Constants
ARRAY(16,8)	=		Temperature variation of elastic constants
TEMP	=	T	Temperature
D11, D22, D33			Deformation Potentials
A2(I)	=	a_{2i}	Zeta Function
NEWE(I)	=	η	Macdougall and Stoner Tabulations
F32(I)	=		
F(I)	=		
WFD(1)	=		
W2FD2(I)	=		
W3FD3(I)	=		
DELCN(N)	=	ΔC_{ij}	Electronic Contribution to the Elastic Constants

```
C ELECTRONIC CONTRIBUTIONS TO THE ELASTIC CONSTANTS OF BISMUTH
C THE FERMI ENERGY IS CALCULATED BY AN ITTERATIVE PROCESS TO FIT THE
C REQUIRED CARRIER CONCENTRATION. THE 4 F.N.P. MODEL IS USED
      REAL NEW,FKNP2,FKNP32,BOLTZ,TEMP,EGG,CNO,NC,MASS,EMASS,TMASS,PIE,
     1PLANK,DEFORM,FASS
      REAL NE,F,F32,F,WFD,W2FD2,W3FD3
      INTEGER VALNO
      DIMENSION ARRAY(16,8),CN(7),C(7),DEF(7),DELCN(7),RATIO(7),PV(14),V
     1(14),VQ(14),VD(14)
      DIMENSION NE,F(241),F32(241),F(241),WFD(241),W2FD2(241),W3FD3(241)
      DIMENSION A2R(6),R2(6)
      PIE=3.142
      PLANK=6.626E-27
      BOLTZ=8.617E-05
      FASS=0.911E-27
      VALNO=5
C READ STATEMENTS
C ZETA COEFFICIENTS
      READ(5,21)(R2(I),A2R(I),I=1,6)
   21 FORMAT(I5,F20.8)
C MCDOUGALL AND STONER TABULATIONS
      READ(5,200)(ENE(I),F32(I),F(I),WFD(I),W2FD2(I),W3FD3(I),I=1,241)
  200 FORMAT(F5.1,F15.6,F20.6,3F10.0)
C DEFORMATION POTENTIALS
      READ(5,60)D11,D22,D23
   60 FORMAT(3F10.2)
C TEMPERATURE DEPENDENCE OF ELASTIC CONSTANTS
      READ(5,61)((ARRAY(MT,MK),MK=1,8),MT=1,16)
   61 FORMAT(8E10.4)
C DEFINITION OF ELASTIC CONSTANTS C11=C(1),C12=C(2),C13=C(3),C14=C(4),
C   C33=C(5),C44=C(6)
C DEFINE DEFORMATION SUMMATIONS DEF(1)-C11,DEF(2)=C12,DEF(3)=C13,DEF(4)=C14
C   DEF(5)=C33,DEF(6)=C44
      D11=D11*1.6021E-12
      D22=D22*1.6021E-12
      D23=D23*1.6021E-12
      DEF(1)=-((D11-D22)     )*3/2
      DEF(2)=+((D11-D22)**2)*3/2
      DEF(3)=0.0
      DEF(4)=-3*(D11-D22)*D23
      DEF(5)=0.0
      DEF(6)=-12*(D23**2)
      DEF(7)=DEF(1)
      WRITE(6,700)
  700 FORMAT(10X,'ELECTRONIC CONTRIBUTIONS TO THE ELASTIC CONSTANTS OF B
     1ISMUTH')
      DO 301 MA=1,5,1
      DO 300 MB=1,9,1
C ELECTRON CONCENTRATION
      NC=MB*(1.0E16*(10**MA))
  101 WRITE(6,140) NC
  140 FORMAT(10X,'ELECTRON CONCENTRATION=',E10.4)
      DO 401 LB=1,16
  120 FORMAT(1X,'TEMP',2X,'FERMI',8X,'DELCN',7X,'RATIO',8X,'V1',5X,'V2',
     15X,'V3',5X,'V4',5X,'V5',5X,'V6',5X,'V7',5X,'V8',5X,'V9',5X,'V10',/
     22X,'V11')
      TEMP=ARRAY(LB,1)
C TEMPERATURE VARIATION OF L-POINT ENERGY GAP AND BAND-EDGE EFFECTIVE MASS
      EGG=(13.6+2.1E-03*TEMP+2.5E-04*(TEMP**2))*1.0E-03
      BET=7.06-(3.2E-03*TEMP)+(7.4E-06*(TEMP**2))
      COR=(7.6/BET)**(2./3.)
      MASS=0.0159*COR
      CONST=4*VALNO*4.831E15/SQRT(PIE)
      DO 401 LA=2,8,1
      C(LA-1)=ARRAY(LB,LA)
  401 CONTINUE
C ULTRASONIC VELOCITIES-NO ELECTRONIC CONTRIBUTION
      CALL VEL(C,VC)
C CALCULATION OF THE FERMI ENERGY-
  100 CNO=CONST*((MASS*TEMP)**1.5)/2
      DELT=(-1*PIE*VALNO*(2*MASS*FASS)**1.5)*SQRT(1.38E-16*TEMP)/((1*(PL
     1ANK**2)))/PLANK
      DELT=DELT/6.0
      NEW=0.0
   20 CALL FERMI(0.5,NEW,FKNP2,A2R,R2)
      CALL FERMI(1.5,NEW,FKNP32,A2R,R2)
      SUM=((FKNP2+(2*BOLTZ*TEMP/EGG)*FKNP32)*CNO)-NC
      IF(SUM)21,21,22
   21 NEW=NEW+10.0
      GOTO20
   22 NEW=NEW-10.0
      IF(NEW.LT.9.0)GOTO70
   29 CALL FERMI(0.5,NEW,FKNP2,A2R,R2)
      CALL FERMI(1.5,NEW,FKNP32,A2R,R2)
      TUM=((FKNP2+(2*BOLTZ*TEMP/EGG)*FKNP32)*CNO)-NC
      IF(TUM)23,23,24
   23 NEW=NEW+1.0
      GO TO 29
   24 NEW=NEW-1.0
      IF(NEW.LT.17.0) GOTO70
   25 CALL FERMI(0.5,NEW,FKNP2,A2R,R2)
      CALL FERMI(1.5,NEW,FKNP32,A2R,R2)
      RUM=((FKNP2+(2*BOLTZ*TEMP/EGG)*FKNP32)*CNO)-NC
      IF(RUM)26,26,41
   26 NEW=NEW+0.1
      GOTO25
   41 NEW=NEW-0.1
   42 CALL FERMI(0.5,NEW,FKNP2,A2R,R2)
      CALL FERMI(1.5,NEW,FKNP32,A2R,R2)
      VUM=((FKNP2+(2*BOLTZ*TEMP/EGG)*FKNP32)*CNO)-NC
      IF(VUM)43,43,27
   43 NEW=NEW+0.01
      GO TO 42
   70 CALL FERMI(TEMP,CNO,F,F32,NEW,NC)
   27 FEN=NEW*BOLTZ*TEMP
      IF(NEW.LT.0.0) GOTO103
      IF(NEW.LT.20.0)GOTO101
      CALL FERMI(-0.5,NEW,FKNN2,A2R,R2)
      CALL FERMI(0.5,NEW,FKNP2,A2R,R2)
      GOTO102
```

```
101 NUM=(NEW*10)+41
    MUM=(NEW+0.1)*10+41
    CALL DATE(NEW,DATA)
    IF(NEW-4.0)300,301,301
300 FKNN2=2*(WFD(NUM)+DATA*(WFD(MUM)-WFD(NUM)))*1.0E-5
    GOTO302
301 FKNN2=2*(WFD(NUM)+DATA*(WFD(MUM)-WFD(NUM)))*1.0E-4
302 FKNP2=F(NUM)+DATA*(F(MUM)-F(NUM))
    GOTO102
103 CALL FERM4(-0.5,NEW,FKNN2)
    CALL FERM4(0.5,NEW,FKNP2)
102 TEMP=TEMP
C ELECTRONIC CONTRIBUTION FOR EACH ELASTIC CONSTANT
    DO62 N=1,7
    DELCN(N)=DELT*DEF(N)*(FKNN2+(6*BOLTZ*TEMP*FKNP2/EGG))
    RATIO(N)=DELCN(N)/C(N)
    CN(N)=C(N)-DELCN(N)
 62 CONTINUE
C ELECTRONIC CONTRIBUTION TO THE ULTRASONIC VELOCITIES
    CALL VEL(CN,V)
    DO500 NZ=1,1
    VS(NZ)=VO(NZ)-V(NZ)
500 CONTINUE
    WRITE(6,450) TEMP,FEM,MASS,(DELCN(NF),NF=1,7)
450 FORMAT(F6.0,9E12.4)
200 CONTINUE
60  CONTINUE
201 CONTINUE
    STOP
    END


    SUBROUTINE FERM1(CAY,N,FKN,A2B,B2)
C CALCULATES FK(NEW) FOR NEW GREATER THAN 20
    INTEGER B2
    REAL N,SUM,FKN
    DIMENSION A2B(6),B2(6)
    SUM=0.0
  3 DO2 I=1,6
    SUM=SUM+A2B(I)*(N**(-B2(I)))
  2 CONTINUE
    FKN=(N**(CAY+1))*(SUM+1)/(CAY+1)
    RETURN
    END


    SUBROUTINE FERM2(TEMP,CNO,F,F32,NEW,NO)
C CALCULATES FERMI LEVEL FOR 0-NEW-20 (USING THE MACDOUGALL AND STONER
C TABULATIONS)
    DIMENSION F(241),F32(241)
    REAL TEMP,BOLTZ,EGG,F,F32,NEW,NO
    INTEGER NUM
    BOLTZ=8.617E-05
    EGG=(13.6+2.1E-03*TEMP+2.5E-04*(TEMP**2))*1.0E-03
    NEW=-4.0
  1 NUM=(NEW*10)+41
    SUM=((F(NUM)+(3*BOLTZ*TEMP*F32(NUM)/EGG))*CNO)-NO
    IF(SUM) ,2,3
  2 NEW=NEW+4.0
    GOTO1
  3 NEW=NEW-3.0
    IF(NEW.LT.-5.0) GO TO 12
  6 NUM=(NEW*10)+41
    SUM=((F(NUM)+(3*BOLTZ*TEMP*F32(NUM)/EGG))*CNO)-NO
    IF(SUM)4,4,5
  4 NEW=NEW+1.
    GOTO6
  5 NEW=NEW-0.9
  7 NUM=(NEW*10)+41
    SUM=((F(NUM)+(3*BOLTZ*TEMP*F32(NUM)/EGG))*CNO)-NO
    IF(SUM)8,9,9
  8 NEW=NEW+0.1
    GOTO7
  9 NUM=((NEW-0.1)*10)+41
    STF=F(NUM)-F(MUM)
    STF32=F32(NUM)-F32(MUM)
    DO10 J=1,10
    F12=F(MUM)+STF*(0.1*J)
    X=0.01*J
    F31=F32(MUM)+STF32*(0.1*J)
    SUM=((F12+(3*BOLTZ*TEMP*F31)/EGG))*CNO-NO
    IF(SUM.GT.0.0)GOTO11
 10 CONTINUE
 11 NEW=(NEW-0.1)+X
    RETURN
 12 CALL FERM3(TEMP,CNO,NO,NEW)
    RETURN
    END


    SUBROUTINE FERM3(TEMP,CNO,NO,NEW)
C CALCULATES FERMI LEVEL FOR NEW LESS THAN 0.0
    REAL TEMP,CNO,NO,NEW
    BOLTZ=8.617E-05
    EGG=(13.6+2.1E-03*TEMP+2.5E-04*(TEMP**2))*1.0E-03
    NEW=-3.0
  1 CALL FERM4(0.5,NEW,FKNP2)
    CALL FERM4(1.5,NEW,FKNP32)
    SUM=((FKNP2+(2*BOLTZ*TEMP/EGG)*FKNP32)*CNO)-NO
    IF(SUM)1,2,2
  2 NEW=NEW-1.0
    GOTO 4
  3 NEW=NEW+1.0
  4 CALL FERM4(0.5,NEW,FKNP2)
    CALL FERM4(1.5,NEW,FKNP32)
    SUM=((FKNP2+(2*BOLTZ*TEMP/EGG)*FKNP32)*CNO)-NO
    IF(SUM)3,3,5
```

```
   NEW=NEW-0.1
   GOTO4
 6 NEW=NEW+0.1
 9 CALL FERMI4(0.5,NEW,FKNP2)
   CALL FERMI4(1.5,NEW,FKNP32)
   TUM=((FKNP2+(2*BOLTZ*TEMP/EGC)*FKNP32)*CNC)-NC
   IF(TUM)8,7,7
 7 NEW=NEW-0.01
   GOTO9
 3 NEW=NEW+0.01
   RETURN
   END


   SUBROUTINE FERMI4(CAY,NEW,FKN)
C CALCULATES FK(NEW) FOR NEW LESS THAN 0.0
    REAL CAY,NEW,FKN,TOTAL
   DIMENSION GAMMA(3)
   SQRTPI=SQRT(3.14)
   GAMMA(1)=SQRTPI
   GAMMA(2)=SQRTPI/2
   GAMMA(3)=3*SQRTPI/4
   JAY=CAY+1.5
   TOTAL=EXP(NEW)
   TOTAL=TOTAL-(EXP(2*NEW)/(2**(CAY+1)))
   TOTAL=TOTAL+(EXP(3*NEW)/(3**(CAY+1)))
   FKN=GAMMA(JAY)*TOTAL
   RETURN
   END


   SUBROUTINE VEL(CN,V)
   REAL CN,PV,V
   DIMENSION CN(7),PV(14),V(14)
   PV(1)=CN(1)
   PV(2)=((CN(7)+CN(6))+SQRT((CN(6)-CN(7))**2+4*(CN(4)**2)))/2
   PV(3)=((CN(7)+CN(6))-SQRT((CN(6)-CN(7))**2+4*(CN(4)**2)))/2
   PV(4)=((CN(1)+CN(6))+SQRT((CN(6)-CN(1))**2+4*(CN(4)**2)))/2
   PV(5)=CN(7)
   PV(6)=((CN(1)+CN(6))-SQRT((CN(6)-CN(1))**2+4*((CN(4)**2)))/2
   PV(7)=CN(3)
   PV(9)=CN(6)
   PV(9)=((CN(1)+CN(5))/2+CN(6)-CN(4)+SQRT((CN(1)/2-CN(5)/2-CN(4))**2
  1+((CN(3)+CN(5)-CN(4))**2)))/2
   PV(10)=(CN(7)+CN(6))/2+CN(4)
   PV(11)=(((CN(1)+CN(5))/2+CN(6)-CN(4)-SQRT((CN(1)/2-CN(5)/2-CN(4))**
  12+(CN(3)+CN(6)-CN(4))**2))/2
   PV(12)=((((CN(1)+CN(5))/2+CN(6)+CN(4)))+SQRT((CN(1)/2-CN(5)/2+CN(4
  1))**2+(CN(3)+CN(6)+CN(4))**2)))/2
   PV(13)=((CN(7)+CN(6))/2-CN(4)
   PV(14)=((((CN(1)+CN(5))/2+CN(6)+CN(4)))-SQRT((CN(1)/2-CN(5)/2+CN(4
  1))**2+(CN(3)+CN(6)+CN(4))**2))/2
   DO 15 NN=1,14
```

```
   SUBROUTINE LATE(NEW,DATA)
C INTERPOLATION FOR FERMI SUBROUTINE
   REAL NEW,DATA,FRED
   INTEGER NEWT
   FRED=NEW*10
   NEWT=FRED
   SIG=NEWT
   DO1 I=1,10
   DATA=(I*0.1)-0.1
   HALT=FRED-DATA
   IF(SIG-HALT)1,2,2
 1 CONTINUE
 2 DATA=DATA
   RETURN
   END
```

APPENDIX 3

THE LEAST-MEAN-SQUARES COMPUTER PROGRAMME

The elastic stiffness costants are derived from the experimentally measured ultrasonic velocities by a minimisation of the parameter SUMSQ ,

$$\text{SUMSQ} = \sum_{i=1}^{n} \left[\frac{\text{Calculated } \rho V_i^2}{\text{Measured } \rho V_i^2} - 1 \right]^2$$

The computer programme calculates the elastic constants as a function of temperature applying the thermal expansion data of White (1972).

Nomenclature

COEFF (I)	=	V_i	Experimentally measured velocity
ERR (I)	=	$\pm \Delta V_i$	Error in velocity measurement
SOLN (I)	=	C_{ij}	Calculated elastic constant
MAX (I)	=		Maximum elastic constant
MIN (I)	=		Minimum elastic constant
STEP (I)	=	ΔC_{ij}	Change in elastic constant
SMALL	=		Minimum SUMSQ required
DENS	=	$\rho_{R.T.}$	Room temperature density
DELT (N,M)	=		Temperature dependence of the velocities
TEM (I) ALPHAI (I) APPHA2 (I)	=	T	Thermal expansion data of White (1972)
BETAX	=	x axis	Temperature variation of the linear dimensions
BETAZ	=	z axis	
BETAYZ	=	yz axis	
DENS 1	=	ρ_T	Density corrected for thermal expansion
CONST 1 CONST 2 CONST 3 Q	=	SUMSQ	

```
C LEAST-MEAN-SQUARES DETERMINATION OF THE TEMPERATURE VARIATION OF THE
C ELASTIC CONSTANTS-RHOMBOHEDRAL CRYSTAL STRUCTURE
C PV1=X LONGITUDINAL,PV2=X FAST SHEAR,PV3= X SLOW SHEAR,
C PV4= Z LONGITUDINAL,PV5= Z SHEAR
C PV6= -YZ FAST SHEAR PV7= -YZ LONGITUDINAL,PV8= -YZ SLOW SHEAR
C ONE START READ,WRITE,
      INTEGER JAY,CYCLE,TEM
      REAL MA200,MI200,V200,SQ200
      REAL HOLD,SOLN,CONST1,CONST2,CONST3,STEP,MIN,MAX
      DIMENSION TEM(13),ALPHA1(13),ALPHA2(13),ERR(8)
      DIMENSION COEFF(8),MAX(6),MIN(6),STEP(6),SOLN(6),SUMSQ(2),HOLD(6),
     1CORR(6)
      DIMENSION DELT(16,9),V200(8),MA200(6),MI200(6),SQ200(6)
C READ ULTRASONIC VELOCITIES IN UNITS-*10**5 CM/SEC
      READ(5,1)(COEFF(I),I=1,8)
C READ ERRORS IN ULTRASONIC VELOCITIES
      READ(5,6)(ERR(K),K=1,8)
C READ INITIAL CALCULATED ELASTIC CONSTANTS(SOLN) AND LIMITS(MIN MAX)
C IN UNITS *10**11 DYNE/CM**2
      READ(5,2)(MAX(I),MIN(I),STEP(I),SOLN(I),I=1,6)
C READ NUMBER OF ALLOWED CYCLES AND MIN SUMSQ REQUIRED
      READ(5,3)JAY,SMALL
    1 FORMAT(8F[illegible])
    2 FORMAT(4F[illegible]3)
    3 FORMAT(I5,F1[illegible]2)
    6 FORMAT(8F1[illegible].4)
C READ DENSITY GM/CC
      READ(5,8)DENS
    8 FORMAT(F10.5)
C READ TEMPERATURE DEPENDENCE OF VELOCITIES NORMALISED AT 200K
C T[illegible] (K-2[illegible] STEPS OF 20 AND AT 4.2K.
      READ(5,62)((DELT(M,N),N=1,9),M=1,16)
   62 FORMAT(F[illegible]1,8F[illegible]4)
C READ THERMAL EXPANSION COEFFICIENTS-DATA OF WHITE
C 2[illegible] TO [illegible]-10[illegible] IN STEPS OF 1[illegible],4.2K
C TEM=TEMPERATURE,ALPHA1=PARALLEL Z AXIS,ALPHA2=NORMAL Z AXIS
      READ([illegible])(TEM(I),ALPHA1(I),ALPHA2(I),I=1,13)
  [illegible] FORMAT(F[illegible]1[illegible])
    4 FORMAT(1X,'ULTRASONIC VELOCITIES=',/,'PV1=',F10.4,6X,'PV2=',F10.4,6X,'P
     1V3=',F10.4,6X,'PV4=',F10.4,/,'PV5=',F10.4,6X,'PV6=',F10.4,6X,'PV7=
     2',F1[illegible],6X,'PV8=',F1[illegible])
      WRITE(6,5)(MAX(I),MIN(I),STEP(I),SOLN(I),I=1,6)
    5 FORMAT(8X,'MAX',6X,'MIN',9X,'STEP',9X,'SOLN',/,'C11',4F12.4,/,'C12
     1',4F12.4,/,'C13',4F12.4,/,'C14',4F12.4,/,'C33',4F12.4,/,'C44',4F12
     2.4)
      WRITE(6,7)JAY,SMALL
    7 FORMAT(1X,'ALLOWED CYCLES=',I5,5X,'SMALL=',F1[illegible]2)
      WRITE(6,40)DENS
   40 FORMAT(1X,'DENSITY=',F10.3)
      WRITE(6,61)
   61 FORMAT(1X,'TEMPERATURE COEFFICIENTS OF VELOCITIES REFERENCE AT 200
     1',/,[illegible],'PV1',[illegible],'PV2',[illegible],'PV3',4X,'PV4',4X,'PV5',/X,'PV6
     2',[illegible]'PV7',[illegible]'PV8')
      WRITE(6,[illegible])(([illegible]T(M,[illegible]),[illegible]1,[illegible]),M=1,1[illegible])
   [illegible]
```

```
      WRITE(6,4)(COEFF(K),K=1,8)
   66 FORMAT(1X,'TEMP',9X,'C11',9X,'C12',9X,'C13',9X,'C14',9X,'C33',9X,'
     1C44',9X,'C66',5X,'SUMSQ')
      INIT=200
      DO63 M=2,9,1
      V200(M-1)=COEFF(M-1)/DELT(1,M)
      WRITE(6,67) V200(M-1)
   67 FORMAT([illegible]1F[illegible]4)
   63 CONTINUE
      WRITE(6,66)
C ONE END
C TWO START VELOCITY CALCULATED TEMP AND THERMAL EXPANSION CORRECTIONS
      DO10 NA=1,16
      ST1=1.0
      CYCLE=0
      DO65 KA=2,9,1
      COEFF(KA-1)=V200(KA-1)*DELT(NA,KA)
      TEMP=DELT(NA,1)
   65 CONTINUE
      CALL EXPAND(TEM,ALPHA1,ALPHA2,INIT,TEMP,BETAZ,BETAX,BETAYZ)
C PV1,PV2,PV3 X AXIS VELOCITIES -PV4,PV5 Z AXIS VELOCITIES.-PV6.PV7.PV8
C YZ VELOCITIES
C CORRECTION FOR THE TEMPERATURE VARIATION OF THE ULTRASONIC PATH LENGTH
      COEFF(1)=COEFF(1)*BETAX
      COEFF(2)=COEFF(2)*BETAX
      COEFF(3)=COEFF(3)*BETAX
      COEFF(4)=COEFF(4)*BETAZ
      COEFF(5)=COEFF(5)*BETAZ
      COEFF(6)=COEFF(6)*BETAYZ
      COEFF(8)=COEFF(8)*BETAYZ
C CORRECTION FOR THE TEMPERATURE VARIATION OF THE DENSITY
      DENS1=DENS*BETAZ*(BETAX**2)
C TWO END
C THREE START DEFINE LIMITS OF CONSTANTS C11,C33,C44 RIGIDLY DEFINED
      SOLN(1)=(COEFF(1)**2)*DENS1
      MAX(1)=SOLN(1)*(1.0+ERR(1))**2
      MIN(1)=SOLN(1)*(1.0-ERR(1))**2
      SOLN(5)=((COEFF(4)**2)*DENS1
      MAX(5)=SOLN(5)*(1.0+ERR(5))**2
      MIN(5)=SOLN(5)*(1.0-ERR(5))**2
      SOLN(6)=(COEFF(5)**2)*DENS1
      MAX(6)=SOLN(6)*(1.0+ERR(5))**2
      MIN(6)=SOLN(6)*(1.0-ERR(6))**2
      D[illegible] N[illegible],
      COEFF(N)=(COEFF(N)**2)*DENS1
    9 CONTINUE
C THREE END
C FOUR START LEAST MEANS SQUARE FIT
      DO1[illegible] [illegible],JAY
      CYCLE=CYCLE+1
      DO [illegible] I=1,6
      HOLD(I)=SOLN(I)
      CALL SUMMER(SOLN,COEFF,0,DIF)
      CONST1=Q
   42 IF(CONST1.LT.SMALL)GOTO13
      SOLN(I)=HOLD(I)+STEP(I)
      CALL SUMMER(SOLN,COEFF,0,DIF)
      CONST2=Q
      SOLN(I)=HOLD(I)-STEP(I)
      CALL SUMMER(SOLN,COEFF,0,DIF)
```

```
      CONST2=0
      IF(CONST3-CONST1)10,12,12
   10 SOLN(I)=HOLD(I)-STEP(I)
      GOTO20
   12 IF(CONST2-CONST1)13,14,14
   13 SOLN(I)=HOLD(I)+STEP(I)
      GOTO20
   14 SOLN(I)=HOLD(I)
   2  IF(SOLN(I).GT.MAX(I))SOLN(I)=MAX(I)
      IF(SOLN(I).LT.MIN(I))SOLN(I)=MIN(I)
      [illegible](I)=[illegible](I)
   20 CONTINUE
      DO 15 J=1,6
      IF(COMP(J)-HOLD(J))21,15,21
   15 CONTINUE
      IF(C[illegible].LT.[illegible])GOTO30
   16 [illegible]
      DO 34 J=1,6
      STEP(J)=STEP(J)*0.1
   34 CONTINUE
   21 CONTINUE
C     [illegible]
   31 C[illegible]=(SOLN(1)-SOLN(2))/2
      WRITE(6,30)[illegible],SOLN(1),SOLN(2),SOLN(3),SOLN(4),SOLN(5),SOLN(6),C
     1[illegible]CONST1
   30 FORMAT([illegible]1,7E12.4,E8.4)
      DO 35 J=1,6
      STEP(J)=[illegible]EP(J)/STE
   35 CONTINUE
    1 CONTINUE
      STOP
      [illegible]
      SUBROUTINE [illegible]M1(A,COEFF,D,P)
      DIMENSION A(6),[illegible] COEFF(8)
C     [illegible]
      [illegible](A(1)-[illegible])/2
      [illegible]=[illegible]
      [illegible]=(([illegible]A(5))+SQRT((A(5)-A7)**2+4*A(4)**2))/2
      [illegible]=((A[illegible]+A(6))-SQRT((A(5)-A7)**2+4*A(4)**2))/2
      [illegible]
      P(5)=A([illegible])
      [illegible]=([illegible])/2+(-A(4))
      [illegible]=([illegible]+A(5))/2+A([illegible])+A(4))/2
      Y=(S[illegible]T((A[illegible])/2-A(5)/2+A(4))**2+(A(3)+A(6)+A(4))**2))/2
      P(7)=X+Y
      P(8)=X-Y
      C=(P(1)/COEFF(1)-1.0)**2+(P(2)/COEFF(2)-1.0)**2+(P(3)/COEFF(3)-1.0
     1)**2+(P(4)/COEFF(4)-1.0)**2+(P(5)/COEFF(5)-1.0)**2+(P(6)/COEFF(6)-
     21.0)**2+(P(7)/COEFF(7)-1.0)**2+(P(8)/COEFF(8)-1.0)**2
      RETURN
      END
      SUBROUTINE EXPAND(ITEM,ALPHA1,ALPHA2,[illegible],BETAZ,BETAX,BETAYZ
C     THERMAL EXPANSION [illegible]
      [illegible],KAY,INCRE,K
      [illegible] ALPHA1(13),ALPHA2(13)
      [illegible]
      [illegible]
      [illegible]-1
      [illegible]
      [illegible],1,[illegible]
      KAY=[illegible]M(I-1)-[illegible]M(I)
      DO2 I=1,KAY
      IF(INCRE.EQ.0)GOTO10
      FRED=KAY-K
      GAY=KAY
      DA1=ALPHA1(I)+((ALPHA1(I-1)-ALPHA1(I))*(FRED/GAY))
      DA2=ALPHA2(I)+((ALPHA2(I-1)-ALPHA2(I))*(FRED/GAY))
      DA3=DA2+(DA1-DA2)*3.0/[illegible]
      BETAZ=BETAZ*(1-DA1)
      BETAX=BETAX*(1-DA2)
      BETAYZ=BETAYZ*(1-DA3)
      INCRE=INCRE-1
      IF(INCREM.LT.[illegible])GO TO 1[illegible]
    2 CONTINUE
    3 CONTINUE
   10 RETURN
      END
ILF
```

REFERENCES

AKGOZ Y.C., FARLEY J.M. and SAUNDERS G.A. (1972) J. Mat. Sci. 7, 598

ANDERSON O L. (1965) 'Physical Acoustics' Vol.3B, 43, ed. W.P. Mason (Academic Press)

ANTCLIFFE G A and BATE R.T (1966) Phys. Letters 23, 622

ANTCLIFFE G A. and BATE R.T. (1969) Phys. Rev. 160, 531-37

APPS M J (1974) J. Phys. F Metal Phys 4, 47

ARAKI K. and TANAKA T. (1972) Jap. J. of App Phys 11, 472-9

AUBREY J.E. and CHAMBERS R.G. (1957) J. Phys. Chem Solids 3, 128-132

AUGERI R. and FREEDMAN S.J (1967) J. Acoust. Soc. Am. 41, 1369-70

BALAMUTH L. (1934) Phys. Rev. 45, 715

BALSLEV I. (1966) Phys. Rev. 143, 636-47

BARRETT C.S (1960) Aust. J. Phys. 13, 209

BARRETT C.S , CUCKA A.P. and HAEFNER K. (1963) Acta Cryst. 16, 451-453

BATE R.N., EINSPRUCH N.G. and MAY P.J (1969) Phys. Rev. 186, 599

BHARGAVA R N. (1967) Phys. Rev. 156, 785-97

BOYLE W S. and BRAILSFORD A.D. (1960) Phys. Rev. 120, 1943-49

BOYLE W S. and SMITH G.E. (1962) Progress in Semiconductors 7, 3

BRANDT N.B. and SVISTOVA E A. (1970) J. Low Temp. Phys. (G.B.) Vol.2 No.1, p.1-36

BRANDT N.B., SVISTOVA E A. and SEMENOV M.V. (1970) Soviet Phys. Te. (USA) 59, 434-44

BRANDT N B , DITTMAN Kh and PONDMAREV Ya. G. (1972) Soviet Solid State 13, 2408

BRANDT N B , SVISTOVA E.A. and VALEEV R.G. (1969) Soviet Physics JETP 28, 245

BRIDG MAN P.W. (1924) Proc. Natl. Acad Sci. US. 10, 411

BROWN D.M. and HEUMANN F K. (1964) J. App. Phys 35, 1947

BROWN D M. and SILVERMAN S.J. (1964) Phys Rev. A136, 290-99

BROWNELL D M and HYGH E.H. (1967) Phys. Rev. 164, 909

BRUGGER K (1965) J. App. Phys. 36, 759-68

BRUNER L.J and KEYES R W. (1961) Phys Rev Letters 7, 55

CAVE E.F. and HOLROYD L.V. (1960) J. App. Phys. 31, 1357

CHAO P.W., CHU H.T. and KAO Y H. (1974) Phys. Rev. B 9, 4030

CHU H.T. and KAO Y H (1970) Phys. Rev. B 1, 2377-2384

COHEN M.H. (1961) Phys. Rev. 121, 387

COLLAN H K., KRUSIUS M. and PICKETT G.R. (1969) Phys. Rev. Letters 23, 11-13

CUCKA A.P. and BARRETT C.S. (1962) Acta Cryst. 15, 865-72

CULLITY B.D. (1967) 'Elements of X-ray Diffraction' (Addison-Wesley)

De BRETTEVILLE A , COHEN E.R , BALLATO A.D. and GREENBERG I.N. (1966) Phys. Rev. 148, 575

DINGER R.J and LAWSON A.W. (1970) Phys. Rev B 1, 2418-2423

DRESSELHAUS M.S. (1970) The Physics of Semimetals and Narrowgap Semiconductors - Proceedings of Conference held at Dallas. p.3

DUGUÉ M. (1965) Phys. Stat. Sol. 11, 149

ECKSTEIN Y., RENEKER D H. and LAWSON A.W. (1960) J. App. Phys. 31, 1534

EDELMAN V.S. and KHAIKIN M.S. (1966) Soviet Physics JETP 22, 77

EINSPRUCH N.G. and CSAVINSZKY P. (1963) App. Phys. Letters 2, 1

EPSTEIN S. and De BRETTEVILLE A.P. (1965) Phys. Rev. 138, A771

ERFLING M.D. (1939) Ann. Physik 34, 136

FALICOV L.M and LIN P.J. (1966) Phys. Rev. 141, 562

FARLEY J M (1973) Ph.D. Thesis, University of Durham

GALT J.K., YAGER W.A , MERRITT F.R , CETLIN B.B and BRAILSFORD A.D (1959) Phys. Rev. 114, 1396-1413

GOLDSMID H J (1970) Phys. Status Solidi A1, 7-28

GOLIN S. (1968) Phys Rev. 176, 830

GOPINATHAM K.K. and PADMINI A.R.K L (1974a) J Phys. D . App. Phys. 7, 32

GOPINATHAM K.K. and PADMINI A.R.K.L. (1974b) J. Phys. Chem. Solids 35, 1598-98

GOPINATHAN K.K. and PADMINI A.R.K.L. (1975) Solid State Comm. 16, 817-821

GRISON E. (1951) J. Chem. Phys. 19, 1109-1113

HALL J.J. (1967) Phys. Rev. 161, 756

HANSON M. (1958) 'Constitution of Binary Alloys' (McGraw Hill)

HEARMAN R.F.S. (1961) 'An Introduction to Applied Anisotropic Elasticity' (Oxford University Press)

HEBEL L.C. and SMITH G E. (1964) Phys. Letters 10, 273

HERRMAN R., BRAUNE W. and KUKA G. (1974) Phys. Stat. Sol.(b) 61, k77

HERRMAN R., BRAUNE W. and KUKA G. (1975) Phys. Stat. Sol (b) 68, 233

HILL R. (1952) Proc. Physical Soc. (Lond.) A65, 349-54

HOUSTON B.B. and STRAKNA R E. (1964) Bull Am. Phys. Soc. (2) 9, 646

INOUE S. and TSUJI M. (1967) J. Phys. Soc. Jap. 22, 1191

IVANOV G.A. and POPOV A.M. (1964) Soviet Physics Solid State 5, 1754

JACOBSON D.M. (1973) Phys Stat. Sol.(b) 58, 243

JAIN A.L. (1959) Phys. Rev. 114, 1518

JAIN A.L. and KOENIG S.H. (1962) Phys. Rev. 127, 442-6

KAMMER E.W. (1964) J. Acoust. Soc. Am 37, 929-31

KAMMER E.W., CARDINAL L.C., VOLD C.L and GLICKSMAN M.E. (1972) J. Phys. Chem. Solids 33, 1891-98

KAO Y.H. (1963) Phys. Rev. 129, 1122

KATSUKI S. (1969) J. Phys. Soc. Jap. 26, 696

KEYES R.W. (1967) Solid State Physics Vol.20 p.38 (Academic Press)

KEYES R.W. (1961) I.B.M. J. Res. Develop. 5,266

LAX B. (1960) Bull. Am. Phys. Soc. 5, 167

LAX B. (1958) Rev. Mod. Phys. 30, 122

LENKKERI J.T. and LAKTEENKORVA E.E. (1973) J. Phys. F Metal Physics 3, 1781-88

LERNER L.S., CUFF K.F. and WILLIAMS L.R. (1968) Rev. Mod. Physics 40, 770

LERNER B G. and MARTIN L.S. (1972) Phys. Rev. B 6, 3032

LOPEZ A.A. (1966) I.B.M. Journal of Research RW 101

LOVE A.E.H. (1927) 'A Treatise on the Mathematical Theory of Elasticity' (Dover)

MACDOUGAL J. and STONER E.C. (1939) Phil. Trans. Royal Soc. A237, 67

MASON W.P. (1947) Bell Syst. Tech. J. 26, 80

MAYNELL C. (1972) Ph.D. Thesis, University of Durham

MICHENAUD J.P. and ISSI J P. (1972) J. Phys. C . Solid State Physics 5, 3061

MUSGRAVE M.J.P. (1970) 'Crystal Acoustics', Holden-Day (San Francisco)

NOOTHOVEN VAN GOOR J.M. (1971) Phillips Res. Rept. Suppl. 1971 No.4

NOOTHOVEN VAN GOOR J.M. and TRUM H.M G.J. (1968) J. Phys. Chem. Solids 29, 341-45

NOOTHOVEN VAN GOOR J.M and TRUM H.M.G.J. (1969) J. Phys. Chem. Solids 30, 1636-38

NYE J.F. (1957) 'Physical Properties of Crystals' (Oxford Clarendon Press)

OELGARD G. and HERRMAN R. (1973) Phys. Stat. Sol.(b) 58, 181

OKTU O. and SAUNDERS G A (1967) Proc. Phys Soc. 91, 156

PACE N. and SAUNDERS G A. (1971) J. Phys. Chem. Solids 32, 1585-1601

PADADAKIS E.P. (1966) J. Acoust. Soc. America 40, 863-76

PFANN W G. (1958) 'Zone Melting' (John Wiley and Sons)

PHILLIPS N.E. (1960) Phys Rev 118, 644-7

PRATT G.W. and DAS A. (1970) The Physics of Semimetals and Narrowgap Semiconductors - Proceedings of Conference held at Dallas

REUSS A. (1929) Z. Agnew. Math. Mech. 9, 55

SAUNDERS G.A. and SUMENGEN Z. (1972) J. Phys. F : Metal Physics 2, 972

SCHNEIDER G. and TRINKS R. (1972) Z. Naturforsch, 27a, 1639-45

SHOENBURG D. (1939) Proc. Royal Soc. A170, 341

SMITH G.E. (1962) Phys. Rev. Letters 9, 487

SMITH G E., BARAFF G.A. and ROWELL J M. (1964) Phys Rev. 135, A1118-1124

SMITH G.E., HEBEL L.C. and BUCHSBAUM S.J. (1963) Phys. Rev. 129, 154

SMITH G.E. and WOLFE R. (1962) J. App. Phys. 33, 841

THOMAS C.B. and GOLDSMID H.J. (1970) J. Phys C . Solid State Physics 3, 696

TICHOVOLSKY E.J. and MAVROIDES J.G. (1969) Solid State Commun. 7, 927

TILLER W.A , JACKSON K.A., RUTTER J.W. and CHALMERS B. (1953) Acta Met. 1, 428

THOMPSON N. (1936a) Proc. Royal Soc. A155, 111

THOMPSON N. (1938) Proc. Royal Soc. A164, 24

TRUELL R , ELBAUM C. and CHICK B.B. (1969) 'Ultrasonic Methods in Solid State Physics' (Academic Press, New York)

VECCHI M P and DRESSELHAUS M.S. (1974) Phys. Rev. B 10, 771

VOIGT W. (1928) Lehrbuch der Kristallphysik 962

WALTHER K. (1968) Phys. Rev. 174, 782

WATERMAN P.C. (1959) Phys. Rev. 113, 1247

WEHRLI L. (1968) Phys. Kondens Materie, 8, 87

WHITE G.K. (1972) J. Phys. C : Solid State Phys. 5, 2731-45

WIENER D (1962) Phys. Rev. 125, 1226

YIM W.M. and DISMUKES J.P. (1967) J. Phys. Chem. Solids Suppl. 1967, 187-196

GUNTON D J and SAUNDERS(1972) J Mat Sci 7 (1972), 1061 - 1065